Solid State Joining of Dissimilar Titanium Alloys

Todd W. Morton

A dissertation
submitted in partial fulfillment of the
requirements for the degree of

Doctor of Philosophy

University of Washington
2015

Reading Committee:
Brian Flinn, Chair
Ramulu Mamidala, Co-Chair
Paul Edwards

Program Authorized to Offer Degree:
Materials Science and Engineering

University of Washington

Abstract

Solid State Joining of Dissimilar Titanium Alloys

Todd Wesley Morton

Chair of Supervisory Committee:
Professor Brian Flinn and Professor Mamidala Ramulu
Materials Science and Engineering

Solid state joining of titanium via friction stir welding and diffusion bonding have emerged as enablers of efficient monolithic structural designs by the eliminations fasteners for the aerospace industry. As design complexity and service demands increase, the need for joints of dissimilar alloys has emerged. Complex thermomechanical conditions in friction stir weld joints and high temperature deformation behavior differences between alloys used in dissimilar joints gives rise to a highly variable flow pattern within a stir zone. Experiments performed welding Ti-6Al-4V to β21S show that mechanical intermixing of the two alloys is the primary mechanism for the generation of the localized chemistry and microstructure, the magnitude of which can be directly related to pin rotation and travel speed weld parameters. Mechanical mixing of the two alloys is heavily influenced by strain rate softening phenomena, and can be used to manipulate weld nugget structure by switching which alloy is subjected to the advancing

side of the pin. Turbulent mixing of a weld nugget and a significant reduction in defects and weld forces are observed when the β21S is put on the advancing side of the weld where higher strain rates are present.

Chemical diffusion driven by the heat of weld parameters is characterized using energy dispersive x-ray spectroscopy (EDS) and is shown to be a secondary process responsible for generating short-range chemical gradients that lead to a gradient of alpha particle structures. Diffusion calculations are inconsistent with an assumption of steady-state diffusion and show that material interfaces in the weld nugget evolve through the break-down of turbulent interface features generated by material flows.

A high degree of recrystallization is seen throughout the welds, with unique, hybrid chemistry grains that are generated at material interfaces in the weld nugget that help to unify the crystal structure of dissimilar alloys. The degree of recrystallization is tied to the localized thermal profile in the weld nugget as well as the heating rates of a given set of weld parameters. Slow kinetics of alpha dissolution relative to the heating rate and process times of friction stir welding suggest an alpha-particle assisted super-transus recrystallization process contributes to a refined grain size in weld parameters utilizing high travel speed.

TABLE OF CONTENTS

LIST OF FIGURES

LIST OF TABLES

ACKNOWLEDGEMENTS

The course work, experiments, writings and presentations that accompany this dissertation to fulfil the requirements for a Ph.D. have taken 8 years of my life to finish. There are innumerable people along the way that have provided their help along the way, and share the credit for this accomplishment.

My academic mentors, Profs. Ramulu and Flinn, took the chance to let me work on a unique project that bridges Mechanical Engineering and Materials Science and Engineering. I very much appreciate the motivation they have provided when I had none, the ideas they provided when mine were convoluted and the freedom they provided to let me be creative while giving the structure I needed to complete the work. Dr. Paul Edwards has been invaluable both as a committee member and for his contributions to the field of my research and his availability and enthusiasm to discuss this work. I am hopeful others benefit from this research, but in the meantime, I am confident to say that I will always be the greatest beneficiary of this work thanks to their mentoring.

My colleagues at The Boeing Company have been an invaluable resource during this endeavor, and I would like to thank them as well. Rod Boyer and Jim Cotton have been a constant source of knowledge and practical experience in my development as a titanium metallurgist, without whom I would have never had the opportunity to research and learn about a subject I find so fascinating. I would also like to thank Marc Petersen for his tireless support as I attempted to make welds, and to Martin Farris for his wealth of metallographic knowledge and support.

I would like to thank the people and organizations that make the Metals Affordability Initiative Program happen, without which I would not have a framework or funding to pursue this research. Specifically, thank you to Megan Harper and John Fanning at TIMET for their help in obtaining materials and their insights.

A special thanks to Arun Devaraj at Pacific Northwest National Laboratory for is enthusiasm and availability in the microscopy time that made this work possible, and to Prof. Kapur for his service on my committee.

Finally, thank you to my family. My parents, brothers and sisters had no choice but to be related to a graduate student, but their encouragement along the way has made the journey so much easier. My loving wife Meghan, who has never known me not as a student, I thank the most for her patience, encouragement and understanding as I spent countless nights, weekends and all the time in between away from her. To our future together – I love you.

CHAPTER 1: INTRODUCTION AND LITERATURE REVIEW

1.1 Overview of Diffusion Bonding and Friction Stir Welding Titanium in Aerospace

The continued development of titanium alloys for aerospace use has allowed their adoption across an increasingly wide variety of platforms, driven by a combination of maximizing performance while reducing overall lifecycle costs. Transitioning away from traditional aluminum built-up structure to titanium assemblies has been mandated by galvanic corrosion considerations when in contact with carbon fiber composite materials, as well as a steady rise in mechanical loading and thermal loading [Boyer, 1996].

The difficulties and expense associated with the production of titanium and the subsequent fabrication of titanium structure has pushed the development of advanced joining and forming processes. The detrimental effects of an as-cast microstructure in titanium to both mechanical performance and formability necessitates solid-state joining processes over traditional fusion welds. Similarly, the relatively poor room-temperature formability of titanium necessitates superplastic forming when complex contours and deep draws are required. Combining these technologies with diffusion bonding allows for complete monolithic structure out of titanium to be developed with minimal machining waste and minimal assembly time; improving both structural performance and cost [Milne, 2011]. As the complexity and number of applications for solid-state joining and superplastic forming in titanium grows, the need has arisen to create structure using multiple titanium alloys to optimize mechanical performance, thermal stability and resistance to chemical attack all while not regressing to built-up, fastener-heavy assembly.

This review intends to assess the state of the literature as it pertains to fundamental understandings of titanium and its metallurgy during friction stir welding of dissimilar alloys.

The complexity of the welding process requires fundamental knowledge of titanium physical metallurgy, phase transformations, diffusion, and thermomechanical processing theory. The mechanics of the friction stir welding process as they relate to material deformation, material flow and heat input will be assessed, as they are critical in understanding the resultant metallurgical structures. Finally, relevant literature in dissimilar alloy friction stir welding will be summarized, with the intention of identifying gaps in the literature as motivation for research.

1.2 Titanium Metallurgy

1.2.1 Alloying Additions

To properly engineer any advanced forming or joining process, an understanding of the material's composition and phases is essential. Pure metallic titanium stabilizes to the hexagonal close-pack (HCP) crystal structure, or α-phase, and exhibits an allotropic transformation at 882.5 °C to a body-centered cubic (BCC) structure, or β-phase. The temperature at which this transformation occurs, the β-transus, can be manipulated up or down with varying alloy additions – categorized broadly into α and β stabilizers. α stabilizers either increase or have no impact on the β-transus temperature, while β stabilizers decrease the β-transus temperature. The most common alpha stabilizers are Aluminum and Oxygen, more broadly however, α stabilizers tend to be Simple Metals and elements of small atomic size of Groups XIII-XVII in the periodic table [Boyer 1994].

The overall discussion of phase stability tends to complicate more as beta stabilizers are introduced – and several treatments of the phenomenon of HCP to BCC transformation have been presented. β stabilizers tend to be Transition Metals of Groups IV-VIII like Titanium itself, and the systematic transition from HCP to face-centered cubic (FCC) crystal structures through groups IV to VIII in the periodic table point to an electronic component where interplay of

valence states and electron/atom ratios can stabilize the β-phase over the α-phase. Low temperature specific heat measurements show that a lower density of states at the Fermi level correlates to a higher phase stability when comparing competing phases against one and other. McQuillan notes in a thermodynamic treatment of phase stability the more open structure of BCC (.68 atomic packing factor) versus HCP (.74 atomic packing factor) has a higher vibrational entropy, and thus as temperature increases, the free energy drops off rapidly for a BCC structure to the point that it becomes energetically more favorable than the HCP phase [McQuillan, 1956][Callister, 2003][McQuillan, 1963]. Thermodynamics also allows for discussion of competition between phases and has been used extensively by Kauffman to model binary and multi-component phase diagrams [Kaufman, 1973].

Beta stabilizers fall into two categories depending on the order of phase transformation they promote as you cool the alloy through a given composition on a phase diagram – beta-isomorphous stabilizers promote a continuous first-order phase transformation and beta-eutectoid stabilizing elements promote a higher order decomposition reaction. As you move to the right through the transition metals, the classification changes from isomorphous stabilizer to eutectoid stabilizer. Isomorphous stabilizers include Vanadium, Niobium and Tantalum all from Group V as well as Molybdium. The major eutectoid stabilizers, Manganese, Iron, Cobalt, Nickel and Copper show a monotonic increase in eutectoid temperature as you progress through the row from left to right. The stabilizing power of a beta stabilizer generally increases as it is farther away from Titanium on the periodic table. The phenomena has been explained with an electronic argument suggesting that as the electrons available in the conduction band increase, so does the screening of the ion core, which would favor a symmetric crystal (eg: cubic) as opposed to a non-symmetric crystal [Boyer, 1994][Agev, 1970].

1.2.2 Strengthening Mechanisms and Microstructural Features

Microscopic analysis of microstructural features in titanium alloys, as with all technical alloys, represents an important method for understanding the chemical compositions and thermomechanical processing history within a piece of material. An understanding of phase equilibrium and it's relation to kinetics can be born out with the various morphologies seen in titanium alloys. In the prototypical α-β alloy Ti-6Al-4V, much of the common morphology present in technical alloys can be demonstrated. A major feature present in this alloy system is the primary, or globular alpha. Depending on thermal history, these equiaxed particles are typically on the order of tens of microns in diameter. Thermomechanical processing at temperatures below the beta transus can break up and refine these particles to a consistent and uniform size, while directional processing (e.g. rolling) will present primary alpha particles with a higher aspect ratio. Also present are colonies of alpha platelets that result from the transformation of the beta phase upon cooling. This colony, or acicular α, an order of magnitude smaller than the primary alpha particles in this case, precipitate from β grain boundaries, oriented along one of 12 preferred, or habit, planes in the β BCC system and grow into the bulk of the BCC crystal. As the strain energy from the alpha and beta phase lattice mismatch increases, additional alpha platelets can precipitate normal to an existing platelet to continue the phase transformation in the most energetically favorable manner. In a microstructure dominated by globular alpha and acicular alpha in a matrix of transformed beta, a balance of strength and toughness is achieved that is often desirable for structural applications [Boyer, 1994].

As Ti-6Al-4V is heated above the beta transus and cooled again, the complete dissolution of the α-phase and its precipitation yields a different morphology, referred to as either Widmanstatten or basket-weave alpha. The coarseness of the alpha platelettes is often controlled

most readily by varying the cooling rate of the material. With a high density of crack inhibiting grain boundaries, toughness of the material is maximized at the expense of strength and elongation, while the presence of large prior beta grain boundaries allow for earlier crack initiation in high-cycle fatigue loading scenarios [Boyer, 1994].

Similarly, with a solutionizing heat treatment designed to largely (but not completely) dissolve large, globular alpha particles, rapidly quenching the material and a subsequent ageing heat treatment, a new microstructure can be observed. Finer alpha particles evenly dispersed throughout the beta matrix provide higher levels of precipitation hardening than both a globular primary alpha or Widmanstatten alpha structure, and a higher strength level as predicted by the Hall-Petch relationship. Fine grain size also maintains resistance to crack initiation in fatigue loading, at the expense of elongation and fracture toughness [Boyer, 1994][Callister, 2003]. A summary of microstructures achieved by various thermal processing routes in Ti-6Al-4V can be seen in F**igure 1-1.** Titanium alloys are also capable of evolving a variety of metastable and phases including the ω-phase and diffusionless martensites either via extreme cooling rates, long dwell times at temperature or strain mechanisms.

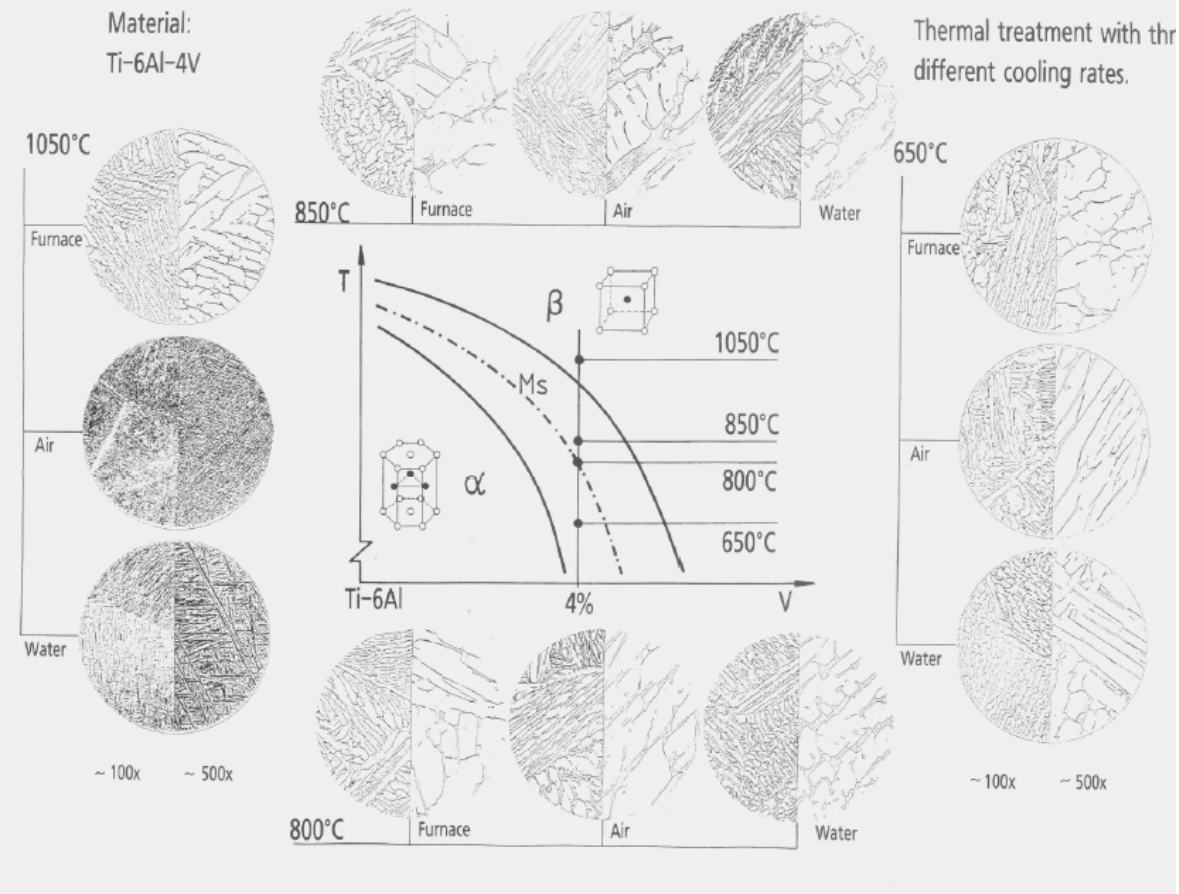

Figure 1-1: Microstructures of Ti-6Al-4V upon various thermal treatments [Boyer, 1994].

1.2.3 Thermomechanical Processing

Titanium base alloys, as with most metals, show a large variation in microstructure and resultant mechanical properties based on how and when heat and deformation are applied. Although reasonable ductility for engineered applications can be demonstrated in most technical alloys at room temperature and down to cryogenic temperatures in the case of α-alloys, high-temperature deformation is needed both to refine the microstructure and produce a shape that can be economically machined into a component.

Titanium alloys exhibit superplasticity at temperatures above ~750C in the case of fine grained α-β alloys strained a relatively low rates, and is dominated by a grain slip mechanism, or

in the case of superplasticity in the β-field, by a diffusion-creep mechanism [Hammond, 1978]. Strains well over 500% can be achieved in some cases without inducing cracks or strain-induced porosity. This can be useful in forming complex sheet structure, as well as intricate isothermal forgings where the continuous work promotes recrystallization and a fine globular alpha and transformed beta microstructure.

The increase in ductility demonstrated above the β transus promotes the use of β-field work, and is often one component of a multi-step breakdown from ingot to usable product form useful for refining the coarse β structure present in as-cast titanium alloys. However, due to subsequent precipitation behavior of the α phase, it is often impossible to achieve a uniform microstructure and deformation while in the α-β phase field must be employed during the final steps. In practice, high temperature work often takes place across multiple phase fields during a single operation due to cooling by the tooling or adiabatic heating from the deformation. Balancing the need for aggressive deformation to produce a refined microstructure with the limitations of tooling, equipment and the implications of crossing the β-transus leads to a very tightly controlled processing window. Strain hardening induced during higher strain rate deformations can be used to induce recrystallization during a subsequent anneal, or simply stress-relieved.

1.2.4 Solid State Diffusion in Titanium

In the discussion of solid state joining techniques often prescribed for maintain the desirable mechanical properties of titanium, diffusion becomes the mechanism of producing a metallurgical bond. The applicability of diffusion theory and the resultant equations is reliant on high quality experimental data to determine diffusion coefficients via penetration curves for a

given material system, and titanium is no exception. Hendricks [Hendricks, 1962] prepared a series of experiments that remains one of the most useful collection of diffusion data for the study of technical alloy compositions, covering self-diffusion of titanium and the interdiffusion of zirconium, molybdenum and oxygen in both α- and β-titanium. Data was generated by producing binary compositions of titanium and the elements mentioned above, and roll bonding the binary alloy together with pure titanium to create a diffusion couple that could subsequently be annealed at various times and temperatures. The diffusion couples were sectioned and analyzed using x-ray spectroscopy to generate concentration profiles, an example of which is shown in **Figure 1-2**.

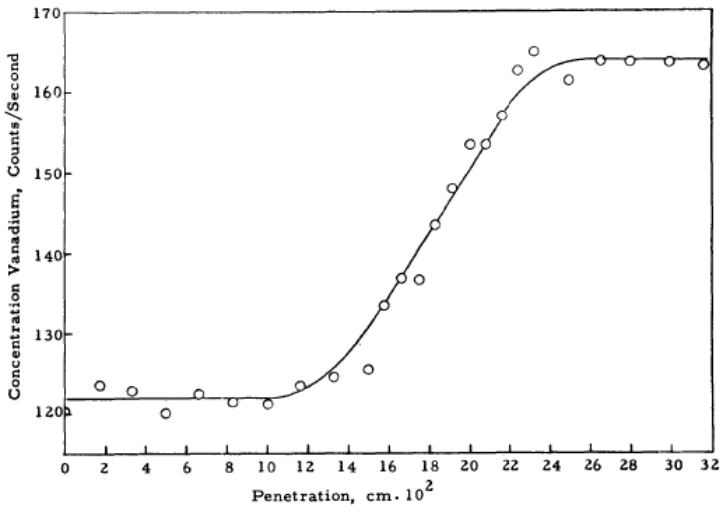

Figure 1-2: Penetration curve of Ti/Ti-5V diffusion couple, annealed 16 hours at 1200°C [Hendricks, 1962].

The work of Elliot is of particular importance to the phenomenon under study in this work due to isolation of diffusion coefficients for the elements, relative concentrations and temperatures that present themselves in the friction stir welding of dissimilar titanium alloys. The findings of Elliot regarding diffusion coefficients of alloying elements in titanium are summarized in **Figure 1-3**.

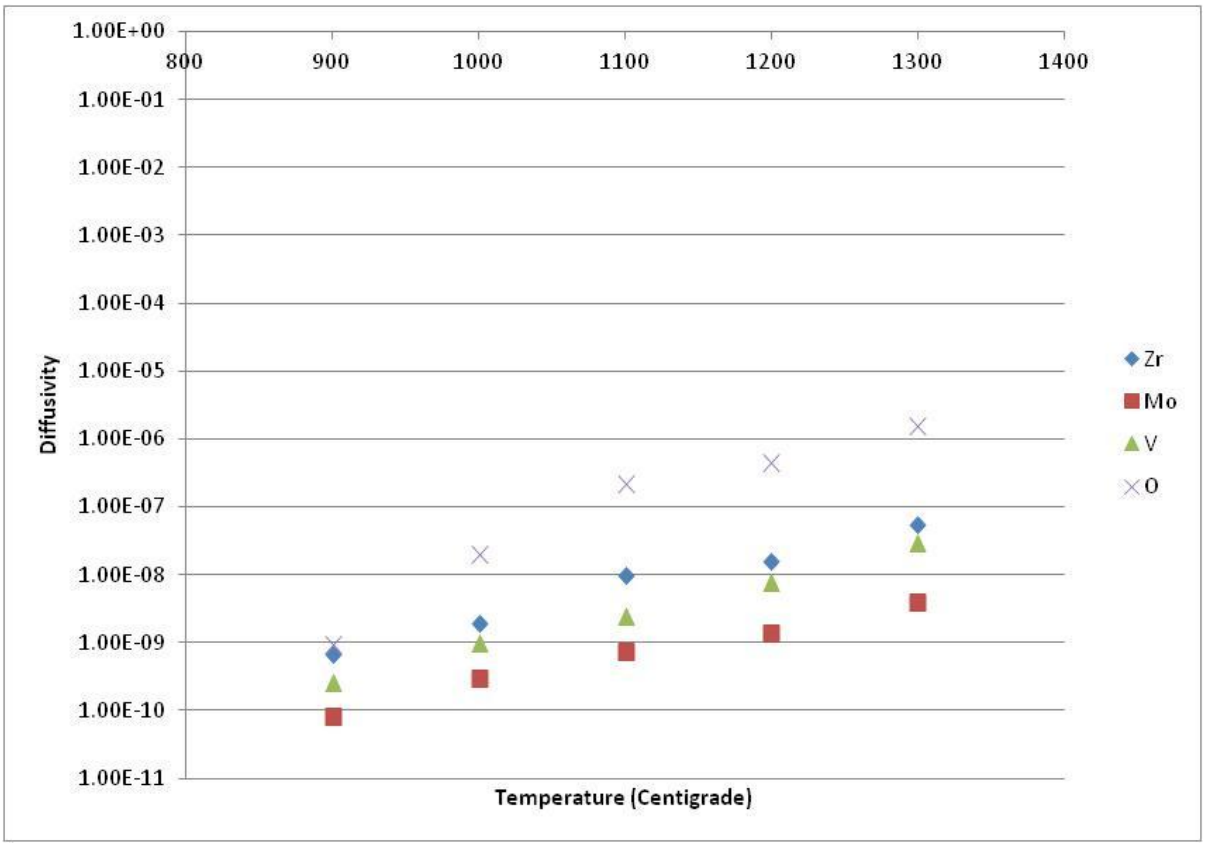

Figure 1-3: Diffusivity of selected elements through β-titanium, replot of data from Hendricks [Hendricks, 1962].

Each element relies on a unique interplay of its bonding relationship with titanium and different diffusion mechanisms to determine its absolute diffusivity through a titanium matrix. The isolation and study of each of these factors is key to the understanding of diffusion. Onodera [Ondera, 1993] explored the relationship of atomic size and bond strength versus diffusivity, shown in **Figures 1-4** and **1-4b**, showing that smaller atom radii correlates to a faster diffusion rate, up to the point of Vanadium. Beyond Vanadium, it becomes clear that atomic bonding plays a large role in the diffusivity of alloying elements in β titanium. Additional sensitivity of the diffusion process to the local state of the crystal is demonstrated in experiments by Araki [Araki, 1997], where pressures of 0.1MPa and 3.0GPa were applied to diffusion couples containing small amounts of Cobalt and Nickel, known fast-diffusers in Titanium, and measured the

penetration profiles, showing a reduction in the diffusivity as the pressure is increased. Although high pressures compress a crystal structure and would theoretically lower the distance an atom would need to travel for diffusive motion to a new lattice site, it also reduces the volume present in interstitial sites that can be vital for facilitating diffusive motion, even for atoms that occupy substitution sites in a crystal.

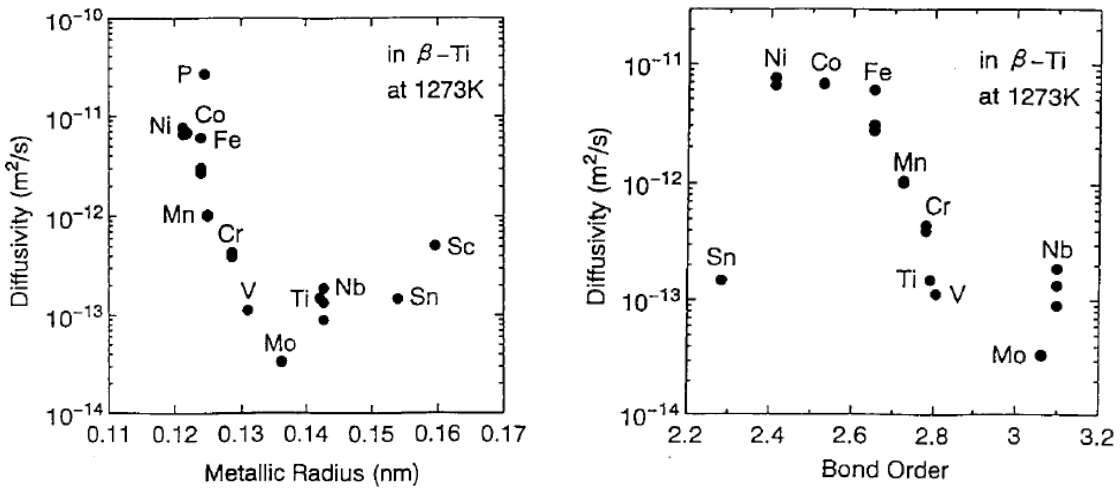

(a) **(b)**

Figure 1-4(a): Diffusivity in titanium versus atomic radius **(b)** diffusivity in titanium versus atomic bond strength [Ondera, 1993].

Localized chemistry modifications, particularly with large additions of β stabilizers can affect the diffusivity of interstitial elements; as shown by Christ [Christ, 2009] in a series of experiments demonstrating the impact of Vanadium and Molybdenum on Hydrogen diffusivity. By varying the concentration of Vanadium and Molybdenum, a wide variety of microstructures could be generated, ranging from a near-α to a completely stable β-alloy, allowing for confirmation of slower diffusion of Hydrogen through the α-phase as platelettes and β-grain boundary alpha was present. Use of the Matano method during analysis also confirmed that the

diffusivity of Hydrogen was independent of Hydrogen concentrations, up to the 1500ppm concentrations seen in the experimental data. Diffusivity of Hydrogen was shown to increase as β-stabilization increased, shown in **Figure 1-5**, which can be easily translated into commonly used meta-stable β technical alloys.

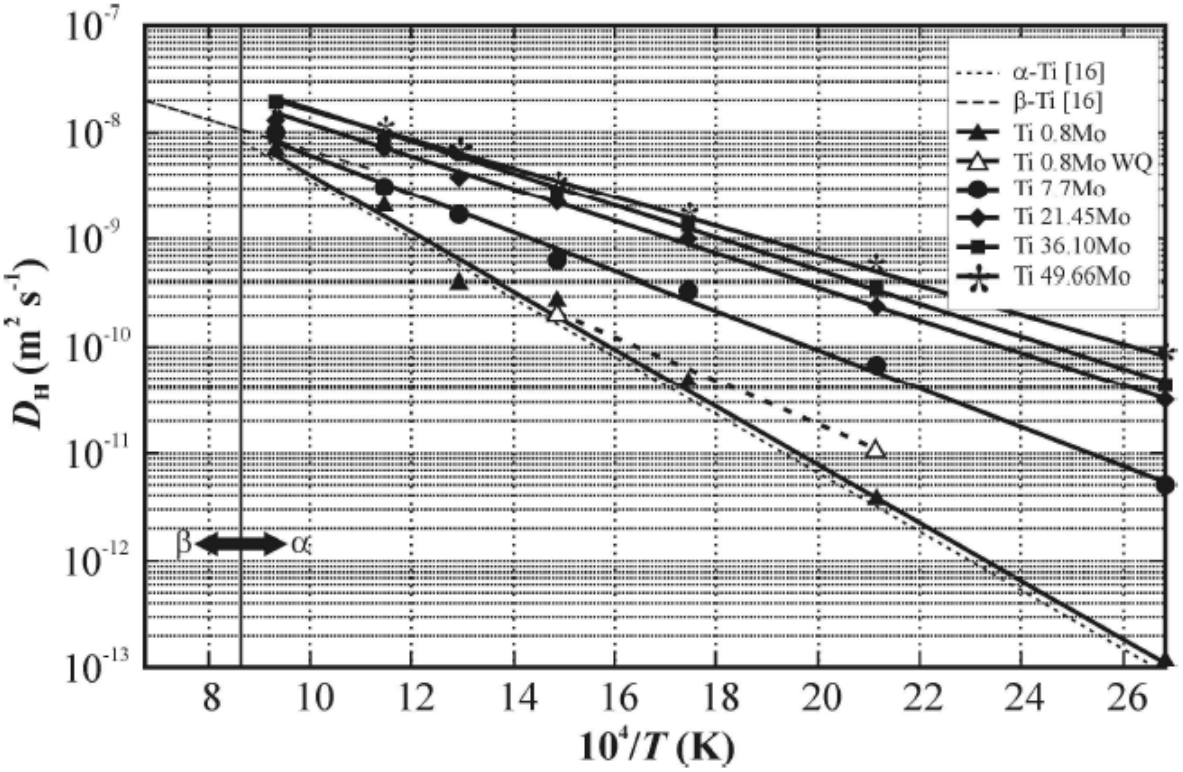

Figure 1-5: Diffusivity of Hydrogen in titanium alloys containing various concentrations of Vanadium and Molybdenum [Christ, 2009].

The emergence of high-precision analytical techniques has also allowed for more accurate measurement of diffusion in α-titanium, historically problematic due to the very slow diffusion at temperatures below the β-transus, a summary of which can be found in a review by Nakajima [Nakajima, 1993]. Mirassou [Mirassou, 1997] employs Rutherford Backscattering Spectromotry (RBS) and Heavy Ion RBS to generate very precise concentration profiles over

small length scales, and is able to generate diffusivity Arrhenius plots with very high agreement for multiple α-stabilizing elements, shown in **Figure 1-6.**

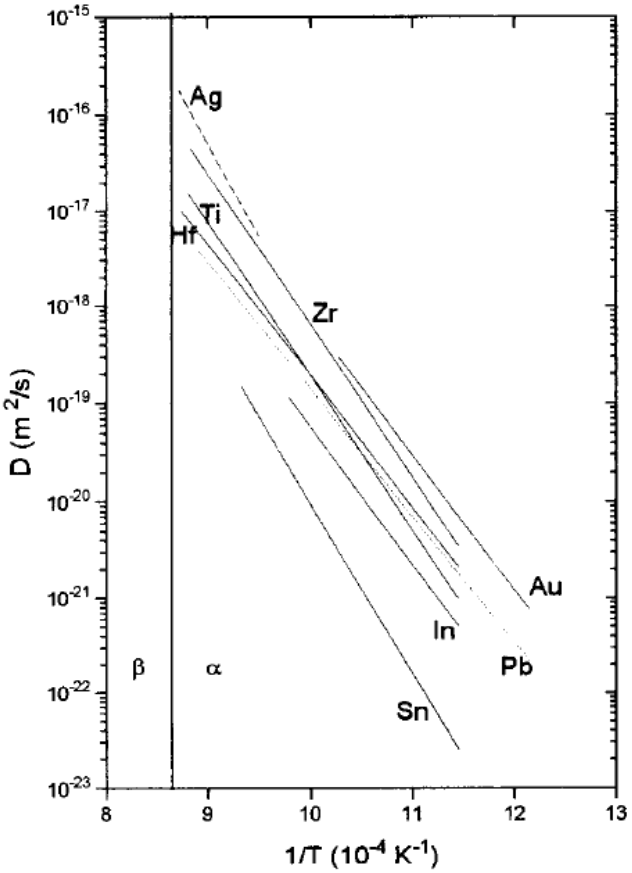

Figure 1-6: Diffusivity of selected α-stabilizers through α titanium [Mirassou, 1997].

Putting diffusivity into practice to engineer solutions to metallurgical problems in titanium is clearly a difficult problem – several mechanisms come into play for a given element, which is compounded by the tendency of technical alloys to use multi-component systems and complex microstructure features to derive their favorable properties. The advent of numerical simulations and models has allowed complex diffusion models to yield practical insights into the evolution of microstructural features, such as the modeling α platelette precipitation and growth

performed by Malinov [Malinov, 2005]. Using the thermodynamics database provided by Thermocalc, a series of experiments using Ti811, Ti-6242 and Ti-6Al-4V was run using a high-temperature stage for microscopy of the nucleation and growth of alpha particles in-situ. This technique, along with numerical simulations, allows for a complete description of the morphology and kinetics to be presented based on first-principles as well as experimental observation, beyond simple equilibrium distributions predicted by phase diagram calculations.

1.2.5 Kinetics and Microstructure Evolution

The nature of titanium microstructure in technical alloys cannot be well understood by only focusing on equilibrium conditions. The vast majority of processing routes to develop favorable structures in a given alloy system are instead designed to take advantage of or fight against the kinetics of transformation. Brun [Brun, 1998] summarized the practical points of grain refinement and recrystallization in α-β titanium alloys, noting the difficulty in obtaining fine grain size while working only in the single phase region (above the β-transus). Recrystallized grains nucleate from inhomogeneities in the microstructure, such as deformed grain boundaries, and grow until they meet an existing boundary. **Figure 1-7** shows recrystallization times at high temperatures and high strains can occur in a matter of minutes, implying that grain growth occurs quickly thereafter. Managing grain growth at high temperatures, the dynamic recovery at high temperatures in the single phase region, as well as texture effects due to excessive directional deformation make thermodynamic processing high in the α-β phase field the dominant method for gain refinement in titanium.

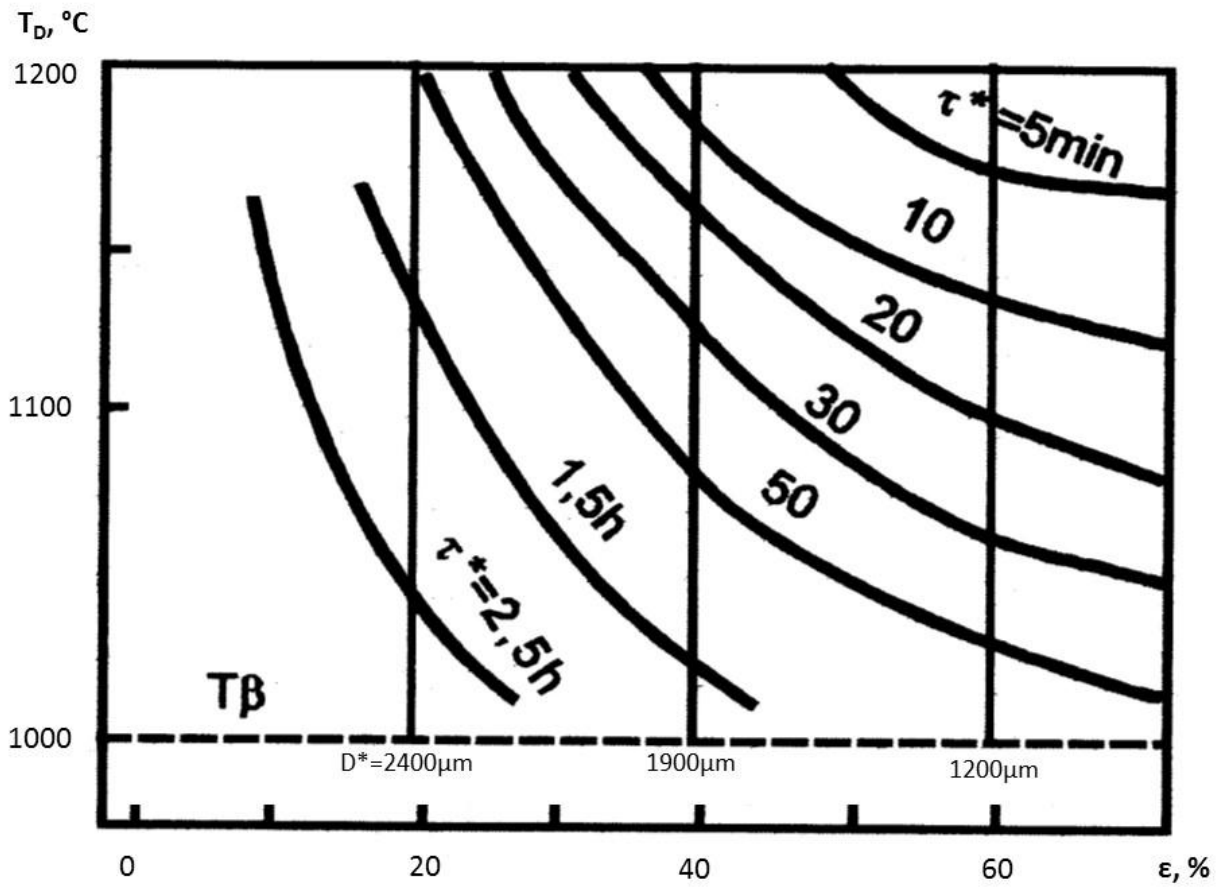

Figure 1-7: Diagram of complete recrystallization time in BT23 alloy at total strains and temperatures for three different beta grain sizes. Annealing temperature is equal to deformation temperature. [Brun, 1998]

Retaining α phase of any kind and adding thermomechanical deformation greatly aids in recrystallization response. An intragranular dispersion of α phase, whether that be lath-like or equiaxed in morphology, acts as nucleation sites for the recrystallization of the β grains. Volume fraction of α is less important than the spacing between particles – recrystallized grain nuclei need to reach critical size to survive, and closely spaced α particles can interfere with this. This is balanced with a finer dispersion of α leading to more nucleation sites and the pinning of grain boundaries to prevent excessive grain growth while at the working temperature.

The accessibility of synchrotron radiation sources has led to more recent investigations into the kinetics of α to β phase transformation upon heating. The near real-time collection of x-ray diffraction patterns using synchrotron sources can resolve in-situ phase transformation, as shown in the Ti-6Al-4V system by Elmer [Elmer, 2005]. Alpha dissolution upon heating, shown in **Figure 1-8**, begins to lag as heating speed increases. The transformation to BCC was determined to be a diffusion-limited growth problem, limited by the diffusivity of Vanadium (the primary β stabilizer in Ti-6Al-4V). Diffusion distances of Vanadium for a given heating profile correlate well to the observed phase transformations, leading to an overall discussion of phase transformation being governed by localized element partitioning between the α and β phases being rebalanced by diffusion. This understanding of phase transformation kinetics in titanium is consistent in other technical alloys, both α-β and metastable β alike, with similar studies being carried out in Ti17 [Bruneseaux, 2008], Ti-6Al-6V-2Sn [Barriobera-Villa, 2015a], and Ti-10V-2Fe-3Al [Barriobera-Villa, 2015b].

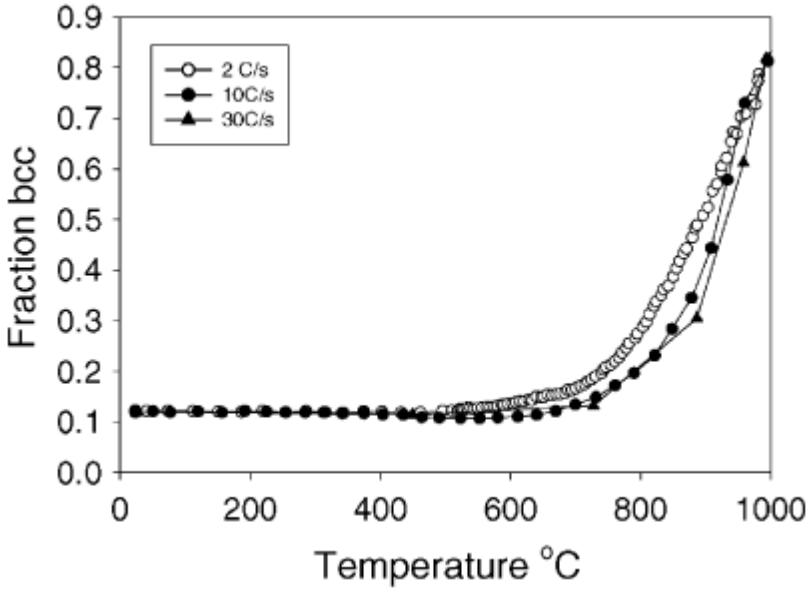

Figure 1-8: Volume fraction of BCC in Ti-6Al-4V with various heating profiles [Elmer, 2005].

The kinetics of transformation and recrystallization processes is highly dependent on the total strain imparted to the material, but also important is the strain rate. At a given temperature the strain rate will define the balance of dislocation formation, dislocation annihilation and material relaxation, all of which drive evolutions in the microstructure. Ding [Ding, 2002] demonstrated this effect with a series of hot compression experiments in Ti-6Al-4V at different temperatures and strain rates, shown in **Figure 1-9**. Lower temperatures show an initial yielding of the material that depends on the strain rate applied, and a continual softening that is attributed to adiabatic heating and the associated increase in β phase. As the temperature increases, the continued softening is replaced by a steady state stress, where the material has begun to dynamically recrystallize.

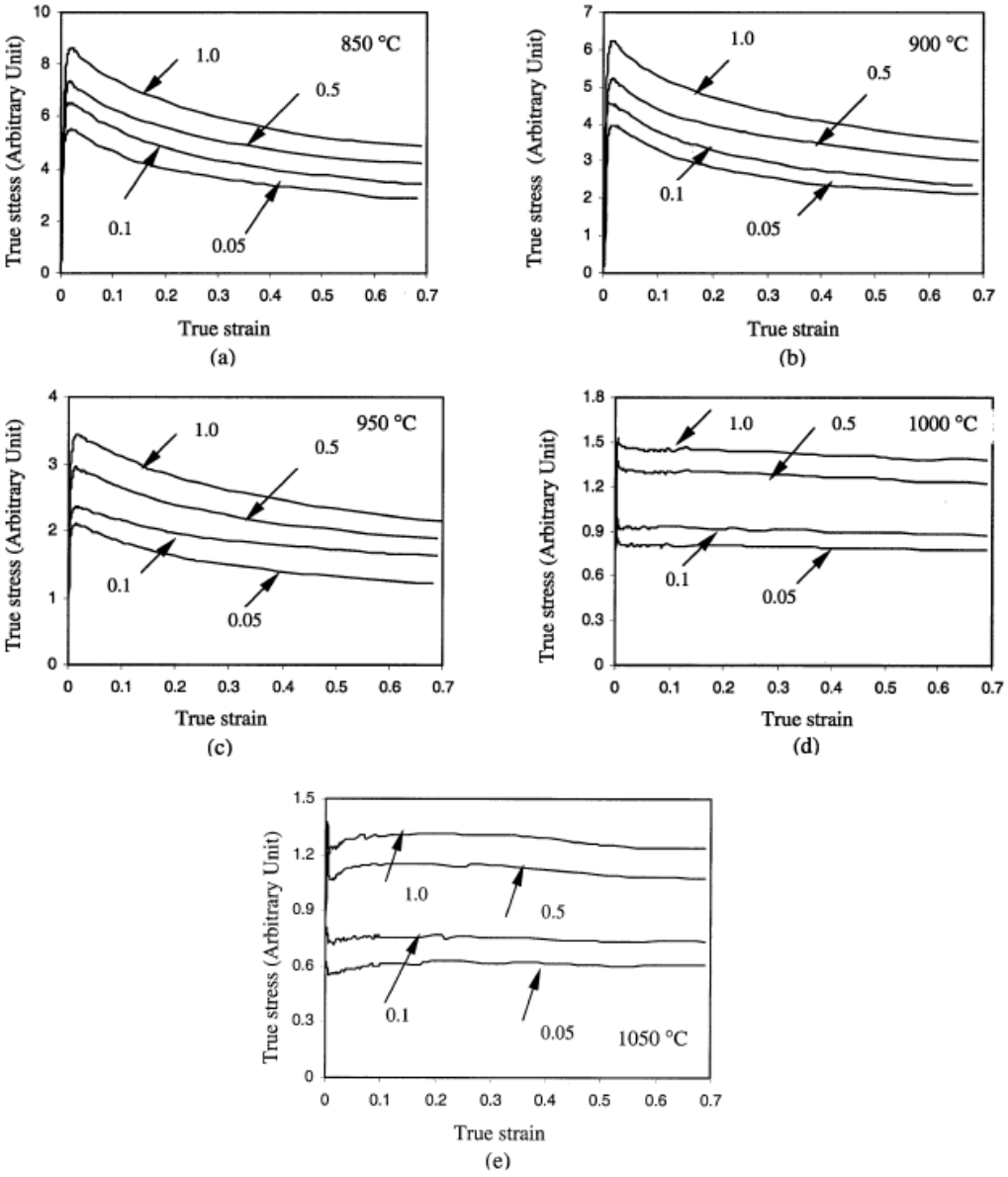

Figure 1-9: Flow stress-true strain curves for different hot pressing temperatures and strain rates: (a) 850 °C, (b) 900 °C, (c) 950 °C, (d) 1000 °C, (e) 1050 °C [Ding, 2002].

Results such as those generated by Ding agree with and add understanding to processing maps developed by Tamirisakandala and others [Tamirisakandala, 2003][Prasad, 1998]. Shown in **Figure 1-10**, a processing map for Ti-6Al-4V gives an idea of where key mechanisms in the microstructure evolution begin to take shape, relative to temperature and strain rate. Plots such as

these are useful in designing a process, or in understanding an unknown process condition based on the resultant structure of the metal. Considerable effort has been expended by the titanium metal working industry as a whole on understanding flow stresses, process windows and the effects on the resultant microstructure due to the economic implications, with key works on Ti-6Al-4V[Seshacharyulu, 2000], alpha and near-alpha alloys[Weiss, 1999] and beta alloys [Weiss, 1998][Karasevskaya, 2003] all available.

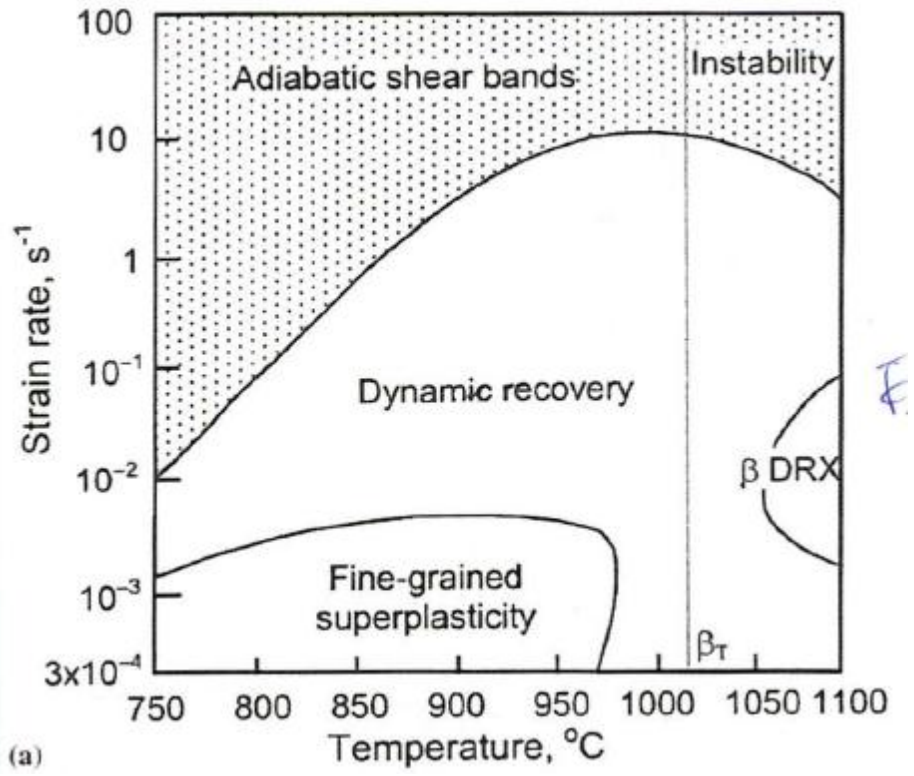

Figure 1-10: Processing map for Ti-6Al-4V with an equiaxed starting microstructure. [Tamirisakandala, 2003]

Lee expanded the study of processing regimes in Ti-6Al-4V further by exploring very high strain rates to establish the sensitivity of the material to more extreme processing windows [Lee, 1998]. Although variations in strain rate sensitivity and yield strength are seen

relative to strain rate changes, it can be concluded that yielding and strain rate sensitivity are dominated by the working temperature, and are inherently thermally activated processes. This is represented graphically in **Figure 1-11 (a)** and **(b)**. Even at temperatures well above the β-transus, where significant material softening occurs, the strain rates generated were enough to induce fractures, and the precursor adiabatic shear banding, shown in **Figure 1-12**.

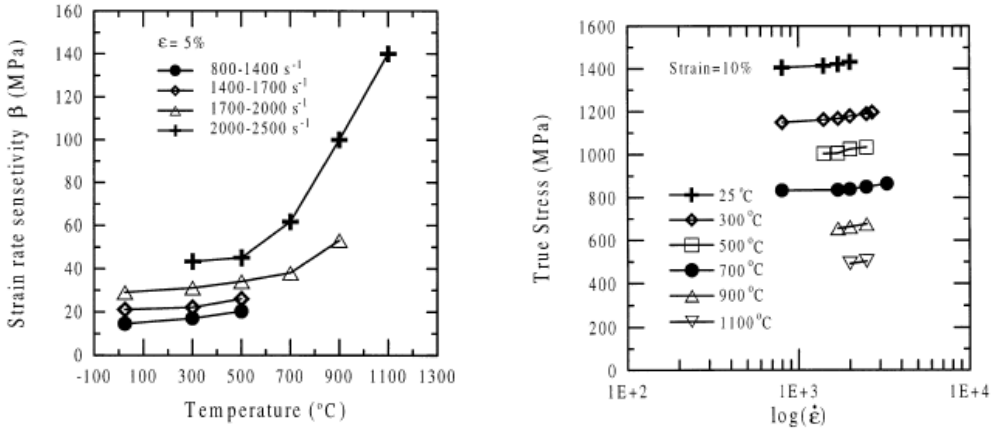

(a) **(b)**

Figure 1-11: **(a)** Strain rate sensitivity as a function of temperature for different strain rates. **(b)** Influence of strain rate on flow stress as a function of temperature [Lee, 1998].

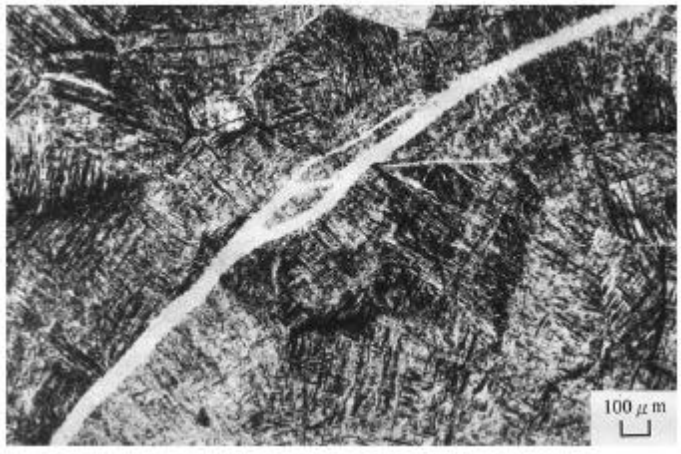

Figure 1-12: Adiabatic shear band obtained at strain rate of $2x10^3$ s^{-1} at 1100°C [Lee, 1998].

1.2.6 Overview of Selected Technical Alloys

The discussion of the manufacture and use of titanium must always be focused on a specific sub-set of alloys due to the wide variety of available alloys and the unique processing conditions and applications presented by each alloy. With the focus of this work being on solid state welding and joining, alloys have been selected to represent a typical cross-section of alloys that would be procured in sheet gauges and processed into aerospace structures.

Although pure titanium solely retains the α phase, the vast majority of aerospace titanium usage is comprised of α-β alloys, namely Ti-6Al-4V, where it enjoys over 80% of all tonnage used [Boyer 1994]. As one of the oldest technical alloys, Ti-6Al-4V is well-understood and available in the most widely used product forms, including forgings, plate, sheet, extrusions, castings and powder metallurgy preparations. Although formable, the cold-forming limits of Ti-6Al-4V preclude cold-rolling and thus coil production; sheet gauges are produced by pack-rolling, a method where multiple sheets of material are welded into a pack separated by steel sheets and rolled as if it were thick plate. The alloy itself presents itself as an adequate performer in all technical applications of note – it can be solution treated and aged to moderately high strengths, beta-annealed for high damage tolerance or mill annealed for a balance of mechanical properties. Additionally, processing routes have been developed to produce fine-grained material suitable for super-plastic forming at lower temperatures. The broad production base and mature scrap-handling stream for Ti-6Al-4V allows for competitive prices as well as the availability of highly targeted chemistries within the specification windows to maximize specific mechanical properties, producibility of specific product forms or improved corrosion performance. No discussion of titanium alloys is complete without the inclusion of Ti-6Al-4V, and as such, it is

widely considered the baseline material to compare the performance of other alloys and processing routes against.

In spite of the dominance of Ti-6Al-4V, a new generation of competitor alloys has been developed in pursuit of lowering the cost of implementing titanium structures. One such alloy is Ti54M, developed and produced by TIMET Inc [Kosaka, 2003]. The chemistry of Ti54M is very similar in bulk to Ti-6Al-4V, where a nominal 5% Aluminum and 4% Vanadium comprise the bulk of alloying additions. The key differences lie in the minor alloy additions, where Ti54M allows higher limits of 0.4% Iron and 0.25% Oxygen and the addition of 0.6% Molybdenum. The potency of iron as a β-stabilizer as well as the Molybdenum addition makes for a lower β-transus, and impart additional workability benefits. Ti54M's chemistry allows for cold-rolled coiled product, better cold formability and better hot-working behavior at rolling and forging temperatures to improve yields, while providing mechanical properties similar to that of Ti-6Al-4V. There has also been extensive work done to characterize the machinibility of Ti54M, where improvements over Ti-6Al-4V have been demonstrated. The higher limits and additions to the minor alloying elements also provide the option of using additional types of scrap when producing an ingot, which is generally viewed as a potential cost savings.

One of the shortcomings of Ti-6Al-4V is in its performance at high temperatures. Ti-6Al-2Sn-4Zr-2Mo-0.08Si (Ti-6242S, or just Ti-6242) was developed in the late 1960's to address this need. Although Ti-6242 is considered a near-α alloy, the most common heat treatment form is a two-step, sub-transus duplex anneal that yields a structure very similar to a mill annealed α-β alloy and is used to optimize high temperature creep resistance [Boyer, 1994]. Although Ti-6242 is available in all of the common mill product forms, its wide usage in turbine engines and hot-section aerospace structure makes castings and sheet the bulk of Ti-6242. The difficulty in

working and forming Ti-6242 makes for very expensive material in thinner gauges due to yield losses, and as such, is only used as a necessity when the needs of the application demand its usage over something more affordable, such as Ti-6Al-4V.

Metastable β alloys are capable of furthest extremes in performance and processing for titanium alloys, and TIMET's Beta 21S (B21S) is no exception. Designed specifically for corrosion and high-temperature oxidation resistance, B21S is a unique approach to alloy design that attempts to exploit Wagner-Hauffe Theory to account for the vacancies formed in the corrosion resistant surface nanolayer of TiO_2 present in all titanium alloys [Ferguson, 1968]. The vacancies form at oxygen sites in the lattice due to the need to maintain electro neutrality in the TiO_2 crystal, and the addition of a nominal 3% Niobium allows for vacant lattice points to be filled on account of the additional valence electron provided by the Niobium. A fully dense oxide crystal can inhibit the diffusion of oxygen, which promotes an embrittling surface layer of α after long-term thermal exposure. Rounding out the composition is 15% Molybdenum to provide heavy beta stabilization without the detrimental effects to oxidation resistance that using Vanadium presents, as well as 0.2% Silicon for high temperature strength and creep resistance and 3% Aluminum and 0.13% Oxygen as α-stabilizers to add a degree of strength and heat treatment response while maintaining ductility. B21S, thanks to its high levels of β stabilization, is generally cold rolled to coils of thin-gauge strip and foils for fabrication into honeycomb and heat shield structure. Several heat treatments are available, although it is common to sacrifice strength and use a solution treated and overaged (STOA) condition to maximum thermal stability.

1.3 Diffusion Bond Processing

Diffusion bonding has emerged as a high quality method of joining materials that prove difficult to join by more traditional means, as well as a route to monolithic structures. This includes materials that are difficult to machine and fabricate and thus mechanically join, materials with extremely high melting points where fusion welding is impractical, and in the case of titanium, where the microstructure of as-cast titanium resulting from a fusion weld nugget leads to poor mechanical properties and formability [Milne, 2011].

Diffusion bonding relies primarily on two mechanisms to transfer mass and create a bond: creep and diffusion. At the macro-scale, creep is the plastic deformation over time of material under applied load, which can be accelerated by temperature and at the atomic scale, diffusion is the movement of atoms from a crystal lattice site or interstitial site to an adjacent site using thermal vibrations of the atoms as the driving force. Creep is necessary for the practical fabrication of a diffusion bond due to the microscopic surface imperfections of the two pieces of material that need to be joined. Intimate contact needs to be achieved before diffusion between two pieces of material can occur, and the pressures and temperatures of the diffusion bonding process ought to be selected with consideration of the creep response of the material being bonded – amorphous materials such as glasses and select polymers need little to no temperature elevation to creep, where thermally stable materials such as refractory metals can require temperatures of several thousand degrees to creep to a useful degree. Models predicting creep of of the bond interface before diffusion occurs often rely on a regular saw-tooth pattern as an abstraction of surface roughness present from machining or grinding for the sake of computational simplicity. This in turn allows for a void geometry such as a rhombus or cylinder to be selected at the theoretical material interface on which to carry out calculations of void

shrinkage due to plastic deformation of the material, as shown in **Figure 1-13** [Peng, 2004] Creep behavior and shear forces that drive plastic deformation of material near the interface to cause void shrinkage have largely been explained through adaptations to models of compaction and sintering under isostatic pressure in powder metallurgy systems.

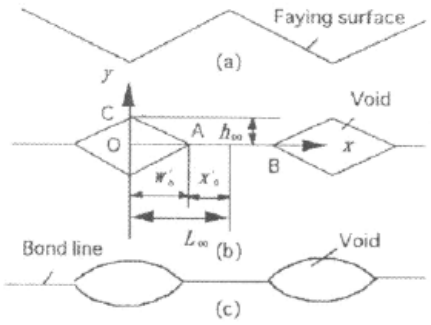

Figure 1-13: Diffusion bond interface geometric abstraction [Peng 2004].

A sound mechanical interlock is the first aspect of a diffusion bond, and the principles of diffusion comprise the second. Temperatures for diffusion bonding are generally above half the melting point of the material system to take advantage of the exponential increase in diffusivity that occurs with temperature. As temperature rises, thermal vibrations of individual atoms in the crystal lattice drive excursions further and further away from the atom's nominal position in the lattice, allowing for smaller atoms to slip from one interstitial position to the next, as well as atoms in the lattice moving from one position to another. An increase in temperature also creates a larger volume of vacancies within a given crystal structure, shown in **Equation 1-1** opening up more potential sites for an atom to move into via diffusive movement. The random jumping of atoms in a diffusion process will be influenced to produce predictable movements of concentrations by several factors, including free surfaces, grain boundaries, concentration gradients and phase transformations; in the case of titanium alloys, the dissolution of the HCP α-

phase and a predominance of the BCC β-phase as temperature increases and the material approaches the β-transus increases diffusivity [Shewmon, 1989][Sanders, 2004].

$$\frac{n_v}{n_o} = e^{-H_f/RT}$$ **Equation 1-1** [Abbaschian, 1991]

Where:

n_v = number of vacancies

n_o = number of atoms

H_f = Heat of activation required to form one mole of vacancies

R = universal gas constant

T = temperature

To date, there is very little published work on the bonding of dissimilar titanium alloys confined to the alpha and beta phases, with much of the focus of the literature on diffusion bonding an alloy to itself, or in the bonding of titanium to other alloy systems such as intermetallic-containing gamma titanium alloys, stainless steels, aluminums and copper-cobalt alloys [Sanders, 2004][Rahman, 2010][Orhan, 2001][Tuppen, 2005][Wang, 2006][Jiangwei, 2002][Tuppen, 2005].

1.4 Friction Stir Welding of Titanium

Friction stir welding (FSW) is a solid-state joining process used primarily to join pieces of sheet metal together to form complex built up structure that otherwise would have to be produced with fasteners or fusion weld joints. FSW falls into the large subset of joining processes that rely on large plastic deformations to create either a mechanical or metallurgical interlock between two or more work pieces. Joining by plastic deformation can be a purely mechanical, cold joint such as a rivet, cold swage or more modern processes such as hydroforming or electromagnetic forming, as well a joining process that produce heat and thus a

metallurgical bond, such as roll bonding, extrusion and the various forms of friction welding [Mori, 2013]. Initial developments in FSW were centered around low strength, low melting point ductile metals such as aluminum and copper as a method for improved joint quality in what was deemed an already joinable material system. With the increasing focus on titanium usage in the aerospace industry, as well as the continued development of tooling materials, weld parameters and welding equipment within the FSW community, titanium FSW began development in earnest in the 1990's and has emerged as an enabling technology for advanced structure in hard metals [Edwards, 2010a].

Fundamentally, the process involved traveling a rotating tool through a piece of material in a highly controlled way. By choosing the tooling material and geometry, anvil material, tool rotation speed, tool travel speed and force applied, a weld joint can be produced without melting the material; this is shown schematically in **Figure 1-14a**.

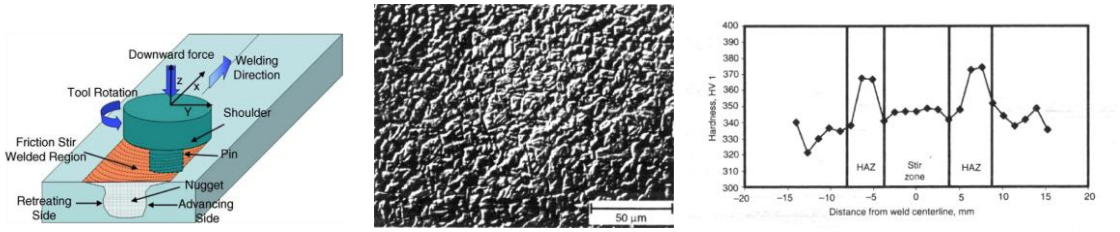

Figure 1-14: (a) Friction stir weld schematic [Mishra, 2005]. **(b)** Ti-6Al-4V weld nugget microstructure, near top surface [Leinert, 2000]. **(c)** Microhardness plot transverse to weld [Leinert, 2000].

The selection of parameters becomes important in ensuring that the material stays in a desirable temperature regime while producing a full penetration weld without a detrimental heat affected zone or damage to the actual welding equipment from excessive forces [Edwards, 2010c]. While weld temperatures can greatly exceed the beta transus in a typical titanium alloy [Edwards, 2010b], the plastic deformation imparted by the tool's rotation and travel refines the

microstructure, combined with the quenching effect of proper thermal management, resulting in a fine-grained equiaxed microstructure show in F**igure 1-14b**, as opposed to a basketweave, beta annealed microstructure that would occur with a simple thermal excursion. The selection of parameters and materials in the production of a FSW joint and produce a wide variety of complex structures and potential defects throughout the weld nugget and heat affected zone, and a full discussion of the standard features and terminology as well as process controls of a FSW process is presented by Threadgill [Threadgill, 2007], Edwards [Edwards, 2010c] and Gibson [Gibson, 2013], respectively.

The fine grained microstructure of the recrystallized weld nugget has shown mechanical properties generally equivalent with the base metal in the case of Ti-6Al-4V mill annealed plate for those parameters critical to commercial aerospace, namely strength, fatigue and fracture toughness. Material that has seen thermal exposure during the weld process but no work shows a minor drop in strength, as shown by microhardness data in **Figure 1-14c.** Superplasticity, if inherent in the alloy, can be maintained with a properly performed FSW process, allowing for subsequent forming operations in the fabrication of complex structures [Edwards, 2010a].

The mechanics of the stirring and deformation processes proves to be a complex phenomenon, and is heavily dependent on the position relative to the shoulder and the pin of the tool for the location in question. It has been shown by Cho [Cho, 2005] that the rotational component (as opposed to the tool translation) is the dominant influence on the deformation of the metal, resulting in a simplified understanding of the stresses imposed by the tool that suits the smooth tapered pins used in titanium FSW, as shown in **Figure 1-15**, where shear is parallel to the tool translational direction while tangent to the advancing and retreating side of the tool and normal to the translational direction while in the primary wake of the tool. Initial understandings

of the modeled deformation mechanics published by Cho and subsequent work confirming this mechanism by measuring crystallographic texture evolution in stainless steel [Cho, 2006][Cho, 2008] have seen analogues in aluminum alloys as well. Experiments by Fonda in the Aluminum-Lithium alloy 2195 also show a characteristic shear texture in the stir zone, as well as the generation of banded microstructures where strains surrounding the tool become uneven [Fonda, 2004].

Fundamentally, the description of the deformation being shear-dominant in the stir zone remains consistent when the process is performed in titanium. This has been confirmed by assessing deformation crystallographic textures in Commercially Pure Titanium (nearly 100% HCP α-phase) [Mironov, 2009], by Mironov in Ti-6Al-4V on the retained β phase that demonstrated simple shear texture [Mironov, 2008], in thin β21S sheet material on the β phase [Reynolds, 2005], and in the α alloy Ti-5111[Knipling, 2009].

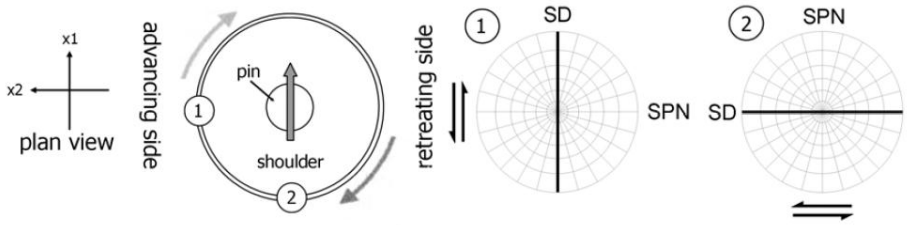

Figure 1-15: Schematic of shear stress imposed by the tool in friction stir processing at two locations, showing the shear direction (SD) and shear plane normal (SPN) [Pilchak, 2007].

Outside of the primary stir zone there is a transition zone, consisting of a thin band surrounding the primary stir zone that shows evidence of deformation, however, the material has

not received enough strain or temperature to fully recrystallize in the same way as the primary stir zone. As in traditional welding processes, there remains a narrow HAZ where the process alters the metal solely by virtue of the heat input of the process as the material transitions to unaltered base metal. These zones are shown schematically in **Figure 1-16**.

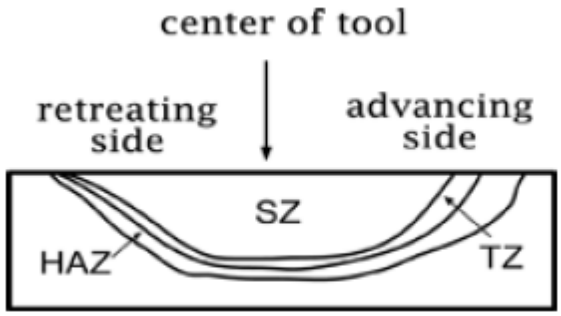

Figure 1-16: Schematic of stir zone (SZ), transition zone (TZ) and heat affected zone (HAZ) present in friction stir processing of titanium [Pilchak, 2007].

The displacement of the material as the tool translates and rotates through the stir zone proves to be complicated, and several investigations have been made into the translational movement of material as it interacts with the tool. Seidel [Seidel, 2001] showed the relative magnitude of the turbulence in the material as it interacts with the top, bottom, advance and retreating side of the tool by using steel shot tracer strips implanted in an aluminum friction stir weld, shown schematically in **Figure 1-17a.** The resultant welds were x-rayed, the results of which are shown schematically in **Figure 1-17b**, and it is shown that material interacting with the bottom of the pin, further away from the tool shoulder, follows a more regular and predictable deposition in the wake of the tool, while material more closely engaged with the shoulder of the tool shows much more turbulence and irregularity in its deposition pattern.

Material closer to the centerline of the tool shows a more disturbed deposition in the wake as compared to material more tangential to the tool.

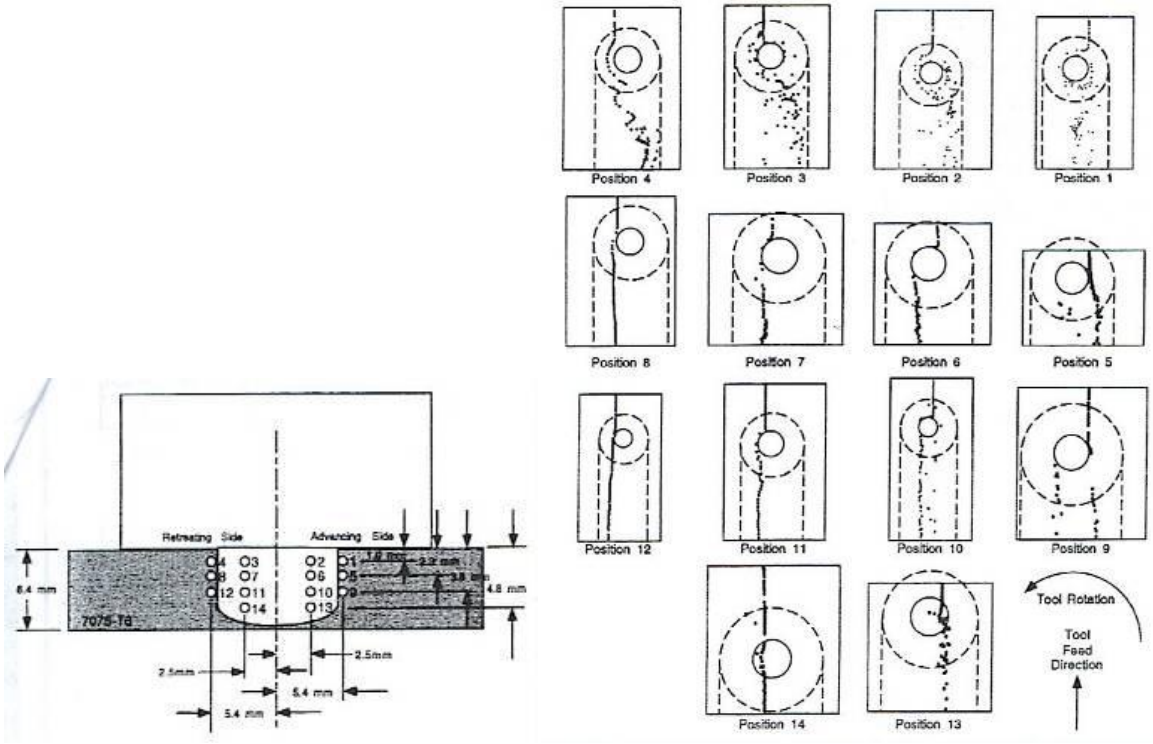

Figure 1-17: (a) Schematic of steel shot strip locations and **(b)** schematic representation of resultant x-ray analysis [Seidel, 2001].

Edwards expanded the investigation of material flow into Ti-6Al-4V FSW using a Tungsten-Rhenium powder as a tracer. A groove was machined in both sides of a butt weld and filled with tracer powder, as shown in F**igure 1-18**. The tool offset from the material interfaces was varied to engage the tracer powder at various locations relative to the centerline of the tool and produce a wider range of flow behavior.

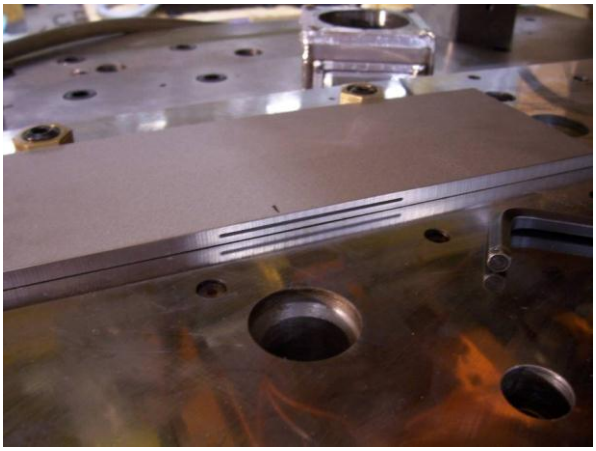

Figure 1-18: W-Re tracer powder placed in the tool path of butt weld in Ti-6Al-4V plate [Edwards, 2010a].

Welds where the tool was retracted mid-weld were x-rayed and CT scanned to detect the W-Re powder and characterize the material flow, an example of which is shown in **Figure 1-19**. The smooth pins used in titanium FSW processes yield relatively uniform material distributions, and show evidence of forcing material towards the root of the weld due to the forging loads placed on the heel of the tool as it travels. It was also observed that the periodicity and quality of the tool marks left by the shoulder of the tool on the material surface, meaning the regular spacing of the grooved pattern and the consistency of shape among individual grooves, strongly correlated with a regular deposition of crescent shaped concentrations of tracer powder throughout the length of the weld nugget. Experimental observations showed that unstable or oscillating forge loads on the tool produced unstable or oscillating depositions of tracer powder as well, while proper selection of weld parameters gave the tool the requisite time needed to soften the material in its path via frictional heating before traveling forward and extruding the softened material into a regular, onion-like pattern in its wake.

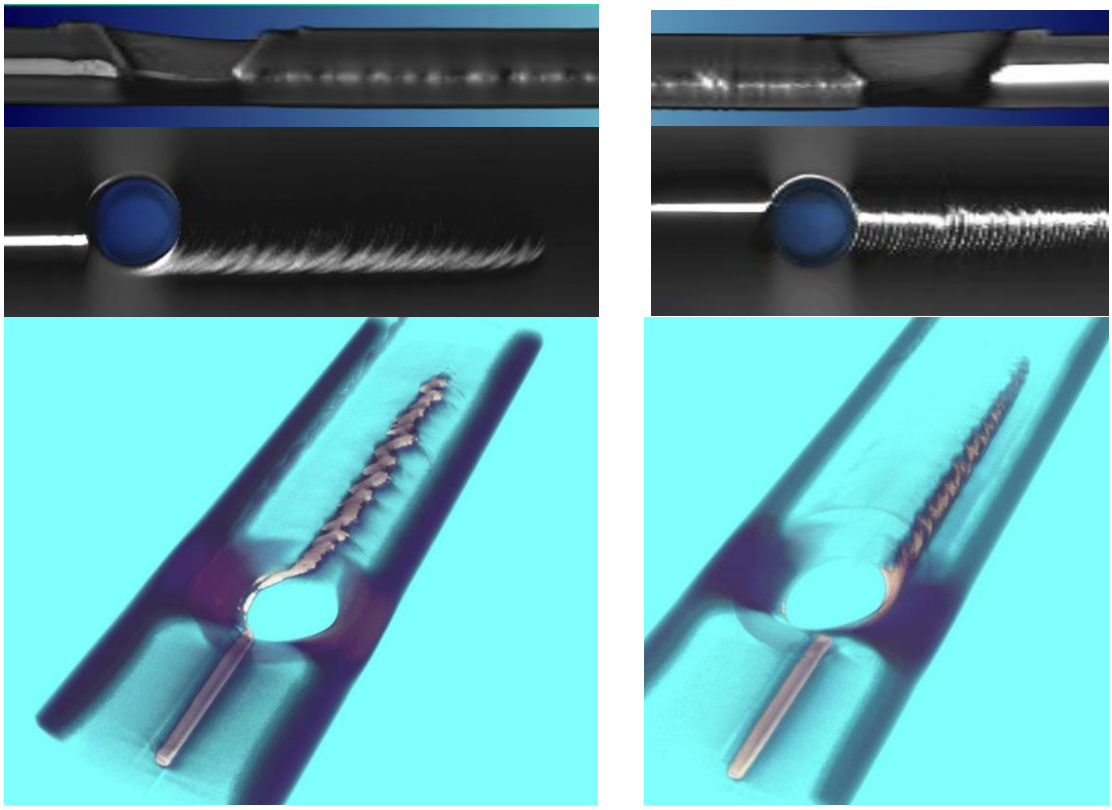

Figure 1-19: A CT scan comparison of material flow in Ti-6Al-4V via W-Re tracer powder for material engaging the advancing side (left) and retreating side (right) of the tool [Edwards, 2010a].

More recent experimental work by Fonda in the material flow in aluminum FSW systems has observed grain structure and texture periodicity and irregularities correlating to pin rotation and translation parameters. This led to the conclusion that the material flow is a localized, periodic extrusion process, driven by eccentricity in tool rotation. This in turn gives rise to a characteristic onion-ring or banded microstructure features that are seen in friction stir welds of all alloys [Fonda, 2013].

The creation of stable, usable joints in titanium via FSW processing has necessitated a great deal of work studying process parameters at various material thicknesses. The bulk of the work is dominated by Ti-6Al-4V due to its extensive application in industry. Thinner stock (2mm) has been successfully welded at 400RPM with travel speeds of 25, 50 and 100mm/min, with the author

reporting extensive dynamic recrystallization throughout the stir zone as well as sub-transus temperatures. Grain sizes increased as travel speed increased, attributed to less dynamic recrystallization [Liu, 2010]. At 3mm thick, Zhang investigated producing welds at a travel speed of 60mm/min and a rotation speed of 300-600RPM, in 100RPM increments. 300 and 600RPM rotation speeds produced defects along the bottom edge of the stir zone, while the 400 and 500RPM conditions produced defect-free welds. Microstructures in the stir zone showed heavy dynamic recrystallization and super-transus heating, with finer grain sizes observed as distance increased from the center line of the weld. This is attributed to the higher heat input in the center of the weld [Zhang, 2008]. At 6mm, several studies have been performed at 100mm/min travel speed and 275RPM spindle rotation speed [Leinert, 2000][Jata, 2004][Ramirez, 2003]. Microstructures again show super-transus heating and heavy deformation in the stir zone, with little correlation to the starting microstructure of the material. Fine beta grains, on the order of 10 microns, are observed and are attributed to the short spike above the transus combined with heavy deformation, while observed grain boundary alpha is attributed to relatively slow cooling rates. A more extensive look at the processing window for 3, 6, 9 and 12mm sheet material was conducted by Edwards [Edwards, 2010c], and highlights the delicate nature of achieving a full-penetration weld with no undercut, little to no tool wear and no internal defects. Ideal parameters are summarized in **Table 1-1,** and are the result of experimentation that is further rationalized by heat input calculations. Tensile performance in the 3mm joints showed failures in various sections of the weld, with consistent tensile ultimate strengths of 1110-1130MPa and elongations generally falling at 8-10%. Microstructure observations are consistent with previous literature, namely sub-transus refined structure in the 3mm thick joints, moving to a fully transformed, recrystallized structure in the thicker joints.

Table 1-1: Ideal friction stir weld parameters for Ti-6Al-4V butt joints [Edwards, 2010c].

Material Thickness (mm)	Pin Rotation Speed (RPM)	Pin Travel Speed (mm/min)
3	300	75
6	280	100
9	270	65
12	170	65

25mm thick joints in Ti-6Al-4V have been produced [Edwards, 2011] as well. Using parameters of 150RPM pin rotation speed and 75mm/min pin travel speed, stable welds were achieved and showed a strength degradation of 8% relative to the base metal, while elongation improved by 23% relative to the base metal. The microstructure was very coarse compared to FSW joints in thinner gauges, and showed no retained primary alpha, with significant grain boundary alpha and coarse alpha platelets in prior beta grains.

Outside of Ti-6Al-4V, experiments by Reynolds in FSW of Beta21S are of note [Reynolds, 2005]. Using 1.6mm thick sheet, welds were produced at 200RPM pin rotation speeds with pin travel speeds of 50, 150, 200 and 300mm/min. Defect-free welds were produced in all process conditions, showing equiaxed refined grains throughout the stir zone and a crystallographic texture consistent with shear deformation of BCC metals.

1.5 Friction Stir Welding of Dissimilar Alloy Systems

The absence of a solidification microstructure in the resultant weld nugget of the friction stir process has opened the door for a much wider variety of joints using dissimilar constituent

materials. While welds of dissimilar materials are possible using fusion welding techniques, the impact of brittle intermetallic phases in the weld nugget limit their usefulness in engineered applications that consider durability and damage tolerance as design requirements. Examples of FSW in dissimilar systems of various configurations can be found throughout the literature, including aluminum to brass, aluminum to copper, aluminum to commercially pure titanium and a full range of joints containing ferrous alloys as well [Dressler, 2009][Chen, 2008][Esmaeili, 2012][Deng, 2013][Akinlab, 2012]. Esmaeili conducted a narrow investigation into the defects of aluminum 1050 to CuZn30 brass friction stir welds [Esmaeili, 2012], focusing on macro scale joint damage such as voids and tunneling defects. Shown in **Figure 1-20a**, several cross sections and radiographic images correlated the presence of coarse fragments of brass in the aluminum matrix with the presence of tunneling and void defects. The formation of coarse brass fragments is attributed to higher temperatures needed to soften brass as compared to the aluminum alloy. By offsetting the tool towards the aluminum side of the joint, the effects of coarse brass particles can be mitigated to produce a more uniform joint, also shown in **Figure 1-20b.**

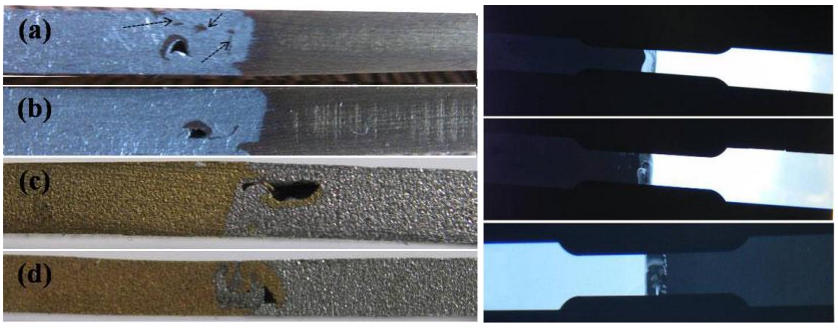

(a) **(b)**

Figure 1-20: (a) Example of weld coarse brass particles and the associated tunneling defects. **(b)** Radiographic inspection of aluminum (light) to brass (dark) FSW joints using offsets ranging from 0 (bottom) to 1mm (top) [Esmaeili, 2012].

Akinlabi performed a series of experiments using 5754 aluminum and C11000 copper, focusing on heat input versus the evolution of weld structure, characterized by conductivity and microhardness [Akinlab, 2012]. Increases in microhardness were observed at the weld interfaces, as well as grain refinement throughout the stir zone and thermomechanically affected zone. Akinlabi asserts that the presence of intermetallic compounds are responsible for the increases in microhardness, although no additional evidence of intermetallic phases, such as microscopy or x-ray diffraction is presented. Similarly, calculated heat inputs are presented with electrical resistivity, although no attempt is made to correlate heat input with grain size or other aspects of the evolution of structure and properties that are of interest to those pursuing structural applications for FSW.

Chen demonstrated the evolution of new phases in a narrow band between ADC12, a silicon-containing aluminum alloy designed for casting, and commercially pure titanium, an alloy of titanium, oxygen and trace contaminants, showing the presence of intermetallic Ti_3Al in a region approximately 5 microns wide at the interface of the aluminum and titanium [Chen, 2008]. Lap joints were welded, which limits the rotational stirring between material systems and makes for a narrow band of interaction between the aluminum and titanium, shown with SEM and qualitative EDS in **Figure 1-21a and Figure 1-21b** respectively.

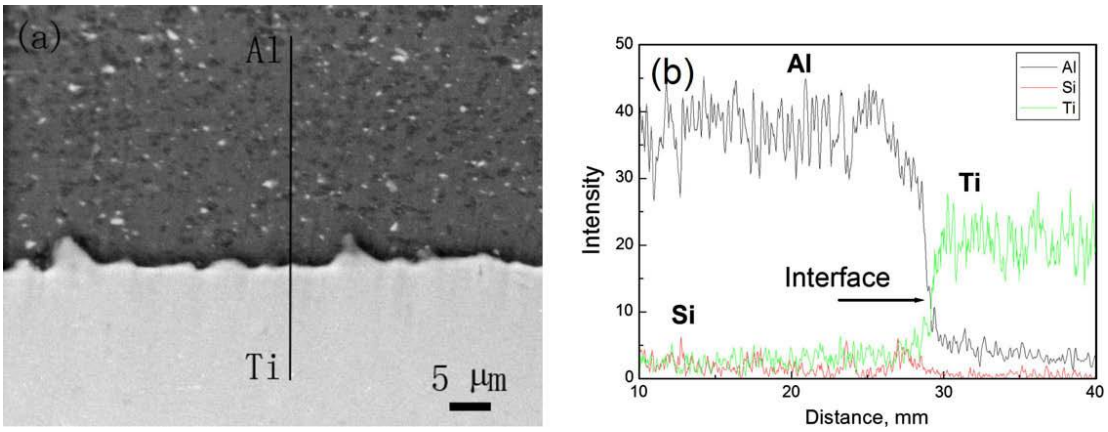

Figure 1-21: (a) SEM image of Al-Ti interface of a FSW butt weld (b) EDS line scan [Chen, 2008].

Although much of the work referenced studies weld parameters and their relationship to macro-scale weld defects important to the mechanics of the weld process itself, such as void formation, it stops short of a complete metallurgical exploration of the formation and stability of the phases observed. However, the presence of intermetallic Ti_3Al is confirmed with x-ray diffraction, and Chen proposes that the formation of the phase is not simply resultant of the heat input to aluminum and titanium in intimate contact, but rather integral to the process itself – the formation of Ti_3Al is an exothermic reaction, and the additional heat added to the material interface by its formation aids in the joint quality.

Further exploration of Ti-Al joints is presented by Li et al [Li, 2013], with metallurgical analysis presented and a goal of minimizing intermetallic phases while producing a structurally sound joint. This is achieved in part with a modified butt joint design, in an effort to reduce overheating in the aluminum alloy and promote mixing between the two material systems, shown in **Figure 1-22.**

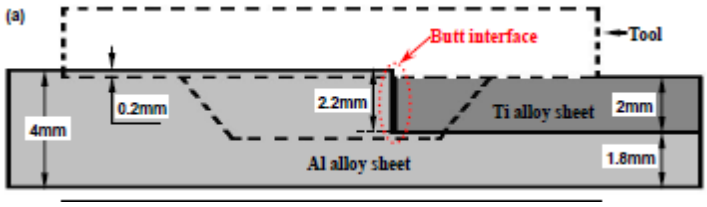

Figure 1-22: Schematic of modified butt joint design [Li, 2013].

Strengths of 92% of the base aluminum alloy were achieved in some cases, and it is of note that the welding regimes were much closer to that of a typical aluminum FSW joint as compared to a titanium FSW joint – rotation speeds and feed rates were on the order of 1500RPM and 60mm/min, producing what one would assume to be a very hot weld. Metallurgical analysis focused on plastic flow patterns of the joint and of the Ti/Al interface points, shown in **Figure 1-23.** Energy dispersive x-ray spectroscopy shows the diffusive mixing of the aluminum and titanium in **Figure 1-23(e)**, although no further discussion is presented, rather, microstructures and mechanical property discussion focuses on avoiding bulky concentrations if intermetallic Ti/Al compounds that promote brittle behavior and identifying particle-reinforced composite behavior from the breakup and dispersion of titanium into the aluminum.

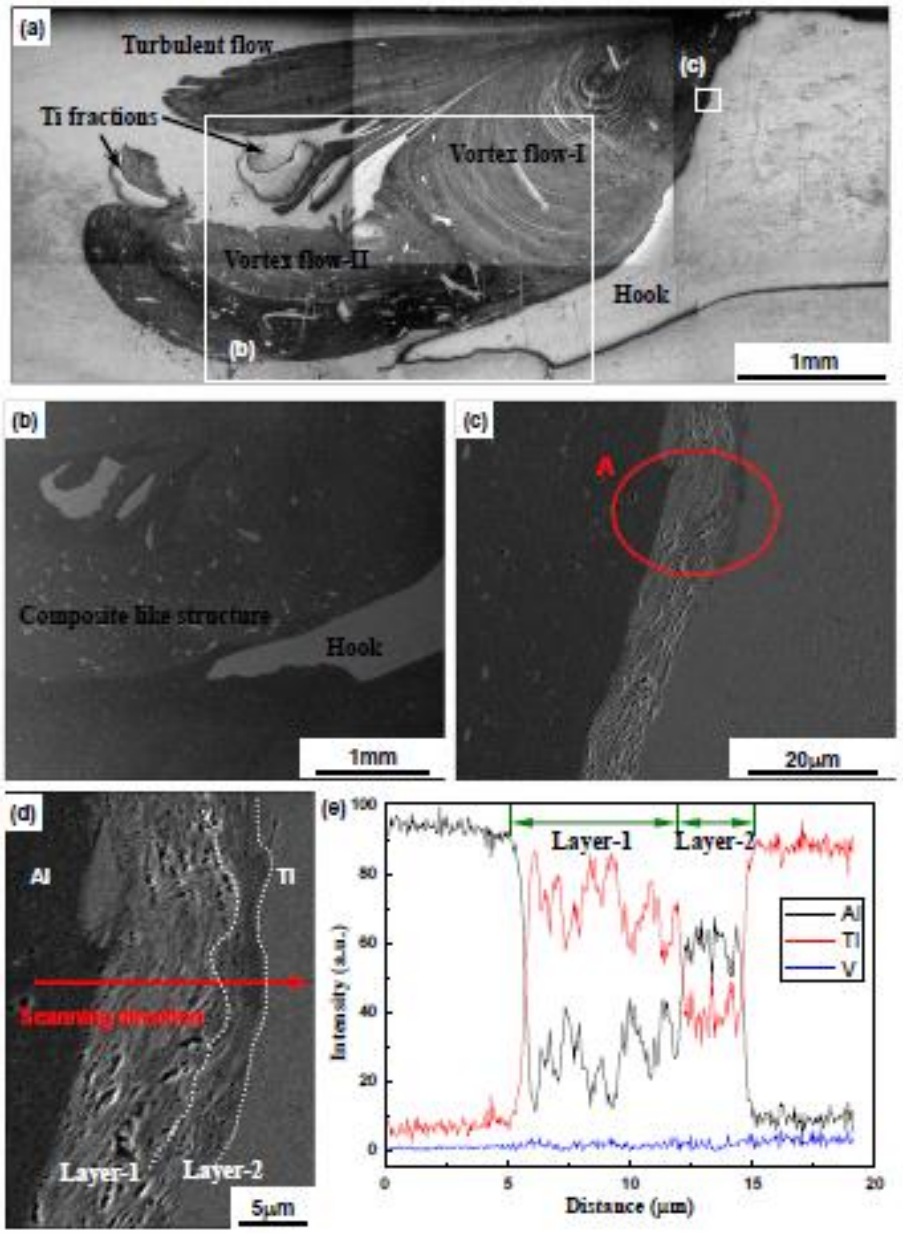

Figure 1-23: (a-e) Macro and microscopic analysis of Ti/Al FSW joints prepared at 1800RPM and a travel speed of 60mm/min on a 0.5mm thick butt joint. **(e)** EDS analysis of Ti/Al interface [Li, 2013].

It is difficult to draw meaningful parallels to the joining of dissimilar titanium alloys from work that is mainly focused on joining dissimilar material *systems* rather than dissimilar alloys within a given system. In addition, the welding parameters and tooling configurations used in titanium are very much specialized for that application. Little definitive literature exists for the

joining if dissimilar titanium alloys. Trapp [Trapp, 2003] shows FSW joints between combinations of Ti-6242 and Ti17 (a heavily alloyed β-alloy designed for high temperature turbine applications), but again, the published work is only a demonstration of the viability of creating a sound joint rather than an investigation into the metallurgical transactions taking place. Shown in **Figure 1-24**, Trapp demonstrates the stirring zone structure that can be expected from stirring an α-β alloy and a β-alloy, and makes note of the alpha structure that is resultant from various post-weld heat treatments, as well as demonstrating mechanical properties.

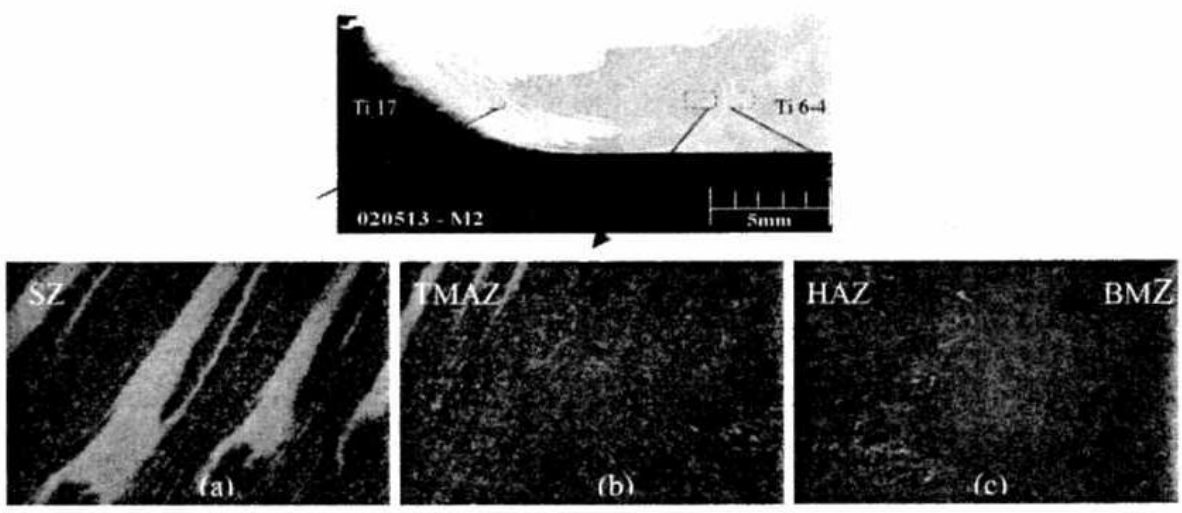

Figure 1-24: Weld nugget structure of a Ti-6Al-4V and Ti17 FSW butt joint [Trapp, 2003].

1.6 Computational Modeling of Friction Stir Welding

As computational modeling of materials has matured and computational power has increased, high-deformation, complex processes such as FSW are within reach of more researchers. Although computational work is generally focused on understanding the mechanics of the processes and the specifics of a given material system become secondary, there is still

valuable understanding that can be applied to dissimilar titanium alloy friction stir weld butt joints.

Buffa [Buffa, 2006a] created simulations using DEFORM 3D, a software package specifically developed for the forging and thermomechanical processing industry. Using a thermo-mechanically coupled, rigid-viscoplastic material description with a continuum assumption for the weld seam, three dimensional predictions for heating were obtained for an aluminum butt weld. A strong dependence on rotation speed (as opposed to travel speed) is noted for material heating. The cylindrical pin geometry is a closer relative to the conical pin used in titanium FSW joints than a threaded tool is, but the author still recognizes the short comings in predicting Z-axis material flow with the presented model. Still, flow patterns are presented, shown in **Figure 1-25**.

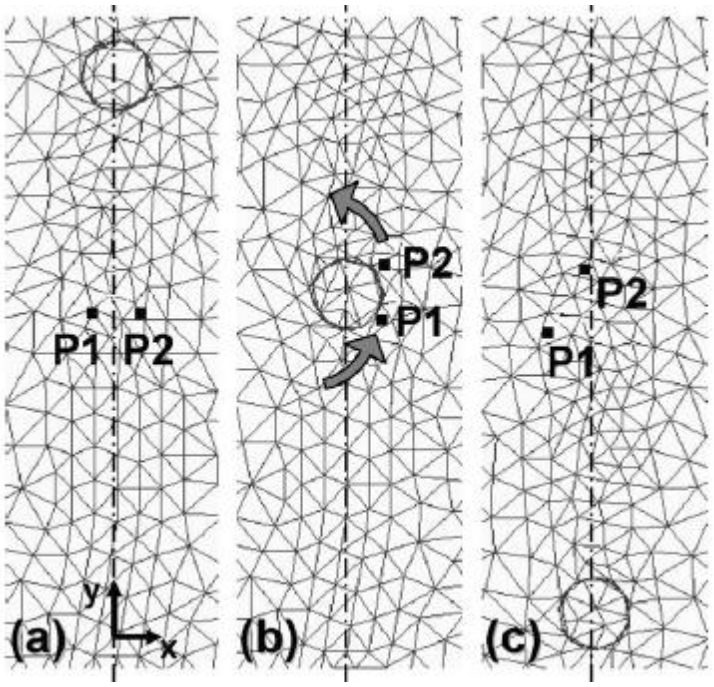

Figure 1-25: Simulated particle flow pattern during welding [Buffa, 2006a].

Buffa continued this work, and explored simulations leading to discussions of conical pin geometries and their effect on weld heating and material flow [Buffa, 2006b]. Shown in **Figure 1-26**, various angles of conical pins were simulated, showing variations in absolute strain rate for a given location, as well as increasing asymmetry from advancing to retreating side. Although the study is limited to the aluminum alloy AA7075, correlations are made between predicted strain rates and the dynamic recrystallization of the alloy.

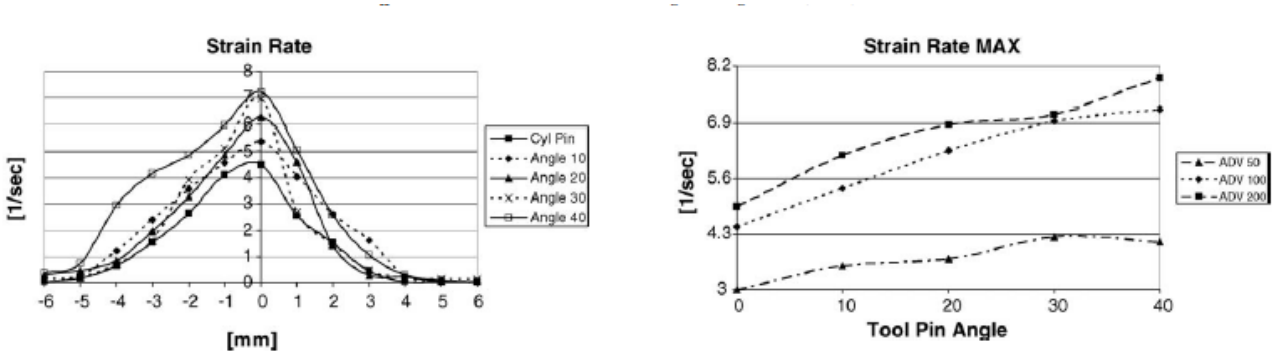

Figure 1-26: Strain rate distribution in a X-Z section at various pin angles (left) and maximum strain rate versus pin angle (right) [Buffa, 2006b].

Similar studies have been carried out in subsequent years, expanding the base of numerical solutions in FSW to encompass power and torque requirements, material flow and more complete understandings of heat transfer, generally in aluminum alloys [Arora, 2008][Zhang, 2009][Lorrain, 2010]. Specifically in titanium, finite element simulations have been correlated with weld results in lap joints using thin sheets of Ti-6Al-4V [Buffa, 2013]. Temperatures and strains were calculated (**Figures 1-27** and **1-28**), showing a process that generates temperatures very near the β-transus of Ti-6Al-4V with heavy strains distributed unevenly throughout the weld nugget. By correlating observed microstructures with simulated

total strains and temperatures in various regions, a process map can be generated, shown in **Figure 1-29**.

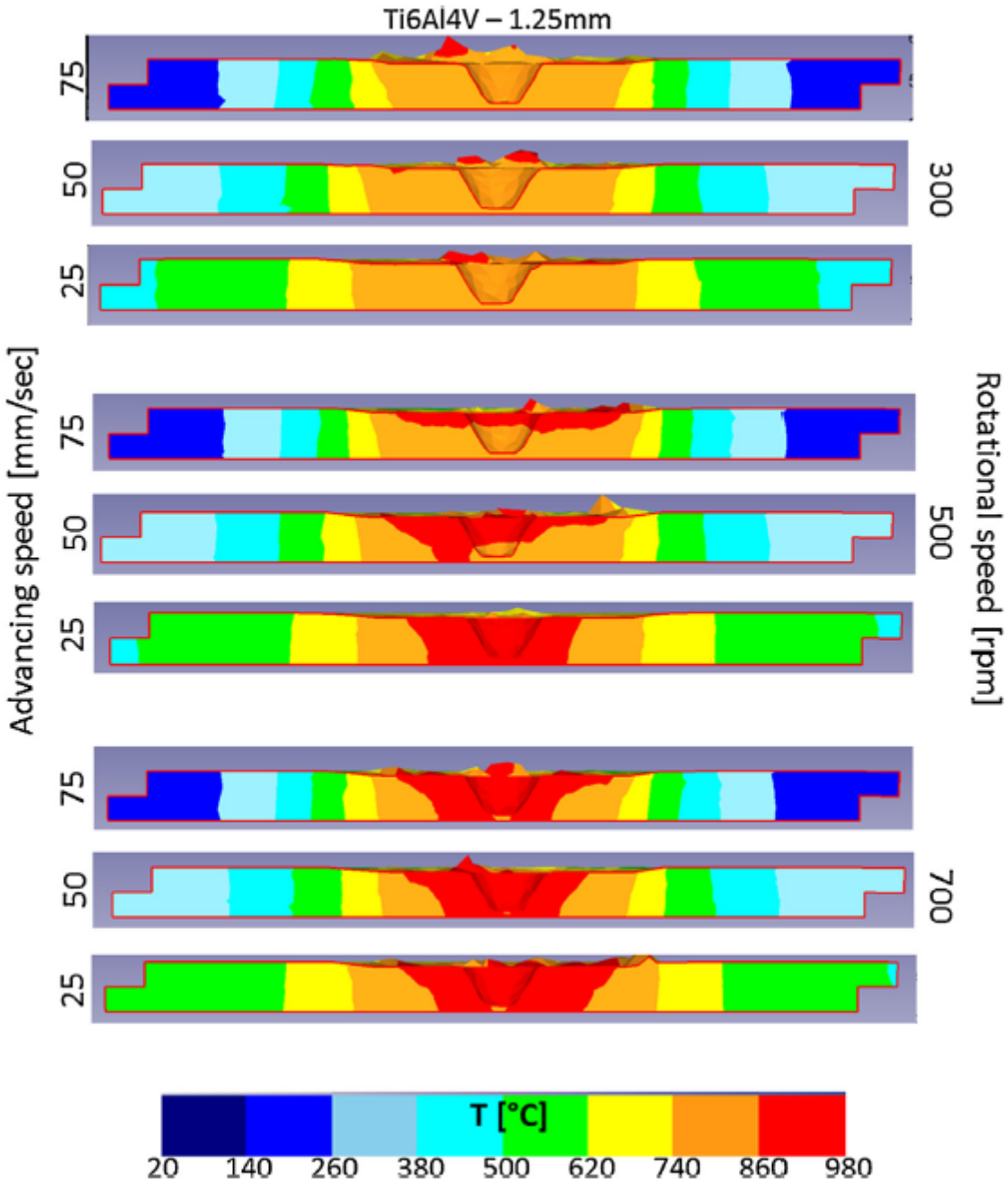

Figure 1-27: Temperature distribution in a weld cross section as a function of process parameters [Buffa, 2013].

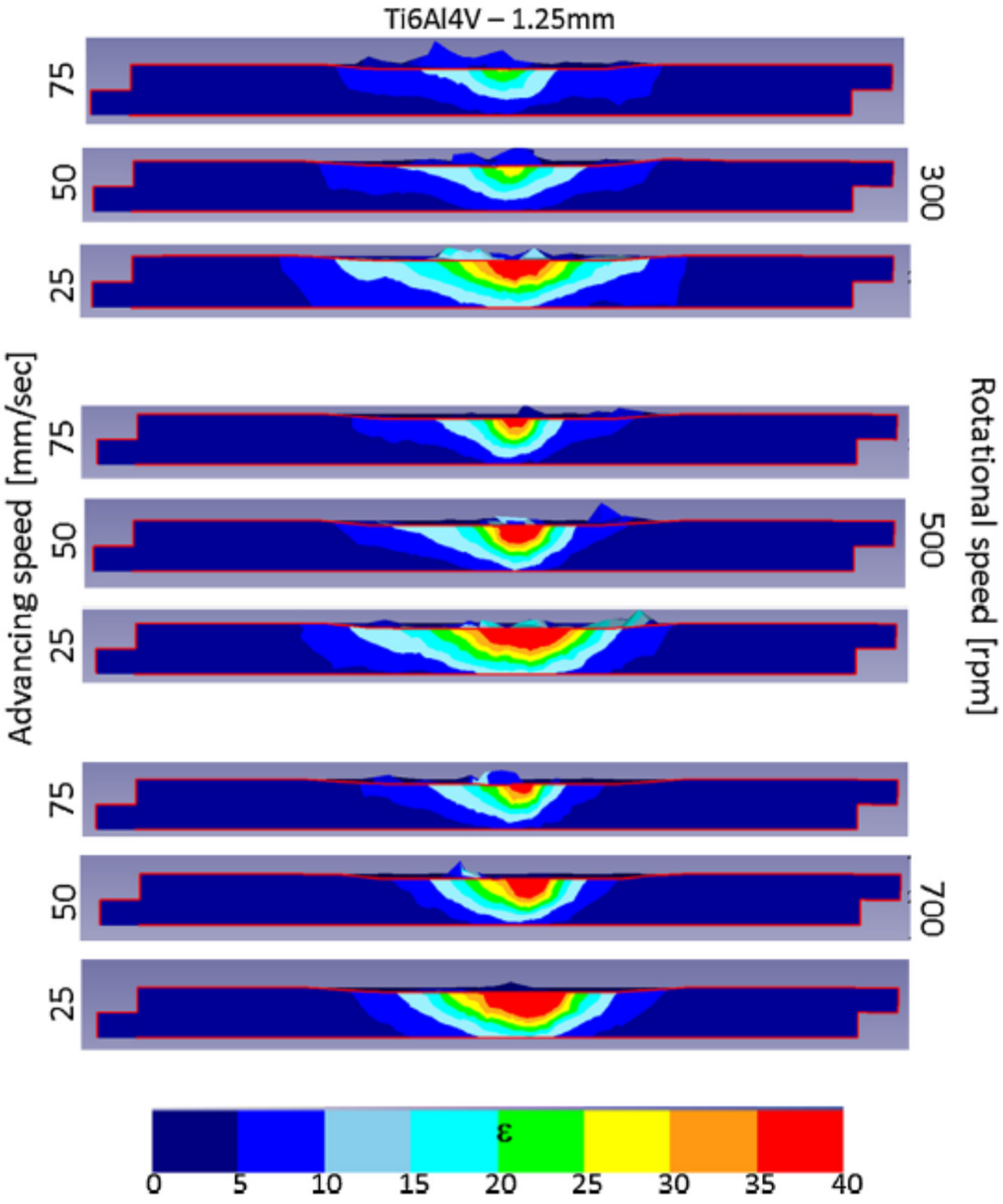

Figure 1-28: Effective strain distribution in a weld cross section as a function of process parameters [Buffa, 2013].

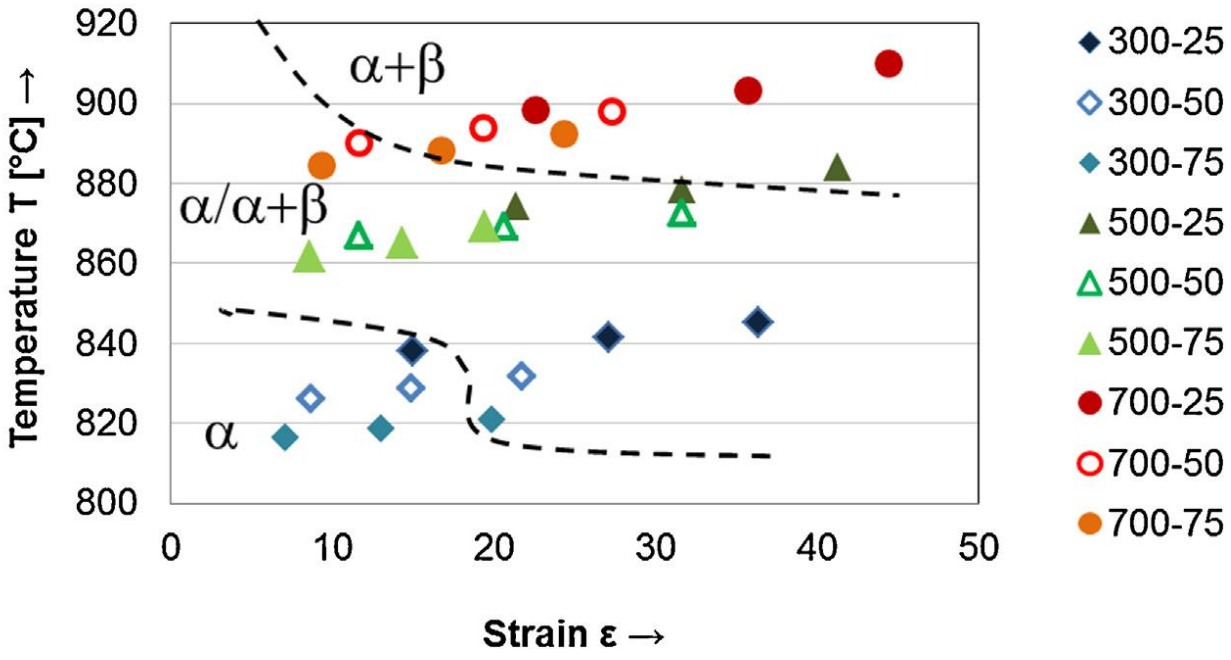

Figure 1-29: Observed microstructures in Ti-6Al-4V lap joint welds of various conditions, plotted relative to total strain and temperature [Buffa, 2013].

1.7 Summary of Reviewed Literature

In this literature review, a background is provided in titanium metallurgy, highlighting phase transformation [Barriobera-Villa, 2015b][Malinov, 2005][Williams, 1973][Kaufman, 1973], diffusion [Araki 1997][Mirassou, 1997][Ondera 1993][Christ 2009][Nakajima, 1993][Malinov, 2005][Shewmon, 1989] and thermomechanical processing's influence on microstructure features [Brun, 1998][Ding, 2002][Tamirisakandala, 2003][Prasad, 1998]. This body of literature is well-established, and is primarily focused on process regimes useful to the metal working industry (eg. Forging and rolling at homogenous temperatures). More recent work has established titanium's response under high strain rates [Lee, 1998] and rapid heating rates [Elmer, 2005][Bruneseaux, 2008], meaning that basic metallurgical principles are still established and relevant to the much more dynamic friction stir welding process.

Diffusion bond processing is only briefly reviewed, as it is not the primary focus of this study – bonding of titanium is an established process, and can be related to simple geometric models for bond formation that rely on creep deformation and ultimately interatomic diffusion. Practical literature is not available for dissimilar titanium alloy joints.

Friction stir welding in titanium has been reviewed, with a focus on titanium metallurgical processes. Aluminum friction stir welding has a well-established body of literature, with significant contributions in not only process parameters and metallurgical processes, but also computational and empirical models [Threadgill, 2007][Mori, 2013][Gibson, 2013][Seidel, 2001][Buffa, 2006a][Buffa, 2006b][Arora, 2008][Lorrain, 2010]. The differences in tool design and material behavior when comparing aluminum to titanium and other hard metals is significant, although understanding of the basic deformation mechanism and thus the basis for computational models is transferable between the alloy systems [Pilchak, 2007][Cho, 2008][Fonda, 2004]. Titanium alloys, including commercially pure, α, α-β and metastable β alloys have been shown weldable in the literature [Ramirez, 2003][Reynolds, 2005][Knipling, 2009][Jata, 2004][Mironov, 2009]. There is significant focus on Ti-6Al-4V due to its ubiquity in industry, and thus the process window at multiple thicknesses is established and correlated to microstructure features and mechanical performance [Edwards, 2010a][Edwards, 2010b][Edwards, 2010c][Liu, 2010][Mironov, 2008] .

Dissimilar alloy friction stir welding is a relatively unstudied field, focused mainly on soft metals such as aluminum, copper and brass. Examples in literature involving titanium are very limited, such as work joining commercially pure titanium to aluminum, in a joint configuration and with process parameters well outside of the established titanium process windows [Dressler, 2009][Chen, 2008][Esmaeili, 2012][Deng, 2013][Akinlab, 2012][Lee,

2013]. Friction stir welding of dissimilar titanium alloys is limited a single paper, joining Ti-6Al-4V to Ti-17, which takes the form of a communication and does not document full process parameters or microstructures [Fonda, 2004].

Friction stir welding of dissimilar titanium alloys requires research if there is to be an understanding of the influence of composition, microstructure and mechanical behavior differences between alloys has on the welding process. Current understanding of material flow in FSW joints is based on homogenous material properties on the advancing and retreating side of the pin, and this needs to be expanded to account for the difference in deformation behavior in dissimilar alloys. Similarly, the formation of a metallurgical bond between dissimilar alloys requires investigation to better understand the dominant mechanisms that will define the local chemistry and microstructure in a weld nugget. Defining these basic mechanisms of the formation of the macro and microstructure is a critical step in the development of a usable process window and ultimately application of dissimilar titanium alloy friction stir welding.

CHAPTER 2: RESEARCH MOTIVATION AND METHODS OF APPROACH

Based on the identified gaps in published literature, this research intends to expand the published work on solid state joining phenomenon observed between dissimilar titanium alloys, particularly in the area of friction stir welding.

2.1 Motivation

The key objectives of this research are as follows:

- Define microstructure conditions present in dissimilar titanium alloy joints after friction stir welding
- Differentiate between diffusive and mechanical mixing within the stir zone and describe the composition gradients found in within the weld
- Develop understanding of trends in microstructure and macrostructure feature size and morphology based on weld parameters and input materials in dissimilar titanium alloy friction stir welds
- Develop understanding of process parameters needed to optimize weld quality in dissimilar titanium alloy friction stir welds

2.2 Methods of Approach

This research was accomplished as a collaboration between the University of Washington, Boeing, Pacific Northwest National Laboratory and the Metals Affordability Initiative Consortium. The project was carried out in three phases, with the intention of developing understanding and analytical approaches during the first two phases to be applied to a more rigorous, designed experiment in phase three. The methods and objectives for each phase are outlined below:

1. **Diffusion Bonding Preliminary Experiments**

- A wide range of process temperatures and titanium alloy combinations were surveyed for overall bond line quality and characteristic defects.
- Metallographic mounts were prepared and assessed for variations in microstructure features as they related to process conditions and to better understand the characteristics of note as two microstructures bond to one and other.
- Ti-6Al-4V/β21S diffusion bonds were further analyzed used electron microscopy and energy dispersive x-ray spectroscopy. This serves to characterize phases and particle morphology as well as chemical gradients at dissimilar alloy interfaces without needing to consider heavy mechanical deformation as well.

2. Friction Stir Welding Preliminary Experiments

- A selection of α-β and near-α titanium alloy combinations using standard titanium friction stir weld parameters were sectioned for metallography and surveyed for defining macrostructure characteristics and any defects present.
- The most widely dissimilar alloy combination (based on phase composition) was selected for further electron microscopy. Areas of interest in the weld nugget were identified based on unique interfaces between alloys and the resultant microstructure features.
- Techniques for energy dispersive x-ray spectroscopy were developed to provide a qualitative chemistry gradient at micro-scale interfaces to better understand micro and macro mechanisms for material interface evolution.
- A method was developed to calculate local temperatures within the stir zone based on diffusion principles and x-ray spectroscopy data.

3. Ti-6Al-4V/β21S Friction Stir Welding Experiment

- An experimental matrix consisting of 9 welds was developed to produce extremes of material stirring behavior based on alloy combination, thermal management practices as well as spindle rotation and travel speeds.

- Metallographic specimens were extracted to assess weld defects, microstructure features as well as overall macrostructure patterns in the stir zone.
- MicroCT scans were utilized to obtain three-dimensional volumetric data on several centimeters of weld length, allowing a more comprehensive view of how material flow changes with weld parameters.
- Machine loads were analyzed to correlate load data with macrostructure mixing features and defects observed.
- A comprehensive set of energy dispersive x-ray spectroscopy line scans and SEM images were collected at multiple locations (kept consistent between all welds) to characterize diffusive bonding between alloys at key locations throughout the stir zone. X-ray diffraction patterns were taken to view phase orientations at locations of interest as well.

CHAPTER 3: DIFFUSION BONDING EXPERIMENTS AND RESULTS

3.1 Overview

Using a subset of the alloys discussed in Section 1.6 to better understand the general behavior of solid state joining in titanium alloys of different compositions, a matrix to assess the relative quality of diffusion bonding has been selected using several different alloys and temperatures. Shown below in **Table 3-1,** it is of note that only three of the bond conditions involving Beta 21S occur at temperatures below the nominal beta transus of 799°C (1490°F). Although Beta 21S is considered highly thermally stable, excursions above the beta transus will eliminate the microstructural features of the standard solution treat and over-age (STOA) heat treatment.

Table 3-1: Diffusion bond test matrix.

Alloy 1	Alloy 2	Bonding Temperature (C)							
		732	760	788	816	843	871	899	927
Ti-6242	Ti-6242					x	x	x	x
Ti-6242	Ti-64				x	x		x	x
Beta 21S	Beta 21S					x	x	x	x
Beta 21S	Ti-6242					x	x	x	x
Beta 21S	Ti-64				x	x	x	x	x
Beta 21S	Ti-64 Fine Grain	x	x	x	x	x			
Ti-64	Ti-64				x	x	x	x	x

3.2 Diffusion Bond Fabrication

The sub-scale diffusion bonding specimens used parameters as close to a production-scale process as possible. Material to be diffusion bonded was first cleaned with a vapor degreaser and a nitric-flouride flash etch to remove any light surface contamination. Diffusion packs were seam welded together, and an evacuation tube was welded into place on one side of the diffusion pack. While vacuum is applied to the tube, the tube is closed out with a weld to seal

the pack, and the outside is coated with graphite and boron nitride lubricant. A representative picture of a diffusion bond pack is show in **Figure 3-1**. Bonding is carried out at various temperatures for two hours, with a two sheet bladder providing 2 MPa of pressure on the pack, which is shown at completion in **Figure 3-1**.

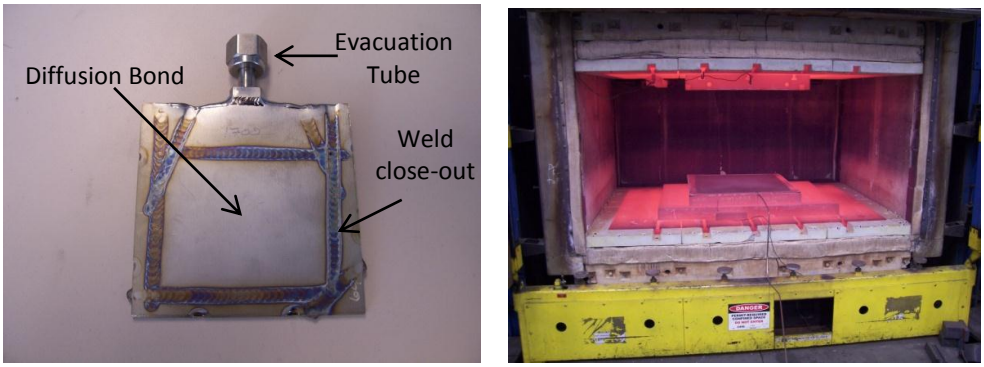

Figure 3-1: (a) Representative diffusion bonding pack configuration, after evacuation and close-out. **(b)** Completed diffusion bond pack, in press.

3.3 Microscopy and Microhardness

Specimens to be used for optical microscopy were excised from the diffusion bond pack via abrasive water jet cutting. Subsequent cutting to size was performed with a Struers 20S25 cutoff disc flooded with coolant to avoid heating the specimens during cutting. Metallographic specimens were mounted in Struers Durofast resin, and rough prepared using 60, 120, 240, 400 and 600 grit silicon carbide wet sanding discs. Care was taken to avoid excessive pressure and metal smearing. Polishing was accomplished using an ATA Saphir 550 autopolisher with 9 micron, 6 micron, 3 micron and 1 micron diamond suspension polishes on a MD Plan cloth. Pressures never exceeded 25 Newtons to avoid smeared metal and grit pickup. Between each polishing step, the mounts were rinsed with soap and water, and ultrasonicated in deionized water and etched with Krolls reagent. Final polish was accomplished with a Vibromet 1

vibratory polisher overnight, using .05 micron colloidal silica grit suspended in deionized water. Etching for microstructural examination was performed with Kroll's Reagent and ammonium biflouride.

Microstructural examination was performed on a Leica DM4000 M optical microscope with an attached Spot Insight 2MP digital camera using Spot Pro image collection software. Micrographs were collected at 100x and 500x magnification using unpolarized light. Images were adjusted to increase contrast.

Microhardness measurements were taken using LECO AMH 43 Microhardness Testing System on the Vickers scale, with a 100g load for 15 seconds. Measurements were taken in a line pattern, as shown in **Figure 3-2**.

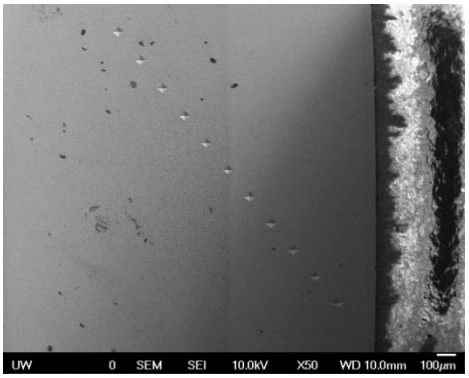

Figure 3-2: SEM image depicting microhardness traverse pattern across diffusion bond line, 50x.

Scanning electron microscopy (SEM) and energy dispersive x-ray spectroscopy (EDS) were carried out using a JEOL 7000 electron microscope system. Images were collected using an acceleration voltage of 10KeV, while EDS collection was done in a line of 50 discrete points, at a beam acceleration voltage of 20KeV and a dwell time of 5000ms per point.

3.4 Results and Discussion

3.4.1 Optical Microscopy

Optical examination of the metallographic specimens results show the expected trend of decreased voids and increasing homogenization of microstructure features along the bond interface with temperature. In the case of Ti-6Al-4V to Ti-6Al-4V, shown in **Figure 3-3**, diffusion bonding was apparent at even the lowest temperature of 815°C (1500°F). As the temperatures increased to 871°C (1600°F), the aspect ratio of the unbounded regions along the bond line decreased, demonstrating that diffusive mass transfer had occurred. The microstructure at the bond line showed a distinct mismatch between the two pieces of metal at lower temperatures, and as creep and diffusion occurred at higher temperatures, the bond line gradually became wavy and unclear, with a fully homogenous microstructure with no voids was achieved at a bonding temperature of 927°C (1700°F). The microstructure of Ti-6Al-4V responded as one would expect with a high sub-transus heat treatment – primary alpha dissolved and the volume fraction of transformed beta increased as the temperature increased. Microharness results show, on average, an increase in hardness in the base metal as the bonding temperature increased.

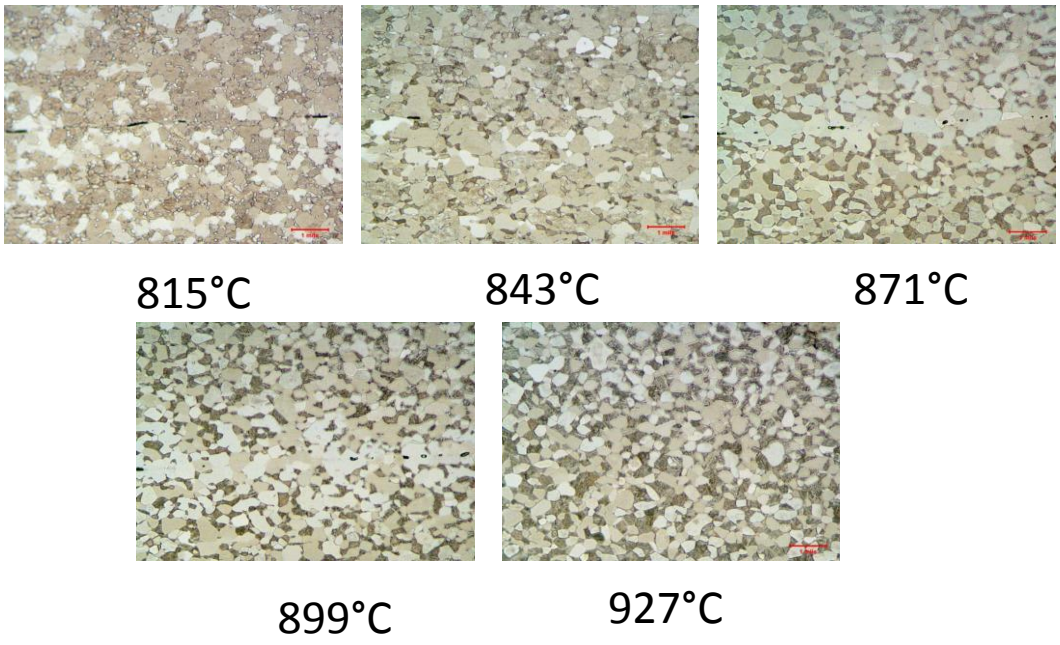

Figure 3-3: Ti-6Al-4V diffusion bond transverse metallographs, 200x magnification.

Similar results were obtained in the bonding of Ti-6242 to itself, and Ti-6Al-4V to Ti-6242. The quality of the bonds in Ti-6242 versus that of Ti-6Al-4V at a given temperature were noticeably lower – which is to be expected, considering the additional silicon present in the alloy to slow high-temperature creep. In general, hot deformation of Ti-6242 requires higher temperatures or forces as compared to Ti-6Al-4V. Diffusion effects, however, remained similar. In areas where intimate contact via creep had been achieved, the same changes in bond line geometry and microstructure at the local bonding area were observed at the same temperature as that of Ti-6Al-4V bonding to itself. Interdiffusion of alloying elements within a titanium matrix depends on microstructure and temperature, rather than the high temperature yield and flow stress of the alloy. This implies that in difficult to creep alloy systems, a quality diffusion bond could still be achieved with careful surface preparation to maximize contact, and an increase in pressure to speed up creep response.

Diffusion bonds where the Beta 21S alloy was utilized had much less uniform results than that where two alpha-beta alloys were being bonded together. Even in the case of a Beta 21S to Beta 21S bond, shown in **Figure 3-4,** there was still large concentrations of disbonded regions in the bond interface, even at the highest temperature of 1700F. Areas of the bond line that show contact also demonstrated localized homogenization of microstructure features, however, achieving intimate contact between the two pieces of material appears to be more difficult than in the case of bonds containing an α-β alloy. Although Beta 21S has lower room temperature tensile strength than any of the other alloys in the study, the high silicon content of 0.2% increases high temperature tensile properties and the large beta grain size makes for material less prone to creep deformation at elevated temperatures by reducing the impact of grain boundary slippage as a creep mechanism. Diffusion and microstructure evolutions can be clearly observed in areas where the two pieces of metal remained in contact, however. In those isolated areas where diffusion was able to occur, the same phenomenon of grain boundaries merging and microstructure morphology homogenization could be observed.

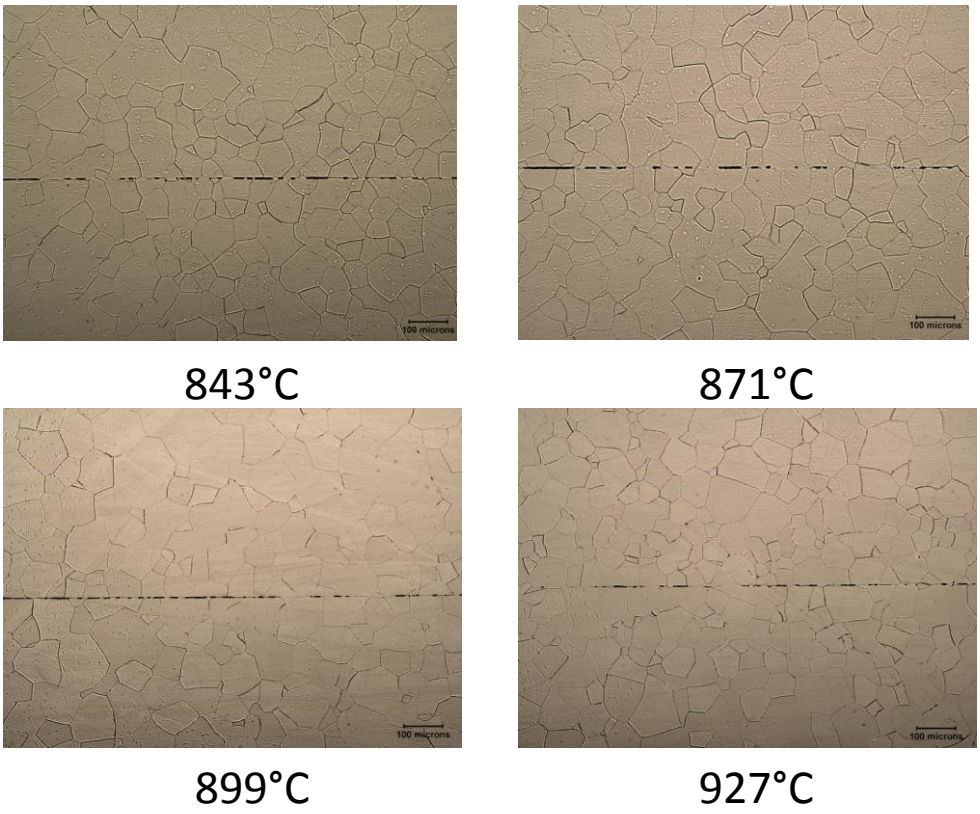

Figure 3-4: Beta21S diffusion bond transverse metallographs, 100x magnification.

Diffusion bonds using any of the alpha-beta alloys bonded to Beta 21S showed an interesting mix of successful bonds and microstructure features at the bond interface not observed in diffusion bonds fabricated with α-β/α-β alloy combinations or Beta21S/Beta21S bonds. Metallographic preparation of these samples proves difficult due to the different material removal behavior during mechanical polishing of the alloys and the resistance to acid attack demonstrated by Beta 21S. Intimate contact appears achievable even when only one alloy is capable of substantial creep, allowing for interdiffusion to occur. The same general trends of bond line and porosity evolution hold true in these bonds as well – intimate contact is followed by lowering of the aspect ratio of any voids and the homogenization of the local microstructure to eliminate any evidence of the bond as the temperature increases. However, as diffusion

increased with temperature, it became clear that the local region around the bond line had a distinctly different chemical composition than either alloy. Shown in **Figure 3-5**, hotter bonds show a band of Widmanstatten alpha structure, demonstrating a composition of alpha stabilization capable of a large volume fraction of alpha phase at a near-equilibrium slow-cool condition and a level of beta stabilization capable of lowering the beta transus below 927°C (1700°F). With neither base alloy capable exhibiting the same phase morphology from a heat treatment to 927°C (1700°F), it is clear that a new alloy has formed in a band around the former interface.

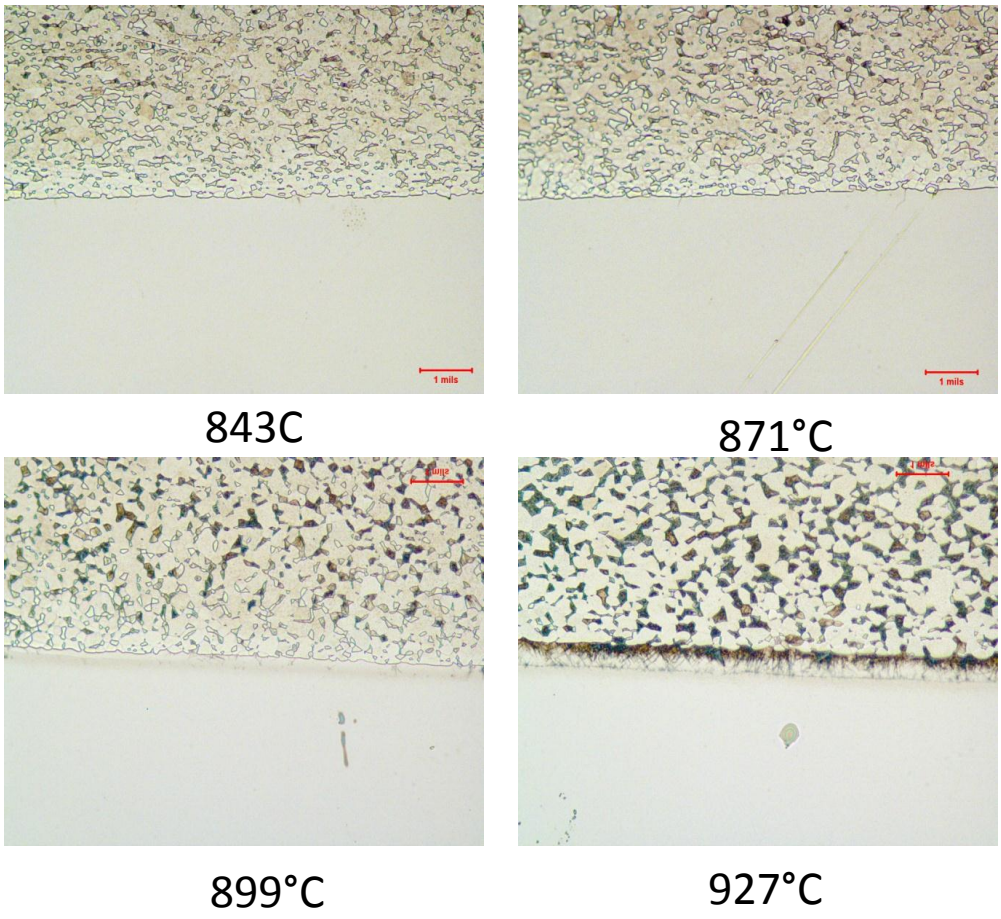

Figure 3-5: Beta21S to Ti-6242 diffusion bond transverse metallography, 200x.

3.4.2 Microhardness

Microhardness traverses across the bond line showed a trend in the response of a given alloy to heat treatment, however, the length scales of the diffusion band proved difficult to characterized with microhardness indents. Bonds of expected low mechanical integrity, such as the 1500F Ti-6Al-4V-Beta21S bond shown in **Figure 3-6**, still showed a minor increase in microhardness when the indenter is centered on the bond line itself. This could simply be from a limitation of hardness testing in and of itself, where the material is loaded heavily in compression and geometry effects mask the low quality of the bond itself, where as a shear pull-off test or a tensile test would show a lower integrity bond. As the temperature of the bonding cycle increases and the diffusion band widens between the alloys, there is a modest smoothing of the jump from the hardness value of the Ti-6Al-4V to the Beta21S, showing evidence of a compositional gradient.

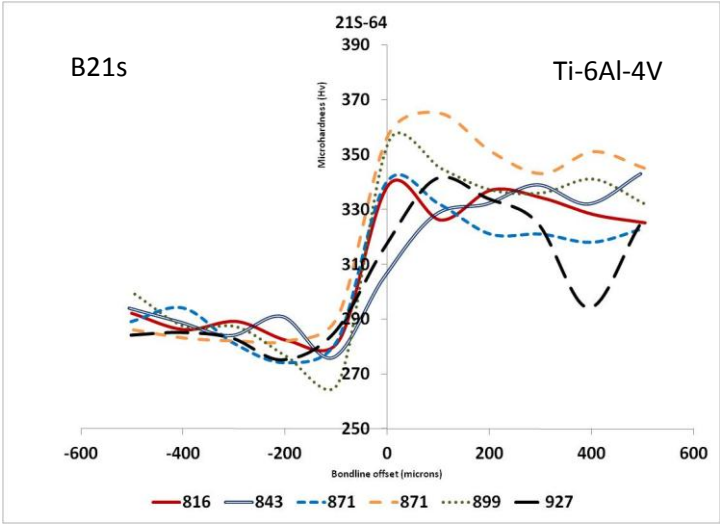

Figure 3-6: microhardness profile of Ti6-Al-4V diffusion bonded to Beta 21S at various temperatures.

The alpha-beta alloys tested showed an increase in hardness as the temperature of the bonding cycle increased, until the hottest temperatures were reached. This is most likely attributed to residual solid solution strengthening of the beta phase as α particles dissolve into the

beta matrix, leaving additional α-stabilizing elements in the BCC structure as well as very fine α precipitates resulting from the relatively rapid cooling cycle. The Beta21S material shows no discernible hardness difference with the various thermal cycles, which is to be expected based on the low volume fractions of α phase having a lesser impact on mechanical properties as their size and distribution changes.

3.4.3 Scanning Electron Microscopy

Electron microscopy examination of the Ti-6Al-4V-Beta21S diffusion bond system was selected due to the pronounced compositional and microstructural differences between the two alloys, and served as confirmation of the diffusive behavior observed in the optical micrographs. **Figure 3-7a**, showing the bond at 815°C (1500°F), shows a distinct interface between the Beta 21S material and the Ti-6Al-4V. With the Kroll's etch attacking the alpha phase, very little etching is seen in the Beta 21S, while the Ti-6Al-4V appears in deep relief. There appear to be small, equiaxed alpha particles that have etched out of the Beta21S, although this looks to be isolated to the region near the bond line. An EDS line scan shows no distinguishable diffusion, with anomalies in the data points near the interface, presumably from the masking effect of the interface step during x-ray detection.

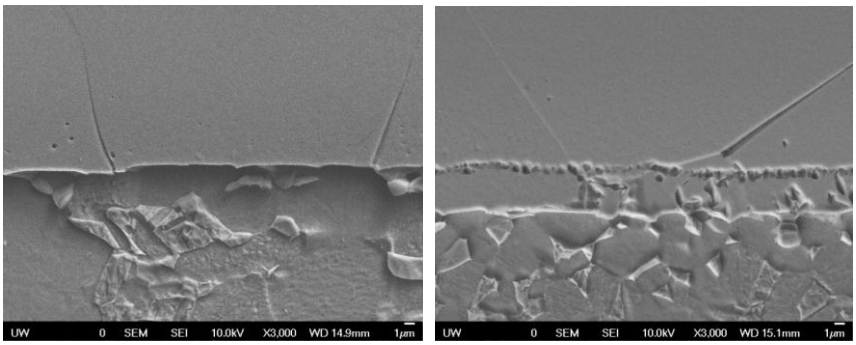

(a) **(b)**

Figure 3-7: (a) Beta21s (top) bonded to Ti-6Al-4V at 815°C (1500°F), 3000x magnification.**(b)** Beta21s (top) bonded to Ti-6Al-4V at 843°C (1550°F), 3000x magnification.

A bonding temperature increase of 28°C (50°F), **Figure 3-7b**, shows a noticeable difference in alpha morphology near the interface. A linear array of equiaxed alpha particles parallel to the bonding interface is seen approximately 4 microns from the primary alpha particles of the Ti-6Al-4V, separated by a band of stabilized beta phase. It is unclear if this band of small alpha particles are the result of residual alpha stabilization at the bond interface followed by subsequent growth of the large, Beta 21S beta grains into the Ti-6Al-4V microstructure, or diffusion of alpha stabilizing elements from the Ti-6Al-4V into the Beta 21S. There appears to be a higher concentration of alpha particles near the beta grain boundaries within the Beta 21S. It is again unclear if this is due to the preferential nucleation at heterogeneous sites along the grain boundaries or a higher local concentration of alpha stabilizing elements due to higher grain boundary versus bulk diffusion rates. An EDS line scan was performed parallel to the bond interface, shown in **Figure 3-10**, through the more alpha-dense region did not show a discernable increase in alpha stabilizing elements.

At 871°C (1600°F), **Figure 3-8a**, there appears to be a more subtle change in the microstructure. Away from the bond interface in the Beta 21S material, there is a noticeable coarsening of the alpha particles as compared to a bond performed at 843°C (1550°F). There is

an increase in the aspect ratio of the nucleated alpha particles near the bond interface, although the difference is minor. Considering that both bond temperatures are well above the nominal beta transus of Beta21S, we could not be seeing additional growth of existing alpha phase. Any change in the volume fraction of alpha phase in the Beta 21S material would rely on an increase in alpha stabilizing elements via diffusion from the Ti-6Al-4V or an increased dwell time in the temperature band suitable for alpha particle growth due to the slower cooling times that coincide with a hotter diffusion bonding cycle.

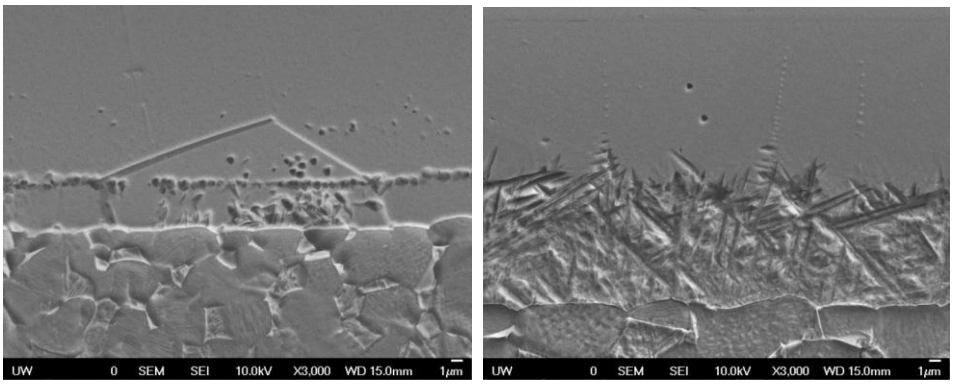

(a) **(b)**

Figure 3-8: (a) Beta21s (top) bonded to Ti-6Al-4V at 871°C (1600°F), 3000x magnification.**(b)** Beta21s (top) bonded to Ti-6Al-4V at 927°C (1700°F), 3000x magnification.

The highest temperature bond, 927°C (1700°F), shows a noticeable change in the microstructure band surrounding the bond interface in **Figure 3-8b**. What was demonstrated in the optical micrographs as a dark band now shows clearly to be Widmanstatten structure. The depth of etch attack of the secondary alpha platelets suggest a coarser platelet further from primary alpha particles of the Ti-6Al-4V. This would imply this was the initial site of nucleation of the alpha platelets, which was demonstrated in lower temperature bonds. As the platelets

coarsen they provided additional nucleation sides, forming the basketweave structure that becomes increasingly fine as it moves away from the initial site of nucleation.

EDS analysis showed an emergence of a widening diffusion band as temperature increases during the bonding cycle. **Figure 3-9** shows a plot of the molybdenum content across the complete range of diffusion bond temperatures in the Ti-6Al-4V to Beta 21S system. The 815°C (1500°F) bonding temperature shows a sharp transition in the Molybdenum content as the bond line is crossed, which is to be expected, considering the lack of intimate contact between the two materials. In all but the hottest bond condition, there appears to be very similar levels of Molybdenum in the Beta 21S half of the joint, however, there is a sharp difference between the 843°C (1550°F) bond condition's Molybdenum content in the Ti-6Al-4V side of the bond as compared to the 871°C (1600°F) and 899°C (1650°F) condition. This could be an effect of phase transformations upon cooling from a higher temperature driving localized composition changes, or simply passing a concentration threshold that becomes readily detectable outside of the noise inherent in EDS data sets.

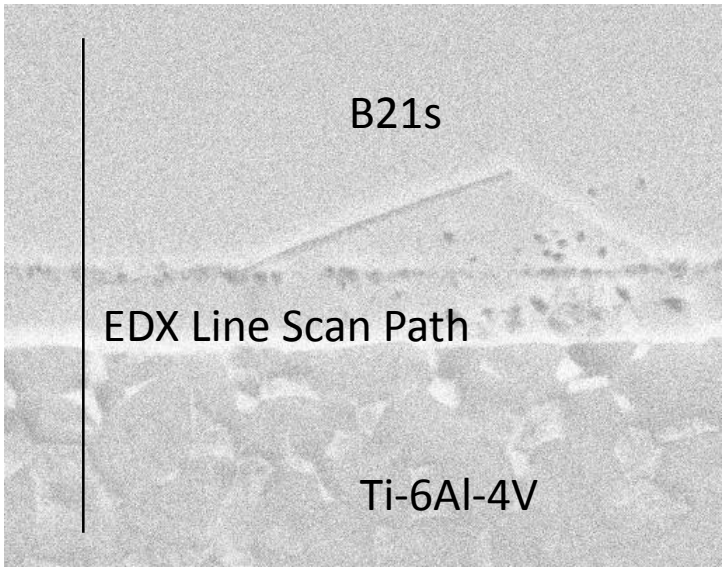

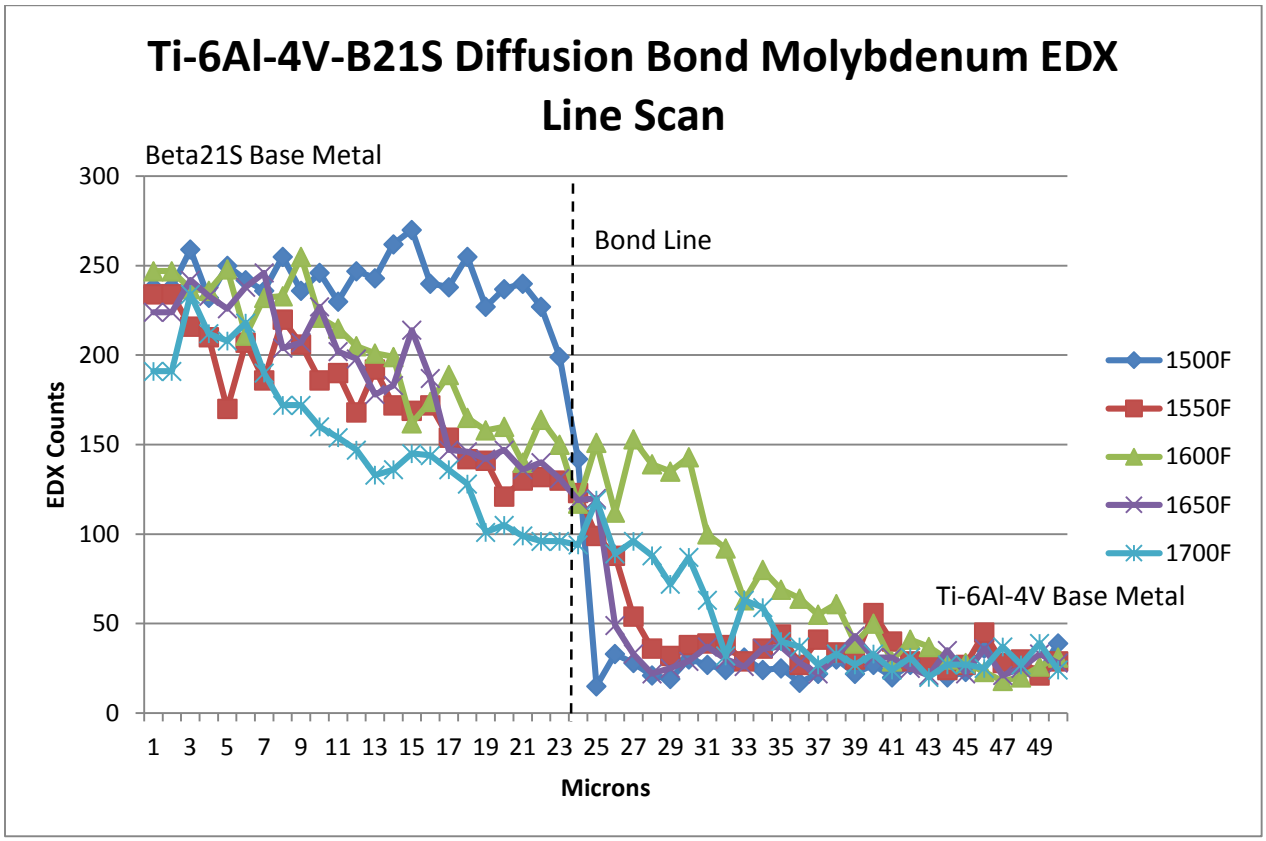

Figure 3-9: Beta21S to Ti-6Al-4V EDS line scan transverse to bond line molybdenum content. Image denotes representative EDS line scan path for all samples.

Attempts were made to discern composition differences in the alpha-rich grain boundary areas of the Beta21S material, both in the 843°C (1550°F) condition and the 871°C (1600°F) condition. In the 843°C (1550°F) bond, a line scan was performed parallel to the bond line, through the grain boundaries with higher levels of alpha particles, shown in F**igure 3-10**. The results are inconclusive, and there is nothing that can be definitively said about composition differences. Similarly, two line scans were performed perpendicular to the bond line, one through an alpha-lean area and another through a grain boundary alpha-rich area. Again, no definitive conclusions can be drawn about the composition differences in the two regions. The size of the particles or relatively minor composition differences between the alpha particles and their surroundings could prove difficult to characterize, given the 1 micron spot size and the detection limits of the EDS method.

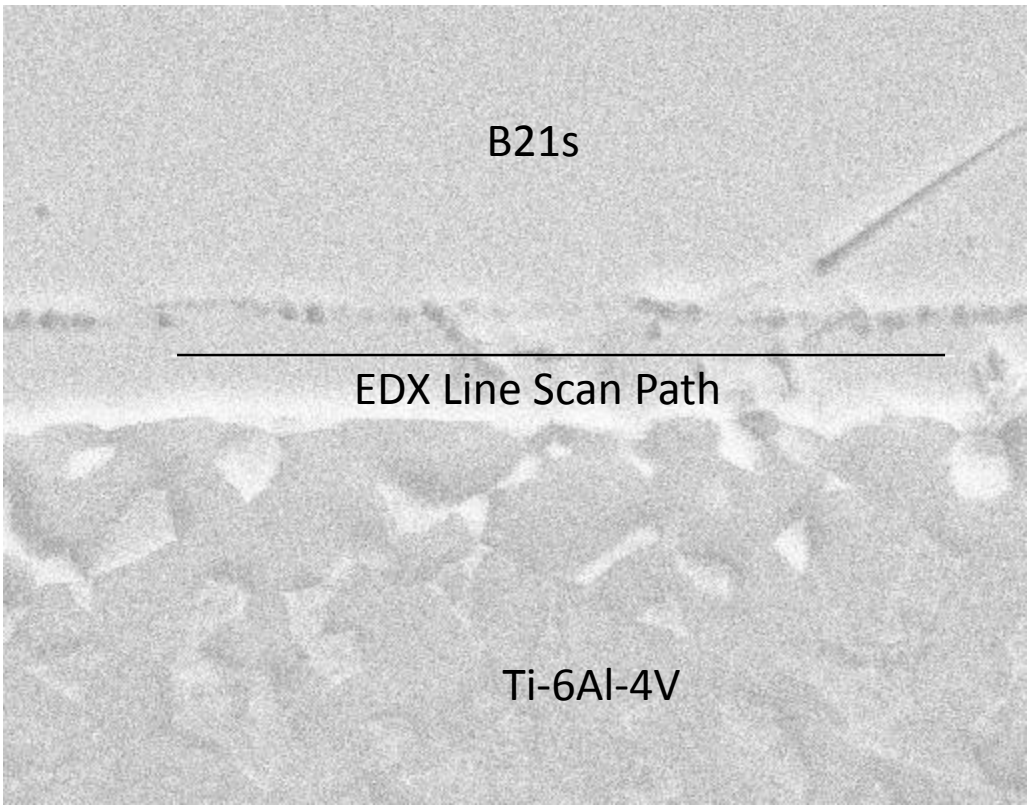

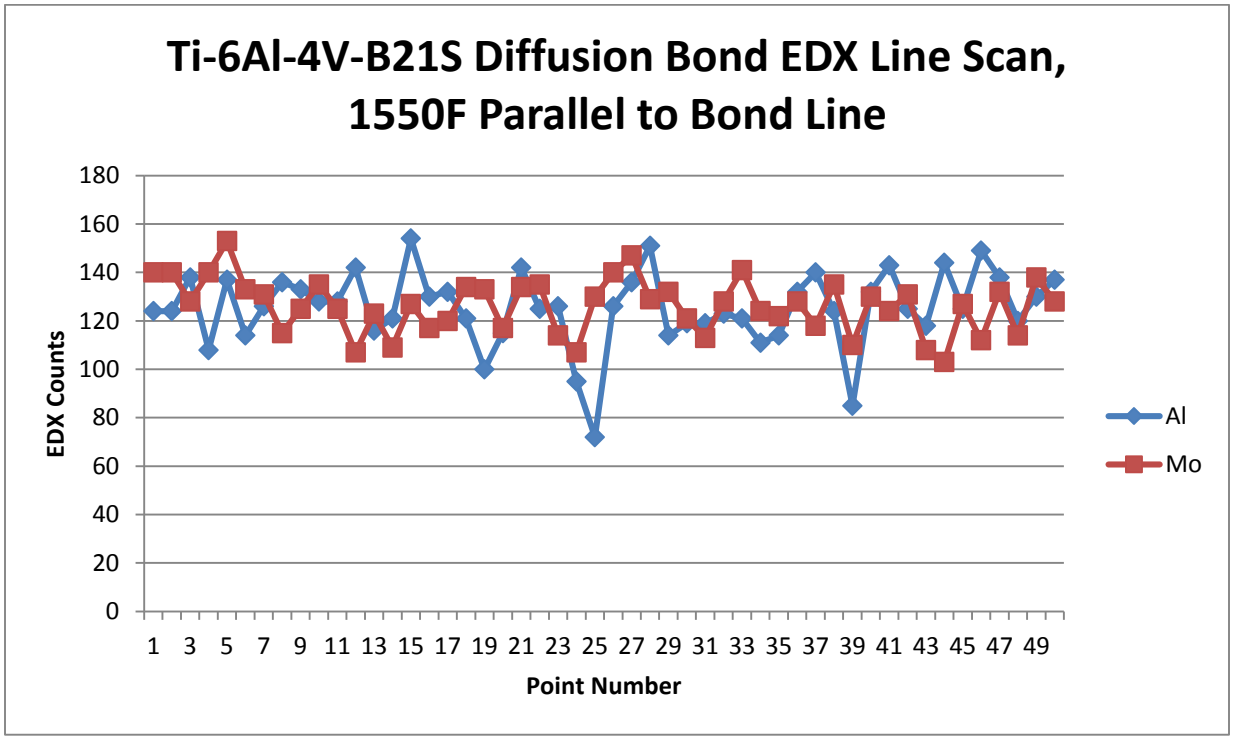

Figure 3-10: Beta21S to Ti-6Al-4V EDS line scan parallel to bond line molybdenum and aluminum content.

3.5 Diffusion Bonding Summary and Conclusions

Diffusion bonding of dissimilar titanium alloys showed the importance of differentiating the controlling factors in a diffusion bond's microstructure and macrostructure during analysis:

- At least one alloy needs to be capable of creeping to the point of consistent intimate contact at the temperature selected to produce a defect-free bond line.
- Grain structure mismatches can still occur in the absence of bond line defects; fully homogenized bond line microstructures require significant increases in time or temperature beyond the time and temperature required to eliminate most bond line defects.
- Diffusive mixing of dissimilar alloys can be evidenced by chemical gradients as well the precipitation of new microstructure features, however, microstructure features need to be interpreted in relation to the composition of the alloy in question and the working temperature.
- Even simple diffusion calculations are not possible without more insight into the creep behavior and timing, as well as the influence of the formation of new phases and grain boundaries.

Overall, the diffusion bonding experiments do not prove a definitive model or complete understanding of diffusion bonding in dissimilar titanium alloys and the mechanical joining process must be considered at the same time. However, the microstructures and chemical analysis performed serve a valuable platform to compare other solid state joining processes against. By demonstrating bonding defects, microstructure mismatches, fine particle and full basketweave alpha precipitates, as well as chemical gradients not evidenced by the

microstructure across multiple temperatures, one can begin to understand the interplay of mechanics and diffusion in more complex joining processes.

CHAPTER 4: FRICTION STIR WELDING EXPERIMENTS AND RESULTS

4.1 Overview

Friction stir weld joints were prepared using a variety of tool rotation speed, tool travel speed and alloy combinations, shown in **Table 4-1** and **Table 4-2**, designed to produce a variety of microstructure conditions. Process conditions were chosen to be within the boundaries for Ti-6Al-4V shown to produce full penetration, porosity-free welds [Edwards, 2010c]. Not all weld alloy combinations and parameter conditions possible from **Table 4-1** and **Table 4-2** were made available for this work due to material limitations. Of the available welds, a subset were selected for sectioning and detailed characterization. These weld conditions are noted with a circled X in **Table 4-2** and are detailed in Section 4.5.

Table 4-1: Experimental weld parameter matrix.

Weld Parameters		Spindle Speed (RPM)		
		225	275	325
Travel Speed (mm/min)	100		X	
	125	X	X	X
	150		X	

Table 4-2: Friction stir weld butt joint alloy combinations.

Weld Combinations		Alloy A				
		Ti54M	Ti-6Al-4V	Ti 6242	Ti-6Al-4V - FG	Ti-6242 - FG
Alloy B	54M	X	X	X	X	X
	Ti-6Al-4V		X	X		X
	Ti-6242			X		
	Ti-6Al-4V - FG				X	X
	Ti-6242 - FG					X

4.2 Friction Stir Weld Fabrication

Friction stir butt welds were fabricated using a Transformation Technologies Inc. friction stir weld machine owned and operated by The Boeing Company, shown in **Figure 4-1(a)** on sheets of 4.5mm (.180”) nominal thickness. The pin is composed of a precision ground tungsten lanthanide alloy, shown in **Figure 4-1(b)**.

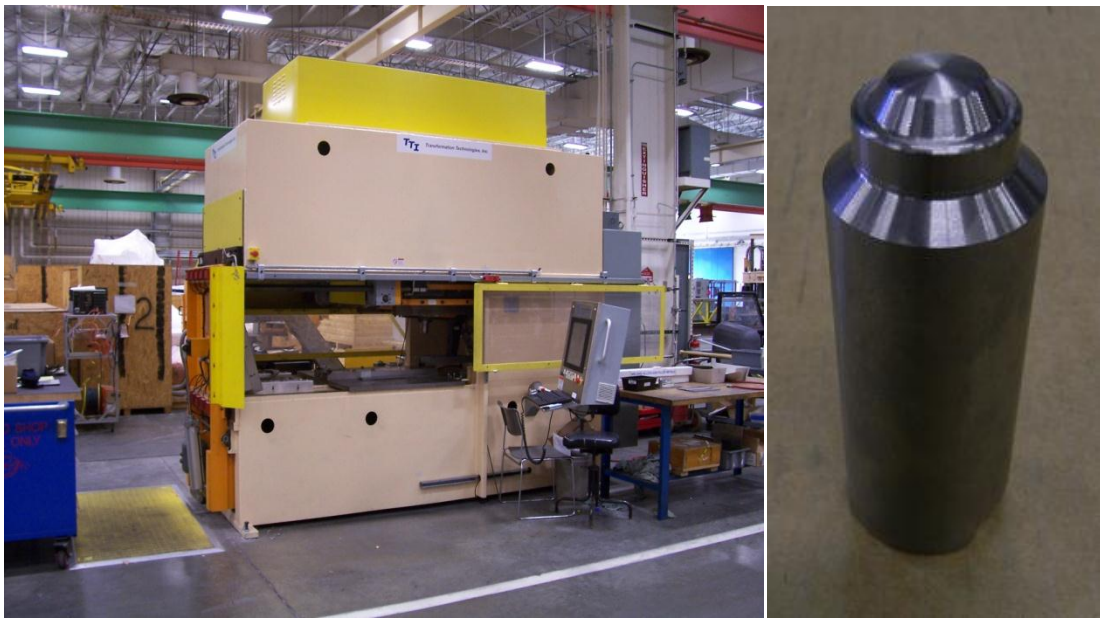

(a) **(b)**

Figure 4-1: (a) Friction stir weld machine **(b)** Tungsten-Lanthinide friction stir weld tool.

Weld seams were approximately 12” in length, using the rotation speeds and travel speeds listed in **Table 4-1**. Welds were visually inspected for uniformity and surface condition as well as x-ray inspected for internal defects**.** All panels were given a 30 minute stress relieve cycle at 732°C (1350°F) and sectioned for characterization using waterjet abrasive cutting. A representative weld joint is shown in **Figure 4-2.**

Figure 4-2: Typical friction stir butt weld.

4.3 Metallography

Metallographic specimens for optical and electron microscopy were mounted in Struers Durofast resin, and rough prepared using 60, 120, 240, 400 and 600 grit silicon carbide wet sanding discs. Care was taken to avoid excessive pressure and metal smearing. Polishing was accomplished using an ATA Saphir 550 autopolisher with 9 micron, 6 micron, 3 micron and 1 micron diamond suspension polishes on a MD Plan cloth. Pressures never exceeded 25N to avoid smeared metal and grit pickup. Between each polishing step, the mounts were rinsed with soap and water, and ultrasonicated in deionized water and etched with Krolls reagent. Final polish was accomplished with a Vibromet 1 vibratory polisher overnight, using .05 micron colloidal silica grit suspended in deionized water. Etching for microstructural examination was performed with Kroll's Reagent and ammonium biflouride.

Micrographs were captured using a Leica DMI5000 M at 100x magnification and montaged using the software package supplied with the microscope.

4.4 Scanning Electron Microscopy and EDS

SEM and EDS were performed using a FEI Serion microscope at an acceleration voltage of 10KeV for image capture and 20KeV for EDS data collection. Processing of EDS data and identification of peaks was performed using Oxford AZtec EDS analysis software**.**

4.5 Results and Discussion

4.5.1 Weld Macrostructure and Optical Microscopy

Welds containing Ti-6242 were the focus of the microscopic characterization, representing the broadest difference in composition, microstructure and mechanical properties when compared to the other alloys chosen in the study. The baseline homogenous welds of Ti-6242 fine grain to Ti-6242 fine grain, shown in **Figure 4-3(a-e)** show very little distinction from one and other based on weld parameters. The shape of the heat affected zone band on the retreating side of the weld changes in shape, with a small bulge depending on weld parameters, presumably from differences in heat input. In Plate **(e)** there is evidence of lack of penetration at the root of the weld, and each plate shows a unique pattern of tooling marks that vary in periodicity and amplitude, but appear to be uniform on both the retreating and advancing side of the weld. The microstructure is heavily refined – there are fine, elongated alpha particles throughout the weld nugget, characteristic of precipitation upon cooling through the beta transus and heavy mechanical deformation. The heat affected zone is very narrow, showing dissolution of the alpha phase due to heating.

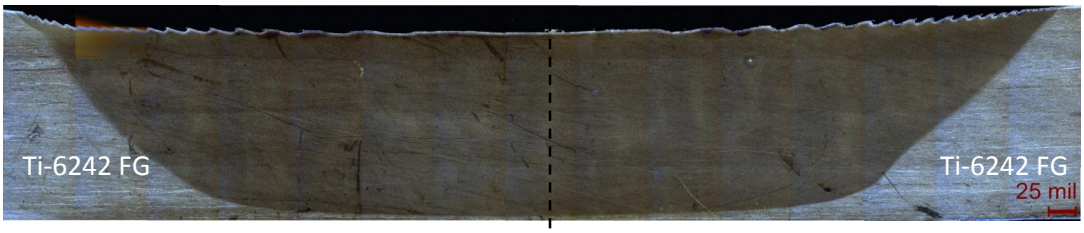

(a)

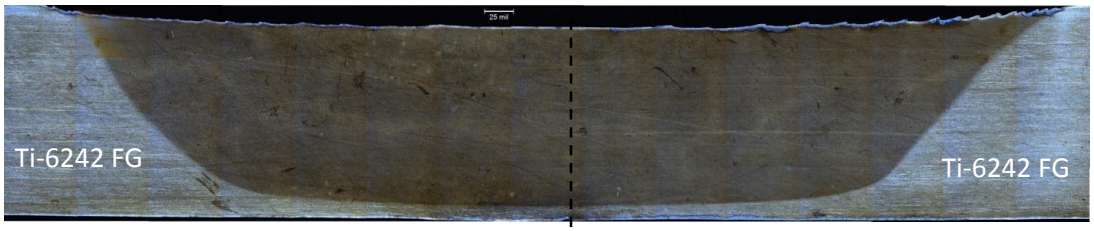

(b)

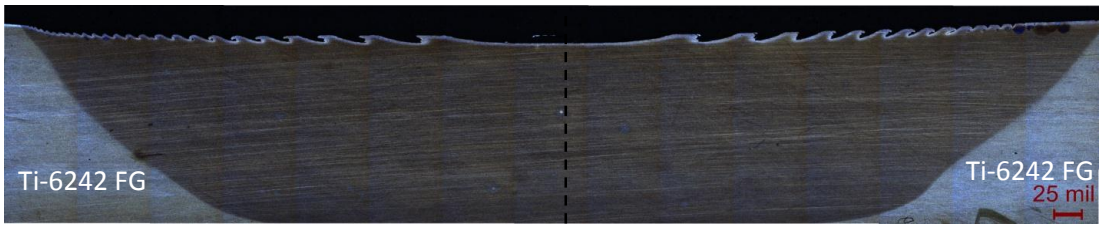

(c)

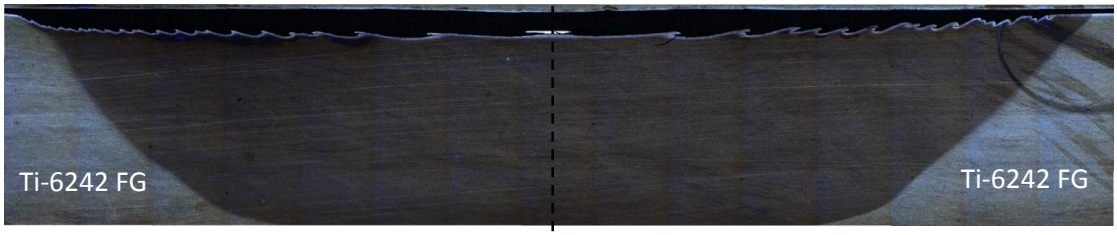

(d)

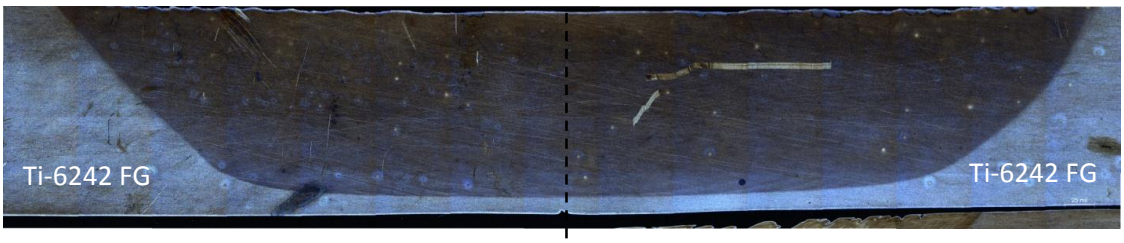

(e)

Figure 4-3: Ti-6242 fine grain welded to Ti-6242 fine grain at **(a)**275RPM and 125mm/min **(b)**275RPM and 150mm/min **(c)**325RPM and 125mm/min **(d)**275RPM and 100mm/min **(e)**225RPM and 125mm/min. Dashed line denotes original material interface.

Analysis of a dissimilar alloy combination, Ti-6242 fine grain (light, retreating side) and Ti-6Al-4V (dark, advancing side), showed cohesive welds in all conditions – there is no evidence of seams, tears or cracks, shown in **Figure 4-4(a-c)**. In plate **(a)**, there is highly turbulent mixing at the root of the weld, increasingly so on the advancing side. The Ti-6242 material has been sheered and moved in large sheet-like pieces into the Ti-6Al-4V material. The microstructure of both alloys shows very fine acicular alpha particles from heating above the beta transus, refined by mechanical deformation, in the weld zone. There is a very fine heat affected zone surrounding the weld nugget, evidenced by the dissolution of the alpha structure present in the base metal. Plate **(b)** shows the same microstructural characteristics throughout the various regions of the weld, however the macrostructure is changed significantly. The patterns show a distinct periodicity in the Ti-6242 material deposited into the advancing side, with finer and finer lath widths as they approach the heat affected zone. The periodicity is also demonstrated in the more turbulent root of the weld. Plate **(c)** shows very little pattern in the material deposits, and very violent mixing. There is a much higher concentration of Ti-6Al-4V deposited into the retreating side of the weld nugget as compared to either plates **(a)** or **(b)**, as well as the turbulent region at the root of the weld continuing in small bands upwards towards the weld face. In all cases, the tooling marks on the face of the weld correlate loosely to the macrostructure of the weld – more periodic and regular laps and gouges on the face of the weld also produce more regular intervals of material deposits within the weld nugget. More irregular tool marks in terms of both position and depth also produced more turbulent deposits of material in the weld nugget.

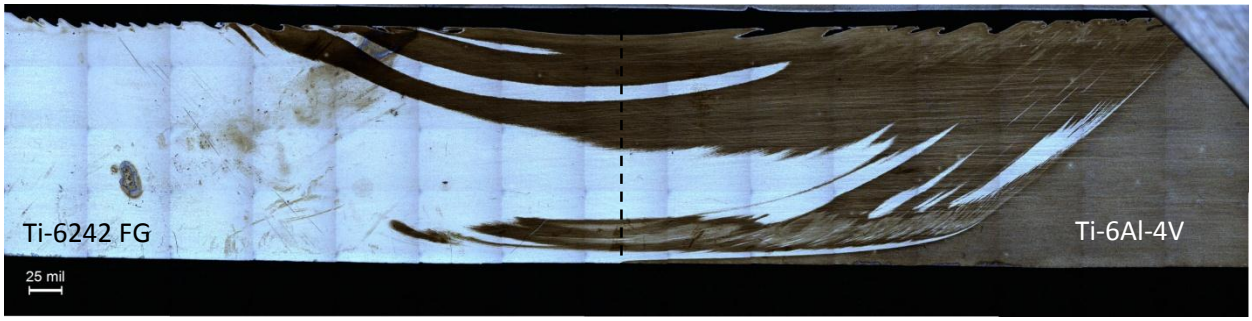

(a)

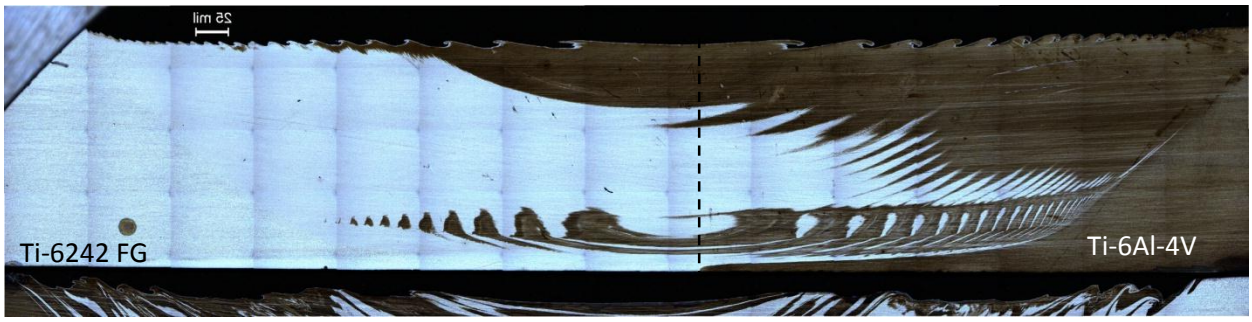

(b)

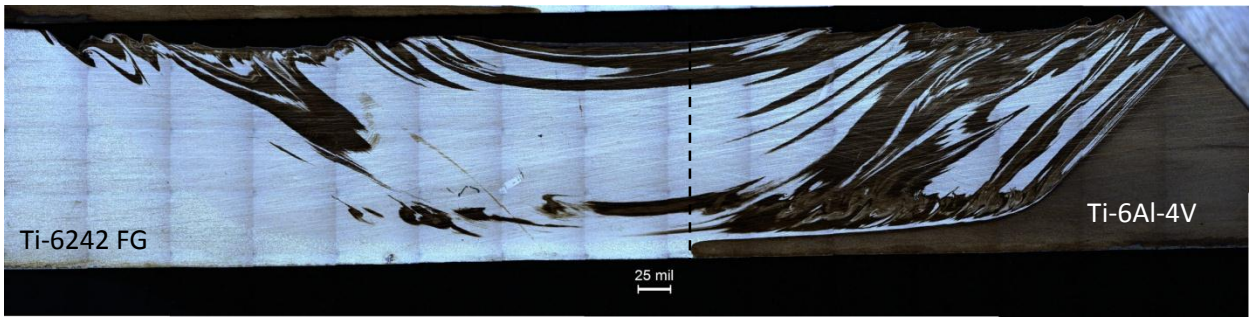

(c)

Figure 4-4: Ti-6Al-4V (dark, right side) welded to Ti-6242 fine grain (light, left side) at **(a)** 325RPM and 125mm/min **(b)** 275RPM and 100mm/min **(c)** 225RPM and 125mm/min. Dashed line denotes original material interface.

Welds composed of Ti-6242 (light, retreating side) and Ti54M (dark, advancing side) shown in **Figure 4-5**, show similar characteristics to the Ti-6242 fine grain / Ti-6Al-4V standard grain welds in their macrostructure, which can be expected based on the similarities between Ti-6Al-4V and Ti54M. Plate **(a)** shows larger ligands of material from the retreating side deposited throughout the advancing side, as well as a turbulent band near the root of the weld. As the tool

marks increase in their periodicity in plates **(b)**, **(c)** and **(d)**, the banding in the depositing of the Ti-6242 into the advancing side of the weld becomes more regular and predictable. Again, the microstructure shows a heavily refined alpha phase as well as a very narrow heat affected zone.

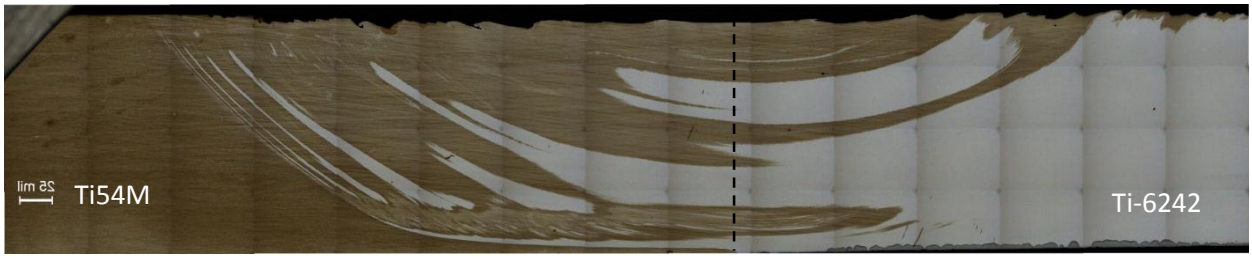

(a)

(b)

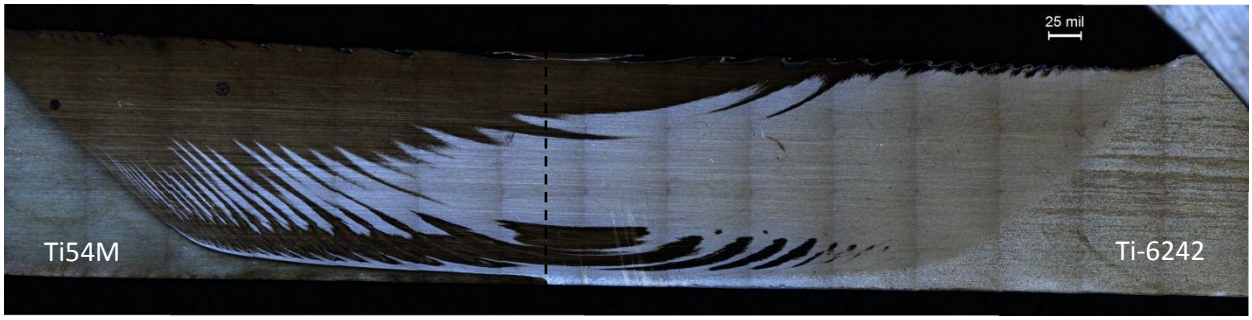

(c)

(d)

Figure 4-5: Welds of Ti-6242 (light, right side) and Ti54M (dark, left side) produced at **(a)**275RPM and 125mm/min **(b)**275RPM and 150mm/min **(c)**275RPM and 100mm/min **(d)**225RPM and 125mm/min. Dashed line denotes original material interface.

4.5.2 Electron Microscopy

Two weld conditions of Ti-6242 to Ti54M, representing the largest difference in chemical composition and phase composition of the test matrix, were selected for further analysis using SEM and EDS to characterize microstructure as well as relative chemical compositions. The welds were produced at 125mm/min travel speed and 225RPM and 275RPM respectively. Positions in the weld were selected to represent the extremes in temperature and mechanical mixing within the weld nugget, shown schematically in **Figures 4-6 and 4-7**.

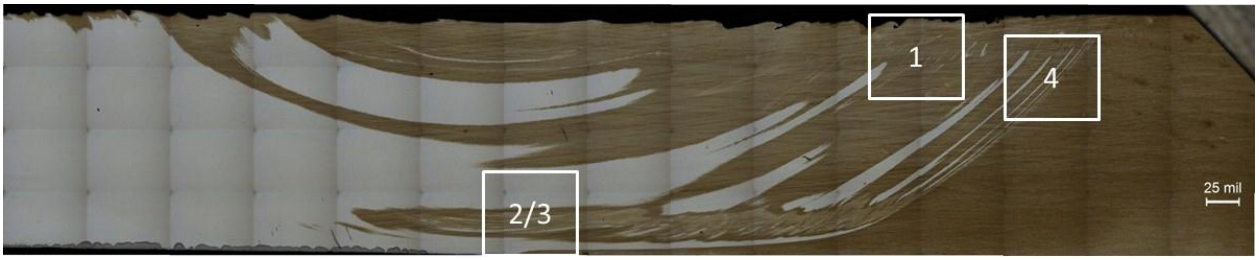

Figure 4-6: Ti-6242 to Ti54M plate 1, 125mm/min, 275RPM SEM and EDS analysis sites.

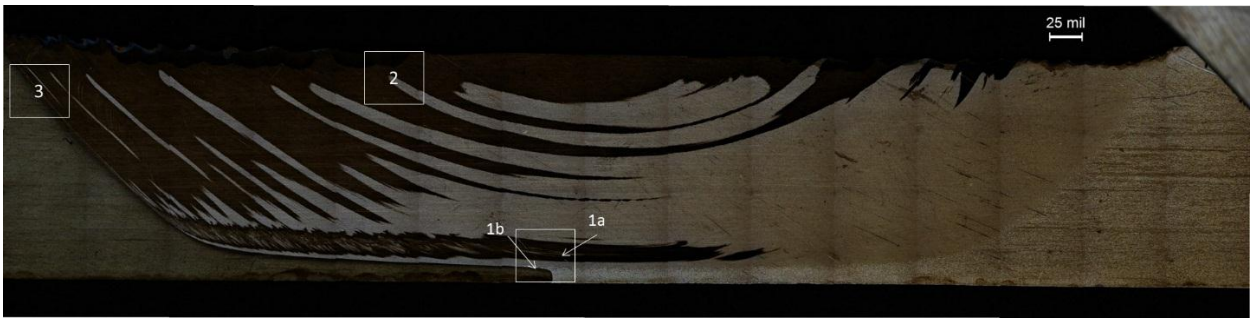

Figure 4-7: Ti-6242 to Ti54M plate 5, 125mm/min, 225RPM SEM and EDS analysis sites.

Looking at a 2500x image from Zone 1 of plate 1, shown in **Figure 4-8,** the fine features of the alpha phase in both alloys are readily apparent. Neither the Ti-6242 (lighter) nor the Ti54M show any evidence of primary alpha, confirming an excursion above the beta transus of sufficient time or temperature to fully dissolve the primary alpha particles characteristic of the parent materials.

Prior beta grain boundaries show more clearly in the Ti-6242, evidencing prior beta grains in the size range of 5-10um; significantly smaller than is generally seen in the parent materials. This conveys the severity of the mechanical deformation inherent in the FSW process as compared to traditional metal working operations – the microstructure of both alloys has been refined by an order of magnitude in a matter of seconds.

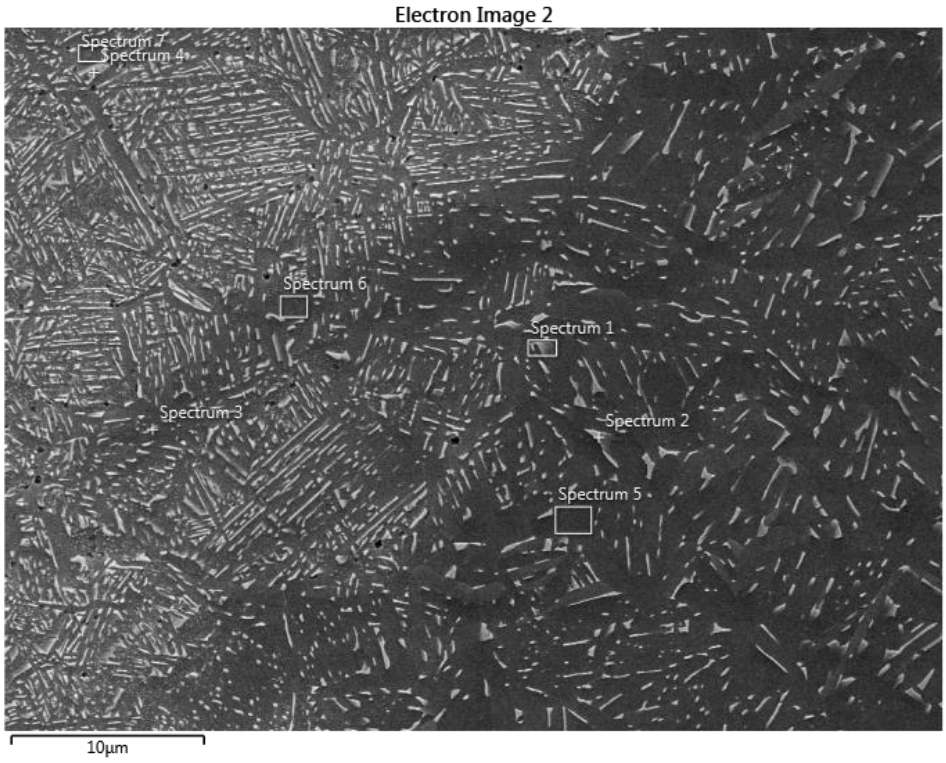

Figure 4-8: Ti-6242 to Ti54M Plate 1 Zone 1 SEM image, 2500x.

There appears to be sub-micron porosity present in both the Ti54M and the Ti-6242. The origin of the porosity has not been confirmed, however the concentration of the porosity near the interfaces of the two materials suggests that this is a result of the mechanical joining of the two alloys. Perfectly round and uniform porosity also suggests that there has been sufficiently high heat while in the absence of mechanical deformation to allow for surface diffusion and pore shrinkage. The alpha structure of both materials shows a lath-like structure precipitated as the

material cooled through the beta transus, with a higher volume percentage in the Ti-6242, as is expected from its chemical composition and higher beta transus. It is not known how much impact the subsequent annealing cycle has had on the alpha structure, although it can be assumed that the alpha phase fully dissolved during the weld process due to the uniformity of the alpha lath size. Undissolved alpha particles would lead to larger, equiaxed particles upon cooling; none of which are observed in the microstructure. There is also a gradient in alpha lath size and density at the material interfaces, which appears to be variable over very short length scales, depending on which specific 'branch' of the material interface is being observed. This suggests a unique and variable mechanical joining and interface morphology of the two parent materials over very short distances that influences the local chemical compositional gradient.

Looking at an analogous location in the weld nugget of Plate 5, shown in **Figure 4-9**, welded at a higher rotation speed to produce a hotter weld, similar microstructural features are observed. A structure devoid of primary alpha, with heavily refined prior beta grains precipitating alpha laths characterizes the microstructure of both alloys. The lower magnification of this image shows to a greater degree the tortuous interface between the two parent materials, with distinct 'branches' along the overall material interface showing various degrees of variation in structure and density of alpha laths.

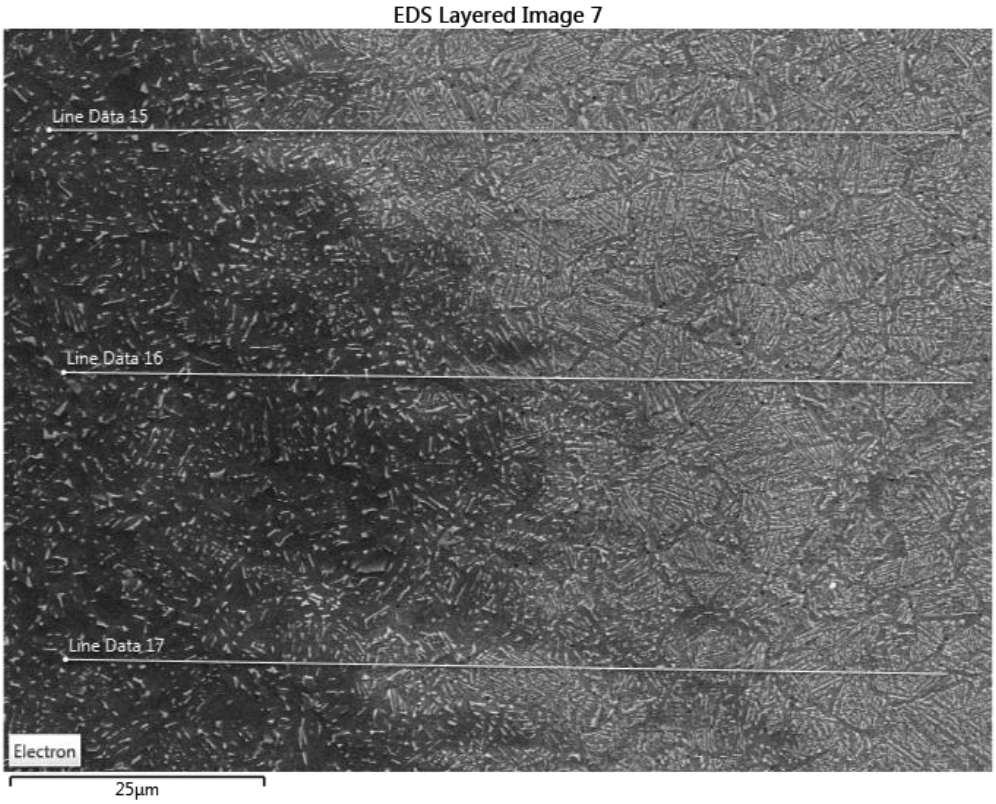

Figure 4-9: Ti-6242 to Ti54M Plate 5 Zone 2, 125mm/min, 225RPM, 1000x SEM image.

Zone 2/3 of Plate 1 (as depicted in **Figure 4-7)**, shown in **Figure 4-10** at 500x and 1000x magnification, depicts the variation in structure seen in the root of the weld. Lower magnification micrographs show this as a turbulent mixing zone, while the higher magnification images show distinct streaks of the two parent materials tens of microns in width – far more narrow than seen in any other portions of the weld. At 2500x, the microstructure is observed to be very similar to the observed structures in the top of the weld. The 'branches' of the interface appear to be of a finer scale, as are the gradients in alpha structure associated with them. Also of note is the higher density of microporosity, although it now appears much more preferentially in the Ti-6242. Taking the fine banding to imply more intense mechanical deformation along with Edwards work showing the relatively lower temperature of the weld root, it is valid to assume the porosity

evidenced preferentially in the alloy with the higher beta transus and higher elevated temperature mechanical properties is in fact strain induced porosity.

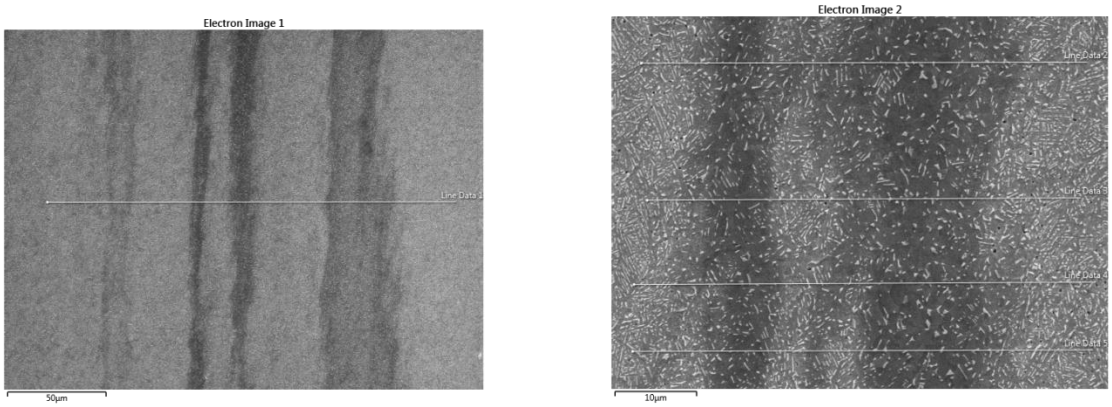

Figure 4-10: Ti-6242 to Ti54M Plate 1 Zone 2/3, 125mm/min, 275RPM, 500x (left) and 2500x (right) SEM image.

4.5.3 Analysis of Chemical Gradients in FSW Structures

EDS analysis reveals that the microstructural gradient also correlates to compositional gradients, shown in **Figure 4-11.** Looking specifically at Zirconium (unique to Ti-6242) and Vanadium (unique to Ti54M), the compositional gradient appears to extend several microns beyond the visual indications of a composition gradient provided by the changes in volume fraction and morphology of the alpha laths. It would make sense to reason that the actual compositional band is narrower and would be more accurately measured with a line scan run perfectly perpendicular to the apparent interface.

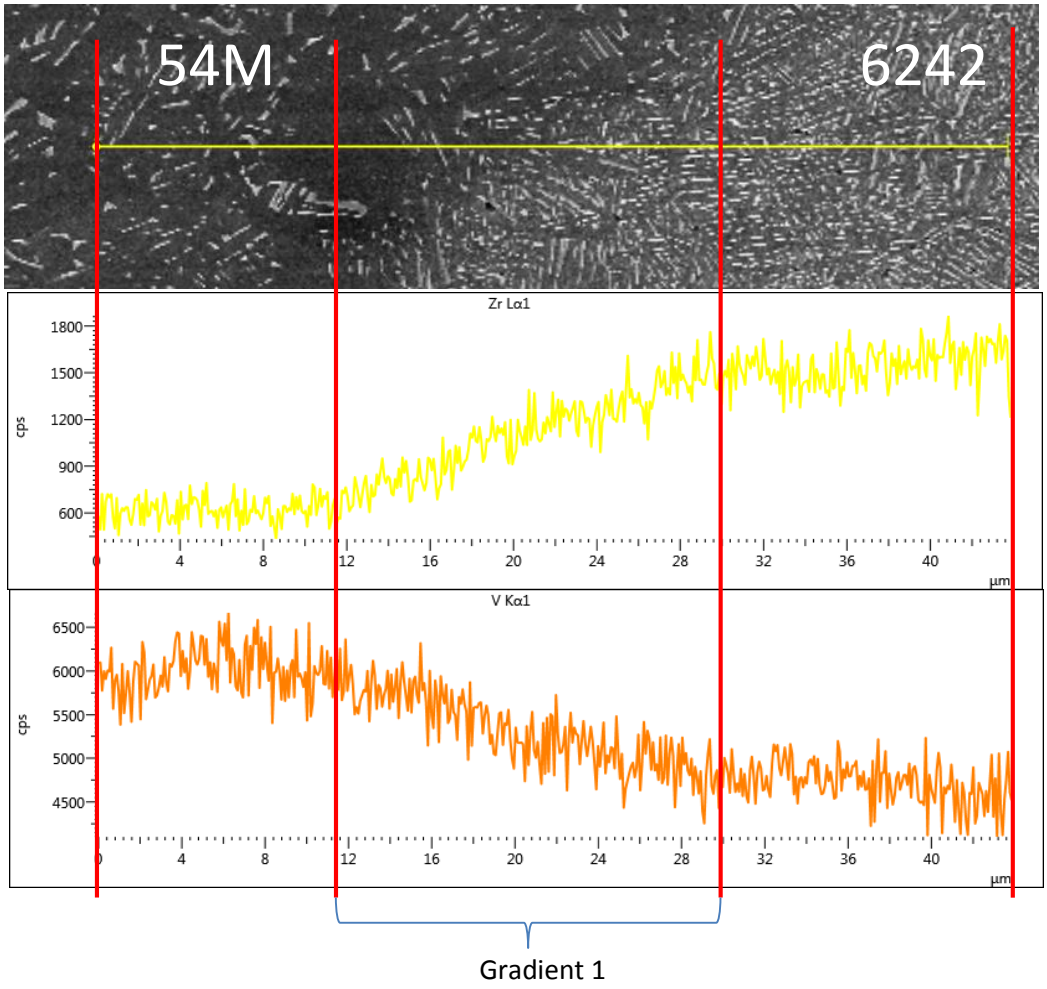

Figure 4-11: EDS line scan for Zirconium and Vanadium, Ti-6242 to Ti54M, Plate 1 Zone 1.

Analysis of the colder root of the weld in **Figure 4-12** that shows that the compositional gradient narrows to coincide with the thinner bands of parent material in the turbulent mixing zone. Compositional gradients are on the order of 5 to 10 microns as opposed to the approximately 20 micron bands observed near the shoulder of the tool.

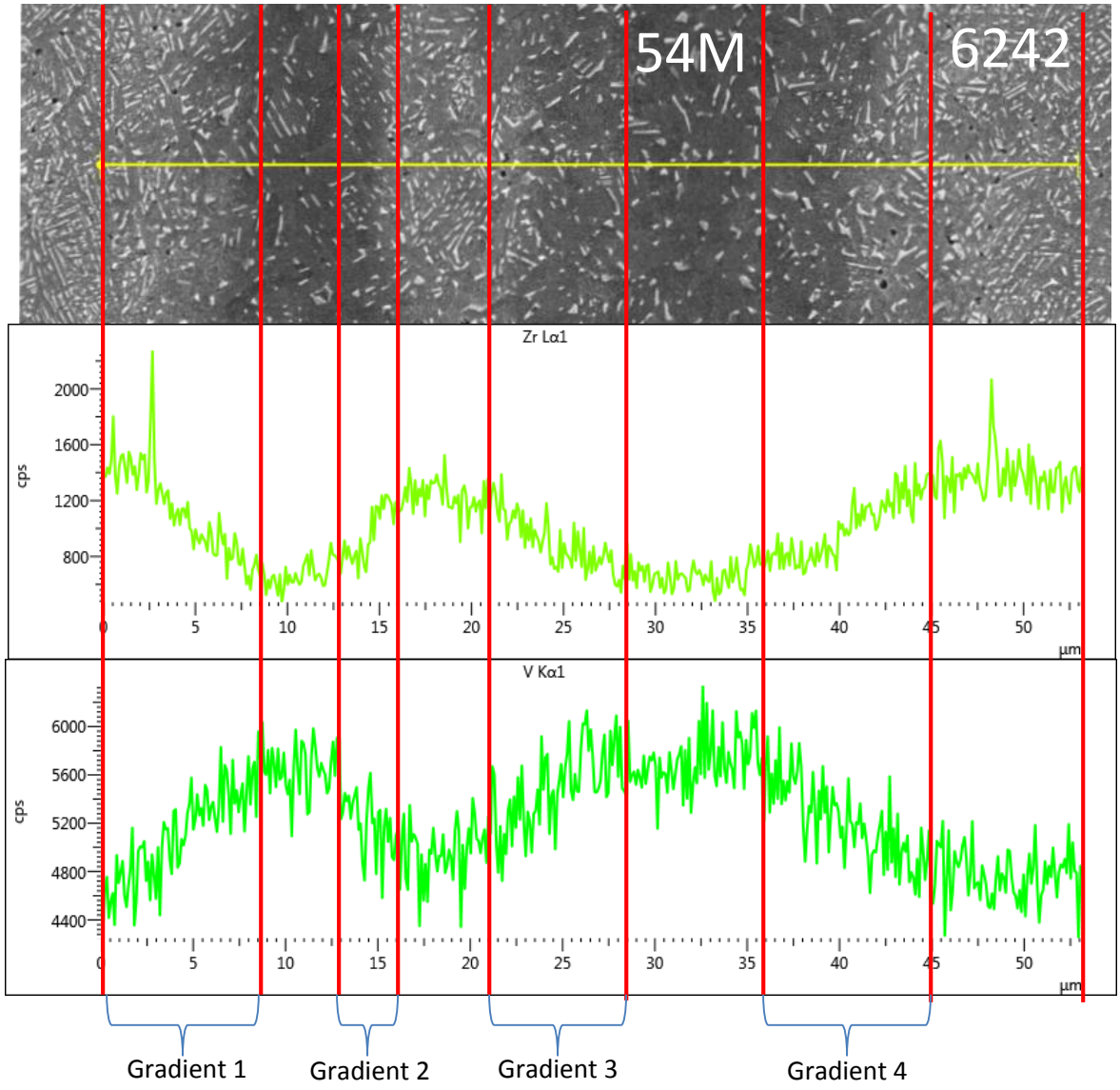

Figure 4-12: Ti-6242 to Ti54M Plate 1 Zone 3, EDS line scan.

Utilizing thermocouple measurements by Edwards of the weld nugget in Ti6Al-4V to Ti-6Al-4V welds as a guide, one can begin to apply Fick's 2nd Law to understand the diffusive component's contribution to the overall structure of the weld. **Table 4-3** and **Figure 4-13** show a generalization of Edwards' findings [Edwards, 2010c], namely a thermal excursion peak in the range of 800C-1150C, with those temperatures being sustained for approximately 5 to 15 seconds, depending heavily on weld conditions.

Table 4-3: Weld temperatures as travel and rotation speeds are varied in Ti-6Al-4V [Edwards, 2010c].

Spindle Speed (RPM)	Travel Speed (mm/min)	Ave. Shoulder Temp (deg C)	Root Temp (deg C)	Tool Size	TC Location
300	100	1082	988	Small	WN
300	100	1038	1010	Small	WN
300	100	1093	1082	Small	WN
400	100	1149	1099	Small	WN
200	100	1004	799	Small	WN
300	50	1032	954	Small	WN
300	150	1060	782	Small	WN
300	100	638	621	Small	Adv
300	100	938	877	Small	Ret
300	100	1077	1010	Big	WN

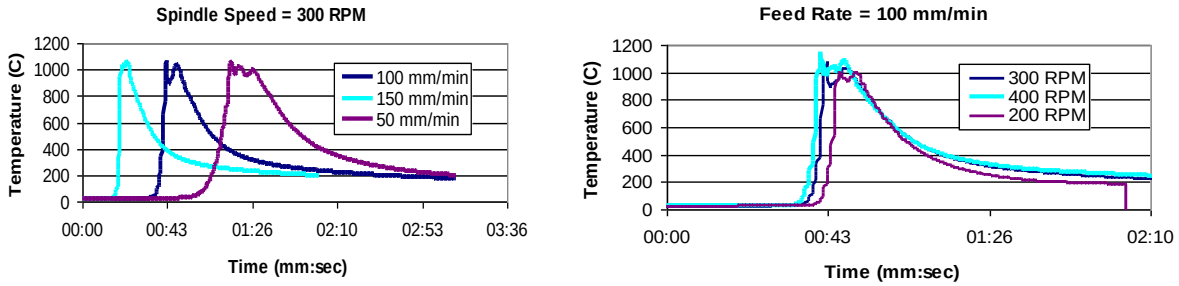

Figure 4-13: Thermal excursion profiles in Ti-6Al-4V friction stir welds [Edwards, 2010c].

A calculation can be set up for the case of Zirconium diffusion, shown in **Equation 4-1** and plotted in **Figure 4-14** utilizing diffusion coefficients generated by Hendricks [Hendricks, 1962]. Fick's 2nd Law requires several assumptions to remain valid, such as a net one-dimensional flow of atoms and a sufficiently large source as to not deplete the end point of the source atoms. Additionally, it is useful to use the assumption that all diffusion occurs while in the beta phase field and the thermal transient takes the shape of a square wave so one can use

readily available diffusivities from literature and simplify calculations to ignore diffusion during heating to peak temperatures. Additional details on this method of calculation can be found in **Appendix A**.

$$N_A(x,t) = N_{A_A} + \frac{(N_{A_B} - N_{A_A})}{2}\left[1 + erf\,\frac{x}{2\sqrt{\widetilde{D}t}}\right] \quad \textbf{Equation 4-1} \text{ [Abbaschian, 1991]}$$

Where:

$\widetilde{D}$ = Diffusivity

x = Distance from initial interface

t = Time

N_A = Atomic percent of element 'A'

N_{A_A} = Bulk atomic percent of element ' A' in Alloy A

N_{A_B} = Bulk atomic percent of element 'A' in Alloy B

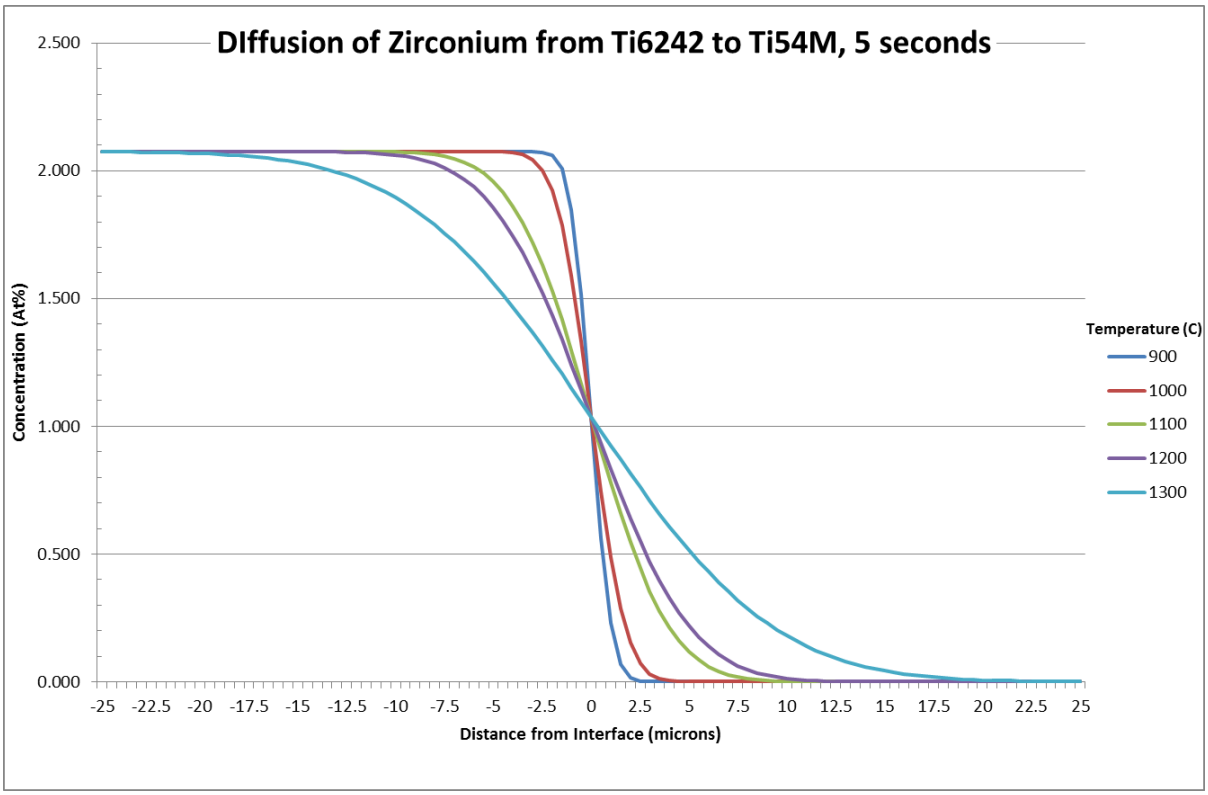

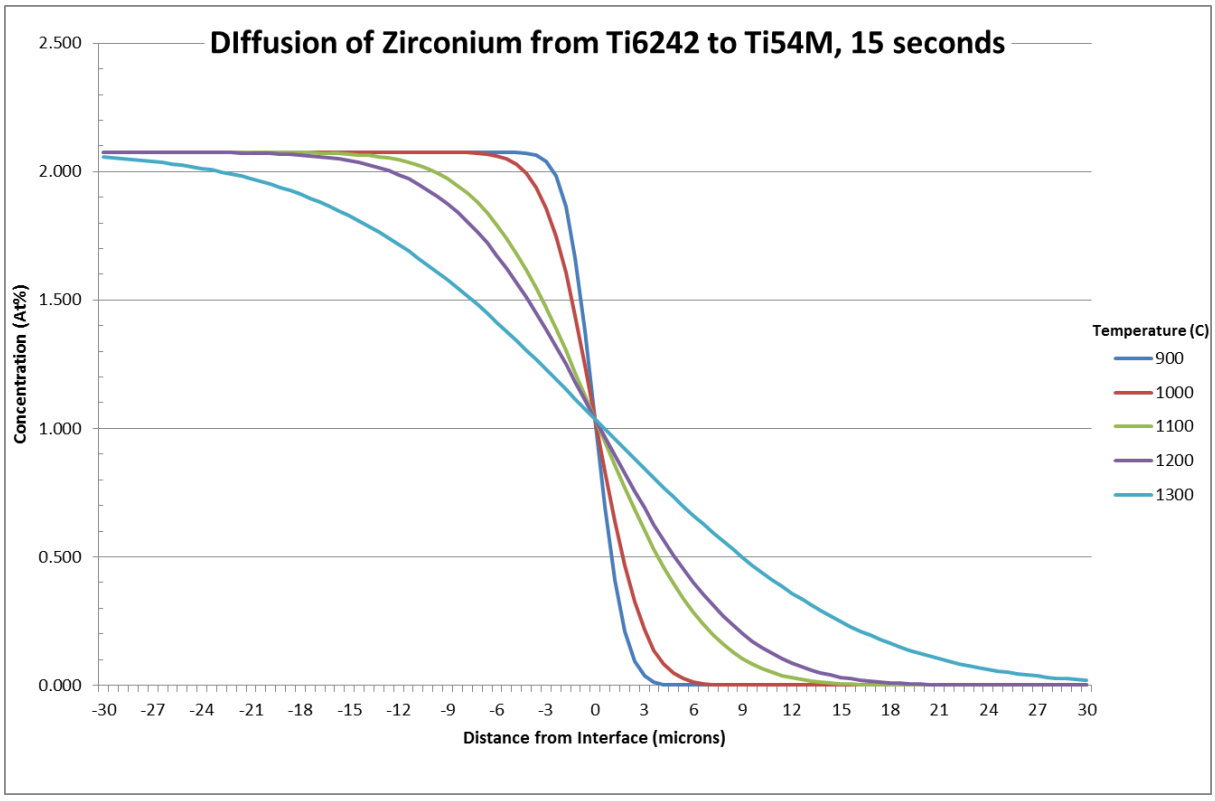

Figure 4-14: Diffusion of Zirconium at various temperatures, 5 (top) and 15 (bottom) seconds.

As is the case with all diffusive mechanisms, the exponential scaling of the temperature component weighs far more heavily on the resultant compositional gradient than the time does. At 1300°C, tripling the time from 5 seconds to 15 seconds yields approximately a 30% increase in the total length of the diffusion zone, where as an increase in temperature from 1200°C to 1300°C more than doubles the length of the diffusive zone. With the relatively high travel speeds of the Ti-6242 to Ti54M welds, we can assume a lower dwell time and will work with an assumed 5 second window for diffusion. **Figure 4-12** has several diffusion bands, all ranging from 5 to 10 microns, which correlates to a working temperature in the 1000-1100°C range.

These calculations represent the highest bounds of what would be expected from a thermocouple experiment similar to that of Edwards' work. However, considering the assumptions made about material interface, chemistry and microstructure and the inherent 10% error associated with the diffusivity, this analysis still shows strong correlation within the experimental evidence. All areas of the weld showed tortuous material interfaces that cannot be attributed to diffusion alone, suggesting that the assumption of a distinct, smooth material interface at the start of the diffusion period are not fully valid. Micro-scale jagged features of the mechanical stirring produce a starting interface of varied composition, and further work is needed to discern the diffusive component and mechanical component of the formation of the interfaces and microstructure features.

4.6 Friction Stir Welding Summary and Conclusions

The analysis of a selection of dissimilar friction stir welds shows validity to the approach selected, as well as helping to define useful avenues to explore in future work:

- Microstructures show no evidence of bonding defects between alloys in the weld nugget, suggesting near-instantaneous heavy deformation and temperatures sufficient to diffusion bond in parallel.
- Alpha particles throughout the microstructure are fine, homogenous and acicular, demonstrating temperatures above the beta transus and complete dissolution of primary alpha particles from the parent alloy.
- Distinct macroscopic mixing features such as lath size, periodicity and turbulence appear to be relatable to weld parameters.
- EDS analysis of material interfaces is sufficient to show discernible concentration gradients of primary alloying elements.
- Analysis of EDS data to determine weld nugget temperatures using Fick's 2nd Law as a basis for diffusion calculations shows good agreement with prior art [Edwards, 2010c].
- EDS and analysis of microstructure features is not sufficient to determine the geometry of the as-stirred interface in the absence of diffusion; additional analysis of particle chemistries and crystallographic orientation is needed to identify the mixing versus diffusive component of the weld nugget formation on the micro scale.

The analysis of friction stir welds in dissimilar titanium alloy systems has revealed several useful methods for characterizing weld nuggets as well as confirming direct observation of weld nugget temperatures demonstrated in the literature. These techniques can now be expanded to other dissimilar titanium friction stir weld joints to aid in comparing the resultant micro and macrostructures with the larger body of literature dedicated to Ti-6Al-4V/Ti-6Al-4V joints, their microstructure, deformation and process conditions.

CHAPTER 5: Ti-6Al-4V TO β21S FRICTION STIR WELD EXPERIMENT

5.1 Overview

Ti-6Al-4V and β21S were selected for this welding experiment for their dissimilarity in multiple areas – alloying elements, density, phase composition, microstructure feature size and high temperature mechanical response. This dissimilarity is thought to better illuminate the effect of process conditions on flow behavior and development of microstructure, as well as provide contrast for certain characterization techniques, such as microCT scanning. Weld parameters were selected to represent nominal parameters for Ti-6Al-4V, as previously identified, as well as additional welds using higher and lower heat inputs. Chemistries for the raw materials used in this experiment are provided in **Table 5-1**.

Table 5-1: Chemistries of weld input stock.

Element, Wt%	Al	V	Mo	Fe	O	Nb	Si	N	H, ppm	Ti
Ti-6Al-4V	6.14	4.07	-	.18	.16	-	-	.005	54	Balance
B21S	2.95	-	15.51	.31	.13	2.85	.22	.009	34	Balance

5.2 FSW Fabrication

Friction stir butt welds were fabricated using a Transformation Technologies Inc. friction stir weld machine owned and operated by The Boeing Company, shown in **Figure 5-1(a)** on sheets of 4.5mm (.180”) nominal thickness. The pin is composed of a precision ground tungsten lanthanide alloy, shown in **Figure 5-1(b)** and **(c)**, with a pin diameter of 12mm a pin angle of 35° and a shoulder diameter of 22.9mm. Both the pin and the tungsten-based anvil were internally water cooled.

(a) **(b)** **(c)**

Figure 5-1: (a) Friction stir weld machine **(b)** Tungsten-Lanthinide friction stir weld tool. **(c)** Pin schematic.

Weld seams were approximately 300mm (12”) in length, using the rotation speeds, travel speeds, pin length and plunge depths listed in **Table 5-2** – each weld was assigned a number, one through nine, which will be referred to frequently through the discussion of the results. Welds were visually inspected for uniformity and surface condition before removal of the weld flash**.** All welds were analyzed in the as-welded condition, and were sectioned for characterization using a water cooled abrasive band saw. A representative weld joint, marked for sectioning is shown in **Figure 5-2.**

Table 5-2: Ti-6Al-4V/β21S weld parameters.

Weld Identification Number	1	2	3	4	5	6	7	8	9
Advancing Side Alloy	Ti-6Al-4V	Ti-6Al-4V	Ti-6Al-4V	Ti-6Al-4V	Ti-6Al-4V	Ti-6Al-4V	Ti-6Al-4V	Ti-6Al-4V	β21S
Retreating Side Alloy	β21S	β21S	β21S	β21S	β21S	β21S	β21S	β21S	Ti-6Al-4V
Stock Thickness (mm)	4.5	4.5	4.5	4.5	4.5	4.5	4.5	4.5	4.5
Weld Seam Length (mm)	274	274	274	268	272	276	274	177	274
Tool Rotation (RPM)	600	400	225	275	275	275	325	150	275
Travel Speed (mm/min)	75	125	100	100	125	150	125	150	275

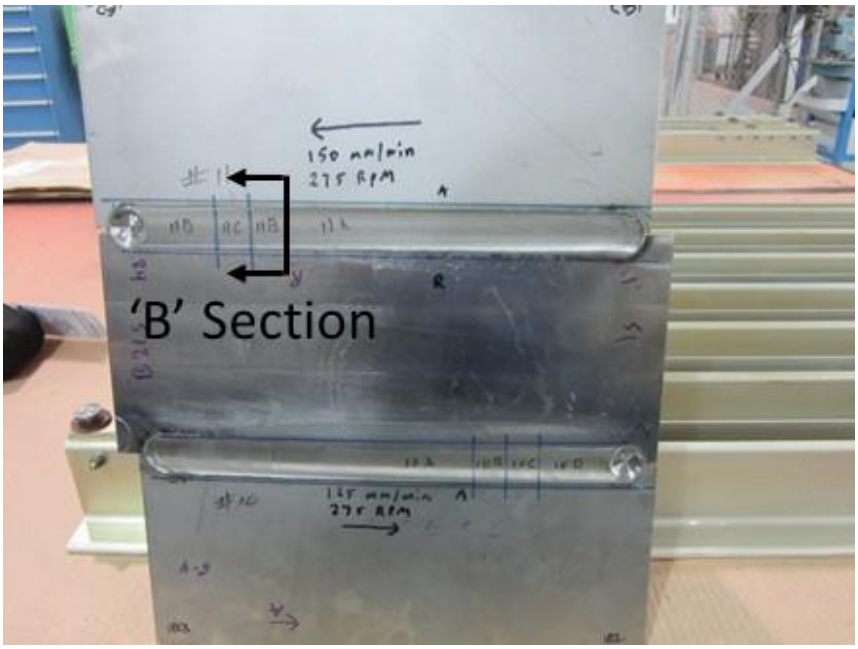

Figure 5-2: Weld 5 and 6, as-welded with flashing removed, marked for sectioning.

The machine is instrumented with load cells to gather in-process force data, using the reference orientations shown in **Figure 5-3a**. An example of a complete load chart, annotated to show the phases of machine operation, is shown in **Figure 5-3b** with a blown-out and replotted region shown with a correlated micoCT scan image. Subsets of the machine loads will be presented throughout the results for discussion, while complete documentation of weld parameters and machine outputs are available in **Appendix B**.

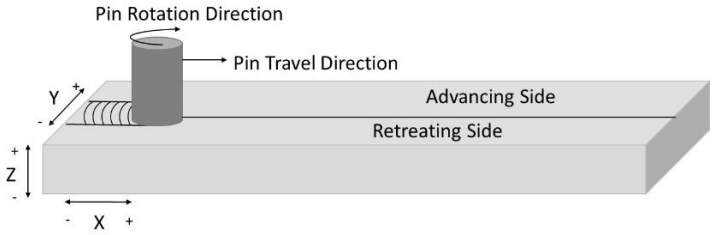

(a)

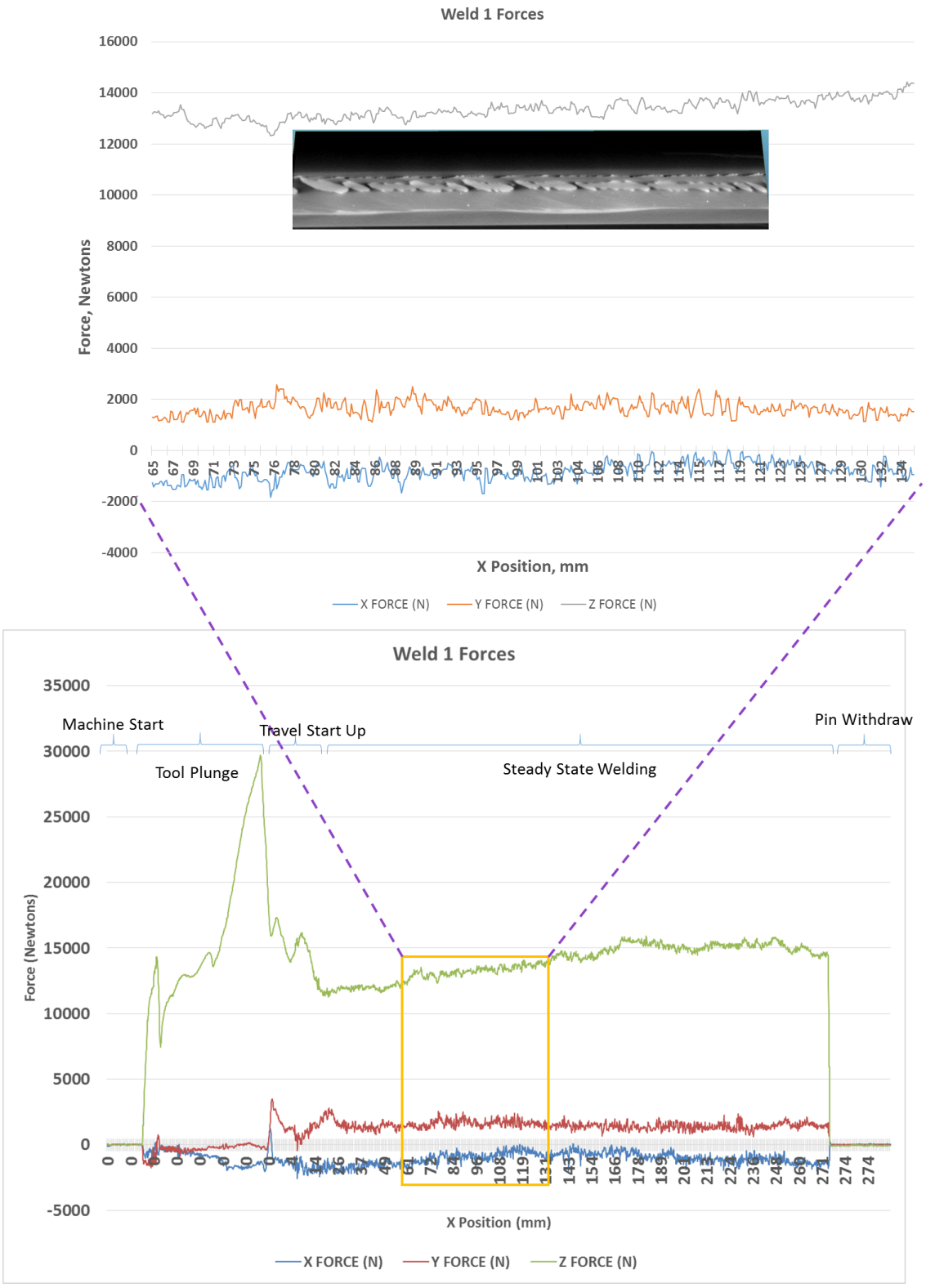

(b)

Figure 5-3:(a) Friction stir weld machine force schematic **(b)** Weld 1 machine load plot, annotated to show stages of machine operation and inset with an appropriately scaled microCT scan.

5.3 Metallography

Metallographic specimens ("B Section", as noted in **Figure 5-2)** for optical and electron microscopy were mounted in Struers Durofast resin, and rough prepared using 60, 120, 240, 400 and 600 grit silicon carbide wet sanding discs. Care was taken to avoid excessive pressure and metal smearing. Polishing was accomplished using an ATA Saphir 550 autopolisher with 9 micron, 6 micron, 3 micron and 1 micron diamond suspension polishes on a MD Plan cloth. Pressures never exceeded 25N to avoid smeared metal and grit pickup. Between each polishing step, the mounts were rinsed with soap and water, and ultrasonicated in deionized water and etched with Krolls reagent. Final polish was accomplished with a Vibromet 1 vibratory polisher overnight, using .05 micron colloidal silica grit suspended in deionized water. Etching for microstructural examination was performed with Kroll's Reagent and ammonium biflouride.

Micrographs were captured using a Leica DMI5000 M at 100x magnification and montaged using the software package supplied with the microscope. Base metal microstructures for the Ti-6Al-4V and β21S are provided in **Figure 5-4**.

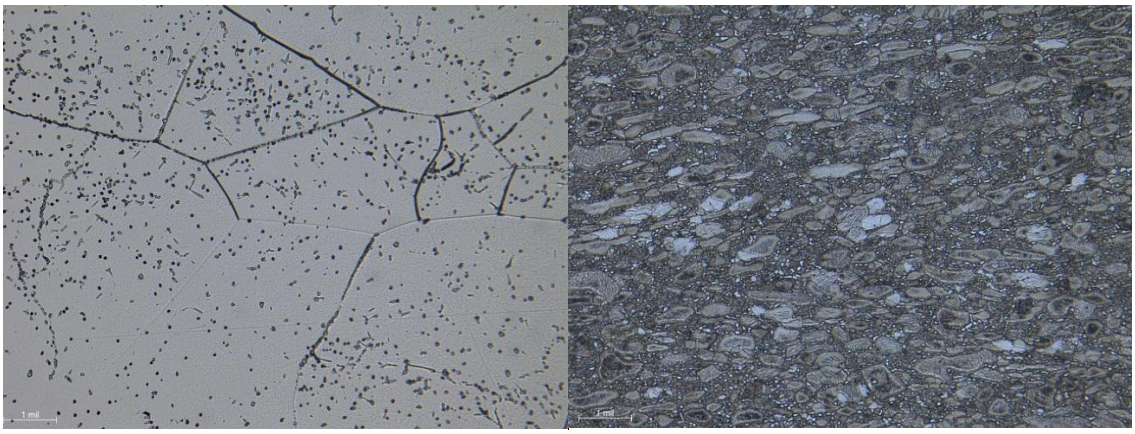

Figure 5-4: Base metal microstructure at 500x magnification for β21S (left) and Ti-6Al-4V (right).

5.4 MicroCT

Micro Computed Tomography (CT) scans were performed on each weld, covering approximately 150mm of weld seam length. Scans were performed using North Star Imaging M500 X-Ray/CT imaging system with a 145 KeV x-ray source and reconstructed using EFX-CT software**.** Several views will be presented for discussion throughout the results, an example of their orientations relative to the sample and machine configuration is shown in **Figure 5-5**.

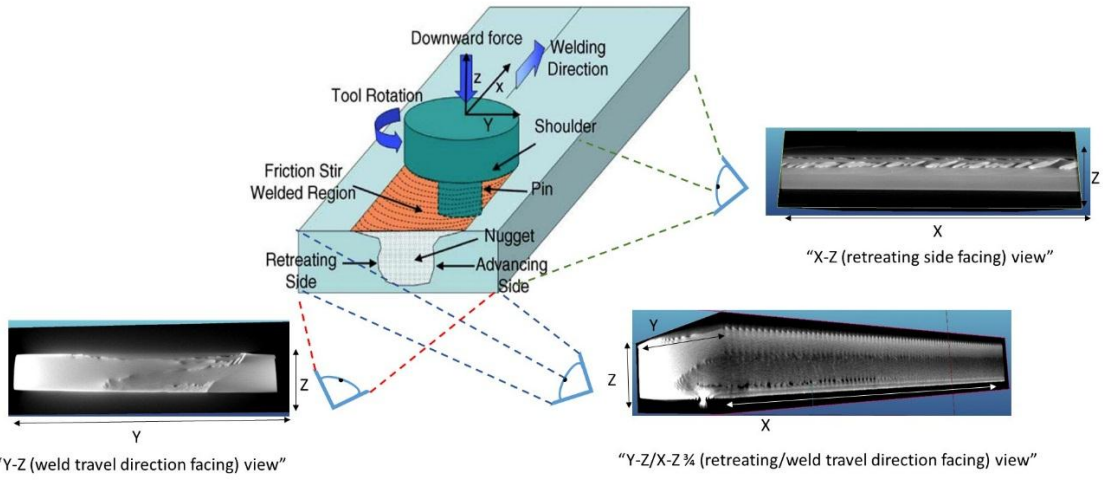

Figure 5-5: Representative microCT cross sections and naming convention shown relative to a FSW schematic.

5.5 SEM and EDS

SEM and EDS were performed using a JEOL JXA-8230 microscope at an acceleration voltage of 10KeV for secondary electron image capture and 20KeV for EDS data collection. EDS line scan data used for plots was smoothed using a 5-point rolling average. Selected plots are shown and discussed in Chapter 5, and a complete data set is available to the reader in **Appendix C**.

5.6 Results and Discussion

A selection of data will be presented and discussed for each weld covering notable aspects of the macrostructure, microstructure and chemistry gradients. Weld parameters were selected to represent known nominal parameters from existing work in Ti-6Al-4V to Ti-6Al-4V butt joints, as well has additional parameters with higher and lower heat inputs. A representation of the parameters in relation to other welds is shown in **Figure 5-6** and it is recommended that the reader familiarize themselves with this chart, as welds will frequently be referred to by only their number.

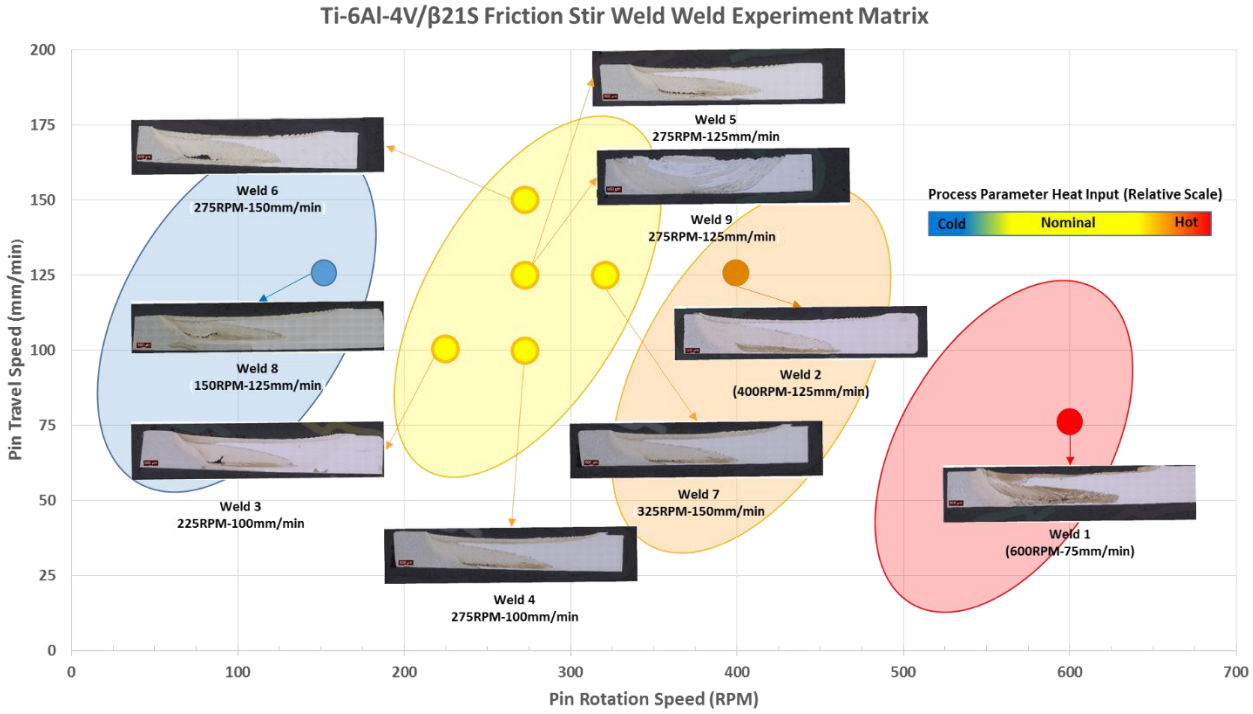

Figure 5-6: Ti-6Al-4V/β21S FSW experimental matrix, depicting relative heat input of pin rotation and travel speed combinations.

5.6.1 Weld 1 – 600RPM/75mm/min

Results

Micro CT scans of Weld 1, shown in **Figure 5-7**, shows the effects of the high heat input that is generated from the 600RPM spindle speed and 75mm/min travel speed process parameters. The Y-Z views show the primary β21S fin (lighter gray) being pulled from the retreating side into the advancing side. As the fin elongates and narrows towards the advancing side, the fin begins to shear apart and unstable boundaries between the β21S and the Ti-6Al-4V begin to deteriorate the primary fin on multiple length scales. Large pieces of β21S separate from the fin tip and are pushed against the heat affected zone, as well as smaller droplets breaking free from protrusions of β21S. The primary fin in general is highly unstable and changes shape unpredictably through the length of the weld. The root of the weld is highly turbulent, showing a cyclonic mixing of very fine Ti-6Al-4V and β21S features. In several views, bright flecks of material are seen embedded in the weld. Although more difficult to see in still images, when panning through the model, the features are largely rounded and transition smoothly as the macrostructure evolves.

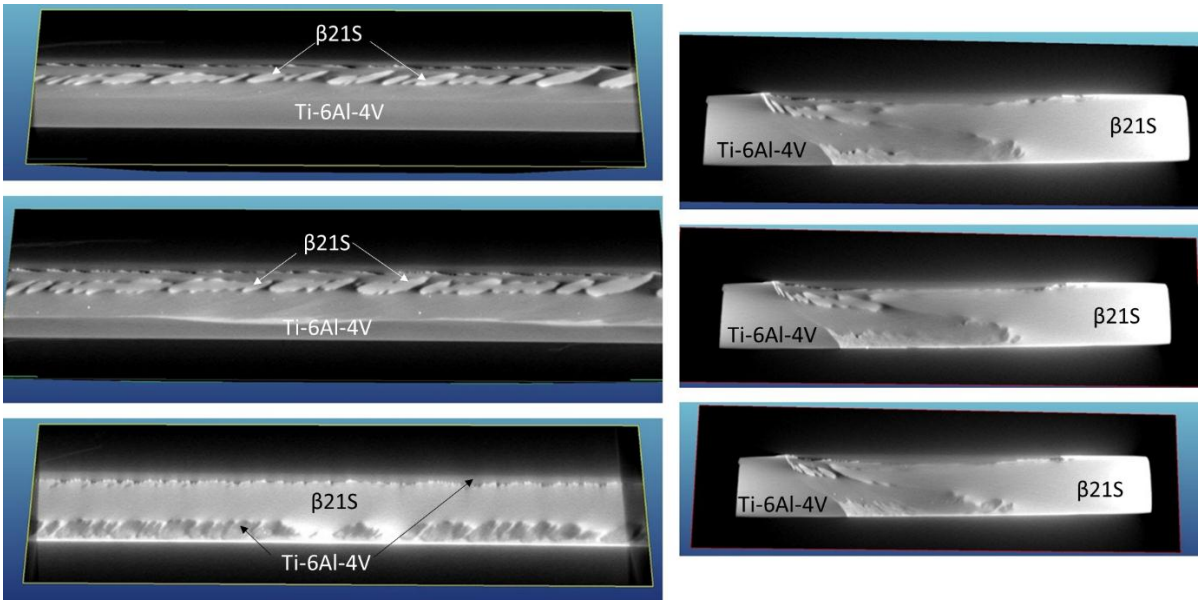

Figure 5-7: Weld 1 micro CT scans. X-Z (retreating-facing) views on the left, Y-Z (weld travel direction facing) views on the right.

A micro CT scan with plotted machine loads, shown in **Figure 5-8**, has little discernable correlation between the large β21S structures and the load peaks themselves, however, compared to the forces of other welds, there is a larger variation in the amplitude of the oscillations in each of the force plots, correlating to the inconsistent deterioration of the primary β21S fin. At 600RPM, the rotational speed of the spindle far outpaces the data collection rate of 9hz, meaning that only large spikes in force and averages should be considered relevant. Of note is that this is the only weld condition where the X force stabilizes at a negative value.

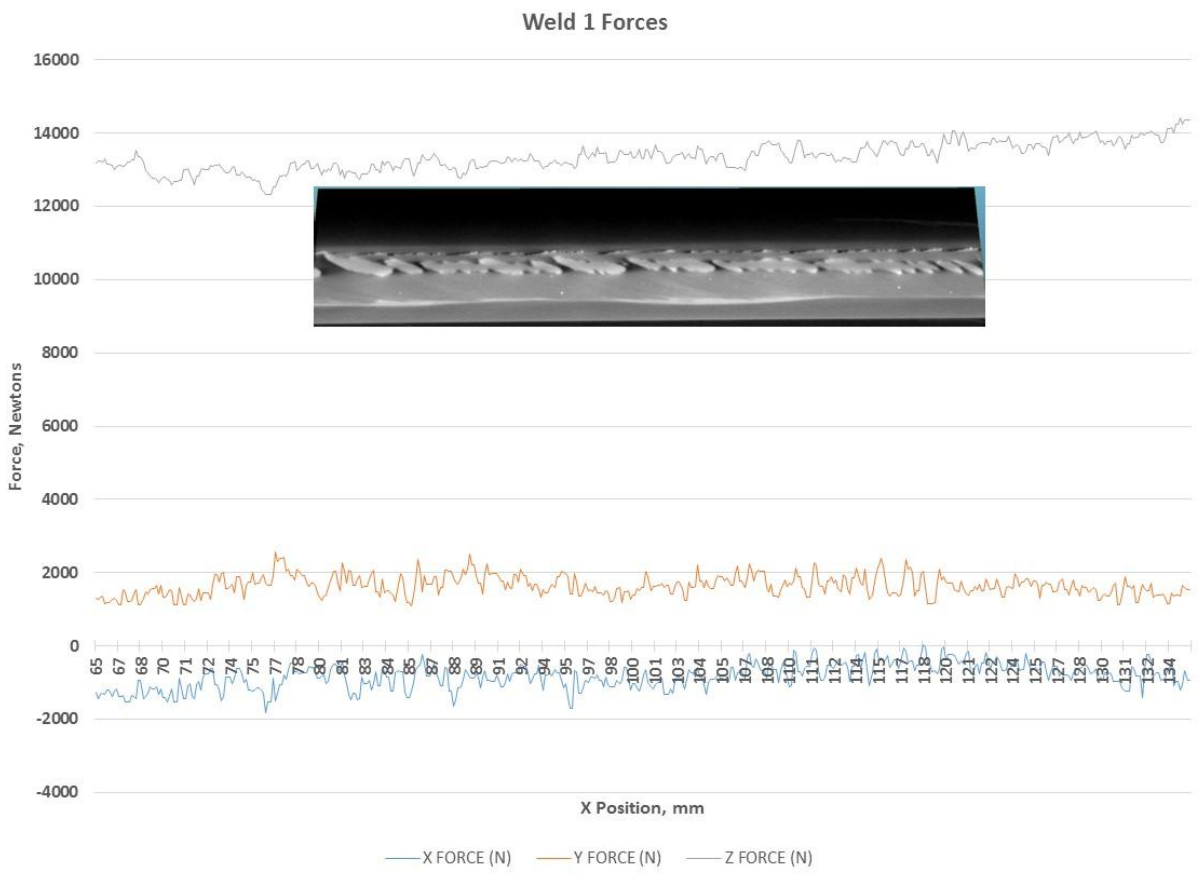

Figure 5-8: Weld 1 forces, shown at the location of a X-Z (retreating-facing) view micro CT scan.

Microscopy of Weld 1, shown in **Figure 5-9**, show features consistent with those observed in the micro CT scans, but with finer detail. The β21S (lighter phase, right side) shows a large primary fin of material being pulled from the retreating side of the tool, thinning as it enters the advancing side of the weld nugget, a characteristic that is seen in all eight welds performed using β21S as the retreating-side alloy. Large globules of β21S have separated from the tip of the fin as it thins and becomes unstable. Areas towards the root of the weld show a fine banded structure of Ti-6Al-4V and β21S, with a line of weld defects along the root of the weld where maximum tool plunge would be. Ti-6Al-4V and β21S are still well-mixed with a turbulent, banded pattern outside of the tool path at the root of the weld, and the Ti-6Al-4V side

of the weld has a large heat-affected zone. The mictrostructure is equiaxed, with the top layer of weld macrostructure showing a microstructure of coarsened widmanstatten α. A series of periodic, fine tooling marks is shown on the top of the weld, as well as an excess of flash and material ejected from the weld nugget.

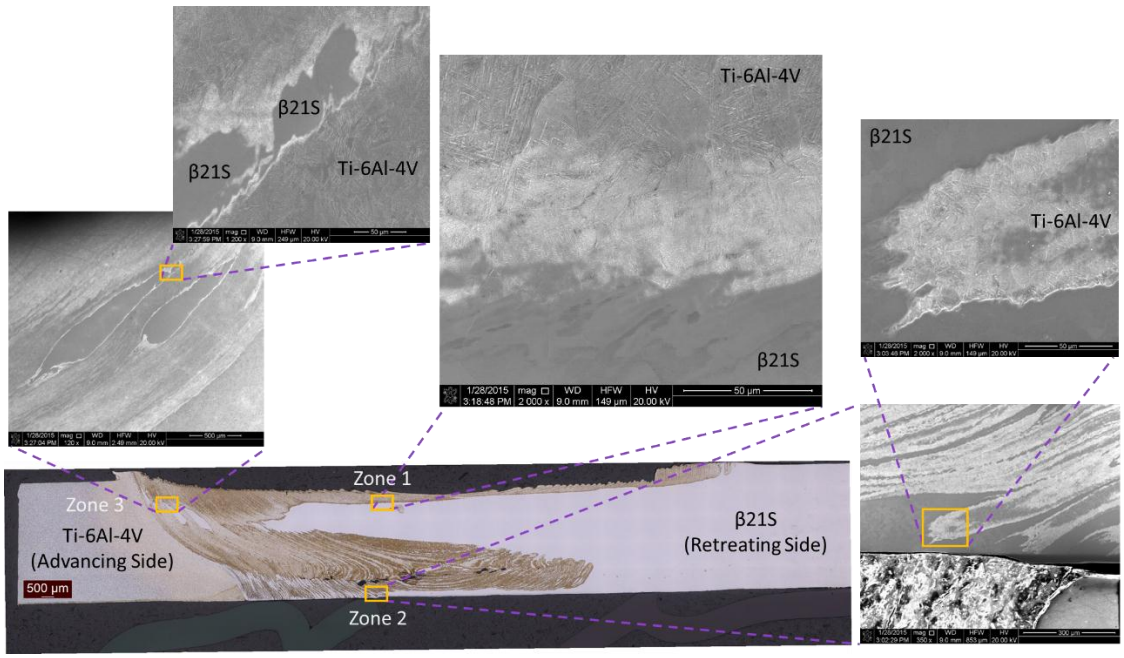

Figure 5-9: Weld 1, Ti-6Al-4V (Advancing side)/β 21S(Retreating side), 75mm/min, 600RPM, montage of 138 100x magnification micrographs, with SEM images of various magnification showing regions of interest.

Zone 1 of Weld 1, at the top of the weld directly below the shoulder of the tool, is the hottest region of the hottest weld condition in the test matrix. The Ti-6Al-4V (top) is fully transformed, showing equiaxed prior beta grains on the order of 20-30 microns. Alpha platelets appear to have nucleated heterogeneously in hybrid grains of Ti-6Al-4V and blurred the initial contact interface of the two alloys.

Zone 2 shows similar microstructural features to that of Zone 1, in spite of the much finer macrostructure featured in the root of the weld. At 350x magnification, intricate mixing of the

two alloys in a banded pattern can be seen, with each band on the order of tens of microns. At 2000x, an individual band of Ti-6Al-4V can be seen in a matrix of β21S. The prior beta structure of the alloy is equiaxed, although with prior beta grains on the order of 10 microns as opposed to the 20-30 micron grains seen in Zone 1. Again, hybrid Ti-6Al-4V/β21S grains can be seen at the top of the Ti-6Al-4V band with shared beta grain boundaries and arrested alpha formation mid-grain. Regions of β21S penetrate the band of Ti-6Al-4V, showing pockets of β21S based material within bands of Ti-6Al-4V. Bright speckles not seen in any other weld samples are present throughout, as was seen in CT scans.

Zone 3 shows large pockets of β21S that have broken off from the primary fin of β21S moving from retreating to advancing side, in a banded matrix predominantly composed of Ti-6Al-4V. Smaller β21S features can be seen breaking from the primary pockets and globularizing. Although it is more difficult to detect grain boundaries and hybrid grains at this location, there are smooth transitions between widmanstatten alpha, finer widmanstatten alpha in the lighter regions and finally full β21S-based compositions in the pockets. The grain size and morphology of the Ti-6Al-4V appears to be much less uniform in the lighter contrast regions of finer alpha features – smaller, more irregularly shaped grains are seen as compared to the roughly 20-30 micron prior beta grains in the parent Ti-6Al-4V.

EDS line data at Zone 1, shown in **Figure 5-10** presents new information about the nature of the microstructure and the mixing process in spite of the complexity. Although the microstructure presents a feathered, unstable interface between Ti-6Al-4V and β21S with a transition in the alpha platelet structure into a transformed Ti-6Al-4V microstructure, the chemistry gradients show a more complex situation. At no point in the 450μm line scan does an element reach a steady composition, instead showing a continual gradient with two, more distinct

transitions between the lighter and darker fields of Ti-6Al-4V based microstructure and the β21S based structure.

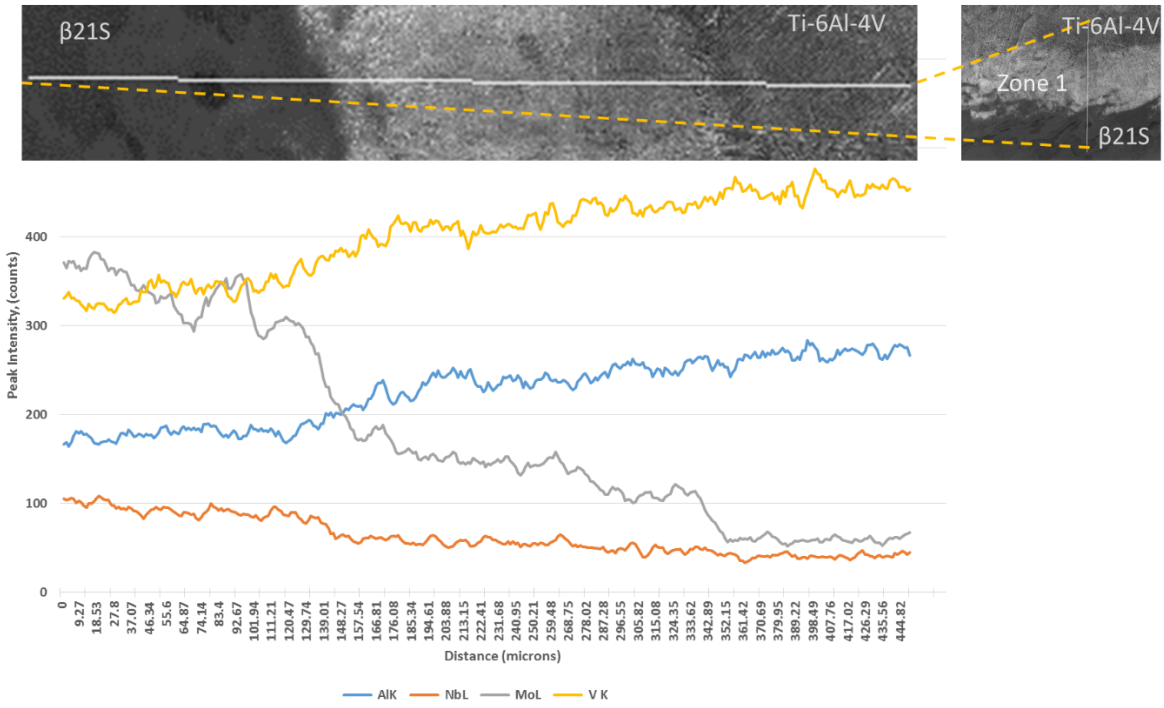

Figure 5-10: Weld 1, Zone 1, Line 1 EDS line scan plot for Al, Nb, Mo and V.

A line scan taken in Zone 2, shown in **Figure 5-11**, shows a more stable transition than is seen in Zone 1, with a concentration gradient of approximately 38 microns shown.

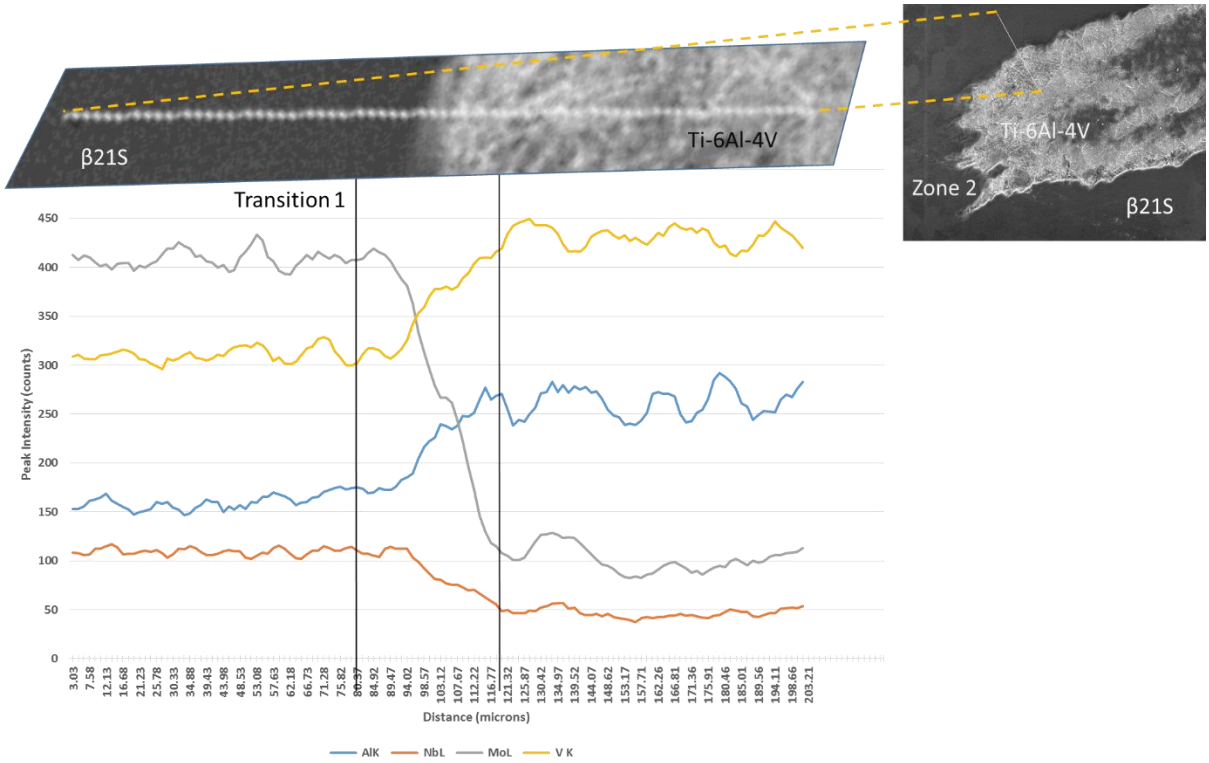

Figure 5-11: Weld 1, Zone 2, Line 1 EDS line scan plot for Al, Nb, Mo and V.

A line scan of Zone 3, shown in **Figure 5-12**, shows multiple chemistry gradients, varying in length from 10 to 30 microns. Wider chemistry gradients from the EDS data correlate well with areas of etch contrast difference.

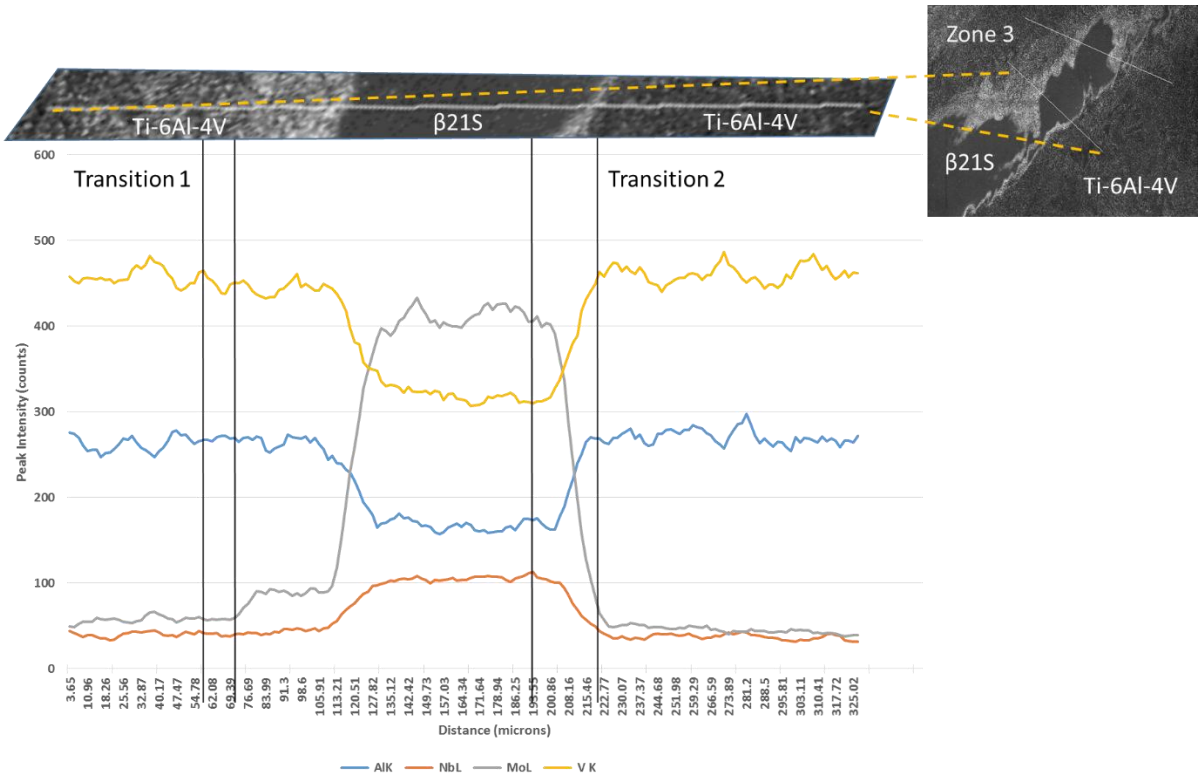

Figure 5-12: Weld 1, Zone 3, Line 1 EDS line scan plot for Al, Nb, Mo and V.

Discussion

The macrostructure images seen in **Figure 5-7** indicate a complex mixing pattern with a steadily evolving and changing geometry on virtually all length scales, owing to the excessive softening of the material from the high heat input of the selected parameters. It is clear that in cases where mixing behavior becomes this unstable and complex, the flows would be best considered with a fluid dynamics approach. This is the only weld with a negative force in the X-direction reported – implying that the pressure built up in the wake of the tool is sufficient to create a force on the pin greater than the forces imparted by the forward translation of the pin. Heavily softened material also appears to have created blocks of material extruded upward in the Z-direction; the result of reacting forge loads. The high heat generated from these parameters also appears responsible for the bright flecks of material seen throughout the weld, and although

no direct observation of these flecks is available in this data set, they have been previously reported on and identified as high-density inclusion from degradation of the pin [Pilchak, 2007].

The mixing patterns in the microstructure, particularly in the root of the weld, are very fine in scale and show interpenetrating turbulent flows of the two alloys that could only be reasonably produced by heavy strains at high temperature. The periodicity of the features, where discernable, shows that even with complex turbulent mixing, the number of rotations the pin makes relative to the distance traveled will still be a defining parameter in the resultant weld nugget structure [Fonda, 2013]. The heat and level of engagement with the pin produced recrystallization throughout the weld, evidenced with the well-equiaxed structures observed. The recrystallization process is very dynamic, and can be seen in places continuing to refine the overall beta grain size as small, unequiaxed grains in Zone 1 are being consumed by larger, more equiaxed grains still growing after nucleation. Also observed is transformed Ti-6Al-4V throughout, evidencing an excursion in temperature beyond the beta transus. Grain size is not consistent through the weld nugget, however, and smaller (but still equiaxed) grains in Zone 2 as compared to Zone 1 point to either additional recrystallization or high heat in Zone 1 causing fast grain growth [Mironov, 2008][Fonda, 2004].

It is also readily apparent that the extremely well-mixed and dynamic structure created by these weld parameters does not provide a steady-state diffusion instance in which to make valid temperature estimations using the methods detailed in Appendix A. **Figure 5-10** shows continual transitions, rather than the sharper, more well-defined transitions seen initially in Chapter 4. This scan, as well as the contrast differences in the microstructure show that there has been a new chemistry, created largely by mechanical mixing, shown as the lighter transition band. Even with a more stable transition, such as Zone 2 in **Figure 5-11**, a calculation using the

38 micron length shown as Transition 1 would yield a temperature of 1525°C for the a thermal spike of 11.68 seconds. With no outside data to compare this result to, it is still reasonable to assume that the relative motion of the two alloys aids in dispersing the alloying elements of Ti-6Al-4V into the β21S and vice versa, which would lead skew a diffusion-only assumption to a higher temperature. Similarly, calculations for the two transitions at Zone 3 in **Figure 5-12** yield results of 1275°C and 1450°C respectively. Although these values are consistent with the visual appearance of the interface, a temperature variation of 375°C over a distance of 150 microns is not reasonable for a material that is undergoing such extensive mixing.

5.6.2 Weld 2 – 400RPM/125mm/min

Results

The macrostructure of Weld 2, shown in **Figure 5-13**, demonstrates regular, periodic features and a consistent mixing pattern through the imaged length of weld. The primary β21S fin is stable through the length of the weld and thins uniformly as it pulled through the wake of the pin into the advancing side of the weld. Instabilities appear at the very tip of the primary fin in the advancing side, breaking into globules of β21S of a relatively consistent size. The periodic sawthooth features seen on the primary fin give rise to the finer scale features seen in the root of the stir zone. Individual, elongated teeth can be seen on the retreating root side of the primary fin becoming unstable and breaking into ribbons and droplets that are carried into the cyclonic mixing of the root zone as the tooth is carried further into advancing side. Fine ribbons if Ti-6Al-4V and β21S can be seen mixing, and rotating to align with the edges of the heat affected zone.

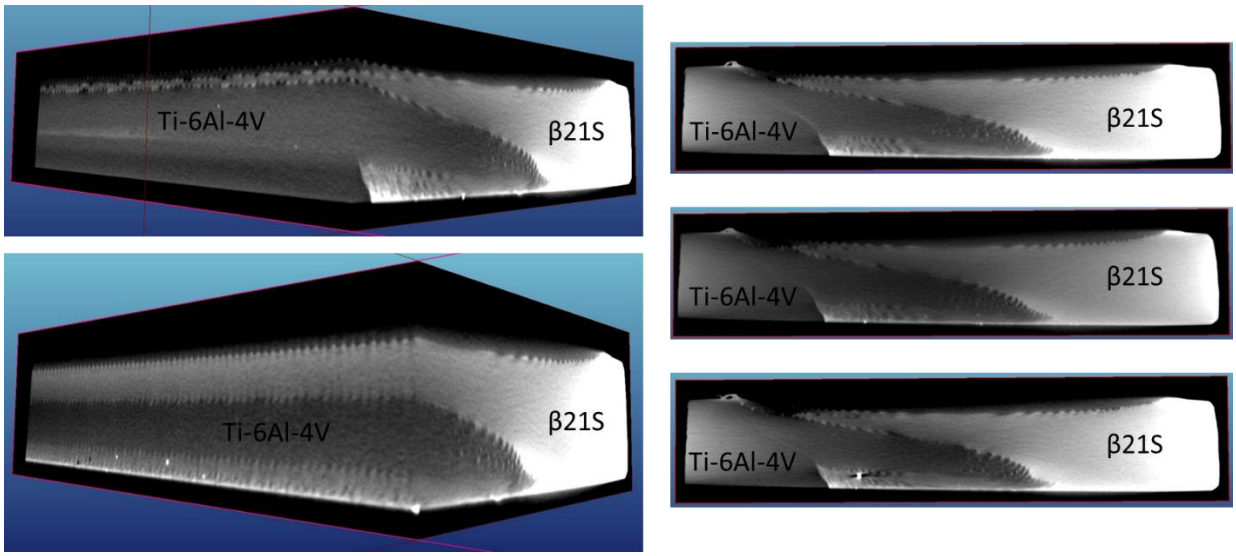

Figure 5-13: Weld 2 micro CT scans. Y-Z/X-Z ¾ (retreating/weld travel direction facing) views on the left, Y-Z (weld travel direction facing) views on the right.

The force plot for Weld 2, shown in **Figure 5-14**, begins to show more discernable correlations to the weld macrostructure. The X and Y force plots are very stable, showing a consistent periodicity and amplitude throughout. Similarly, the sawtooth patterns on either side of the primary β21s show a consistent spacing and height. Although the forge load shows a steady increase in force as well as two variations throughout the length shown, this does not translate directly to any features seen in the microstructure.

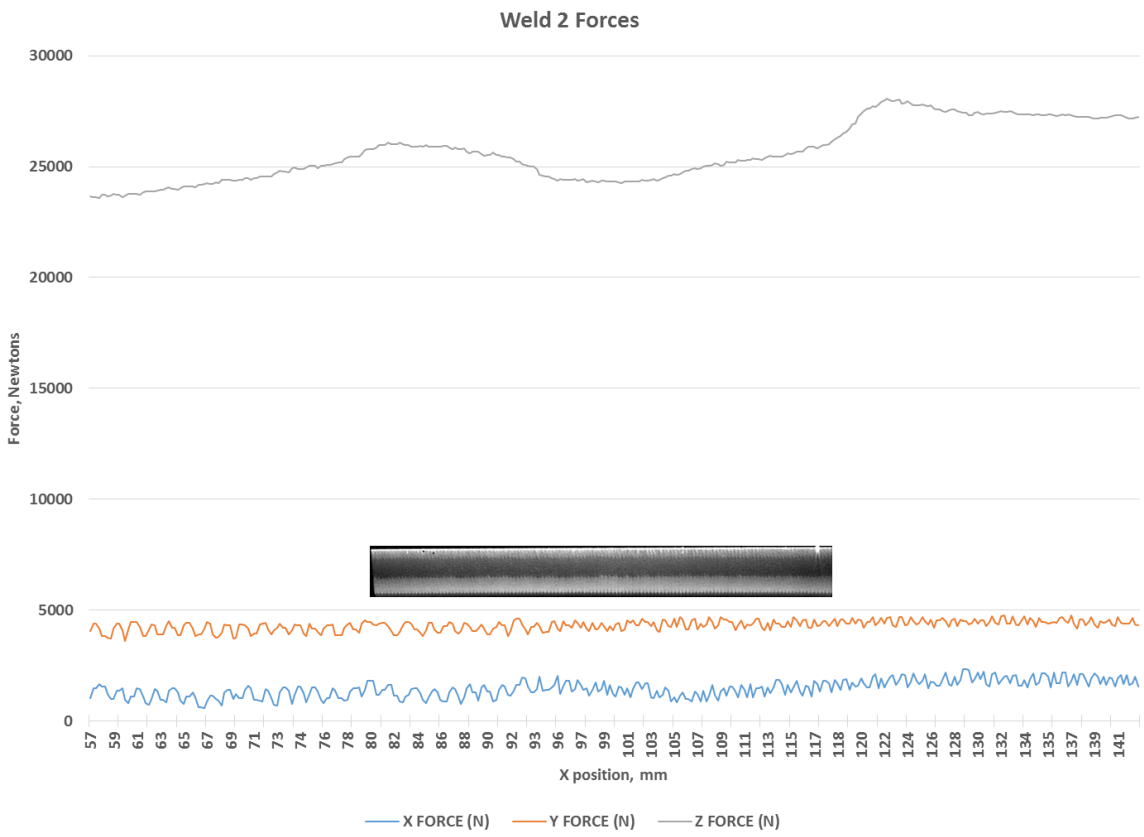

Figure 5-14: Weld 2 forces, shown relative to X-Z (advancing side facing) view micro CT scan.

Microscopy of Weld 2, shown in **Figure 5-15**, shows the only defect-free cross section observed when using β21S on the retreating side. The characteristic fin of β21S is present, with a top layer of Ti-6Al-4V. Globules of β21S are seen in the advancing side of the weld nugget near the top, detached from the tip of the primary fin at regular intervals. The root of the weld shows full penetration, with fine, turbulent mixing of both alloys at the root combined with periodic banding. This banding pattern is roughly equivalent in spacing and magnitude to the saw tooth banding pattern observed on the primary β21S fin. Equiaxed, transformed grains are present throughout the weld nugget, with minor amounts of material ejected from the weld nugget in the Z direction.

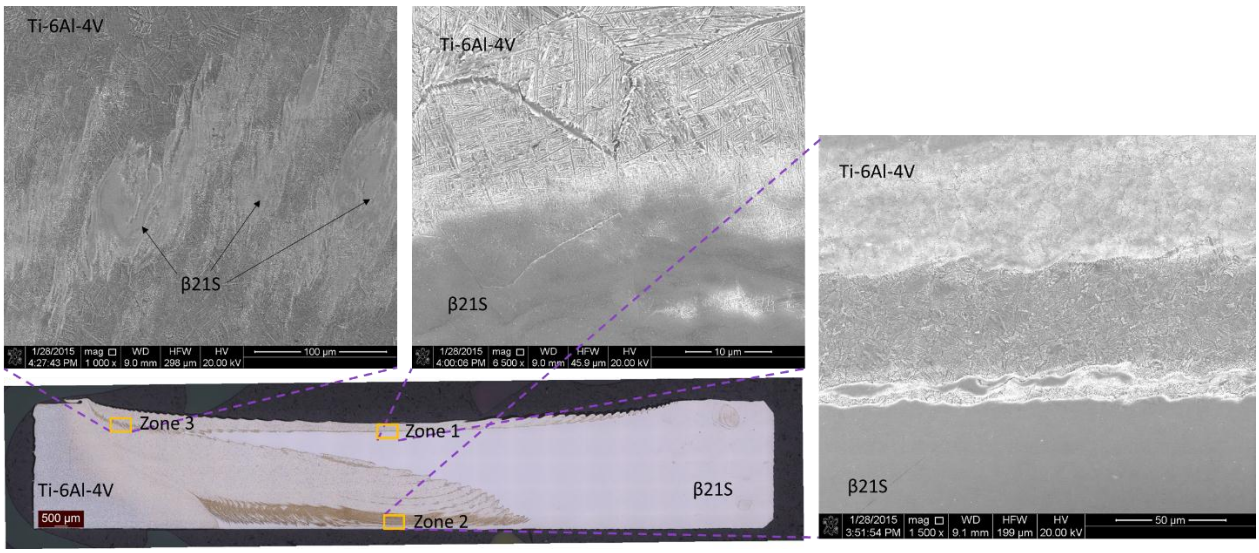

Figure 5-15: Weld 2: Ti-6Al-4V (Advancing side)/β 21S(Retreating side), 125mm/min, 400RPM, montage of 138 100x magnification micrographs, with SEM images of various magnification showing regions of interest.

Zone 1 shows very similar features to that of Zone 1 of Weld – a region of Ti-6Al-4V that has been completely transformed to widmanstatten-α well-mixed with the main fin of β21S. Grain size is on the same order as that of Weld 1, where transformed grains of 20-30 microns make up the majority of the structure, again with Ti-6Al-4V/β21S hybrid grains showing clearly. The hybrid grains are equiaxed and relatively even split between Ti-6Al-4V and β21S within the grain. There is a clear band of finer alpha features at the interface as well as patchy areas of fine widmanstatten-α in the β21S side of the interface.

Zone 2 again shows the much finer-scale mixing of the two alloys compared with Zone 1, with banding patterns on the order of 50 microns. Two distinct bands of α-rich titanium are shown, with an additional band of β21S present as well. Between all bands, turbulence at the interface is seen with fine ligands tens of microns long breaking into adjacent bands. The two α-rich regions have a similar prior beta grain size, although the middle band has a much more coarse and well-defined widmanstatten structure comparatively.

Zone 3 has a mixing pattern showing much more complexity than the banded structures of Zone 1 and Zone 2. The matrix of Ti-6Al-4V has a widmanstatten structure closely resembling that of Zone 1, with equiaxed prior beta grains. The β21S based features are separated from the tip of the primary fin and show a disturbed cyclonic pattern in some areas. The β21S globules show striations and breakage in a regular, banded pattern.

EDS mapping of Zone 3 is shown in **Figure 5-16**. The primary β21S structure appears to be an eddy swirl dissolving into the surrounding Ti-6Al-4V matrix irregularly. Chemical gradients between the two alloys are inconsistent in magnitude and show a wide variety of concentration profiles over short length scales.

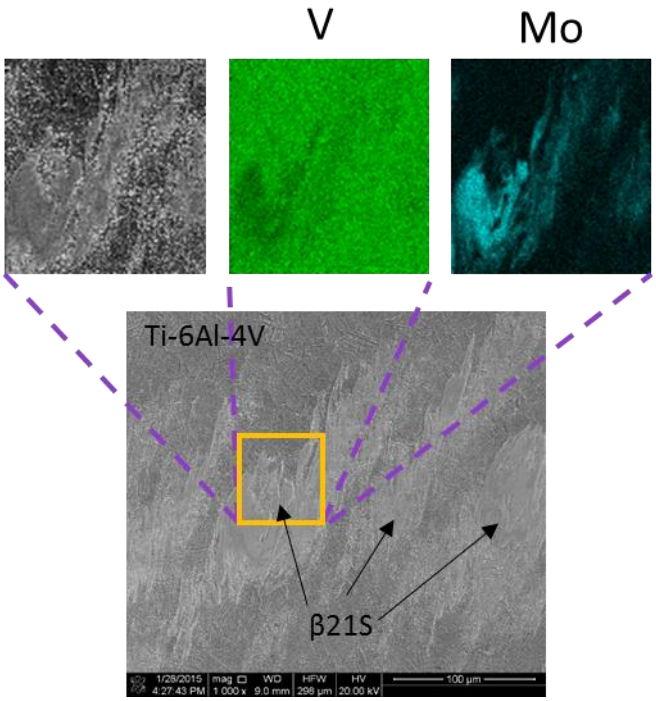

Figure 5-16: Weld 2, Zone 3 EDS Map for Mo and V.

Discussion

The macrostructure of Weld 2, seen in **Figure 5-14**, again shows strong evidence for the consideration of fluid flows as the mechanism for the creation of the macrostructure features. Sharper, more elongated features on the primary β21S fin are initially created by the motion and oscillations of the pin at regular intervals [Fonda, 2013], which then evolve considerably and break away from the fin as droplets and other smaller features as the two alloys flow relative to each other. The material being stirred still appears to be very well softened, however to a lesser extent than is observed in Weld 1, seen by the lesser degree of Z-direction extrusion under the tool shoulder.

Zone 1, in **Figure 5-15**, shows equiaxed transformed grains on the same order as Weld 1, demonstrating a well-recrystallized structure. Hybrid grains at the interface of the two alloys show a relatively equal split of Ti-6Al-4V and β21S within the grain, suggesting that the nucleation point for the grain occurred at the heterogeneous initial interface between the two alloys [Abbaschain, 1991]. Diffusive mixing is still present in the hybrid grains however, seen by the steady transition in the scale of the widmanstatten-α structure in the Ti-6Al-4V side of the interface. Although patchy areas of widmanstatten-α can be seen in the β21S near in the interface, this is likely the effect of taking a two dimensional cross section of a complex, wavy three dimensional interface. Clearly, the generation of interfaces between the two alloys and the resultant structures and chemical gradients has contributions from the mechanical flows, atomic scale diffusion as well as the dynamic recrystallization process. The details and balance of this process vary from zone to zone within the weld nugget, and Zone 3 can be seen again having a well recrystallized structure with diffuse chemical gradients between the alloys, but widely varying in magnitude over short length scales. The motion of the two alloys relative to each other

creates small eddies that mix material much more efficiently than pure diffusion does, as well as larger scale breakage of the β21S globules that appear to be shearing apart in the much more fluid Ti-6Al-4V matrix.

5.6.3 Weld 3 – 225RPM/100mm/min

The macrostructure of Weld 3, representing the cooler end of the nominal process window, is shown in **Figure 5-17**, and presents the same main features as Weld 2. The primary β21S fin is in the same position in the stir zone, however it does not protrude completely across to the advancing size. The sawtooth features are again periodic, but smaller in magnitude and with a wider period. The primary fin again becomes unstable at its tip, but this time breaking into more irregular pieces of a larger size than Weld 2. Defects are present throughout the advancing root side of the stir zone, with a larger, primary defect staying largely consistent, paired with a linear set of smaller defects sharing similar periodicity to the sawtooth pattern seen on the β21S fin.

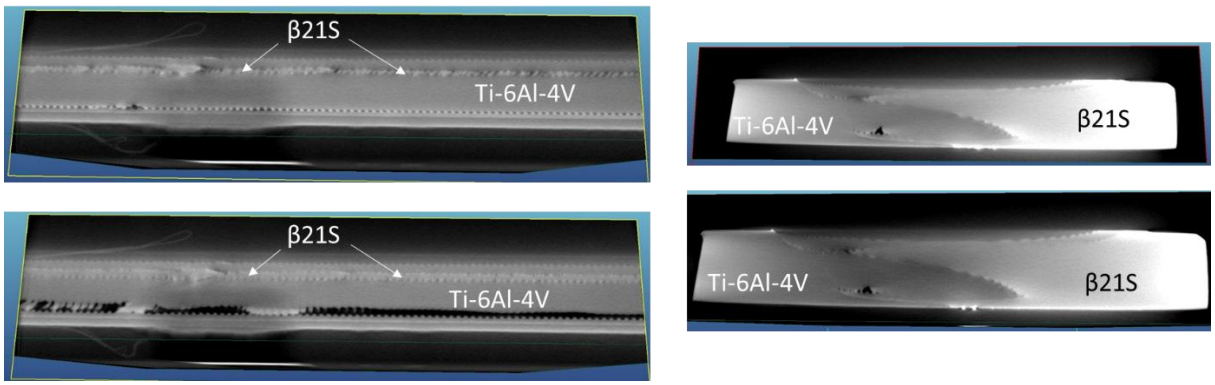

Figure 5-17: Weld 3 micro CT scans. X-Z (retreating side facing) views on the left, Y-Z (weld travel direction facing) views on the right.

Correlating the structures seen in micro CT scans to machine loads, shown in **Figure 5-18**, shows a more direct relationship between the macrostructure and forces as compared to Weld 1 or Weld 2. The periodicity of the line of defects is represented in the periodicity of the X and Y

axis force, which again shows relatively consistent amplitude and frequency relative to the sawtooth patterns of the primary β21S fin. Although defects are present throughout the length of the weld, two large pockets of defects evidence in the weld force plots as localized negative spikes in the X, Y and Z axis.

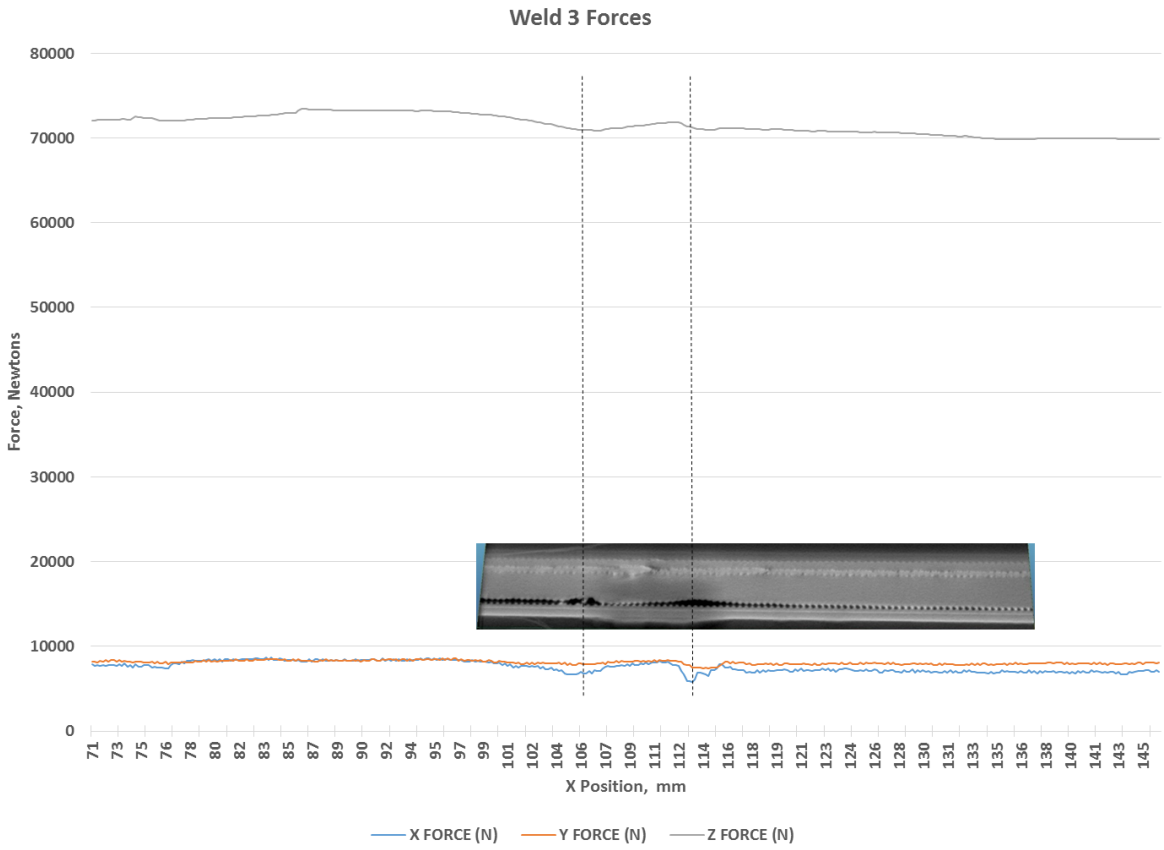

Figure 5-18: Weld 3 forces, shown relative to X-Z (retreating side facing) view micro CT scan.

The microstructure of Weld 3, shown in **Figure 5-19**, shows demonstrates features that are shared by all welds using nominal parameters with Ti-6Al-4V on the advancing side. The primary β21S fin thins as it enters the advancing side of the weld, becoming unstable and breaking into globules as the tip of the fin approaches the heat affected zone on the advancing side. Fine scale banded mixing is present in the root of the stir zone, showing a periodicity in

banding shared with the tool marks on the top of the weld as well as the perturbations in the advancing side root defects and wavy pattern on the primary β21S fin. The microstructure is equiaxed and fully transformed to widmanstatten-α.

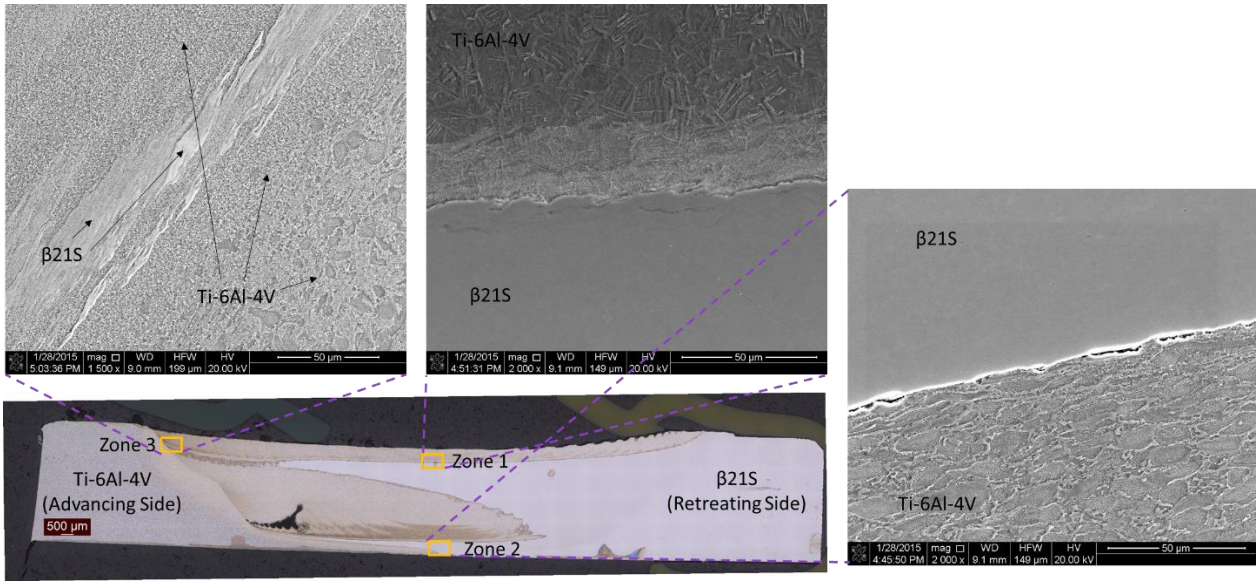

Figure 5-19: Weld 3: Ti-6Al-4V (Advancing side)/β 21S(Retreating side), 100mm/min, 225RPM, montage of 138 100x magnification micrographs, with SEM images of various magnification showing regions of interest.

In Zone 1, there is transformed and equiaxed Ti-6Al-4V, showing prior beta grains on the order of 10 to 20 microns – smaller than is seen in the root Weld 1 and Weld 2. Another notable difference is the lack of hybrid grains, although the banded structure showing multiple microstructure transitions remains, unstable ligands protruding in to the primary Ti-6Al-4V and β21S regions.

Zone 2 shows a distinct difference from the hotter parameters of Weld 1 and Weld 2 in that there is no turbulent mixing of the two alloys completely through the root of the weld. In this case, there are root defects and incomplete bonding of the two alloys and primary-α is retained in

the Ti-6Al-4V, with only minor elongation of the primary-α particles at the interface with the β21S.

In Zone 3 the transition from the heat affected zone in the Ti-6Al-4V into the stir zone is shown. Large, sheared bands of β21S are seen, which originated from the tip of the primary B21S fin of the stir zone. However, in this case the Ti-6Al4V matrix shows a very fine, equiaxed structure with globular primary-α in the stir zone an order of magnitude smaller in grain size than that of its parent material.

An EDS line scan in Zone 1 of Weld 3, shown in **Figure 5-20**, shows patterns seen in Weld 1 and Weld 2. Although the transitional band of structure between the Ti-6Al-4V and β21S is still wide compared to the length scale of diffusion, the transitions are sharp and well defined.

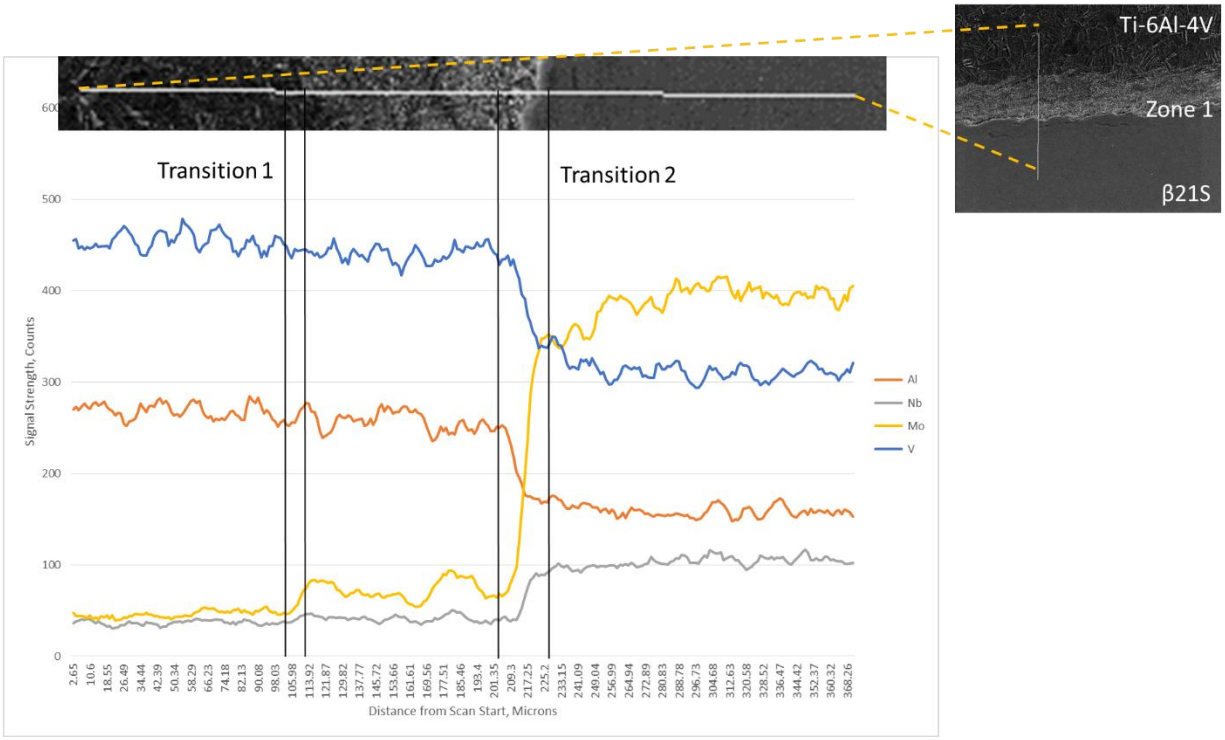

Figure 5-20: Weld 3, Zone 1, Line 1 EDS line scan plot for Al, Nb, Mo and V.

Discussion

Weld 3 evidences the changes in material mixing and flow patterns when moving away from the warmer parameters of Weld 1 and Weld 2 and moving into the nominal process window. Although the characteristic primary fin of β21S is present in **Figure 5-17**, the sub-features are smaller in magnitude. The sawtooth pattern is present and again appears to be initially generated by the motion and oscillation of the pin [Fonda, 2013], however, the sawtooth features do not grow and become unstable in the same way as Weld 1 and Weld 2. Similarly, as the fin breaks up at the tip near Zone 3, it does so in a more regular and stable fashion. With these parameters, there is a significant increase in defects along the advancing side root of the weld, which can also be seen in the load curves of **Figure 5-18**. The periodicity of the defects as well as other macrostructure features correlate well to the periodicity in the X and Y loads, and gross defects can be seen as negative spikes in the X and Y loads. This is a reasonable result, as one would expect that a void would present less material to engage the pin, and thus a lower reaction force on the pin as it travels.

The microstructures seen in **Figure 5-19** also evidence changes consistent with these relatively slow pin translation and rotation parameters [Edwards, 2010b][Fonda, 2004]. Recrystallization is evidenced by well-equiaxed structure throughout, and super-transus heating is also evidenced by transformed alpha structures in Zone 1. However, grain sizes have decreased in Zone 1 relative to the hotter parameters of Weld 1 and Weld 2. Lower heat input would limit grain growth after the nucleation process, however, the change in pin rotation and travel speeds correlating with a change in heat input convolutes the relative contributions of heat versus deformation in the dynamic recrystallization process [Brun, 1998]. Zone 2 appears to have maintained temperatures below the β-transus of Ti-6Al-4V, evidenced by the retained

primary α particles and does not appear to have been deformed in any substantial way, with only minor elongation on the primary α at the interface with the β21S. Zone 3 on the other hand, retains a fine equiaxed duplex microstructure of a finer scale than the base metal, leaving direct evidence of sub-transus dynamic recrystallization at the edges of the stir zone [Brun, 1998][Prasad, 1998]. It is reasonable to assume that the quenching effect provided by the unengaged metal outside of the stir zone is sufficient to keep temperatures below the β-transus, while strains imparted by the pin drive the recrystallization.

Although the mixing appears more stable than Weld 1 or Weld 2, calculations to estimate local temperatures based on diffusion profiles still does not provide conclusive results. In **Figure 5-20**, a diffusion calculation for the chemistry gradient between the Ti-6Al-4V and the transition band, and from the transition band to the β21S yield temperatures of 1250°C and 1450°C respectively. Both temperatures calculated using the diffusion method are significantly hotter than expected [Edwards, 2010b]. Increasing temperatures while moving further away from the shoulder of the tool would be counter-intuitive, and again shows that the metal flow and mechanical mixing of the interfaces has become the dominant mechanism in generating the composition gradients.

5.6.4 Weld 4 – 275RPM/100mm/min

Weld 4, shown in **Figure 5-21**, has similar parameters to Weld 3, but with an increase in spindle speed by 50RPM to 275RPM. A fine band of defects can be seen in the same location in the advancing side root of the stir zone. The sawthooth features are again present, but with the tighter periodicity than Weld 3. The primary β21S fin is larger in volume than in Weld 3, although with a more rounded aspect ratio. The instabilities at the tip of the fin are regular and

fine in scale, breaking into small globules of β21S that continue to mix, dissolve and rotate along the advancing side of the stir zone. With the overall increase in sawtooth features and weld heat, a small increase in inter-alloy mixing in the root of the weld is seen again, as the degradation of the sawtooth features provides β21S for the root stir zone.

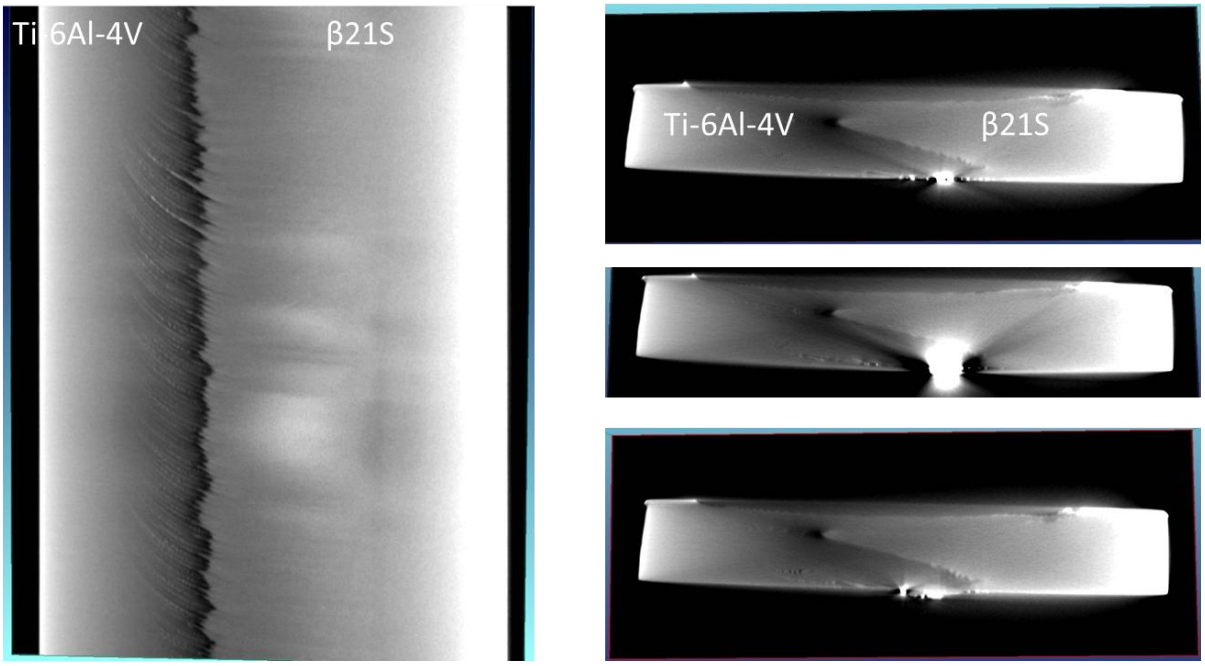

Figure 5-21: Weld 4 micro CT scans. X-Y view (retreating side on the left) on the left, Y-Z (weld travel direction facing) views on the right.

Machine loads for Weld 4, shown in **Figure 5-22** and with forge load only in **Figure 5-23** shows evidence of larger scale features correlating with forge loads. With the void structure largely consistent with the other welds of nominal parameters, the sudden increase and then stabilization of forge loads becomes of interest. Correlating with the increase of forge load is a change in the shape of the primary β21S fin. Shown at two different transverse views in **Figure 5-23,** the thickness of the primary fin increases, representing an increase in the overall volume of β21S engaged in the stir zone, as well as the aspect ratio of the fin itself.

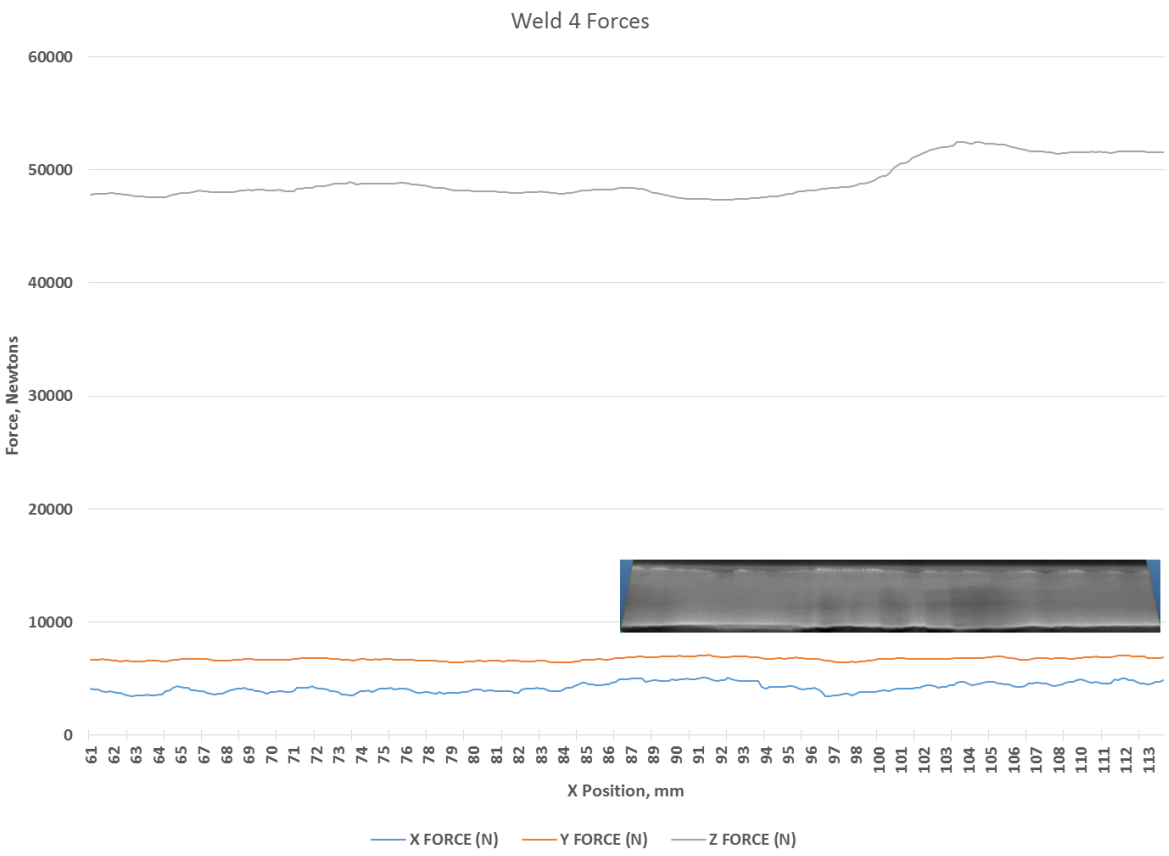

Figure 5-22: Weld 4 forces, shown relative to X-Z (retreating side facing) view micro CT scan.

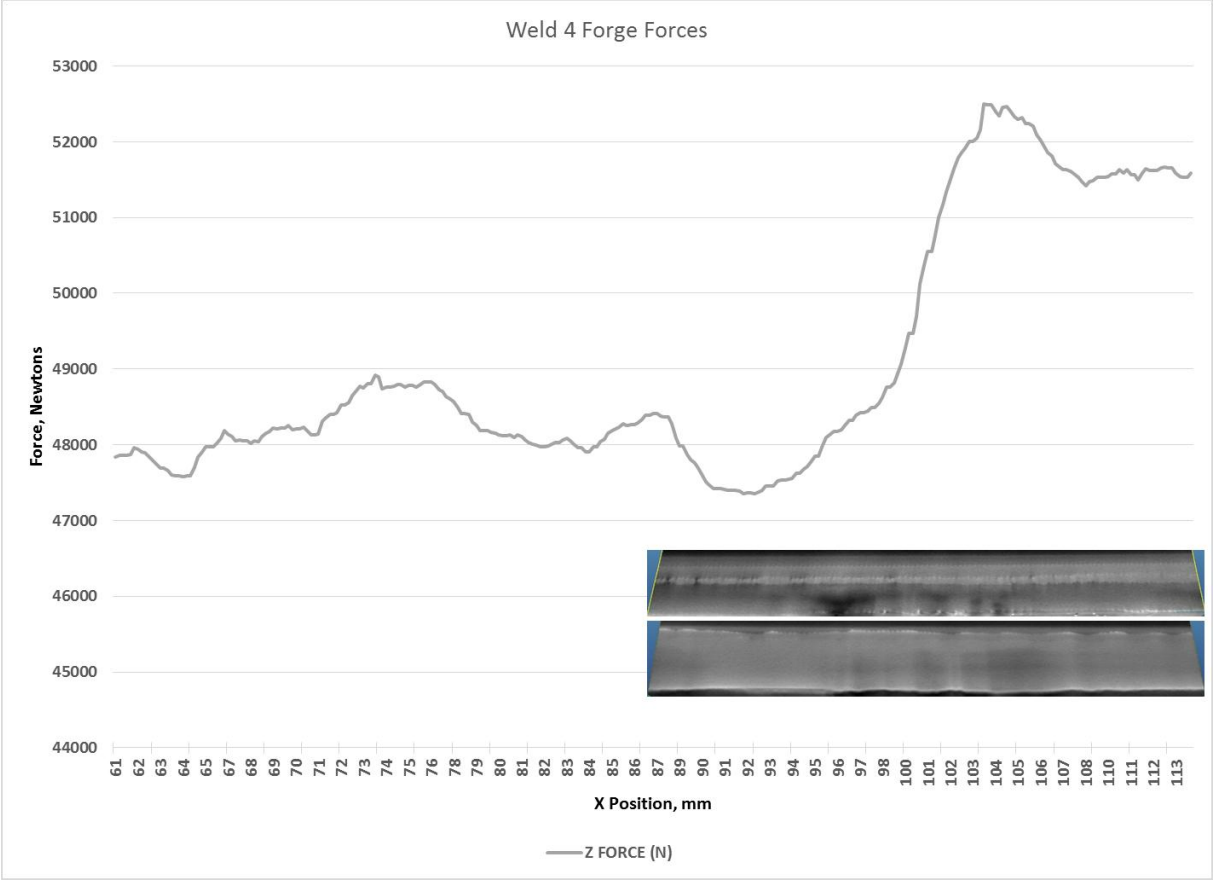

Figure 5-23: Weld 4 forge forces, shown relative to two X-Z (retreating side facing) view micro CT scan.

Microscopy results for Weld 4, shown in **Figure 5-24**, largely shows features already seen in Weld 3, although somewhat exaggerated. The primary β21S fin takes the same position and shape, thinning as it approaches the advancing side. Periodic instabilities are more apparent and extend further into the stir zone. Defects are present in the advancing side root of the weld, taking the form of multiple smaller defects. The bottom mixing zone shows periodic fine striations of both alloys, transitioning to unstable eddies where the striations meet the primary β21S fin on the retreating side or the defects on the advancing side.

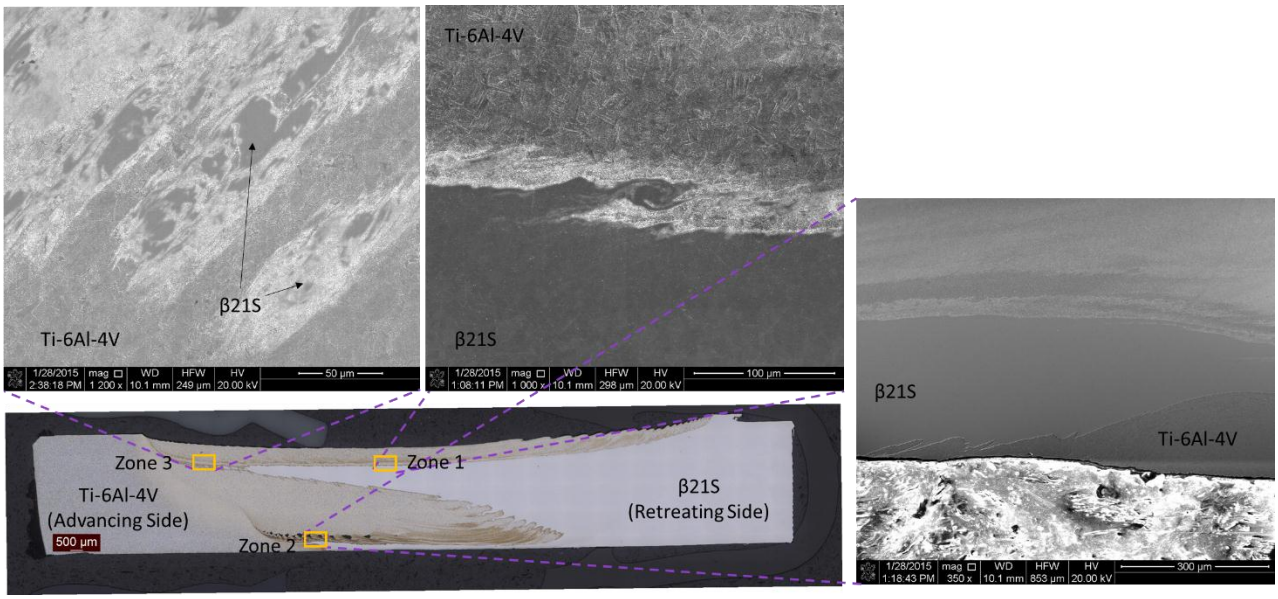

Figure 5-24: Weld 4: Ti-6Al-4V (Advancing side)/β 21S(Retreating side), 100mm/min, 275RPM, montage of 138 100x magnification micrographs, with SEM images of various magnification showing regions of interest.

Zone 1 shows much the same characteristics as that of Weld 3; equiaxed and fully transformed Ti-6Al-4V with prior-β grains on the order of 20 microns are present, although with hybrid grains along the initial material interface as well. The mixing pattern shows an unstable, turbulent mixture with vortices of β21S protruding into the interface of finer transformed Ti-6Al-4V.

Zone 2 shown at low magnification to view the overall mixing pattern and microstructure transitions of the root of the weld. A large piece of β21S is forcing towards the root of the weld, deforming and rounding off the main root ligand of Ti-6Al-4V, shown by the deformed primary-α of the Ti-6Al4V conforming to the contour of the interface. The Ti-6Al-4V changes structure and shows finer, equiaxed grains as it moves into the root region containing a more tortuous interface with the β21S. The more turbulent portion of the root shows banding on several length scales, as well as etch effects hundreds of microns in length. Along many of the banded interfaces is a finer sawtooth pattern, with regular, aligned protrusions into adjacent bands.

Zone 3 shows the same structure and patterns seen in Zone 3 of other welds. The patterns generated by both the mechanical and diffusive mixing of β21S globules into the Ti-6Al-4V matrix are very complex. The matrix of Ti-6Al-4V consists of equiaxed prior-β grains that vary in size from roughly 10-30 microns, a wider variation than has been typically observed. The coarseness of the alpha structure varies widely, and cannot be consistently correlated with proximity to the main globules of β21S.

An EDS line scan of Zone 1 is shown in **Figure 5-25**. Three distinct compositions can be seen, rather than a steady transition between the two base compositions, as has been observed in other welds.

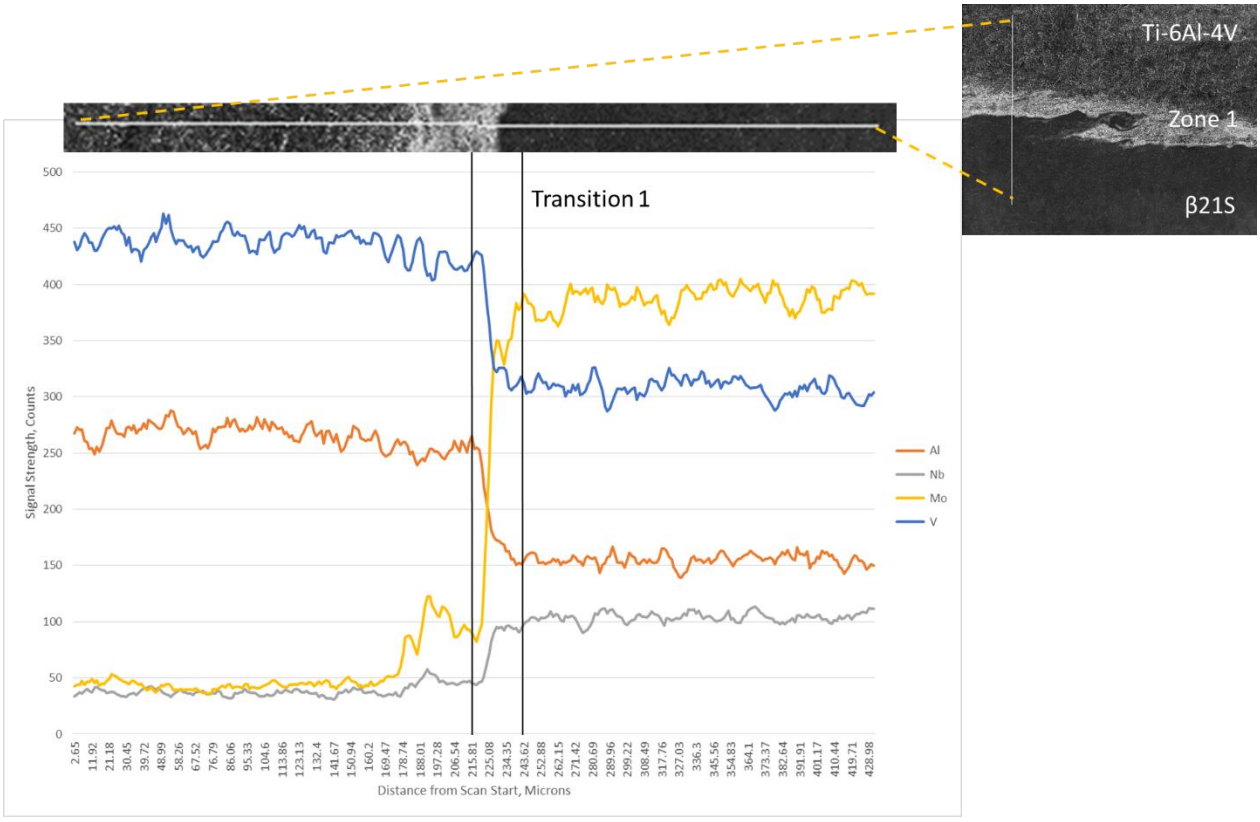

Figure 5-25: Weld 4, Zone 1, Line 1 EDS line scan plot for Al, Nb, Mo and V.

Discussion

Weld 4 represents slightly warmer process paramters than Weld 3 [Edwards, 2010c], and the associated decrease in flow stress at the higher temperatures leads to decrease in defects, seen in **Figure 5-21**. The higher spindle speed relative to Weld 3 changes the macrostructure features in the expected way, namely the periodicity of the sawtooth features and the defects is tighter and of finer scale [Fonda, 2013]. The increased heat of these weld parameters can also be seen in the increase of interalloy mixing at the root of the weld.

The microstructure of Weld 4 presents features already demonstrated previously, with minor changes in character that can be credited to the small increase in heat input versus Weld 3. Recrystallized and transformed Ti-6Al-4V is present throughout, and hybrid grains have again returned in Zone 1, seen in **Figure 5-24**. The increased heat also has increased the turbulence of the interfaces in Zone 1, behavior that is consistent with warmer, softer material behaving in a more fluid manner. The Ti-6Al-4V of Zone 2 shows evidence of softening beyond that of Weld 3, and more deformed interfaces with the β21S are present as well as evidence of recrystallization [Abbaschian, 1991][Tamirisakandala, 2003]. Considering that this material is not in direct engagement with the pin, it shows that full penetration in the weld is not just a matter of heat fusing the seam of the two pieces of material, but rather the friction and pressure of local material flowing in the weld nugget can deform material completely through the root of the weld. Zone 3 again shows evidence of the importance of mechanical mixing in determining the local composition and structure – alpha structures vary widely in coarseness over small length scales and cannot be directly correlated with their proximity to larger globules of β21S and the expected influx of beta stabilizers those large globules would provide via diffusion [Boyer, 1994][Malinov, 2005] .

EDS line scans and local temperature estimates again prove complex. In **Figure 5-25**, if one assumes that the chemistry transition between the lighter basketweave structure and the β21S based structure occurs solely by diffusion in the time period of the peak temperature spike in the weld process, a temperature of approximately 1480°C would be required. This is several hundred degrees hotter than any similarly calculated temperature in the welds of Ti54M and Ti-6242, modeled data from the literature, or in the directly measured thermocouple data of Ti-6Al-4V welds by Edwards [Edwards, 2010b].

5.6.5 Weld 5 – 275RPM/125mm/min

Results

Weld 5, shown in **Figure 5-26**, shares the same pin rotation speed as Weld 4, but increases the travel speed by 25mm/min to 125mm/min. The defects maintain the same periodicity as seen in the sawtooth features and have increased in volume over Weld 4, although the array tends to drift more in location and magnitude than is seen in previous welds. The primary β21S fin is again present. Sawtooth features created by the tool rotation survive further into the advancing side of the stir zone than other nominal parameter welds. Large, high aspect ratio teeth are seen near where the primary β21S fin becomes unstable at its tip and begins to break up. The dissolution and breaking up of the sawtooth features again directly relates to the number and size of β21S/Ti-6Al-4V ribbons seen in the root of the stir zone, the position and timing of when the sawtooth feature becomes unstable and detaches affects the character of the stir zone.

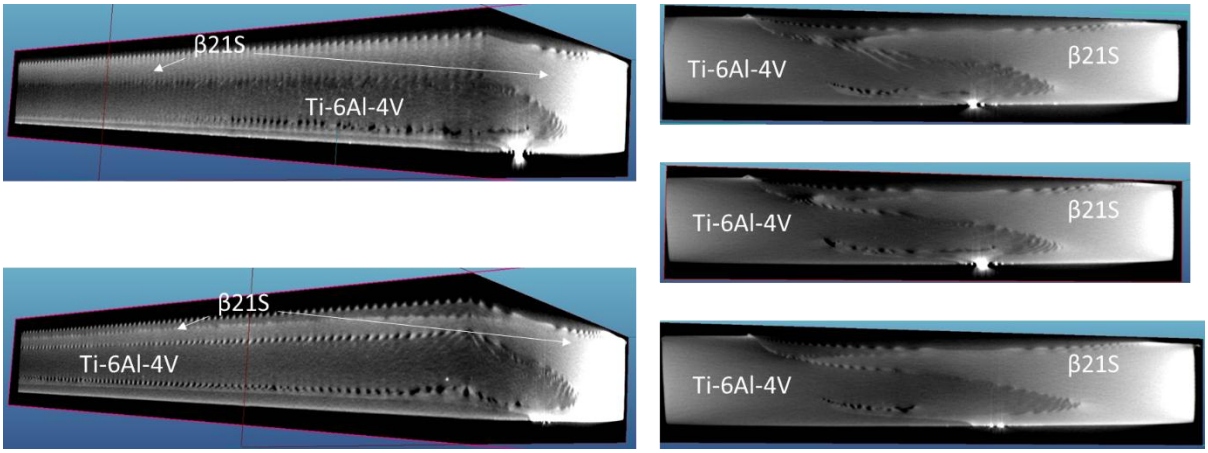

Figure 5-26: Weld 5 micro CT scans. X-Z/Y-Z ¾ (retreating/weld travel direction facing) views on the left, Y-Z (weld travel direction facing) views on the right.

With just lateral forces shown, the force plot of Weld 5, shown in **Figure 5-27**, shows again the direct correlation between changes in defect structure and X and Y forces. The size of the voids in the more stable portion of the weld do not appear to be effected by the small drift in average X and Y loads, the large spikes in loads clearly correlate with and increase concentration and a change in the position of the defects. In other welds, where increased defects can be seen lowering overall forces on the pin, Weld 5 shows distinct positive spikes.

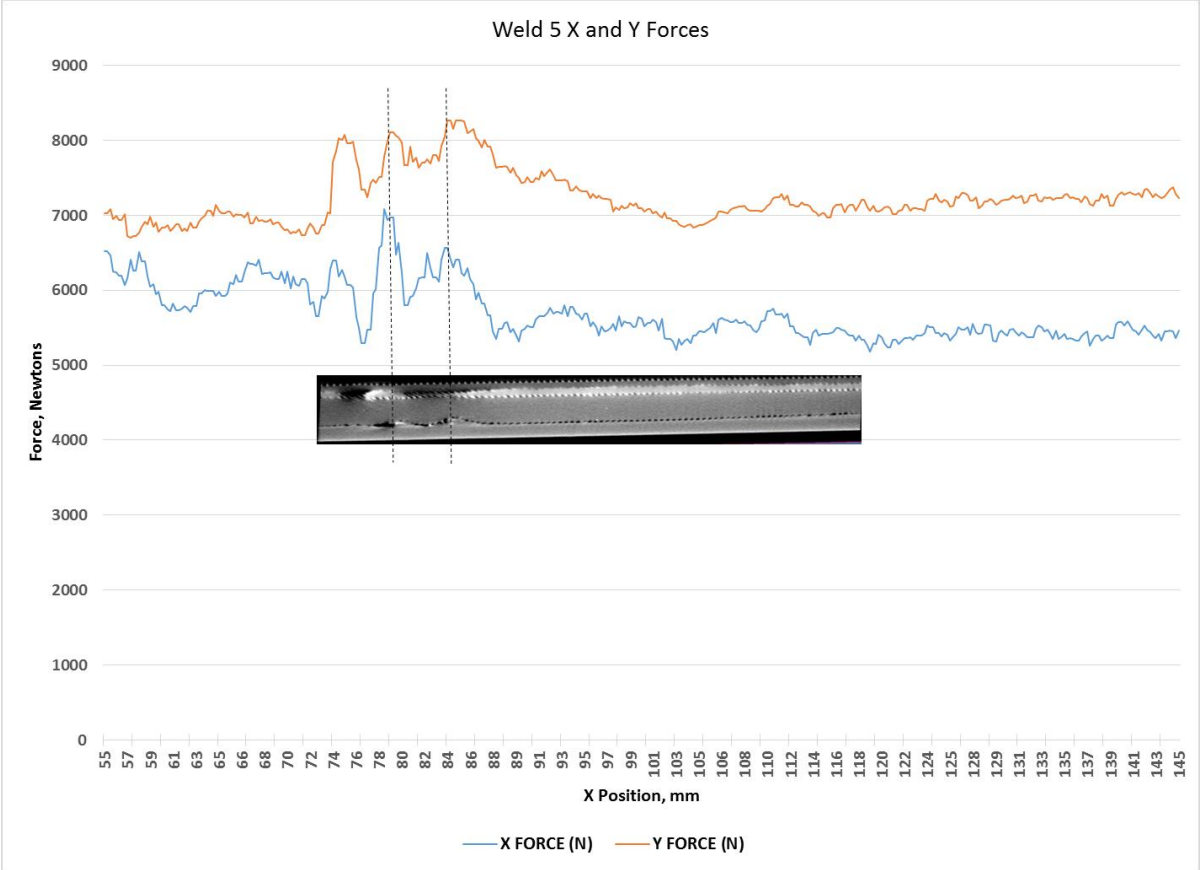

Figure 5-27: Weld 5 lateral forces, shown relative to X-Z (retreating side facing) view micro CT scan.

Microscopy of Weld 5, shown in **Figure 5-28**, shares features already seen in Weld 3 and Weld 4. The primary β21S fin extends well into the advancing side and has periodic instabilities all along its length, as well as a consistent breakage at the tip, forming globules of β21S. The root stir zone shows a less defined periodicity in the banding, and an increase in defects over Weld 4. A row of well-formed eddies on the root of the weld separates the defects from any linear, banded mixing features.

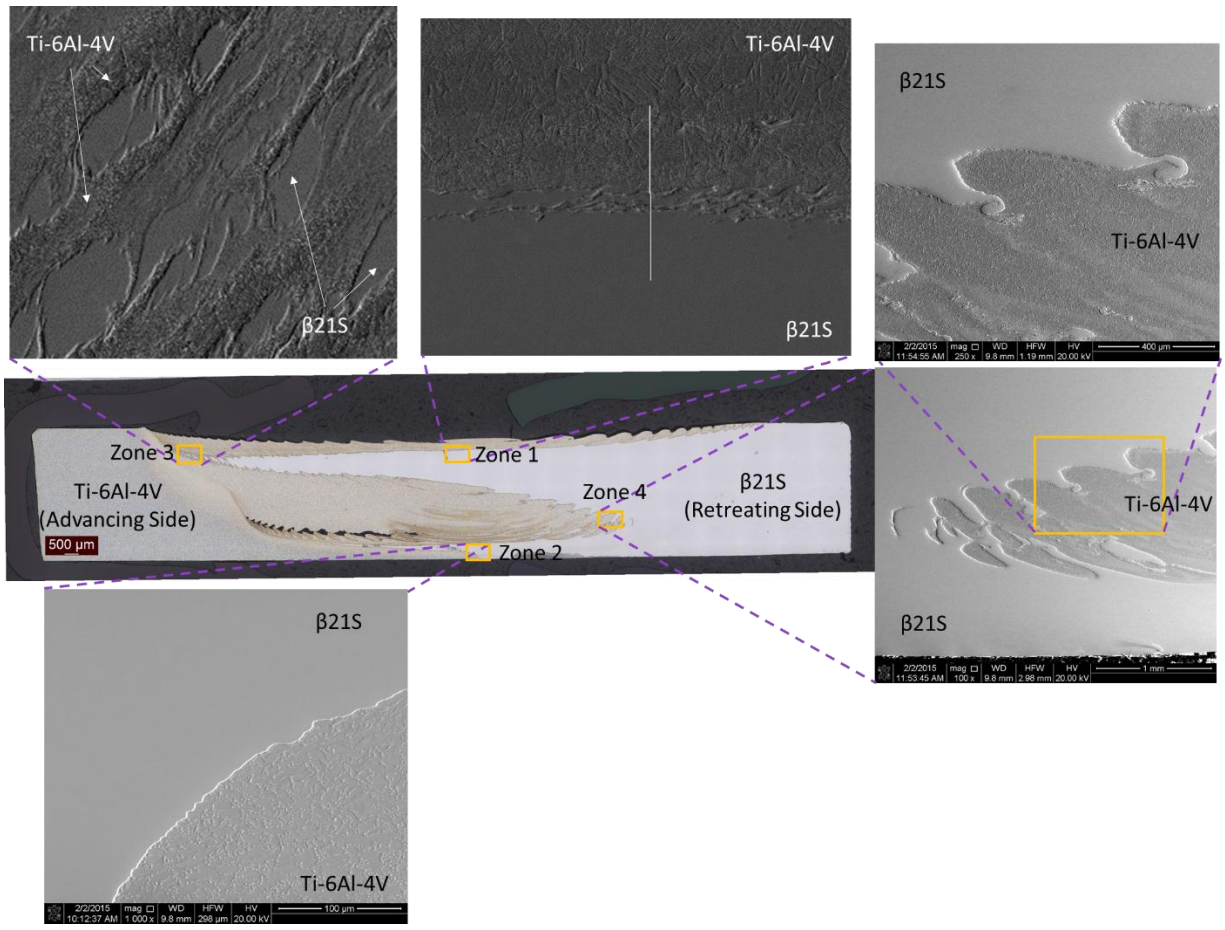

Figure 5-28: Weld 5: Ti-6Al-4V (Advancing side)/β 21S(Retreating side), 125mm/min, 275RPM, montage of 138 100x magnification micrographs, with SEM images of various magnification showing regions of interest.

Zone 1 again shows equiaxed Ti-6Al-4V with a widmanstatten structure, transitioning into the β21S at first with a band of finer widmanstatten structure and finally with a turbulent, evolving interface. Zone 2 shows a defect-free interface at the root of the weld, outside of the primary stir zone. The Ti-6Al-4V has retain its primary α, which is still equiaxed. The interface with the β21S shows only small disturbances. Looking at the advancing side in Zone 3, we see the features that are characteristic of the region: large globules of β21S, breaking up within the matrix of equiaxed and transformed Ti-6Al-4V on multiple length scales, creating a complex and turbulent mix of globules and microstructures. In the retreating side of the nugget, shown as

Zone 4, eddies of β21S can be seen evolving, with fine ligands being ejected from the eddy swirls into the Ti-6Al-4V and finally creating minor etch contrast differences.

In sections of weld that demonstrate little instability, such as Zone 2 of Weld 5, EDS profiles such as those obtained in Chapter 4 can be observed, shown in **Figure 5-29**. A single transition of 5 microns in length can be seen.

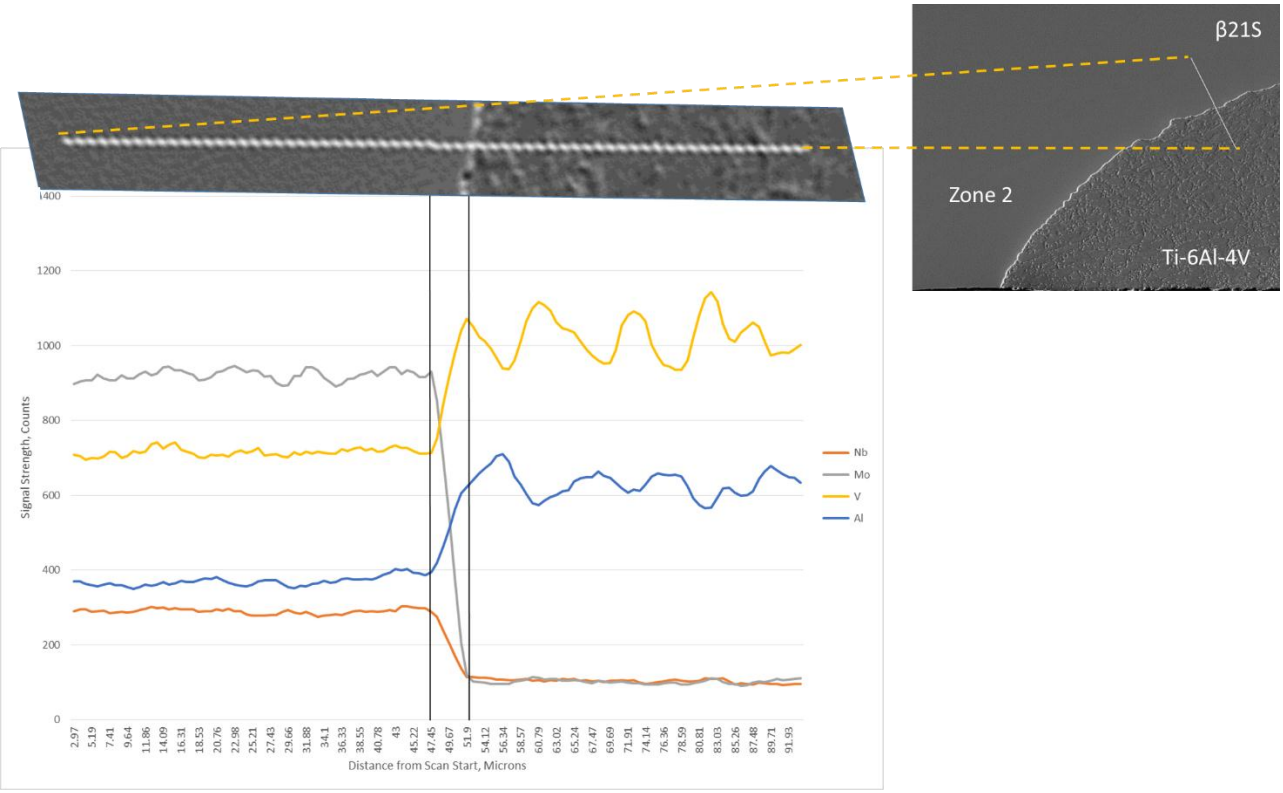

Figure 5-29: Weld 5, Zone 2, Line 1 EDS line scan plot for Al, Nb, Mo and V.

Viewing Zone 3 with EDS mapping, shown in **Figure 5-30**, the evolution of the localized chemical compositions can be observed in parallel with the macrostructure evolution. Areas of fine alpha structure and etch contrast differences correlate well with more diffuse chemical concentrations from the EDS mapping.

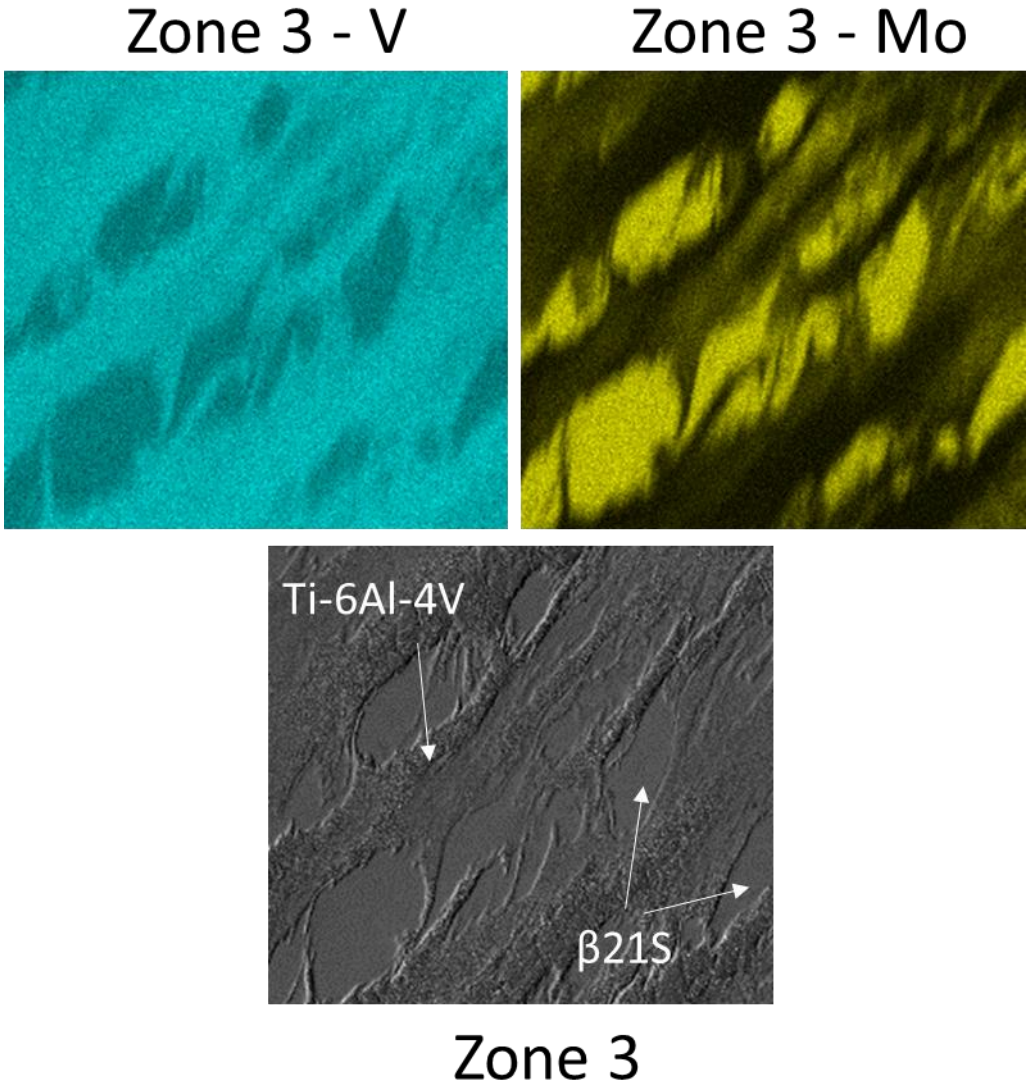

Figure 5-30: Weld 5, Zone 3, EDS Map for Mo and V.

Discussion

The macrostructure of Weld 5, seen in **Figure 5-26**, shows similarities with the other welds of nominal process parameters, and shows behavior consistent with parameters slightly cooler than that of Weld 4 (and warmer than that of Weld 3) [Edwards, 2010c]. Cooling relative to Weld 4 again increases defects as one would expect from cooler metal flow, while sawtooth features on the primary β21S fin survive further into the advancing side of the weld nugget and

are less broken up by heavy mechanical mixing and diffusion. Void structure is largely periodic and consistent, although a period of large voids is shown in both the microCT scans as well as the machine load plots. Unlike the case of Weld 3, the voids appear to correlate with an increase rather than a decrease in the X and Y axis loads, implicating additional changes to the macrostructure in that zone that are not detectable.

The microstructure of Weld 5, seen in **Figure 5-27**, shows the defining characteristics of a nominal parameter weld. Equiaxed, transformed Ti-6Al-4V is seen in Zone 1 and Zone 3, showing super-transus heating and significant dynamic recrystallization, while Zone 2 retains primary alpha and is only lightly disturbed at its interfaces with the β21S. This behavior is consistent with parameters that, in terms of heat input, are between Weld 3 and Weld 4 [Fonda, 2004][Mironov, 2008]. Even in these nominal parameters though, Zone 4 shows highly fluid behavior, with eddies forming and breaking apart, finally being fully absorbed via diffusion and giving rise to the etch contrast that is seen at various locations throughout all weld conditions.

In sections of weld that demonstrate little instability, such as Zone 2 of Weld 5, shown in **Figure 5-29,** temperature calculations from EDS line scans appear to provide more reasonable results. A single chemistry gradient is seen between two stable compositions of Ti-6Al-4V and β21S, and a temperature based on the diffusion zone can be calculated at 1125°C (which was shown to be repeatable in the same field with a second scan). This result is still higher than root temperatures measured by Edwards [Edwards, 2010b] or calculated in Ti54M/Ti-6242 welds, although it is much closer than the difference seen in Zone 1 measurements. 1125°C is also significantly hotter than the nominal β-transus of Ti-6Al-4V, while the microstructure has retained primary α and shows no evidence of an excursion beyond the transus [Boyer, 1994]. This behavior can be contrasted with Zone 3, seen in **Figure 5-30**,

where blockier globules of β21S become unstable and are broken up in the surrounding Ti-6Al-4V matrix, eddies form, continue to break up and eject ever smaller segments of β21S into the Ti-6Al-4V to the point that diffusive mixing can effectively create a locally homogenous chemistry band with the supplied time and temperature. This highlights the notion that large-scale homogeneity in chemical composition within a weld nugget is first reliant on vigorous mechanical mixing before diffusive processes carry out the final smoothing of a local chemistry.

5.6.6 Weld 6 – 275RPM/150mm/min

Results

Weld 6, shown in **Figure 5-31**, increases the travel speed by 25mm/min over Weld 5 while keeping the spindle rotation speed constant. The defect structure in the advancing site root stir zone has evolved again, appearing to have coalesced some of the periodic defects into a larger defect, surrounded by an array of smaller defects, similar to that seen in Weld 3. The primary β21S fin has changed character again, and although the shape is similar to that of Weld 5, the evolution of its shape along the length of the weld is more stable. The fin bulges with a regular period along the weld center line much more apparently than any other weld condition, creating a wave-like effect that propagates into the advancing and retreating side of the fin, stacking up into sawtooth features that rotate and align with the heat affected zone of both sides of the weld. Again, the sawtooth features become unstable, breaking up and dissolving into the Ti-6Al-4V matrix of the root stir zone as is seen in other welds. As the waves propagate along the primary β21S fin, bulges of β21S that reach the tip of the fin are broken off into the matrix of the advancing side stir zone at regular intervals.

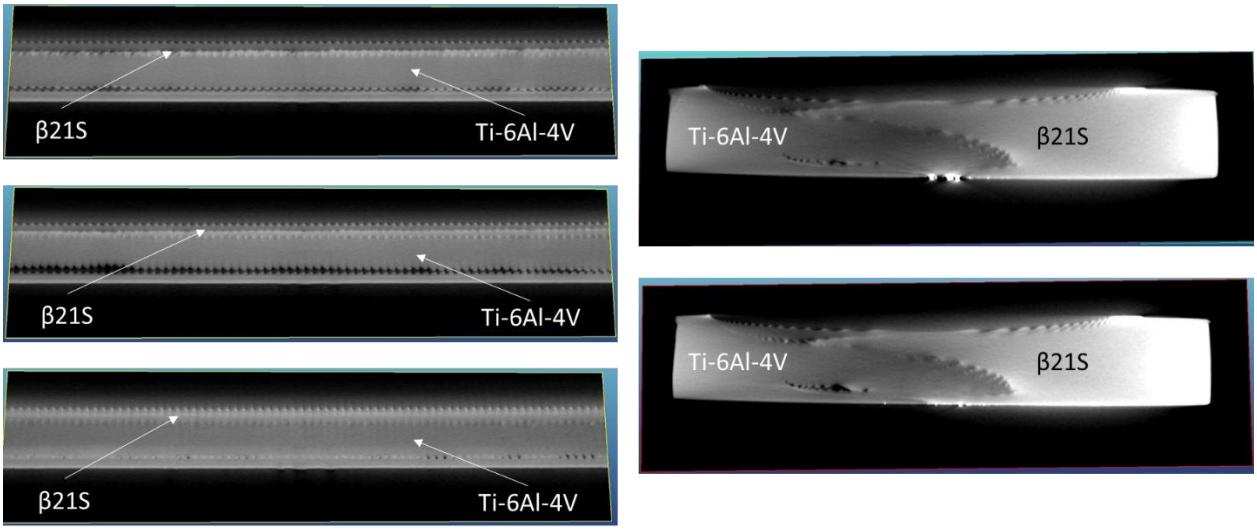

Figure 5-31: Weld 6 micro CT scans. X-Z(retreating side facing) views on the left, Y-Z (weld travel direction facing) views on the right.

Machine load plots for Weld 6, shown in **Figure 5-32**, shows stability in the X and Y forces that correlate well with the structures shown in the stir zone. The void structure and sawtooth patterns remain consistent in magnitude and position throughout the length, agreeing well with the stable loads with no spikes in the X and Y axis. Although a sawtooth pattern is present, it appears less distinct than other welds, with peaks that smear into adjacent peaks – this can also be seen in the X and Y loads, where there is a much less distinct periodicity over short length scales. The forge load shows a steady and stable decrease in load over the length shown, which correlates to a smaller β21S fin (lighter band), the inverse of what was seen in Weld 4.

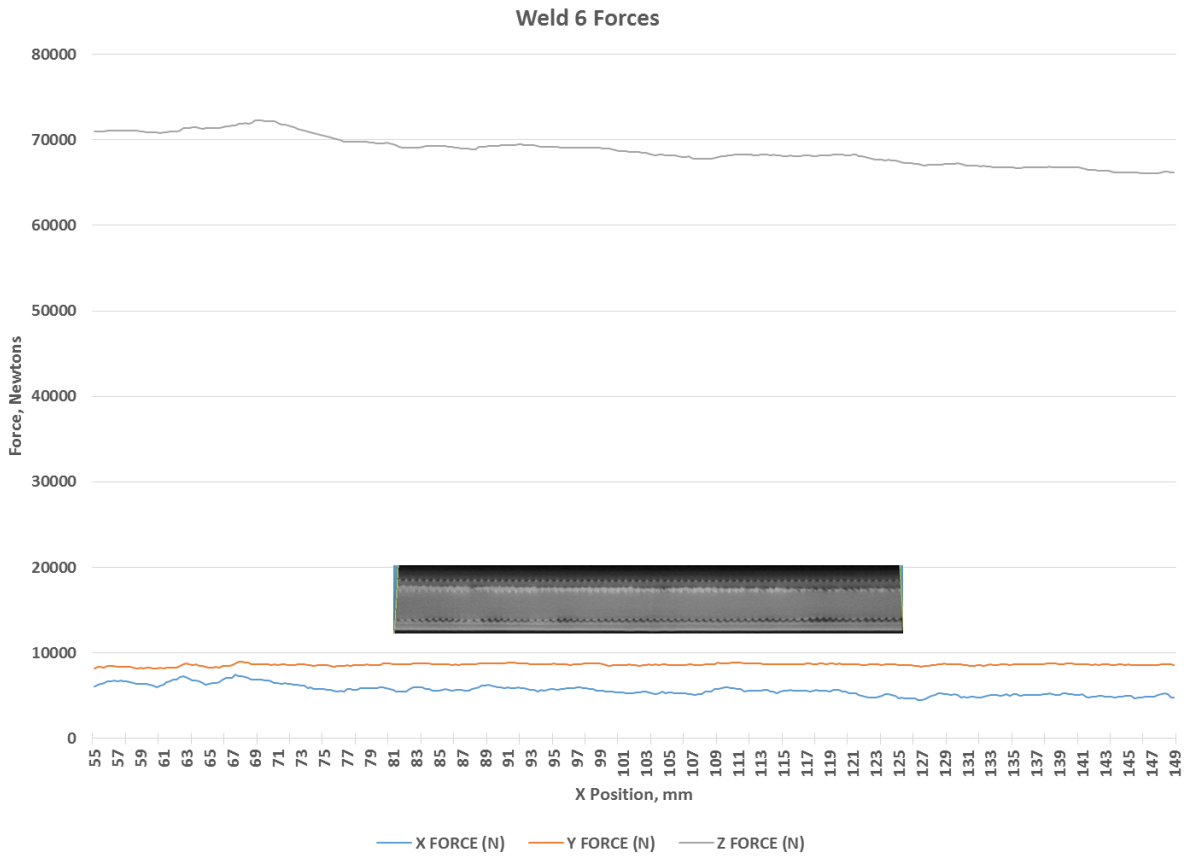

Figure 5-32: Weld 6 forces, shown relative to X-Z (retreating side facing) view micro CT scan.

Microscopy for Weld 6, shown in **Figure 5-33**, shows the larger volume of defects consistent with observations from micro CT scans, as well as the modified shape of the primary β21S fin as compared to other nominal parameter welds. The fin thins out much more rapidly and does not protrude as deeply into the advancing side, presenting less overall volume of β21S in the stir zone. The root of the stir zone is absent of the banded, heavily mixed pattern that has been seen in all other welds, although eddies can still be seen in the retreating side of the stir zone.

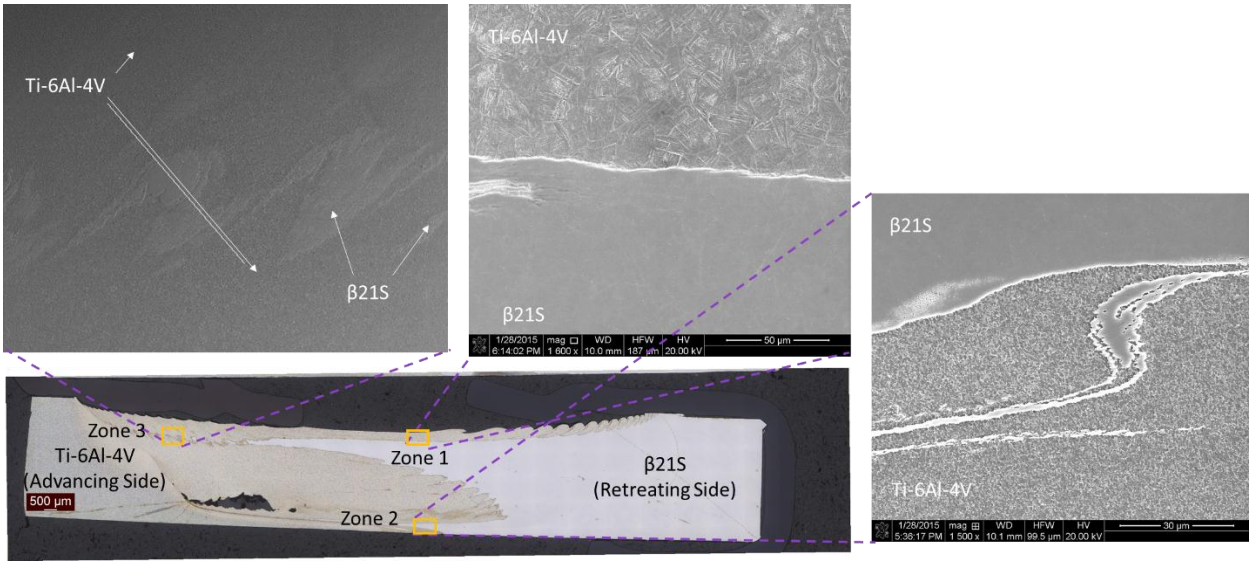

Figure 5-33: Weld 6: Ti-6Al-4V (Advancing side)/β 21S(Retreating side), 150mm/min, 275RPM, montage of 138 100x magnification micrographs, with SEM images of various magnification showing regions of interest.

Zone 1 shows equiaxed and transformed Ti-6Al-4V with prior β grains on the order of 20 microns. Although the majority of the structure is equiaxed, there are smaller, irregularly shaped grains scattered throughout. The primary interface with the β21S is relatively featureless, with minor smearing and protrusions of Ti-6Al-4V into the β21S. A small band of Ti-6Al-4V based material sits in a matrix of β21S and shows a fine transformed structure that transitions to β-phase with little to no alpha, yet a distinct difference from the parent β21S structure.

Zone 2 evidences what appears to be a full-penetration weld root. The Ti-6Al-4V shows fine, globular primary alpha particles in a matrix of transformed beta. Ligands of β21S have protruded into the recrystallized Ti-6Al-4V, but do not show the transitions in alpha particle density and etch contrast that Zone 1 shows. The primary Ti-6Al-4V/β21S interface shows what appear to be mostly dissolved protrusions of Ti-6Al-4V into the β21S, with only scattered globules of primary-α remaining and an etch contrast effect on the β21S matrix.

An EDS line scan of Zone 2 is shown in **Figure 5-34**. There is clearly an additional level of mixing between the two alloys and a refinement of the Ti-6Al-4V microstructure not present in Weld 5, however, the chemistry transitions remain clear and between stable compositions.

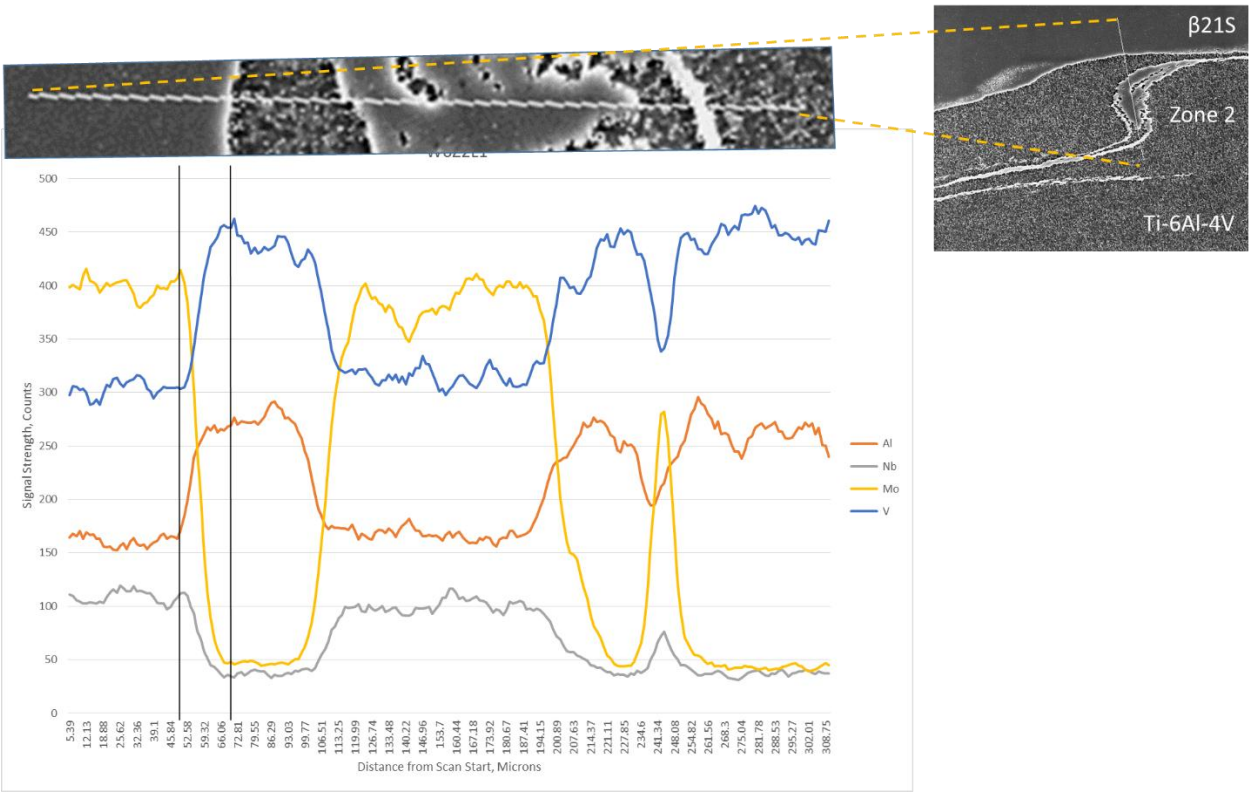

Figure 5-34: Weld 6, Zone 2, Line 1 EDS line scan plot for Al, Nb, Mo and V.

Discussion

The parameters of Weld 6 represent one of the fringes of the nominal set – namely that it produces a relatively low heat input, but accomplishes this by using a high travel speed [Edwards, 2010c]. This in turn creates more pronounced periodic features and mixing action related to the extrusion-like process of the pin traveling [Fonda, 2013]. In the macrostructure, seen in **Figure 5-31**, there is still the expected increase in defects that come with cooler weld parameters, however, the appear to have coalesced into a larger, single defect of greater volume. There also appears to be a direct correlation in the size and stability of the sawtooth protrusions

from the primary β21S and the final breakage of the tip of the fin to produce globules of β21S in the advancing side of the weld nugget.

The microstructure of Weld 6, seen in **Figure 5-32**, helps to differentiate the contribution of strain and heat to the development of the structure in various regions. Although there is still super-transus heating evidenced in Zone 1 by the presence of widmanstatten-α, the smaller grain size and incomplete grain growth where smaller, irregular grains are still being consumed shows how dynamic recrystallization can be driven largely by the strain in the process, however, significant heat is still required to homogenize the grain structure [Boyer, 1994][Prasad, 1998][Brun, 1998]. Similarly, Zone 2 shows heavy recrystallization occurring below the transus, with fine primary alpha being retained. The shift towards heavier strains and mechanical deformation is apparent with the ligands of β21S protruding in the root of the weld, as well as an absence of large regions of etch contrast that would be attributed to diffusive mixing and higher heat. That said, EDS line scans, shown in **Figure 5-34** show an initial transition into Ti-6Al-4V that correlates to a temperature of 1275°C – higher than the same Zone of Weld 5 and contradicting the presumably colder parameters Weld 6 would present [Edwards, 2010b]. This again shows how strong mechanical mixing can serve to amplify the diffusive mixing necessary to create a local chemistry gradient.

5.6.7 Weld 7 – 325RPM/125mm/min

Results

Weld 7 micro CT scans, shown in **Figure 5-35**, represent a high travel speed, high heat input parameter set from the nominal process window. Like Weld 2, Weld 7 translates at 125mm/min, but instead rotates the spindle at 325RPM instead of 400RPM. Weld 7 has an array of defects, similar to other nominal welds; several small defects with a periodicity similar to the

sawtooth features are seen in the advancing side root stir zone. Overall, the macrostrucure features in Weld 7 are very stable. The primary β21S fin extends well into the advancing side of the stir zone, and stays in-tact and consistently shaped through the length of the weld. Sawtooth features are generated in the center of the fin and propagated outward, leading to regular instabilities and breakup of the tip of the fin. Again, sawtooth features that lengthen and increase their aspect ratio become unstable, and are broken up and dissolved into the root of the stir zone.

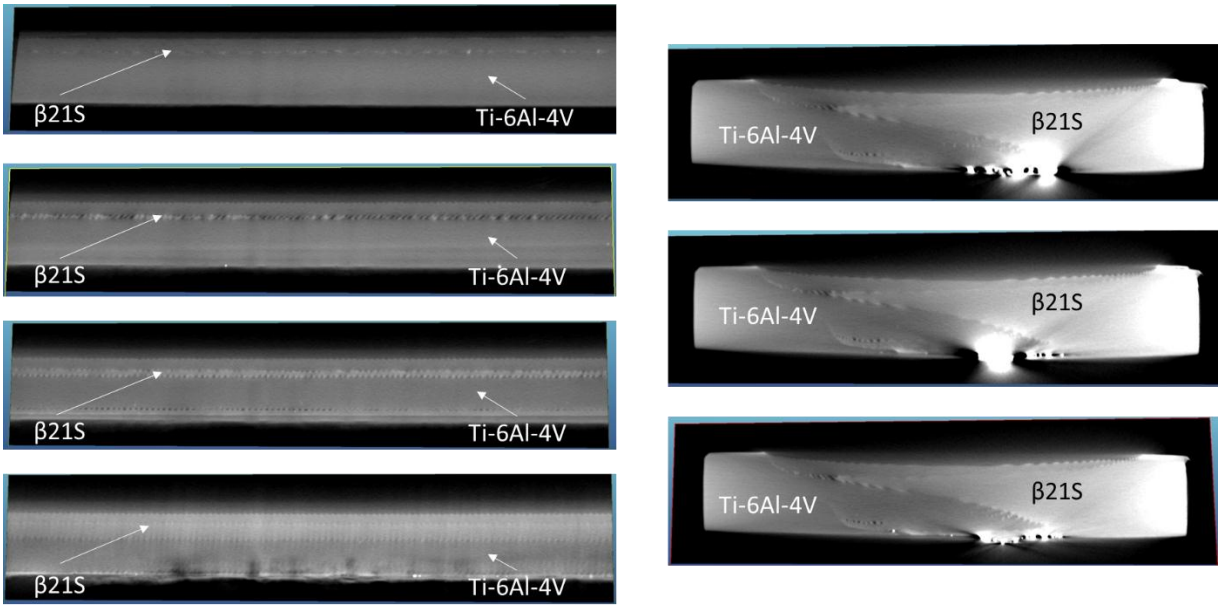

Figure 5-35: Weld 7 micro CT scans. X-Z (retreating side facing) views on the left, Y-Z (weld travel direction facing) views on the right.

Machine load data, shown in **Figure 5-36**, is another example of a very stable weld. The sawtooth pattern, as well as the void structure and position is very distinct and periodic. Similarly, the X and Y loads are very stable, with a consistent periodicity and amplitude of force spikes in the short length scale of the sawtooth features. Forge loads show little drift, and the minor variations seen do not appear to correlate with any of the features seen in the macrostructure.

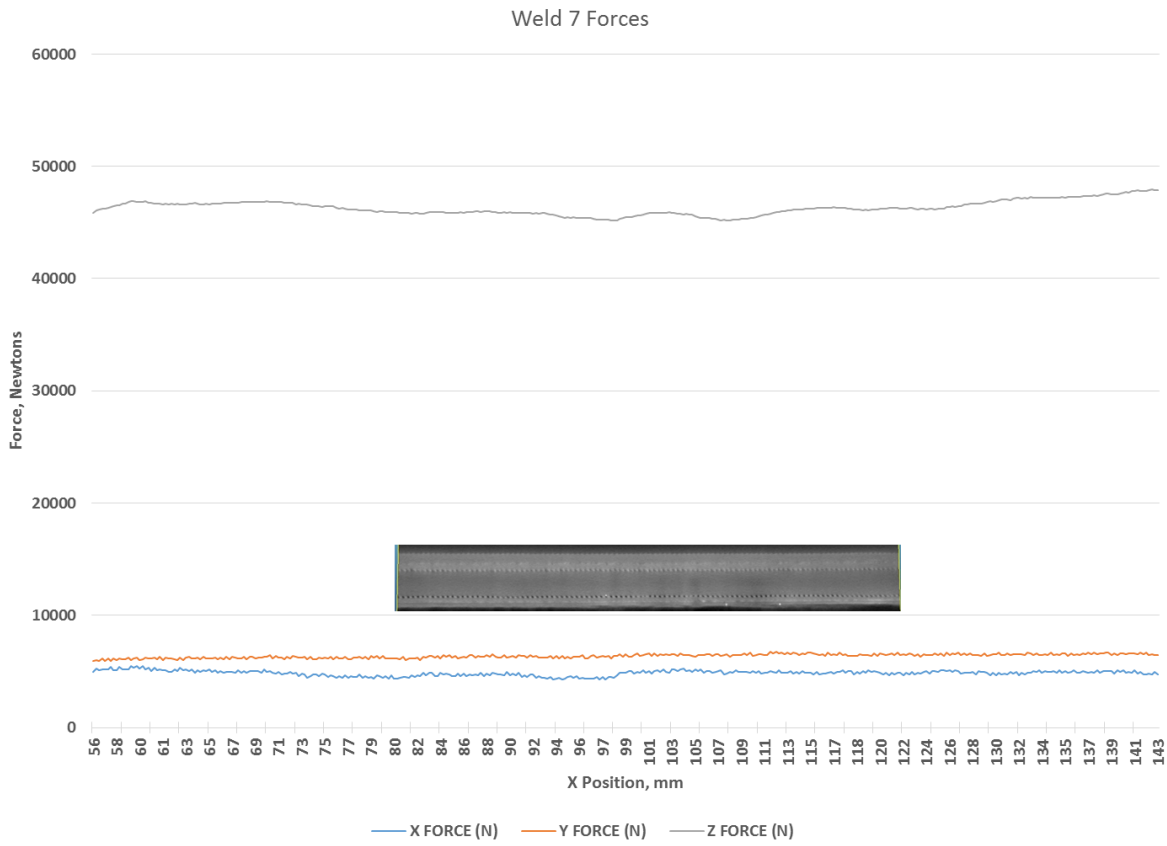

Figure 5-36: Weld 7 forces, shown relative to X-Z (retreating side facing) view micro CT scan.

Microscopy for Weld 7, shown in **Figure 5-**37, is defined largely by the unstable interfaces between the primary β21S fin and the Ti-6Al-4V. Periodic banding and striations are again present in the root of the stir zone, as well as well-formed periodic instabilities and eddies in the root side of the stir zone. A line of defects is present along the advancing side root of the stir zone, forming an array with eddy features.

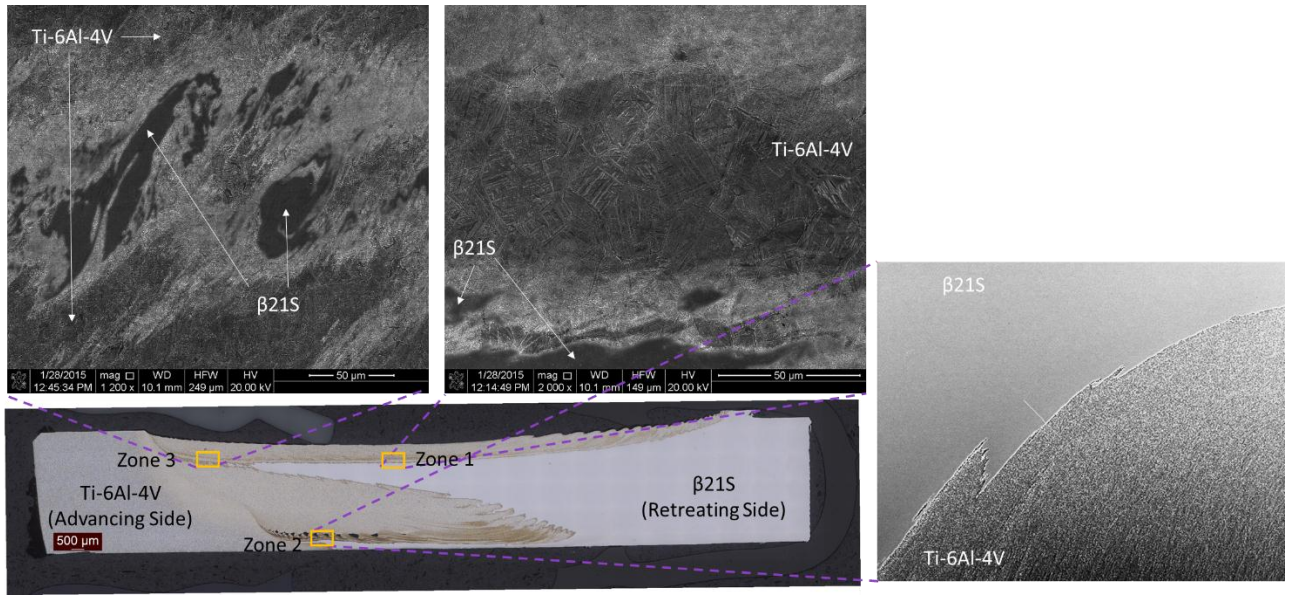

Figure 5-37: Weld 7: Ti-6Al-4V (Advancing side)/β 21S(Retreating side), 150mm/min, 325RPM, montage of 138 100x magnification micrographs, with SEM images of various magnification showing regions of interest.

Weld 7 shows unique mixing features in Zone 1. The Ti-6Al-4V is equiaxed and transformed, but much less uniformly than before. Grains are on the order of 20 microns, although multiple smaller, irregular grains are still present. The widmanstatten-α has coarsened beyond what is observed in other welds with nominal parameters.The interface with the β21S is tortured and irregular, with large and small ligands of Ti-6Al-4V and β21S intermixing and generating variations in α-particle density and size. There is evidence of hybrid grains, although with combinations of microstructures not observed in other welds. Where as Weld 2 and others demonstrated a simple transition from widmanstatten alpha generated by Ti-6Al-4V into a typical β21S grain, here we see transitions from β to very fine widmanstatten-α, to widmanstatten-α. There are also hybrid grains that have transitions from coarse widmanstatten-α into fine widmanstatten-α in several locations.

Zone 3 demonstrates the same features and patterns already seen in Zone 3 of other welds with nominal parameters. Transformed Ti-6Al-4V composes the matrix, and again, globules of

β21S that have separated from the primary fin in the mixing zone are being broken up and turbulently mixing into the Ti-6Al-4V. Diffusive mixing of the two alloys creates multiple transitions in scale and density of α-platelets

Discussion

Weld 7 is on the warmer side of the nominal process window, and shows similar characteristics to other warmer welds in the macrostructure, shown in **Figure 5-35**. Defects have decreased compared to other nominal welds, putting Weld 7 more in line with that of Weld 2 in terms of macrostructure. The primary β21S fin is very stable and again shows how sawtooth features propagating down the fin are the likely contributor to the periodicity and size of globules that break from its tip in the advancing side of the weld nugget.

The microstructure, seen in **Figure 5-37**, shows features that more consistent with higher travel speeds, with an increase in diffusivity that can be attributed to the relatively fast spindle speed of 325RPM [Edwards, 2010b]. Recrystalization is present throughout the microstructure, as evidenced by equiaxed prior beta grains, although there is still incomplete grain growth and homogenization of the structure seen [Boyer, 1994][Prasad, 1998][Brun, 1998]. High heat also has appeared to have coarsened the platelets of the widmanstatten-α in Zone 1, in addition to a level of banding and interfacial mixing not seen in any other weld parameters. The hybrid grains across multiple microstructure bands, combined with etch effects and alpha particle morphology suggests that instabilities between the initial interface of Ti-6Al-4V and β21S evolved and diffused to create a discrete layer with a unique chemistry, which again formed instabilities at its interfaces and evolved yet more discrete bands of microstructure and chemistry. Similar behavior is observed in Zone 3, although the structure and banding is much more consistent with that of

Zone 3 in other welds and implies that similar mechanisms are at work to create more turbulent and diffuse chemistry and microstructure banding, as well as the more orderly layered striations of Zone 1.

5.6.8 Weld 8 – 150RPM/125mm/min

Results

Micro CT scans of Weld 8, shown in **Figure 5-38**, represent the coldest set of weld parameters achievable without overloading the machine and forcing shut down. A large and inconsistent set of defects is seen in the advancing side root stir zone of the weld, varying in location, size and number throughout the length of the weld. The macrostructure features are stable and consistent through the length of the weld. The primary β21S fin, although smaller in volume than other welds, oscillates regularly to generate the sawtooth features that then break up and dissolve in to the root of the weld. The amplitude and aspect ratio of the teeth are low and far fewer fine-scale mixing features are present in the root of the stir zone.

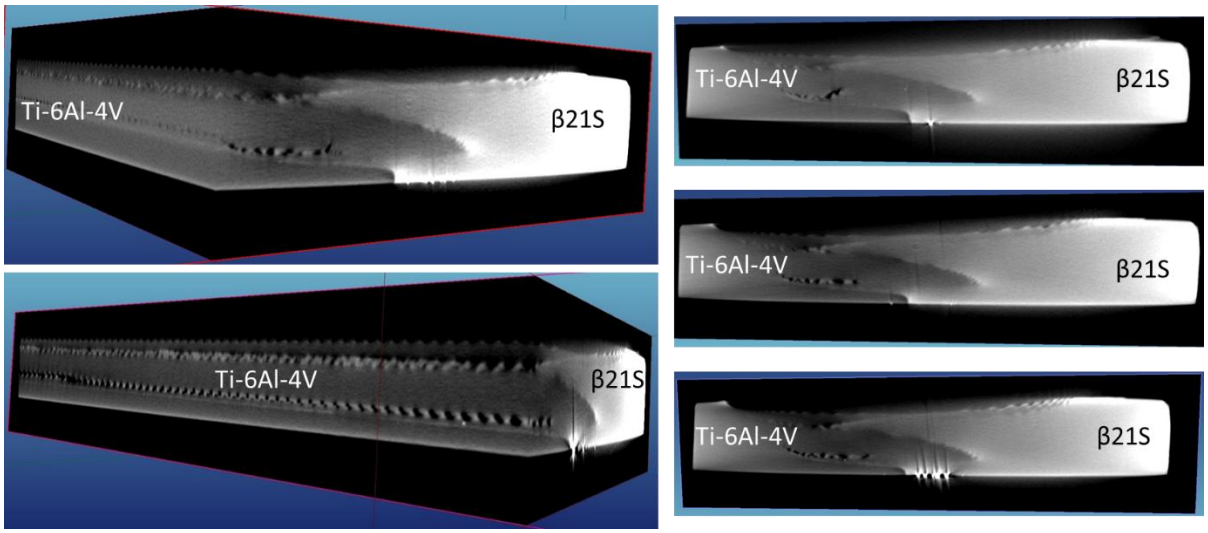

Figure 5-38: Weld 8 micro CT scans. Y-Z/X-Z ¾ (retreating/weld travel direction facing) views on the left, Y-Z (weld travel direction facing) views on the right.

The effect of such cool weld parameters can be seen in the machine load data, presented in **Figure 5-39**. Positive spikes in the X and Y forces show a decrease in defects, followed by a smooth transition to lower overall loads and an increase in defect concentration. Throughout the weld, even with the distinct change in defect concentration, the periodicity of the defects and sawtooth remain in-tact and represented in the X and Y loads.

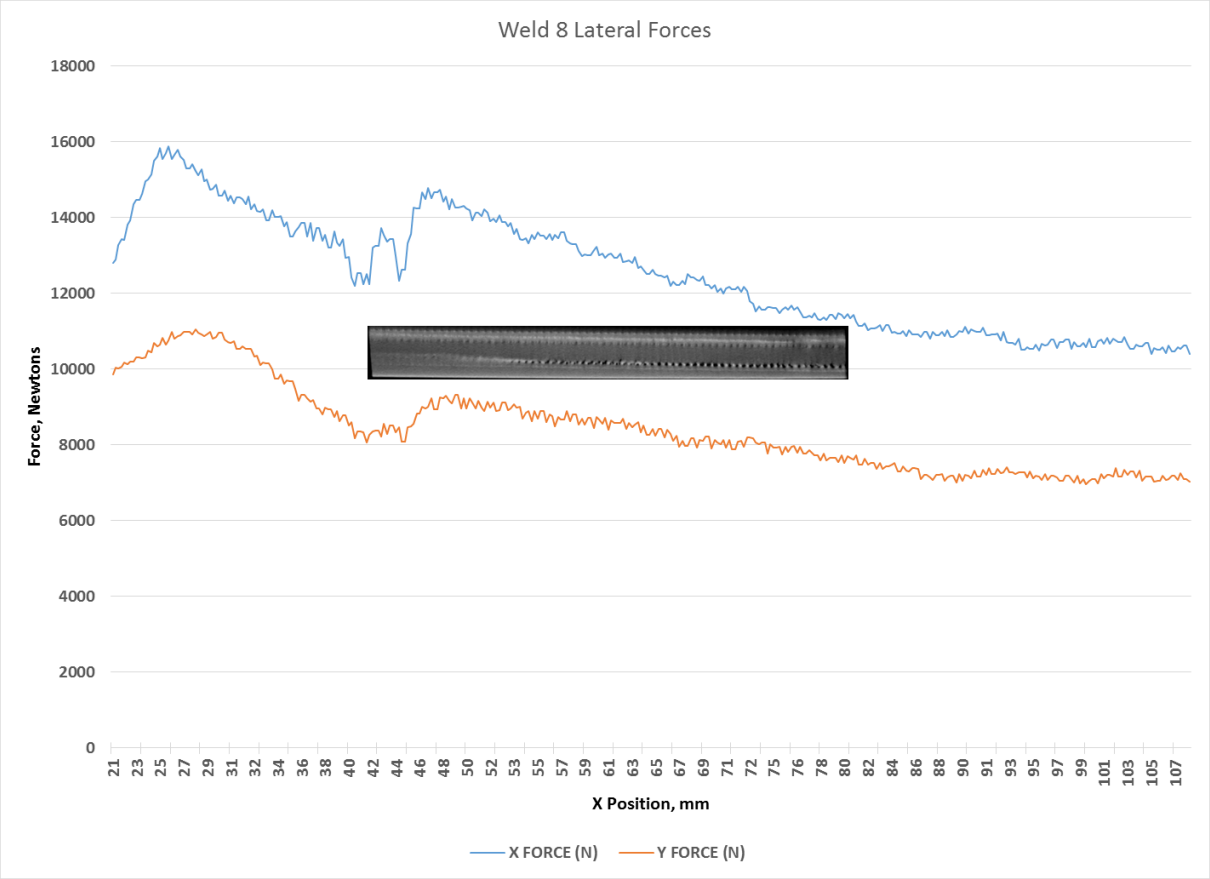

Figure 5-39: Weld 8 lateral forces, shown relative to X-Z (advancing side facing) view micro CT scan.

The microscopy for Weld 8, shown in **Figure 5-40** shows several distinct features not seen in nominal parameter welds. The macrostructure has familiar features as welds produced at nominal conditions, however there is a distinct lack of penetration at the root of the weld, and a larger volume of defects in the advancing side of the weld that move closer to the center of the

weld nugget than other welds. The same characteristic β21S fin is present, as is the top layer of Ti-6Al-4V, however, the β21S fin does not have the same periodic saw tooth pattern of the edges of the root side that the hotter weld conditions show. The heat affected zone is notably more narrow than other conditions and the alpha structures in the Ti-6Al-4V portions of the weld nugget are generally fine in scale. Banded, fine scale mixing at the root of the weld is irregular, and tortured eddies can be seen rising into the center of the stir zone and pushing into the weld defects.

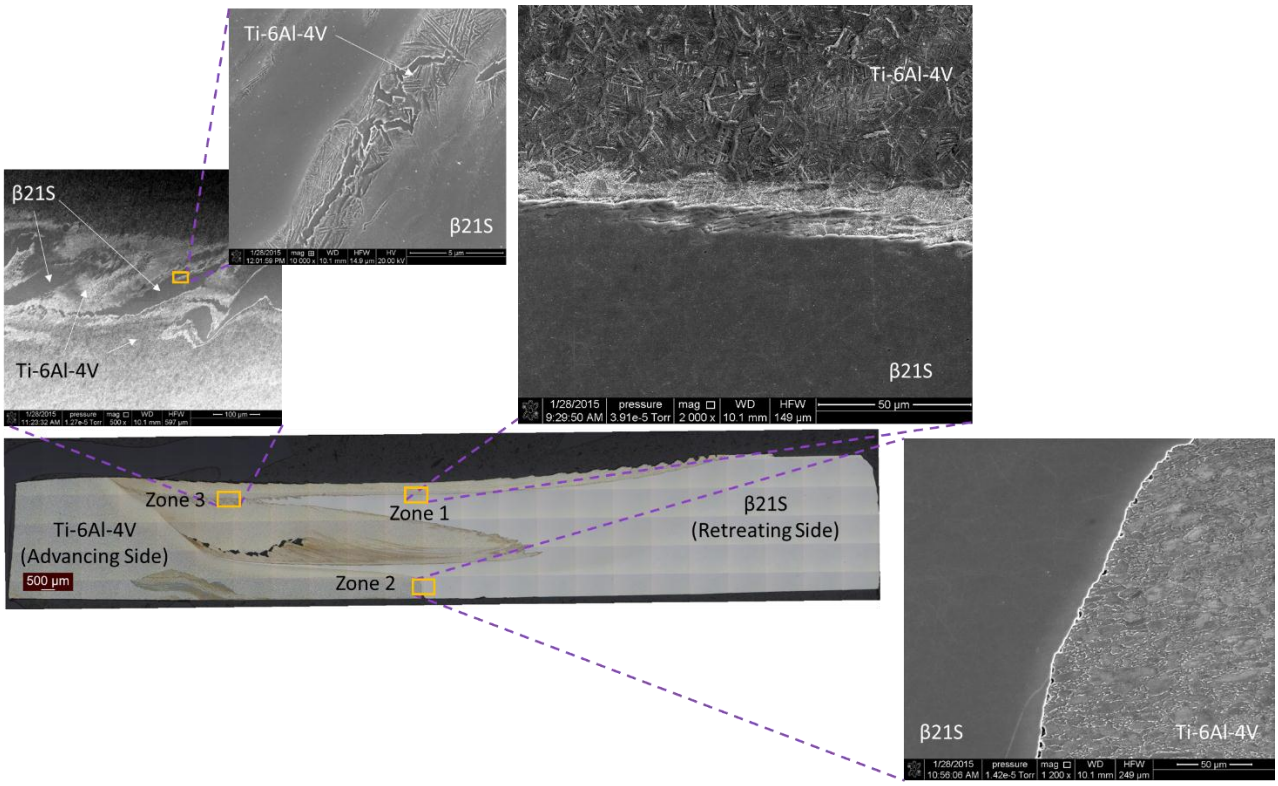

Figure 5-40: Weld 8, Ti-6Al-4V (Advancing side)/β 21S(Retreating side), 125mm/min, 150RPM, montage of 138 100x magnification micrographs, with SEM images of various magnification showing regions of interest.

Zone 1 shows microstructure features very similar to that of welds with more nominal parameters. Well-equiaxed prior-β grains on the order of 20 microns dominate the Ti-6Al-4V region, with no globular primary-α present. Ligands of Ti-6Al-4V are being sheared into the β21S region, with evidence of hybrid grains in the finer ligands.

Zone 2 demonstrates the expected root structure of a very cold friction stir weld. The Ti-6Al-4V has retained its globular primary-α and mill-annealed duplex microstructure. The bonding with the β21S is incomplete, with multiple defects along the interface demonstrating and overall lack of penetration in the weld root. There are no discernable microstructure features along the interface showing deformation.

Although Zone 3 shows similarly complex mixing macrostructure to Zone 3 in other welds, the finer features shown a higher magnification have not yet been discussed. Ligands of Ti-6Al-4V that have penetrated the β21S globules have a transformed widmanstatten-α structure that is present on multiple length scales. The largest α particles are sub-micron in width, and as proximity to β21S decrease, so does the width of the α platelettes. In some cases, the interface with the β21S becomes diffuse and indistinguishable, while in other cases the boundary between the two alloys is distinct.

Zone 3, shown as an EDS map in **Figure 5-41**, shows the complex mixing structure with eddies and instabilities that were seen in Weld 5. Directionality can also be seen in the map, where sharper chemistry transitions are observed on the right side of the β21S features, and more turbulent, diffuse structures are seen on the left.

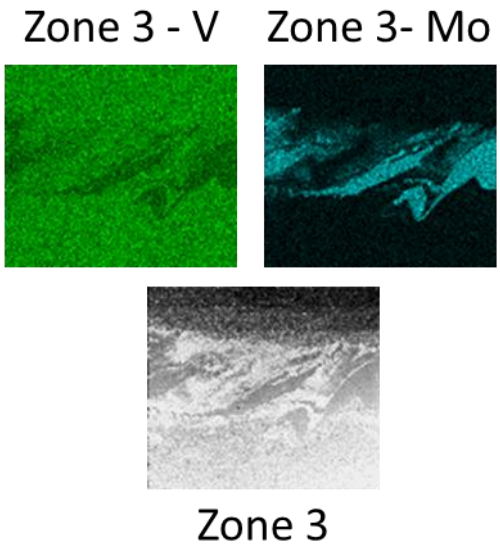

Figure 5-41: Weld 8, Zone 3, EDS Map for Mo and V.

Discussion

The cold parameters of Weld 8 yield macrostructure and microstructure features that are consistent with low heat input. A very large volume of defects if present, seen in the macrostructure views of **Figure 5-38**, and propagate into the center of the weld nugget to a position not observed in any other weld condition [Edwards, 2010b][Edwards, 2010c]. Similarly, the lack of heat and difficulties that presents in flowing metal can be seen in the force plots, where the magnitude of forces is much higher than other welds. Magnitude notwithstanding, force plots remain a useful tool in assessing shifts in mixing and defect formation, and a steady decrease in X and Y forces correlates well to a shift in the position and volume of defects.

Microstructurally, the cold parameters shows expected trends, and features have not coarsened to the extent of warmer welds. Zone 1 still shows evidence of super-transus heating, and the Ti-6Al-4V is fully transformed. Recrystallization is also apparent in the weld nugget, and grain sizes represent the lower end of what has been observed, consistent with a lack of heat to assist in post-nucleation grain growth [Boyer, 1994][Prasad, 1998][Brun, 1998][Pilchak, 2007].

Hybrid grains are present, demonstrating that the process is closely tied to nucleation rather than higher temperature diffusion or grain growth processes, and single beta grains can be seen forming to consume multiple ligands of disparate chemistry in Zone 1 [Abbaschian, 1991]. As would be expected, Zone 2 shows lack of fusion and defects [Edwards, 2010c], with the Ti-6Al-4V retaining its mill annealed duplex structure with elongated primary alpha with no evidence of deformation. Higher magnification views in Zone 3 provide evidence that the breakup and intermixing of the two alloys occurs in similar fashions (both by mechanical stirring and interface instability and by diffusion) at macro- and micro-length scales. The same inconsistency in the nature of the transition between alloys can be seen at very fine length scales, mimicking that seen at lower magnification in all zones with complex mixing.

Even with the colder parameters that were selected, there is still adequate heat to create diffusively mixing structures. EDS mapping of Zone 3 presents evidence of the higher temperature Ti-6Al-4V from the advancing side pulling and redistributing Molybdenum much more effectively than the β21S is able to intake Vanadium. Areas that show etch effects and microstructure transitions still have a nearly undisturbed base of Vanadium present from the parent Ti-6Al-4V, showing that the Ti-6Al-4V is behaving like a solvent and absorbing the β21S as it is broken down by mechanical mixing and diffusion [Hendricks, 1968].

5.6.9 Weld 9 – 275RPM/125mm/min

Results

The macrostructure of Weld 9, shown in **Figure 5-42** using micro CT scans, shares the same parameters as Weld 5, but with the spindle rotation reversed, placing the Ti-6Al-4V on the retreating side. While a primary β21S fin is still present in some sense, it is far less regular. There are still oscillations that lead to waves and sawtooth features, although their scale is an

order of magnitude larger than is seen in other welds and their periodicity and amplitude is far less consistent. Also of note is the lack of defects, whereas Weld 5 had a significant array of defects in the advancing side root stir zone.

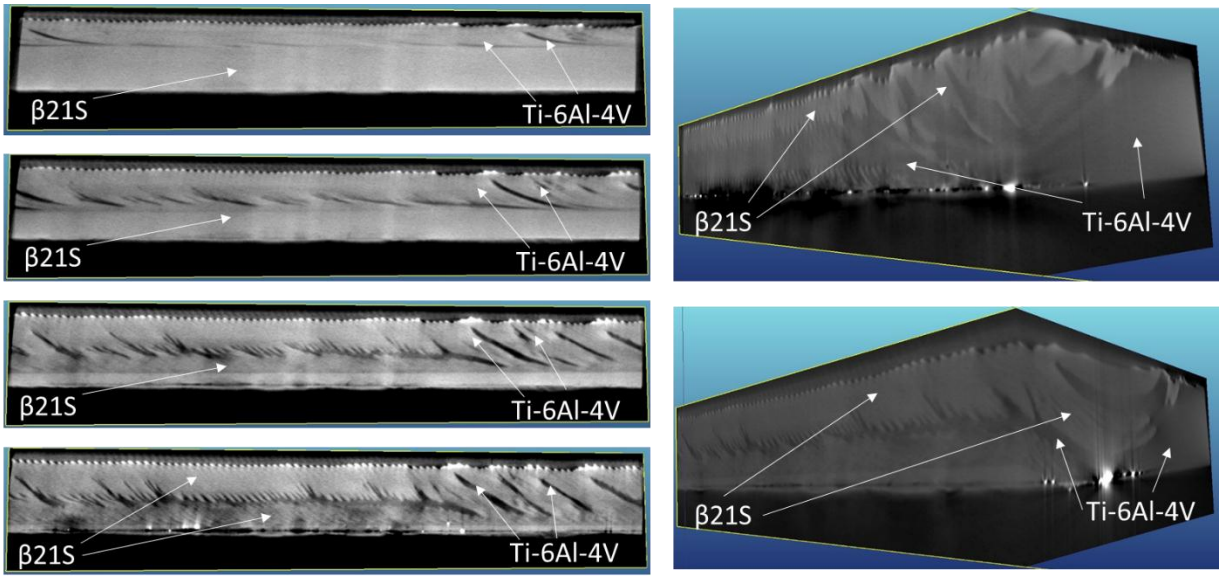

Figure 5-42: Weld 9 micro CT scans. X-Z (retreating-facing) views on the left, Y-Z/X-Z ¾ (retreating/weld travel direction facing) views on the right.

Regardless of the fundamental differences in macrostructure, machine loads, shown in **Figure 5-43**, still correlate well. A regular sawtooth pattern is present in the primary stir zone, albeit of a vastly different character than welds that contain Ti-6Al-4V on the advancing rather than retreating side. In the regions where this sawtooth pattern is stable, so too is the periodicity and amplitude of the force variations in the X and Y axis. The widely spaced swaths of β21S correlate well with larger, periodic spikes in X and Y forces as well, representing a new scale of macrostructure feature being represented in the force plots. The complexity of the stir zone makes direct correlations to forge loads difficult, and no defining features in the macrostructure could be identified that matched the shifts in forge loads over the imaged length.

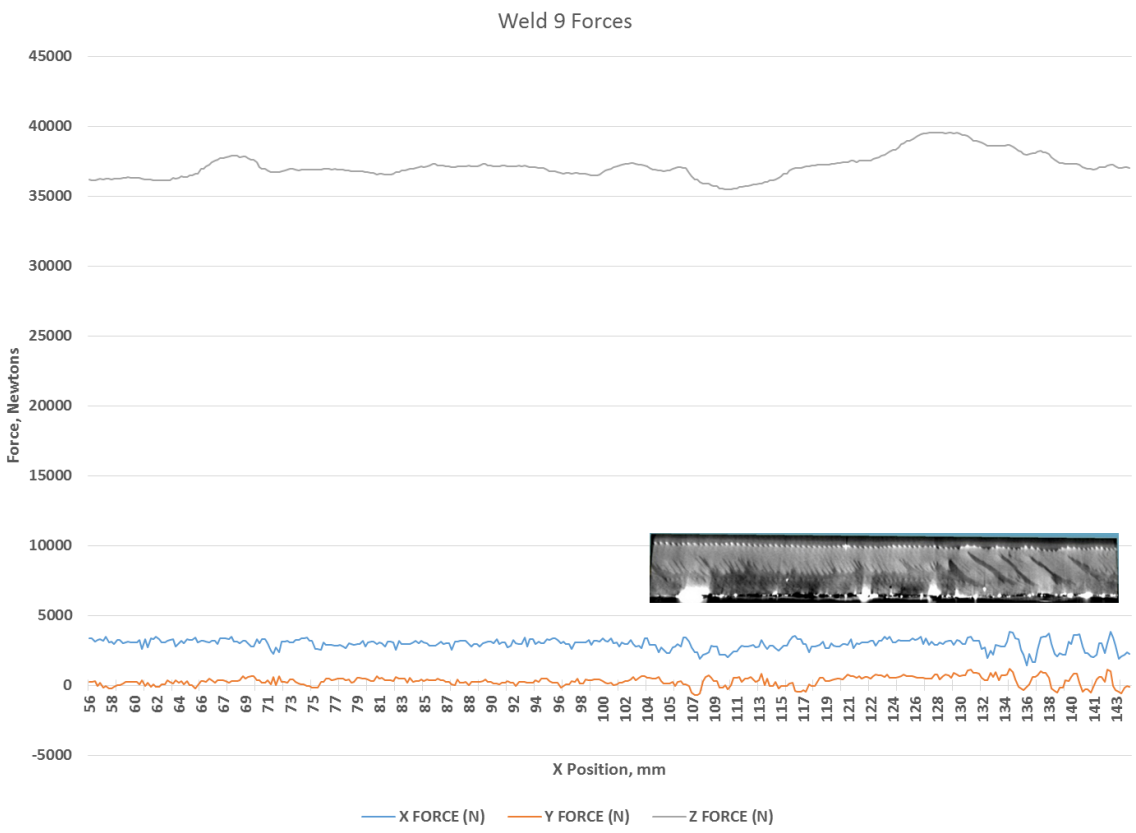

Figure 5-43: Weld 9 lateral forces, shown relative to X-Z (advancing side facing) view micro CT scan.

The microstructure of Weld 9, shown below in **Figure 5-44**, continues to show that the nominal parameters identical to that of Weld 5 can produce drastically different results depending on which alloy is on the advancing or retreating side. The β21S fin seen in all other welds is now replaced by a highly irregular array of large masses of β21S conforming somewhat to the shape of the weld nugget intermixed with similarly sized masses of Ti-6Al-4V. The β21S masses are concentrated on the advancing side and the top half of the weld nugget, with a more turbulent and fine mixing pattern shown near the root of the advancing side. The weld is full-penetration, with no evidence of defects – in stark contrast to the large concentration of defects seen in Weld 5. Equiaxed structure is still present throughout the weld, as is a refined alpha structure in the Ti-6Al-4V, showing both globular alpha as well as widmanstatten-α throughout the weld nugget.

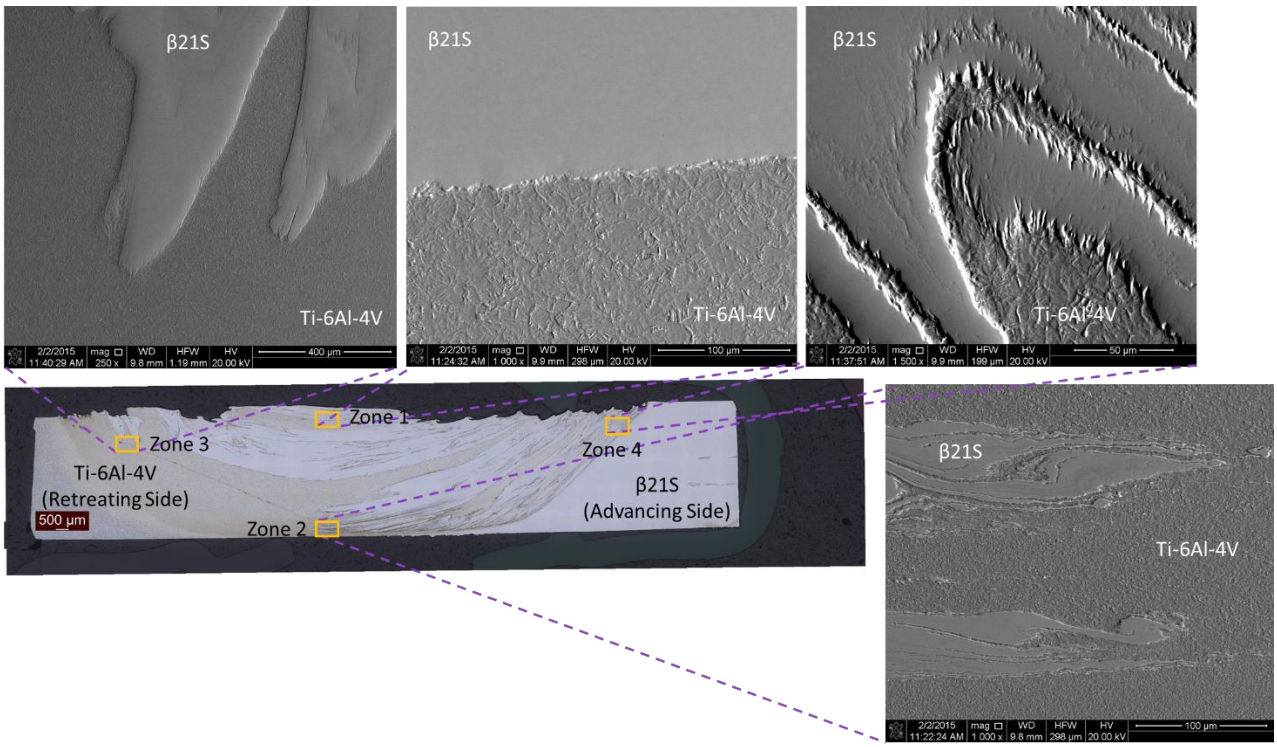

Figure 5-44: Weld 9, Ti-6Al-4V (Retreating side)/β 21S(Advancing side), 125mm/min, 275RPM, montage of 138 100x magnification micrographs, with SEM images of various magnification showing regions of interest.

The Ti-6Al-4V in Zone 1, now on the retreating side, still shows transformation largely to widmanstatten-α structure, although with blocky, globular features that appear to be remnants of primary-α. The interface between the two alloys is largely devoid of the diffusion-related microstructural features seen in the other welds, while the interface itself is jagged and blocky, rather than smeared with ligands and perturbations in the case of the other welds.

Zone 2 shows features again not seen at the root position in other welds. Ligands of β21S are becoming unstable, breaking up and creating swirled globules, as has been seen in Zone 3 of other welds. In this case, however, the matrix of Ti-6Al-4V is refined and has still retained its primary-α and there is not the complexity of microstructural feature transitions seen in similar Zone 3 features.

In Zone 3, we now see interpenetrating swirls of β21S and Ti-6Al-4V, again without the clearly transformed widmanstatten-α structure of other welds. The primary β21S ligands show jagged, tortuous interfaces with the Ti-6Al-4V. Fine, jagged ligands of Ti-6Al-4V appear to be penetrating the primary β21S features, although the two alloys remain largely in-tact. In comparison, Zone 4 on the advancing side of the weld shows similar features to that of Zone 3. Large pieces of β21S have a jagged, sheared interface with the Ti-6Al-4V which again has retained its primary-α.

Looking at Zone 4 using EDS mapping, shown in **Figure 5-45**, shows much different chemical mixing profiles than has been seen on the turbulent advancing sides of all other welds. With no finer scale eddies to dissolve into the matrix, there is very little discernible chemical mixing, and the structure is still dominated by the jagged, shearing breakup of the β21S features.

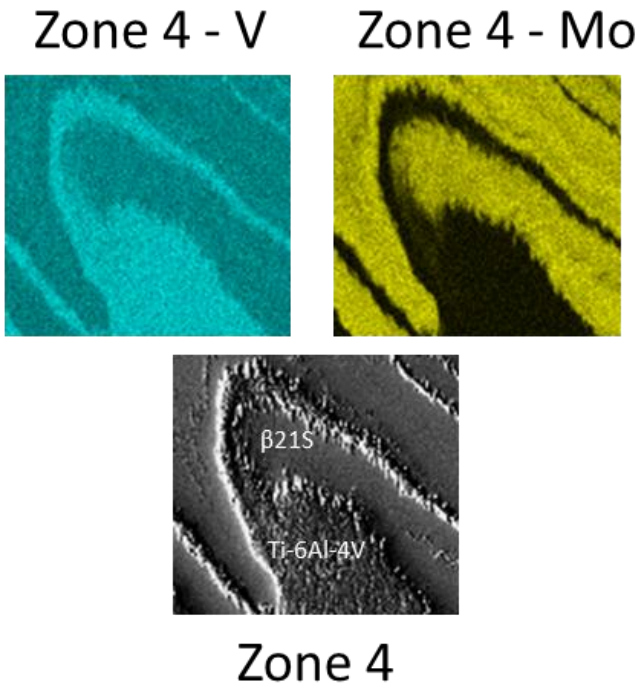

Figure 5-45: Weld 9, Zone 3, EDS Map for Mo and V.

Discussion

In Weld 9's macrostructure, seen again in **Figure 5-43**, quite clearly there is a fundamental shift in how the macrostructure is formed compared to the other 8 welds containing Ti-6Al-4V on the advancing side. The advancing side of the pin has been shown to present larger strains [Buffa, 2006b][Buffa, 2013], and this appears to break up the β21S before it is pulled through to the retreating side and extruded into the tool wake far more effectively than has been seen in other welds [Fonda, 2013]. The notable lack of defects seen in the macrostructure, in contrast with the defects of Weld 5, shows that obtaining a high quality FSW joint is not merely a matter of heat input, but rather the heat input of one side of the weld versus the other, combined with strains, and the particular materials response to that heat and deformation. The softening behaviors of Ti-6Al-4V and β21S at high temperature and high strain rates are different enough that that the differing thermomechanical conditions presented by the advancing and retreating side of the pin cannot be overlooked when choosing weld parameters for a dissimilar titanium weld combination [Seshacharyulu, 2000][Weiss, 1998].

The microstructure in Weld 9 has also changed quite dramatically, seen in **Figure 5-44**, where Zone 1 shows recrystallization throughout, although traces of retained primary alpha in the Ti-6Al-4V suggest temperatures below the beta transus [Boyer, 1994]. Primary alpha in Zone 1 has not been seen even in the coldest parameters where Ti-6Al-4V is on the advancing side, and highlights the disparity in thermomechanical condition presented by the advancing and retreating side of the pin. Zone 2 also shows retained primary alpha in the Ti-6Al-4V, but differing from the other welds, the primary alpha is retained into the stir zone. As is expected, the fine grain size and equiaxed structures are evidence of heavy dynamic recrystallization in the root of the stir zone [Brun, 1998][Prasad, 1998]. Zone 3 is again rather different than any other

weld condition, and the β21S ligands appear to have been sheared heavily, evidenced by the sharp, jagged interfaces with the Ti-6Al-4V, although this effect is likely exaggerated by the relief effect from the acid etching during sample preparation. There is little to no etch contrast effect, which is taken to mean that minimal diffusive mixing has occurred, a notion that is supported by EDS mapping in Zone 4, where sharp delineations between the base materials are still present.

5.7: Summary of Results and Conclusions

The experimental matrix carried out and reported in Chapter 5 used a wide set of process parameters, and in turn created a variety of thermomechanical profiles throughout the stir zone of each weld nugget. Features of note from each weld are summarized in **Table 5-3**, and is followed by discussion of key processes that give rise to the features observed in the experiment.

Table 5-3 Summary of key macro and microstructure observations from Ti-6Al-4V to β21S FSW test matrix.

Weld	Process Notes	Macrostructure Notes	Microstructure Notes
1	600 RPM/75 mm/min – Ti-6Al-4V Advancing Side Very hot. High rotation and low travel speed.	Full penetration, turbulent features throughout. Erratic primary β21S fin breakage.	Well-recrystallized throughout; grain growth in Zone 1. Hybrid grains. Complex and varied chemistry gradients.
2	400 RPM/125 mm/min – Ti-6Al-4V Advancing Side Hot. High rotation speed.	Low defect density. Periodic primary β21S fin instabilities grow to generate finer features.	Banded chemistries in Zone 1 & Zone 2. Distinct hybrid grains. Sheared eddies generate diffuse chemistry in Zone 3.
3	225 RPM/100 mm/min – Ti-6Al-4V Advancing Side Nominal - Cool. Low rotation speed.	High volume of periodic defects. Irregular β21S fin instabilities produce lesser degree of mixing.	Untransformed root and HAZ. Banded chemistry in Zone 1.
4	275 RPM/100 mm/min – Ti-6Al-4V Advancing Side Nominal.	Regular β21S fin with periodic instabilities generate fine features. Eddies throughout advancing and retreating side generate mixing.	Recrystallized, turbulent banding in Zone 1. Sub-transus recrystallization in Zone 2.
5	275 RPM/125 mm/min – Ti-6Al-4V Advancing Side Nominal.	Pervasive sawtooth instabilities on β21S fin. Linear array of periodic root defects. Eddies throughout.	Recrystallized stir zone; untransformed root. Continuously evolving Zone 3 chemistry based on eddie dissolution
6	275 RPM/150 mm/min – Ti-6Al-4V Advancing Side Nominal - Cool, High travel speed.	Perturbations propagate instabilities as sawtooth waves through β21S fin, breaking free into finer features.	Finer recrystallized Zone 1; very narrow banding. Interpentrating β21S ligands in sub-transus recrystallized in Zone 2.
7	325 RPM/125 mm/min – Ti-6Al-4V Advancing Side Nominal – Warm. High rotation speed.	Low defect volume. Nominal instability propagation and separation from β21S fin. Eddies throughout.	Complex, multi-layered bands in Zone 1. Well-recrystallized; multiple hybrid grain styles.
8	150 RPM/125 mm/min – Ti-6Al-4V Advancing Side Cool. Low rotation and travel speed.	High defect volume. Jagged, irregular interface instabilities on β21S fin. Lack of penetration.	Fine recrystallized structure; fine, turbulent bands in Zone 1. Small hybrid grains. Eddy break up with small scale diffusion in Zone 3.
9	275 RPM/125 mm/min –β21S Advancing Side Nominal.	Complex, interpenetrating ligands of both alloys throughout stir zone. Irregular macro features. Low defect volume.	Sub-transus recrystallized Ti-6Al-4V throughout. Smooth interface in Zone 1, eddies in Zone 2 and jagged, sheared ligands in Zone 3 and 4. Finer scale chemistry gradients.

Material Flow

The flow patterns observed in the macrostructures of each weld show trends that can be better understood in context of the flow stresses of the two alloys relative to one and other and the variations of strain rate in the stir zone. Data for Ti-6Al-4V is readily available due to the ubiquity of the alloy in industry [Seshacharyulu, 2000], however, β21S is much less studied and complete flow stress data is not publicly available. An appropriate analogue is Ti-15Mo-3Cr-3Sn-3Al, being a high-strength near-beta alloy with a heavy Molybdenum composition. This data set is still far less comprehensive, but none the less allows for trends to be established [Weiss,

1998]. Shown in **Figure 5-46**, the flow stress for Ti-6Al-4V drops off dramatically as it heats through the β-transus temperature (980°C nominally) [Boyer, 1994], while the Ti-15-3-3-3, with and much lower transus temperature [Boyer, 1994] and without such a dramatic shift in phase composition upon transformation, exhibits a smoother softening curve and maintains a flow stress 100Mpa higher than Ti-6Al-4V at 1100°C.

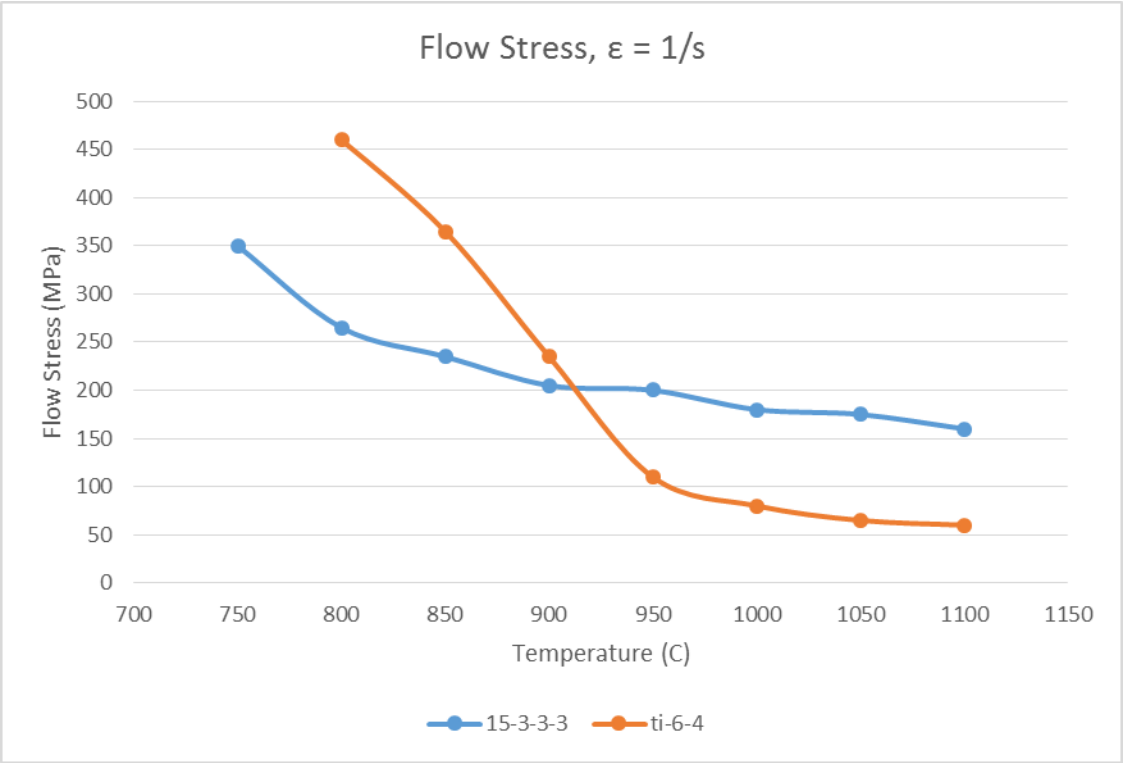

Figure 5-46: Flow stress of Ti-6Al-4V and Ti15-3-3-3 at a strain rate of 1/s (replot of data from [Seshacharyulu, 2000] and [Weiss, 1998]).

Curves such as those presented in **Figure 5-46** are generated by and widely used by the metal working industry, where strain rates less than 1/s are common, and temperatures are largely homogenous throughout the work piece [Weiss, 1998][Weiss, 1999]. Modeling of FSW processing shows a wide variety of strain rates depending on tool and parameters selected, as demonstrated in **Figure 5-47** [Buffa, 2006b]. This modeling work is useful to identify trends in behavior, and significant differences exist between the modeled parameters and those used in the

current experiment: the modeled work piece was 1mm thick 7075 Aluminum alloy, with a 1000RPM pin rotation speed an various travel speeds. The pins used in this current work are much larger to accommodate the thickness of the work piece and parameters are selected for the titanium materials in use, but it can still be established due to established deformation mechanisms of the FSW process, that the 35° pin angle imparts high strain rates universally and a higher degree of strain rate localizations than is seen in tools with shallower angles.

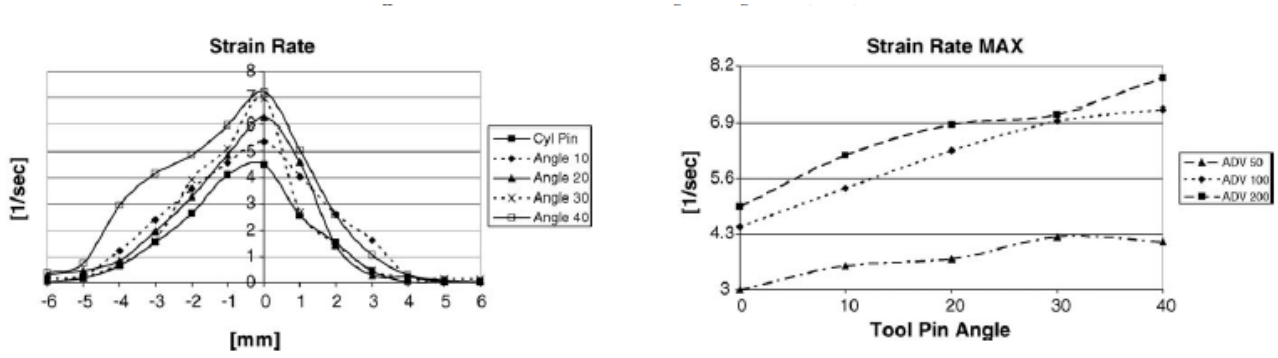

Figure 5-47: Strain rate distribution in a X-Z section at various pin angles (left) and maximum strain rate versus pin angle (right) [Buffa, 2006b].

In highly dynamic processes, it is beneficial to consider the effect of strain rate's effect on flow stress and present the data in terms of dynamic viscosity. Using the relationship $\mu=\sigma/2\dot{\varepsilon}$, flow stress data can be plotted as dynamic viscosity, seen in **Figure 6-3.** This data shows that as strain rates move beyond 1/s, the strain rate term begins to dominate the flow behavior more so than the inherent flow stress of the base material [Lee, 1998], which can serve to mitigate flow stress difference between dissimilar materials when both are subjected to high strain rates. With the varied strain rates predicted through a weld nugget, different zones of the weld nugget will tend to favor a description of material flow based on temperature and flow stress seen in **Figure 5-46** or a description dominated by strain rate effects and dynamic viscosity, as in **Figure 5-48**.

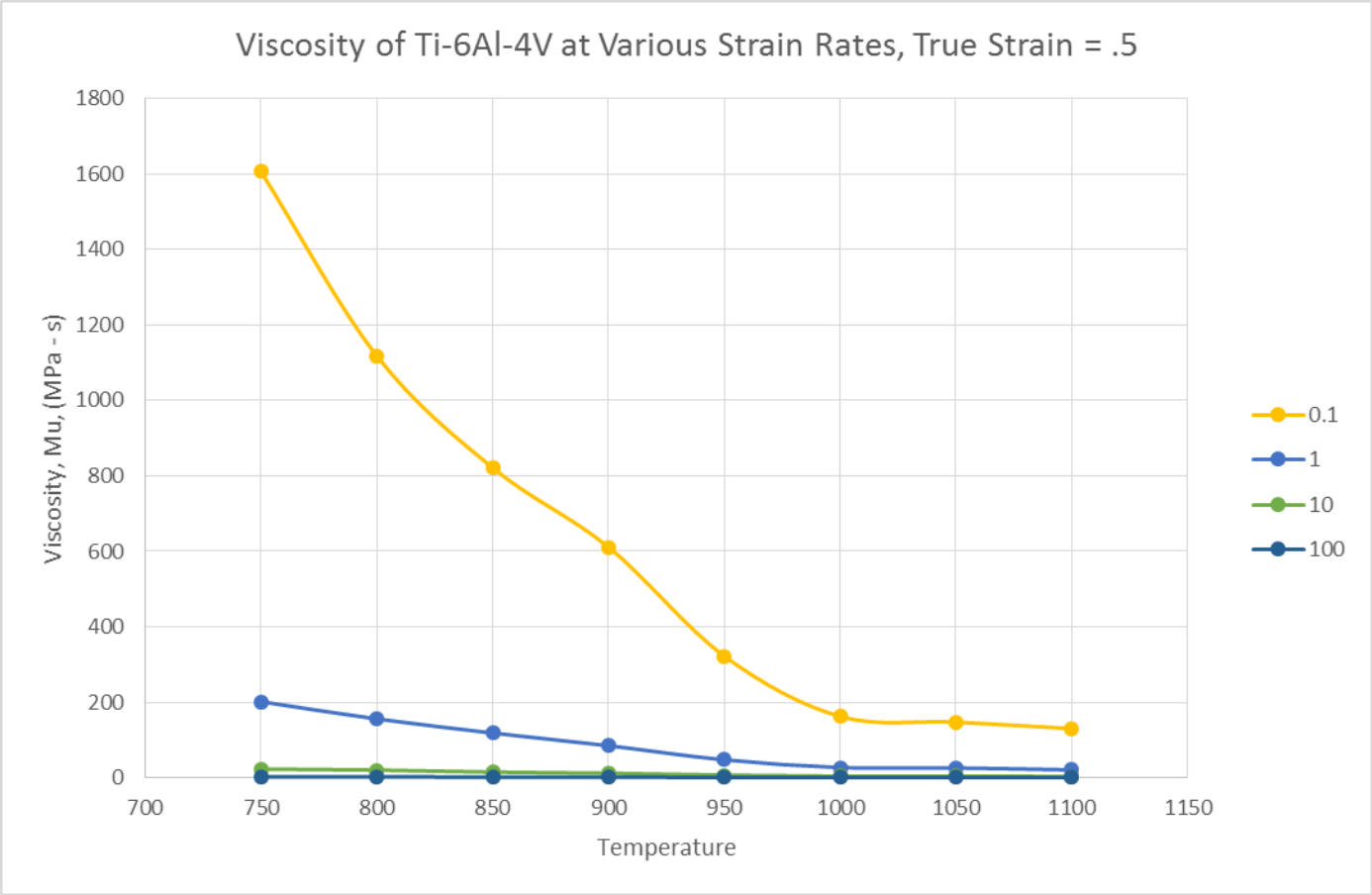

Figure 5-48: Dynamic viscosity of Ti-6Al-4V at various strain rates (replot of data from [Lee, 1998]).

There does not currently exist a direct measurement or reliable modeling of the specific process parameters in this experiment for temperatures or strains within the weld nugget, however, the evidence left in the form of the macrostructure and microstructure combined with understanding of material flow characteristics still allows for a reasonable description of the evolution of the interface between Ti-6Al-4V and β21S at several key locations [Buffa, 2006b][Fonda, 2013][Prasad, 1998][Boyer, 1994][Tamirisakandala, 2003]. In the case of welds 1 through 8, at the hottest, highest strain portion of the welds (Zone 1) [Buffa, 2006a], the advancing Ti-6Al-4V undergoes higher strain rates, heating well beyond its beta transus as it interfaces with the β21S. High strain rates serve to lower the dynamic viscosity of β21S

dramatically as well, minimizing the inherent difference in flow stresses at higher temperatures and making them more readily intermixed. A gradient of strain rates through the top regions of the weld nugget create shear flows of different velocities throughout the weld nugget, which accompanied by a density gradient and the perturbations provided by pin oscillations, gives rise to the often complex and fluid-like interfaces and structures. As the fluid-like interface instabilities evolve into a turbulently mixed band, diffusive mixing at the chemical scale eliminates sharp, prior interfaces between the two alloys in this turbulent zone and a unique chemistry band, with its own composition (and flow characteristics), is formed between the Ti-6Al-4V and β21S. Given time, depending on the process parameters selected, this new band of unique material will continue to interact with the strains and temperatures generated by the pin in this prescribed fashion, creating new complex fluid-like interfaces and evolving more unique chemistry bands, demonstrated by Zone 1 of Weld 1 (**Figure 5-9**) and Zone 1 of Weld 7 (**Figure 5-37**).

In areas of the weld nugget that still present high strain rates and temperatures, such as Zone 3, but to a lesser extent than the maximums seen at Zone 1, variations on this mechanism can be seen as local conditions change. As strain rates lower, the differences in flow stress are more apparent and the softer, more fluidic flows of Ti-6Al-4V tend to break up the larger more monolithic globules of β21S. At this point, the smaller pieces of β21S can readily dissolved and incorporated into the turbulent Ti-6Al-4V matrix.

On the colder, root of the weld, areas outside of the pin's engagement are reliant on the hydrostatic pressure of the stir zone metal and heat transfer to satisfy any conditions necessary for micro or microstructural evolution. In the cases of colder welds such as Weld 3 and 8, the base microstructure is present outside of the stir zone, as there is not sufficient heat to exceed the

β-transus of Ti-6Al-4V nor is the material sufficiently hot to deform from forces imparted by the nugget above it [Boyer, 1994][Tamirisakandala, 2003]. Weld 4 reaches a point where enough heat is present to allow the root Ti-6Al-4V to deform, and the deformation is sufficient to generate dynamic recrystallization, leading for a very fine duplex microstructure. Weld 6 offers the same rotation speed, and while a faster travel speed presents cooler parameters, the higher strain rates from increased travel speed still allow the Ti-6Al-4V to be dynamically recrystallized and even lightly mix with β21S pressed in from the stir zone. As the heat increases beyond nominal parameters in the case of Weld 1 and Weld 2, the root becomes mixed solely by hydrostatic pressure, heat and internal friction with the stir zone.

The unique case of Weld 9, where β21S on the advancing side of the pin, can still be viewed in terms of strain rate effects on material softening in spite of its vastly different macrostructure from Welds 1-8. While the two alloys soften and flow in inherently different ways, the locally higher strain rates and temperatures of the advancing side serve to minimize this difference if the more difficult to deform alloy is place on the advancing side, as is the case of Weld 9. Still, the β21S does not appear to soften to the point seen in Ti-6Al-4V when on the advancing side and thus the finer scale eddy formation and turbulence are absent throughout the weld. Additionally, the overall lack of transformed widmanstatten-α structure seen in the Ti-6Al-4V as compared to Welds 1-8 points to the fluidity and turbulence of the advancing side alloy's motion into the retreating side of the stir zone as a primary mechanism of evenly distributing heat throughout the weld nugget. While heat is still be present in the β21S as it moves from the advancing side to the retreating side, the overall lack of fluidity and tendency to break up and shear apart into larger globules and bands rather than generate fine scale turbulence works with the poor thermal conductivity of titanium to slow the heating and eventual transformation of the

retreating side Ti-6Al-4V as it comes into contact with the β21S. The smoother, more linear decrease in flow stress relative to temperature changes for β21S may also serve in keeping larger globules coherent through the weld process. As adiabatic heating in titanium at high strain rates can lead to local temperature spikes and banded structures due to local decreases in flow stress [Prasad, 1998][Lee, 1998], alloys with less pronounced drops in flow stress as temperature increases can resist this effect and maintain coherent macrostructures under severe thermomechanical processing more readily.

Kinetics and Recrystallization Behavior

Large variations in microstructure feature size can be seen within a weld nugget from the top to the bottom, which are best attributed to the unique combination of high strain rates, high temperatures and fast heating presented by the FSW process. Several weld conditions noted a change in grain size from the top to the bottom of the weld, while welds with very similar parameters provided measurably different grain sizes in the same zone. In **Figure 5-49**, shown below, a comparison of measured grain size between Weld 4 and Weld 6 can be seen. By increasing the travel speed of the pin by 50% at the same rotation speed, a reduction of grain size on the order of 65% is achieved. Even without reliable temperature estimates, it is not reasonable to assume that this is an effect of grain growth due to higher heat levels in Weld 4, considering that low travel speed parameters hot enough to degrade a refractory tungsten alloy pin in Weld 1 yield only incrementally larger grains of 30 microns in what is ultimately a heat driven, diffusion-limited process [Boyer, 1994][Abbaschian, 1991][Hendricks, 1962]. Instead, there must be a difference in the recrystallization behavior that leads to finer grain sizes at high travel speeds.

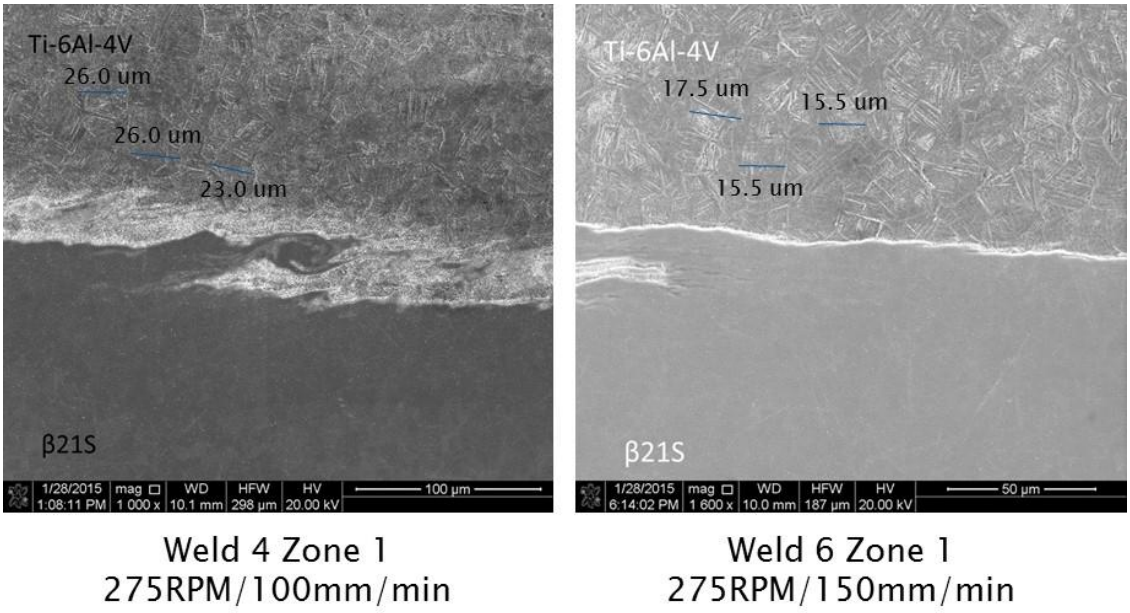

Figure 5-49: Comparison of Ti-6Al-4V grain sizes in Zone 1 of Weld 4 and Weld 6.

FSW is a unique process as far as its implications on kinetics in that it combines rapid heating, rapid cooling and severe deformation. Comparing alpha dissolution kinetics to measured weld thermal profiles, shown in **Figure 5-50**, gives rise to the possibility of heating to a temperature above the beta transus of the alloy, where it can absorb high strains, yet the dissolution of alpha particles lags behind the equilibrium composition. While in the process of dissolving, these alpha particles can still provide a large volume of heterogeneous nucleation sites that in the presence of high strain rates, refine grain sizes dramatically via dynamic recrystallization [Brun, 1998]. While dynamic recrystallization with a homogenous beta phase is possible, it is not recognized as a feasible route for grain refinement on the order seen in a FSW nugget [Brun, 1998][Prasad, 1998][Tamirisakandala, 2003].

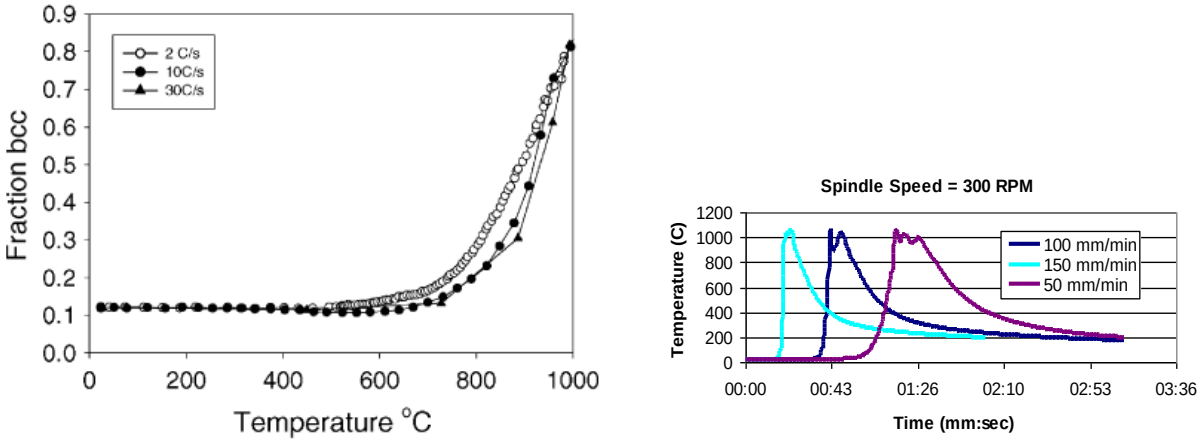

Figure 5-50: Ti-6Al-4V beta composition at various heating rates (left) and thermal profiles of various weld travel rates (right) [Elmer, 2005][Edwards, 2010b]

Comparing the kinetic data of Elmer and the in-process data of Edwards to the process parameters and microstructure data generated in the welds of Chapter 5 shows the proposed mechanism of a short window of super-transus alpha particle assisted dynamic recrystallization to be a viable. Shown in **Figure 5-51** is a simplified schematic of the tool geometry used in the present experiments with a plot that contains calculated dwell time of the root and shoulder over an arbitrary point at various travel speeds, plotted against actual dwell time data gathered from thermocouple experiments by Edwards. At high travel speeds, such as the 150mm/min speed of Weld 6, conservative estimates of heating rate to 1000°C would be on the order of 100°C/s - 200°C/s depending on location relative to the shoulder or tip of the pin, compared to rates of 75°C/s -100°C/s for a 100mm/min travel speed. This rapid heating rate, compared to data from Elmer, shows that there would be significant engagement with the pin (and the high strains it imparts) at the critical temperatures below approximately 925°C, before the exponential nature of diffusion overtakes heating rate effects and completely dissolves any latent alpha particles. During this time window, upwards of 20% additional volume fraction of alpha would be present over the equilibrium composition for a given temperature; the result of alpha particle dissolution

kinetics lagging equilibrium composition upon rapid heating rates. While all weld conditions with Ti-6Al-4V on the advancing side show evidence of super-transus heating, welds with cooler parameters and higher travel speeds gain additional grain refinement from this alpha dissolution kinetic advantage, before deformation and dynamic recrystallization in the homogenous beta phase serves to maintain existing grain size against coarsening due to heating [Brun, 1998][Prasad, 1998].

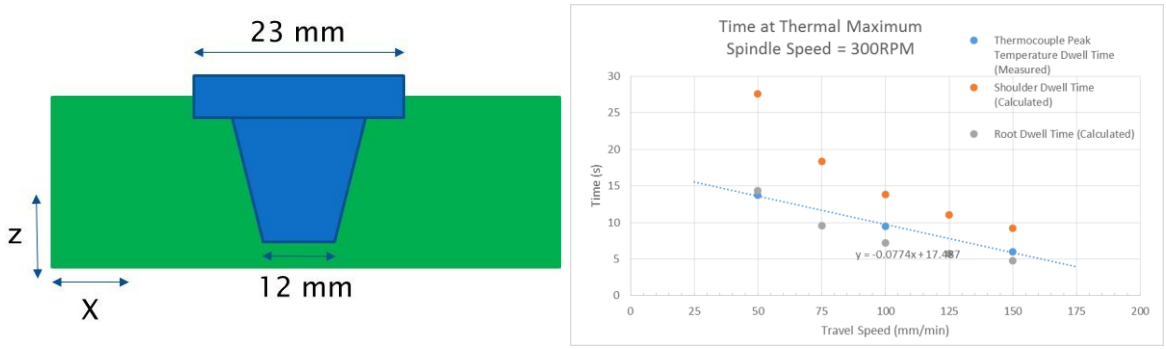

Figure 5-51: Schematic of FSW tool (left) with plots of calculated pin dwell time over a given location compared to measured thermal transients by Edwards (right) [Edwards, 2010b].

Hybrid Grain Formation

In Weld 2, where hybrid grains in Zone 1 were very pronounced, an additional sample was prepared for electron backscatter diffraction. Taking diffraction data from the beta phase in the β21S side and the alpha phase in the Ti-6Al-4V side of the grain separately, shown in **Figure 5-52,** shows a Burgers relationship between the two measurements. Alpha particle precipitation from the beta phase is limited to 12 variants that strongly follow a Burgers relationship to its parent beta phase [Boyer, 1994], illustrated in **Figure 5-53.** Therefore, the diffraction data confirms that the beta phase has identical orientation in the β21S and Ti-6Al-4V side of the hybrid grain. This crystallographically homogenous but chemically heterogeneous grain shows that the creation of the weld nugget microstructure cannot be viewed as an exercise in mechanical mixing followed by chemical diffusion on the atomic scale.

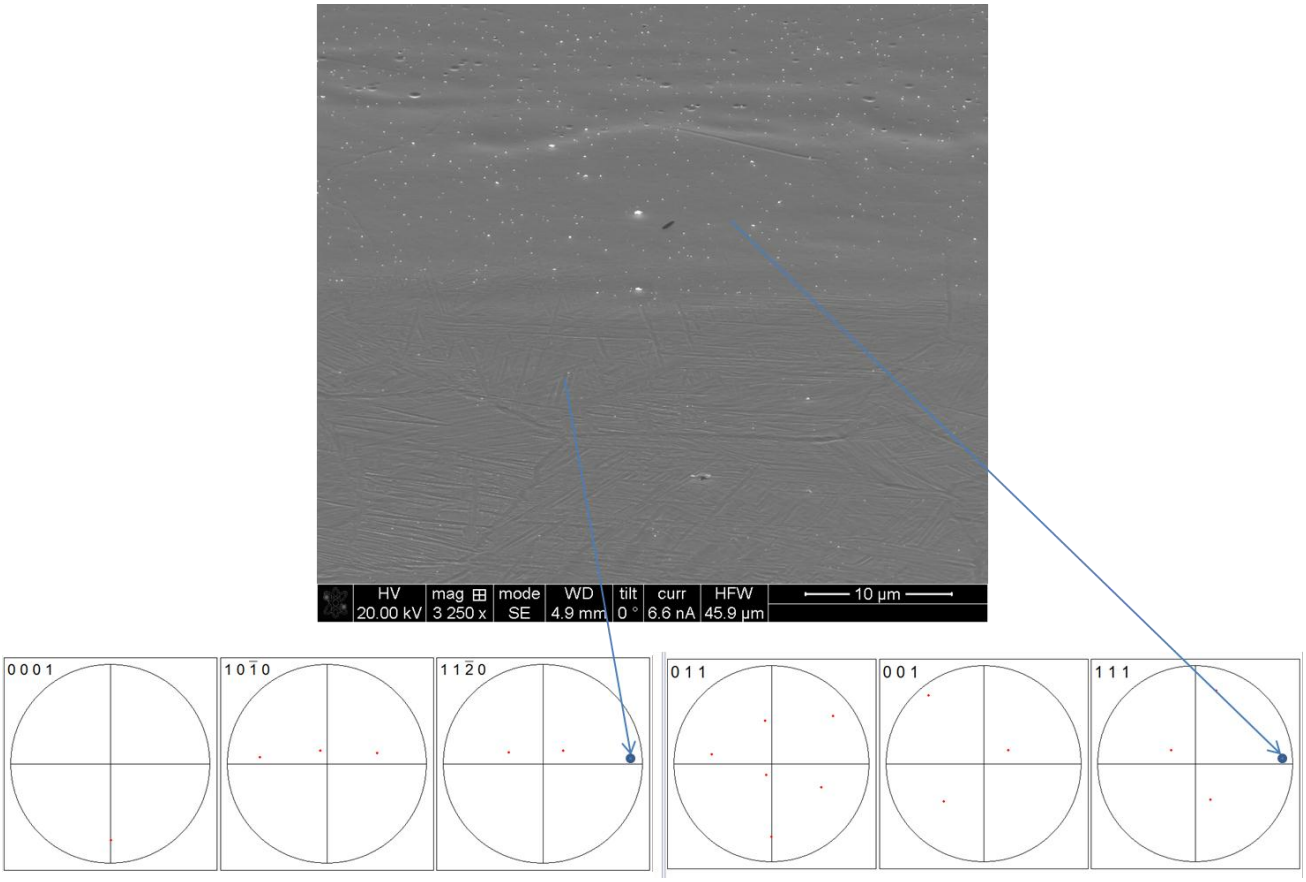

Figure 5-52: EBSD measurements at Zone 1 of Weld 2 of the beta matrix of β21S and a precipitated alpha particle of the Ti-6Al-4V in a hybrid grain.

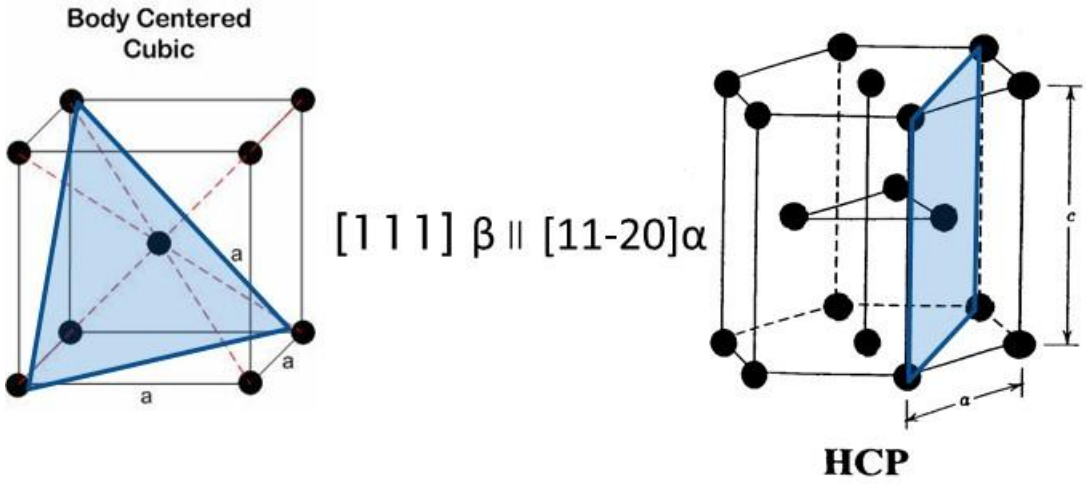

Figure 5-53: Illustration of a Burgers relationship between two planes in the HCP and BCC crystal structures.

The formation of the macrostructure, microstructure and interfaces in dissimilar titanium friction stir welding should be viewed as an iterative, multistep event of differing metallurgical transactions. Frictional heating from the pin rotation and translation softens the parent materials and allows for bulk material flow in the weld nugget and the creation of intimate contact between the alloys during the formation of macrostructures. During material flow, the two materials are deformed with strains and temperatures favorable for recrystallization of both, where fine-scale diffusionless nucleation events in bulk material and at dissimilar material interfaces serve to refine and unify the crystal structure and texture of the two alloys. Finally, heat drives atomic scale diffusion to grow grains and redistribute alloying elements between the two alloys that ultimately serves to define alpha particle morphology and distribution as they nucleate and grow upon cooling. The continuous interplay and iteration of these processes, as governed by the selected weld process parameters and the inherent properties of the parent materials, defines the final macro and microstructure in the weld nugget.

CHAPTER 6: APPLICATIONS AND FUTURE RESESARCH

This research serves to expand the science and understanding of dissimilar titanium alloy friction stir welding, and provide a framework for future research and specific applications. Although no mechanical testing was performed on these specimens, the mechanical soundness of the macrostructure and microstructure will always be an important consideration for the primary industrial users of titanium – aerospace, oil and gas, biomedical and sporting goods. β21S is used mainly for its high temperature stability and corrosion resistance, and must be heat treated accordingly. Typically, a solution treat and overage cycle is selected, and considering the relatively low beta transus of the alloy compared to Ti-6Al-4V, the heat treatment would serve as a duplex anneal heat treatment for the Ti-6Al-4V portion of the joint. The largely transformed structure of the Ti-6Al-4V portions of the weld nugget would be relatively unchanged, coarsening the alpha particle morphology and enhancing ductility in exchange for fracture toughness and crack growth behavior. This weld nugget microstructure would behave similarly to the solution treated and over aged β21S in tensile loading, and it is reasonable to expect strengths similar to that of the parent materials, in the 900-930MPa range, with 6-8% elongations [Boyer, 1994][Boyer, 1996][Edwards, 2010a][Edwards, 2011].

Alloyed titanium is forgiving in regards to its static performance, but can become much more sensitive to chemistry, microstructure and crystallographic orientations when damage tolerance, durability and forming behavior is considered. It is unknown how the macrostructure features would present themselves to a crack tip during crack growth, however, the transformed structure of the Ti-6Al-4V is beneficial in stopping cracks from propagating [Boyer, 1996]. Also important is the well-recrystallized structure and grain hybridization, which eliminates crystallographic texture and orientation differences within the weld nugget as a favorable crack

path. Ultimately, cyclic loading in the high cycle or cold-dwell regime becomes a stochastic phenomenon, and the elimination of defects becomes the driving factor in the performance of the joint over microstructure features. Achieving a defect-free, fully fused weld will by far have the greatest impact on durability and damage tolerance properties.

Defect-free welds should always be a primary consideration when investigating the potential usefulness of a new branch of solid state joining, and by far the most interesting development put forward by the research in that regard is the vastly different characteristics of Weld 5 and Weld 9 that were achieved by simply switching the advancing and retreating side alloy. By putting β21S on the advancing side, the X, Y and Z machine loads relative to Weld 5 are 50%, 4% and 57% respectively. There is clearly a wider set of experimentation that can be carried out here, namely the isolating the influence of a pin side load (Y axis) and the formation of defects, which would have implications on real-time process control of homogenous friction stir welds as well. The alloy combination of Ti-6Al-4V and β21S was selected to be an extreme of what is possible in friction stir welding of dissimilar titanium alloys, but considering the lack of sensitivity in the Ti-6242/Ti-54M joints showed in Chapter 4 as far as defects are concerned, more alloy combinations need to be welded. This is necessary to provide better understand the limits of dissimilar alloy process capability, and to provide predictive capabilities as to optimal process parameters and the resultant weld quality based on the fundamental characteristics (chemistry, structure and mechanical properties) of the input materials. With this in mind, future research topics should include:

- Investigate a wider selection of parameters and their effect on mixing behavior of β21S on the advancing side of dissimilar alloys friction stir welds.

- Investigate pre-heating methods to minimize flow behavior differences in dissimilar alloy friction stir welds.
- Compile a larger scale EBSD data set across multiple weld parameters to better understand crystallographic orientation and texture evolution for different strain profiles.
- Quantify microCT scans and better correlate the data to machine loads to explore real-time process controls
- Optimize post-weld heat treatment to maximize static, durability and damage tolerance mechanical properties
- Integrate findings into friction stir welding finite element simulations that account for strain localization and flow behavior differences in friction stir welds to better predict thermal profiles and microstructure features.
- Consider material flow in dissimilar FSW joints as a fluid dynamics problem to account for flow behavior differences when predicting strains and temperatures during computational modeling

REFERENCES

[Abbaschian, 1991] Abbaschian R., 1991, "Physical Metallurgy Principles, 3rd Edition," Reed-Hill, Boston, MA.

[Ageev, 1970] Ageev, N.V. and Petrova, L.A., 1970, "The Theoretical Basis of the Development of High-Strength Metastable β-Alloys of Titanium (Proc. First Int. Conf. on Titanium, London)," Pergamon Press, p. 809-814.

[Akinlab, 2012] Akinlab E. T., Akinlabi S. A., 2012, "Effect of Heat Input on the Properties of Dissimilar Friction Stir Welds of Aluminum and Copper," American Journal of Material Science, Vol 2(54), p. 147-152.

[Arora, 2008] Arora A., Nandan A., Reynolds A. P., DebRoy T., 2008, "Torque, power requirement and stir zone geometry in friction stir welding through modeling and experiments," Scripta Materiala, Vol. 60, pp. 13-19.

[Araki, 1997] Araki H., Minamino Y., Yamane T., Shirai Y., Miyamoto Y., 1997, "Effect of Pressure on the Fast Diffusion in β-Titanium," Defect and Diffusion Forum, Vol 143-147, p. 125-130.

[Barriobera-Villa, 2015a] Barriobera-Villa P., Requena G., Buslaps T., Alfeld M., Boesenberg U., 2015, "Role of element partitioning on the α-β phase transformation kinetics of a bi-modal Ti-6Al-6V-2Sn alloy during continuous heating," Journal of Alloys and Compounds, Vol 626, pp 330-339.

[Barriobera-Villa, 2015b] Barriobera-Villa P., Requena G., Warchomicka F., Stark A., Schell N., Buslaps T., 2015, "Phase transformation kinetics during continuous heating of a β-quenched Ti-10V-2Fe-3Al alloy," Journal of Materials Science, Vol. 50, pp. 1412-1426.

[Bagariatskii, 1958] Bagariatskii, Yu.A., Nosova, G.I. and Tagunova, T.V., 1958, "Factors in the Formation of Metastable Phases in Titanium-Base Alloys," Sov. Phys. Dokl, Vol 3, p. 1014-1018.

[Boyer, 1994] Boyer R.R., Welsch G., and Collings E.W., 1994, "Materials Property Handbook: Titanium Alloys," ASM International, Materials Park.

[Boyer, 1996] Boyer R. R., 1996, "An overview on the use of titanium in the aerospace industry," Materials Science and Engineering A, 213, p 103-114.

[Brun, 1998] Brun J., Anoshkin N., Shakhanova, G., 1998, "Physical processes and regimes of thermomechanical processing controlling

development of regulated structure in the α +β titanium alloys," Materials Science and Engineering A, Vol 243, pp. 77-81.

[Bruneseaux, 2008] Bruneseaux F., Aeby-Gautier E., Guillaume G., Da Costa Teixeira J., Appolaire B., Weisbecker P., Mauro A, 2008, "In situ characterizations of phase transformations kinetics in the Ti17 titanium alloy by electrical resistivity and high temperature synchrotron X-ray diffraction," Materials Science and Engineering A, Vol 476, pp. 60-68.

[Buffa, 2006a] Buffa G., Hua J., Shivpuri R., Fratini L., 2006, "A continuum based fem model for friction stir welding – model development," Materials Science and Engineering A, Vol 419, pp. 389-396.

[Buffa, 2006b] Buffa G., Hua J., Shivpuri R., Fratini L., 2006, "Design of the friction stir welding tool using the continuum based FEM model," Materials Science and Engineering A, Vol 419, pp. 381-388.

[Buffa, 2013] Buffa G., Fratini L., Shneider M., Merklein M., 2013, "Micro and macro mechanical characterization of friction stir welded Ti-6Al-4V lap joints through experiments and numerical simulation," Journal of Materials Processing Technology, Vol. 213, pp. 2313-2322.

[Callister, 2003] Callister W.D., 2003, "Materials Science and Engineering: An Introduction," John Wiley & Sons Inc., New York, NY.

[Chen, 2008] Chen Y. C., Nakata K., 2008, "Microstructural characterization and mechanical properties in friction stir welding of aluminum and titanium dissimilar alloys," Materials and Design, Vol 30, p. 469-474.

[Cho, 2005] Cho J-H., Boyce D. E., Dawson P. R., 2005, "Modeling strain hardening and texture evolution in friction stir welding of stainless steel," Materials Science and Engineering A, Vol 398, p. 146-163.

[Cho, 2006] Cho J-H., Boyce D. E., Dawson P. R., 2006, "Investigation on Texture Evolution during Friction Stir Welding of Stainless Steel," Metallurgical and Materials Transactions A, Vol 37, p. 1147-1164.

[Cho, 2008] Cho, J-H, Dawson, P. R., 2008, "Modderling Texture Evolution During Friction Stir Welding of Stainless Steel With Comparison to Experiments," Journal of Engineering Materials and Technology, Vol. 130.

[Christ, 2009] Christ H-J., Schmidt P., 2009, "Influence of Beta Stability on Hydrogen Diffusion in Various Beta Titanium Alloys," Defect and Diffusion Forum, Vol 289-292, p. 87-94.

[Deng, 2013] Deng Y. Q., Sheng G. M., Huang Z. H., Fan L. Z., 2013, "Microstructure and mechanical properties of diffusion bonded titanium/304 stainless steel joint with pure Ag interlayer," Science and Technology of Welding and Joining, Vol 18, p. 143-146.

[Ding, 2002] Ding R., Guo Z. X., Wilson A., 2002, "Microstructural evolution of a Ti-6Al-4V alloy during thermomechanical processing," Materials Science and Engineering A, Vol 327, pp. 233-245.

[Dressler, 2009] Dressler U., Biallas G., Mercado U. A., 2009, "Friction stir welding of titanium alloy Ti6Al4V to aluminum alloy AA2024-T3," Materials Science and Engineering A, Vol 526, p. 113-117.

[Edwards, 2010a] Edwards P.D., 2010, "Friction Stir Welding of Ti-6Al-4V Sheet and Plate for Aerospace Structures," Ph.D. Thesis, University of Washington.

[Edwards, 2010b] Edwards P., Ramulu M., 2010, "Peak temperatures during friction stir welding of Ti-6Al-4V," Science and Technology of Welding and Joining, Vol 15, p. 468-472.

[Edwards, 2010c] Edwards P., Ramulu M., 2010, "Identification of Process Parameters for Friction Stir Welding Ti-6Al-4V," Journal of Engineering Materials and Technology, Vol. 132 No. 3.

[Edwards, 2011] P. D. Edwards, G. Coleman, M. Petersen, J. D. Cotton, 2011, "Mechanical Properties of Thick Section Ti-6Al-4V Friction Stir and Electron Beam Welds," Friction Stir Welding and Processing VI (eds R. Mishra, M. W. Mahoney, Y. Sato, Y. Hovanski and R. Verma).

[Elmer, 2005] Elmer J. W., Palmer T. A., Babu S. S., Specht E. D., 2005, "In situ observations of lattice expansion and transformation rates of α and β phases in Ti-6Al-4V," Materials Science and Engineering A, Vol 391, pp 104-113.

[Esmaeili, 2012] Esmaeili A., Besharati Givi M. K., Zareie Rajani H. R., 2012 "Investigation of weld defects in dissimilar friction stir welding of aluminum to brass by radiography," Science and Technology of Welding and Joining, Vol 17, p. 539-543.

[Ferguson, 1968] Ferguson J. M., 1968, "The Oxidation and Contamination of Titanium and its Alloys," DMIC Memorandum 238, Defense Metals Information Center, Columbus, OH.

[Fonda, 2004] Fonda, R. W., Bingert, J. F., Colligan, K. J., 2004, "Development of Grain Structure During Friction Stir Welding," Scripta Materiala, Vol. 51, pp. 243-248.

[Fonda, 2013] Fonda, R., Reynolds, A., Feng, C.R., Knipling, K., Rowenhorst, D., 2013, "Material Flow in Friction Stir Welds," Metallurgical and Materials Transactions A, Vol 44A, pp. 337-344.

[Gibson, 2013] Gibson B. T., Lammlein D. H., Prater T. J., Longhurst W. R., Cox C. D., Ballun M. C., Dharmaraj K. J., Cook G. E., Strauss A. M., 2013, "Friction stir welding: Process, automation, and control," Journal of Manufacturing Processes, Article in Press, DOI: 10.1016/j.jmapro.2013.04.002.

[Hammond, 1978] Hammond C. and Nutting J., 1978, "The Physical Metallurgy of Superalloys and Titanium Alloys (in Forging and Properties of Aerospace Materials)," The Metals Society, p. 75-102.

[Hendricks, 1962] Hendricks P. L., Elliott R. P., Howe E. A., 1962, "Diffusion In Titanium And Titanium Alloys," Armed Services Technical Information Agency, Technical Documentary Report No. ASD-TDR-62-561.

[Hicman, 1969] Hicman B.S., 1969, "Omega Phase Precipitation in Alloys of Titanium with Transition Metals," Trans. TMS-AIME, Vol 245, p. 1329-1335.

[Holmquist, 1998] Holmquist M., et al, 1998, "Hot Isostatic Diffusion Bonding of Titanium Alloy Ti-6Al-4V to Gamma Titanium Aluminide IHI Alloy 01A," Scripta Materiala, Vol. 39 No. 8, pg. 1101-1106.

[Huijie, 2009] Huijie L., Xiuli F., 2009, "Study of Diffusion Bonding of Fine Grain TC21 Titanium Alloy," Rare Metal Materials and Engineering, Vol 38, p. 1509-1513.

[Jata, 2004] K. Jata, P. Subramanian, A.P. Reynolds, T. Trapp, E. Helder, 2004, "Friction Stir Welding of Titanium Alloys for Aerospace Applications: Microstructure and Mechanical Behavior," Proceedings of the Fourteenth (2004) International Offshore and Polar Engineering Conference, 2004.

[Jaggee, 1958] Jaggee R.I., 1958, "The Physical Metallurgy of Titanium Alloys," Progress in Metals Physics, Vol 7, p. 65-163.

[Jiangwei, 2002] Jiangwei R., Li Y., Feng T., 2002, "Microstructure characteristics in the interface zone of Ti/Al diffusion bonding," Materials Letters, Vol 56, p. 647-652.

[Kaufman, 1973] Kaufman L. and Bernstein H., 1973, "Phase Stability and Equilibria as Affected by the Physical Properties and Electronic

Structure of Titanium Alloys Titanium (Proc. First Int. Conf. on Titanium, London)," Pergamon Press, p. 773-800.

[Knipling, 2009] Knipling, K.E., Fonda, R.W., 2009, "Texture Development in the Stir Zone of near-a Titanium Friction Stir Welds," Scripta Materiala, Vol.60, pp. 1097–1100.

[Kosaka, 2003] Kosaka Y., Fanning J. C., Fox S. P., 2003, "Development of Low Cost High Strength Alpha/Beta Alloy with Superior Machinability," TIMET Henderson Technical Laboratory, Henderson NV, USA.

[Leinert, 2000] T. Lienert, K. Jata, R. Wheeler, V. Seetharaman, 2000, "Friction Stir Welding of Ti-6Al-4V Alloys," Proceedings from Joining of Advanced and Specialty Materials, 9-11 October, S. Louis, MO, ASM International, 2000.

[Lee, 1998] Lee W-S., Chi-Feng L., 1998, "Plastic deformation and fracture behavior of Ti-6Al-4V alloy loaded with high strain rate under various temperatures," Materials Science and Engineering A, Vol 241, pp. 48-59.

[Leinert, 2000] T. Lienert, K. Jata, R. Wheeler, V. Seetharaman, 2000, "Friction Stir Welding of Ti-6Al-4V Alloys," Proceedings from Joining of Advanced and Specialty Materials, 9-11 October, S. Louis, MO, ASM International, 2000.

[Li, 2013] Li B., Zhang Z., Shen Y., Hu W., Luo L., 2013, "Dissimilar friction stir welding of Ti-6Al-4V alloy and aluminum alloy employing a modified butt joint configuration: Influences of process variables on the weld interfaces and tensile properties," Materials and Design, Accepted Manuscript, DOI: 10.1016/j.matdes.2013.07.019.

[Liu, 2010] H. Liu, L. Zhou, Q. Liu, 2010, "Microstructural characteristics and mechanical properties of friction stir welded joints of Ti-6Al-4V titanium alloy," Materials and Design, Vol 3, pp 1650-1655.

[Lorrain, 2010] Lorrain O., Favier V., Zahrouni H., Lawrjaniec D., 2010, "Understanding the material flow path of friction stir welding process using unthreaded tools," Journal of Materials Processing Technology," Vol. 210, pp. 603-609.

[Malinov, 2005] Malinov S., Katzarov I., Sha W., 2005, "Modeling, Simulations and Monitoring of Lamella Structure Formation in Titanium Alloys Controlled by Diffusion Redistribution," Defect and Diffusion Forum, Vol 237-240, p. 635-646.

[Mironov, 2008] Mironov, S., Zhang, Y., Sato, Y.S., Kokawa, H., 2008, "Development of Grain Structure in B-Phase Field During Friction

Stir Welding of Ti–6Al–4V Alloy," Scripta Materiala, Vol 59, pp. 27–30.

[Mironov, 2009] Mironov S., Sato, Y.S., Kokawa, H., 2009, "Development of Grain Structure During Friction Stir Welding of Pure Titanium," Acta Materiala, Vol. 57, pp. 4519–4528.

[McQuillan, 1956] McQuillan A.D. and McQuillan M.K., 1956, "Titanium," Academic Press.

[McQuillan, 1963] McQuillan M.K., 1963, "Phase Transformations in Titanium and its Alloys," Metall. Rev., Vol 8, p. 41-104.

[Milne, 2011] Milne K., et al, 2011, "Ultrasonic Non-destructive Evaluation of Titanium Diffusion Bonds," J Nondestruct Eval, Vol. 30 No. 3, p 225-236.

[Mirassou, 1997] Mirassou M. L., Perez R. A., Dyment F., 1997, "Diffusion of Substitutional Solutes in α-Ti Measured by RBS and HIRBS," Defect and Diffusion Forum, Vol 143-147, P. 67-72.

[Mishra, 2005] R.S. Mishra, Z.Y. Ma, 2005, "Friction stir welding and processing," Materials Science and Engineering, Vol. 50 No. 1, pp. 1-78.

[Mori, 2013] Mori, K-i., Bay N., Fratini L., Micari F., Tekkaya E., 2013, "Joining by plastic deformation," CIRP Annals – Manufacturing Technology, Vol 63, p. 673-694.

[Nakajima, 1993] Nakajima H., Koiwa M., 1993, "Diffusion in α-Titanium," Defect and Diffusion Forum, Vol 95-98, p. 775-782.

[Ondera, 1993] Onodera H., Ohyama H., Nakajima H., Takatori H., Fujii H., Maeda T., Takahashi H., Watakabe S., 1993, "Impurity Diffusion Behavior in β-Titanium," Defect and Diffusion Forum, Vol 95-98, P. 729-734.

[Orhan, 2001] Orhan N., Khan T.I., Eroglu M., 2001, "Diffusion bonding of a microduplex stainless steel to Ti-6Al-4V," Scripta Materialia, Vol. 45 No. 4, p 441-446.

[Parris, 1990] Parris W. M., Bania P. J., 1990, "Beta-21S: A High-Temperature Metastable Beta Titanium Alloy," Proceedings of 1990 TDA Conference, Orlando, 1990.

[Peng, 2004] Peng H.E., Feng J and Qian Y., 2004, "A New Model of Interfacial Physical Contact in Diffusion Bonding," J. Mater. Sci. Technol., Vol. 20 No.1, p 109-112.

[Pilchak, 2007] Pilchak A. L., Juhas M. C., Williams J. C., 2007, "Microstructural Change Due to Friction Stir Processing of Investment-Cast Ti-6Al-4V," Metallurgical and Materials Transactions A, Vol 38, p. 401-408.

[Prasad, 1998] Prasad Y. V. R. K., Seshacharyulu T., 1998, "Processing maps for hot working of titanium alloys," Materials Science and Engineering A, Vol 243, pp. 82-88.

[Ramirez, 2003] A.J. Ramirez, M.C. Juhas, 2003, "Microstructural Evolution in Ti-6Al-4V Friction Stir Welds," Materials Science Forum, Vol. 426-432, pp. 2999-3004.

[Reynolds, 2005] Reynolds, A.P., Hood,E., Tang, W., 2005, "Texture in Friction Stir Welds of Timetal 21S," Scripta Materiala, Vol. 52, pp. 491–494.

[Rahman, 2010] Rahman A.H.M.E, Cavalli M.N., 2010, "Strength and microstructure of diffusion bonded titanium using silver and copper interlays," Materials Science and Engineering A, Vol. 527 No. 20, p 5189-5193.

[Sanders, 2004] Sanders D. G., Ramulu M., 2004, "Examination of Superplastic Forming Combined with Diffusion Bonding for Titanium: Perspective from Experience," Journal of Materials Engineering and Performance, Vol 13(6), p 744-752.

[Seidel, 2001] T.U. Seidel, A.P. Reynolds, 2001, "Visualization of the material flow in AA2195 friction-stir welds using a marker insert technique," Metallurgical and Materials Transactions, Nov. 2001, v. 32A, No. 11, pp. 2879-2884.

[Shewmon, 1989] Shewmon P., 1989, "Diffusion in Solids," TMS, Warrendale, PA.

[Steuwer, 2012] Steuwer A., Hattingh D. G., James M. N., Singh U., Buslaps T., 2012, "Residual stresses, microstructure and tensile properties in Ti-6Al-4V friction stir welds," Science and Technology of Welding and Joining, Vol 17, p. 525-533.

[Tamirisakandala, 2003] Tamirisakandala S., Vedam B. V., Bhat R. B., 2003, "Recent Advances in the Deoformation Processing of Titanium Alloys," Journal of Materials Engineering and Performance, Vol. 12, pp. 661-673.

[Threadgill, 2007] Threadgill P. L., 2007, "Terminology in friction stir welding," Science and Technology of Welding and Joining, Vol 12, p. 357-360.

[Trapp, 2003] Trapp T., Helder, E., Subramanian P.R., 2003, "FSW of Titanium Alloys for Aircraft Engine Components," Friction Stir Welding

and Processing II, The Minerals, Metals & Materials Society, p 173-178.

[Tuppen, 2005] Tuppen S.J., Bache M.R., Voice W.E., 2005, "A fatigue assessment of dissimilar titanium alloy diffusion bonds," International Journal of Fatigue, Vol. 27 No. 6, p 651-658.

[Wang, 2006] Wang X-F., Ma M., Liu X-B., Wu X-Q., Tan C-G., Shi R-K., Lin J-G., 2006, "Diffusion bonding of γ-TiAl alloy to Ti-6Al-4V alloy under hot pressure," Transactions of Nonferrous Metals Society of China, Vol 16, p. 1059-1063.

[Williams, 1973] Williams J.C., 1973, "Kinetics and Phase Transformations: A Critical Review of Titanium (Proc. First Int. Conf. on Titanium, London)," Pergamon Press, 1433-1494.

[Zhang, 2008] Y. Zhang, Y. S. Sato, H. Kokawa, S. H. C. Park, S. Hirano, 2008, "Microstructural characteristics and mechanical properties of Ti-6Al-4V friction stir welds," Materials Science and Engineering A, Vol. 485, pp. 448-455.

[Zhang, 2009] Zhang Z., Zhang H. W., 2009, "Numerical studies on controlling of process parameters in friction stir welding," Journal of Materials Processing Technology, Vol. 209, pp. 241-270.

APPENDIX A: DIFFUSION CALCULATIONS

The calculation of concentration profiles in friction stir weld nuggets of titanium makes use of several assumptions to fit the calculation into a known form. All diffusion is assumed to take place under isothermal conditions; the contribution to the diffusion profile from the heat up and cool down is assumed to be trivial due to the exponential nature of the diffusivity as a function of temperature, shown in Equation A-1, as well as sharp heating and cooling transients seen in experimental data, shown in Figure A-1 [Abbaschian, 1991]. Diffusion is assumed occur in fully beta transformed material due to the temperatures observed in prior work as well as the microstructural evidence seen in Chapter 4.

$$\widetilde{D}(t) = D_o e^{-Q/RT}$$ **Equation A-1** [Abbaschian, 1991]

Where:

$\widetilde{D}$ = Diffusivity

D_o = Diffusion frequency factor

Q = activation energy

R = Universal gas constant

T = Temperature

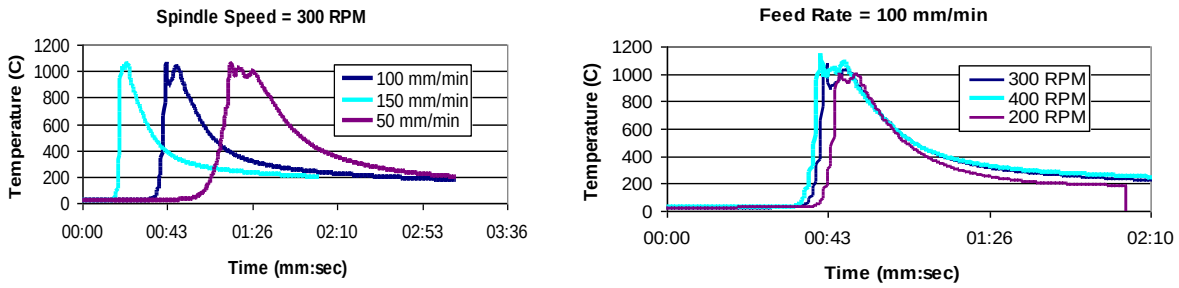

Figure A-1: Thermal excursion profiles in Ti-6Al-4V friction stir welds [Edwards, 2010a].

Diffusivity is held constant due to the relatively minor differences in composition of the two materials in question – the elements being analyzed can be said to diffuse through a titanium matrix diluted by constant amounts of Aluminum and interstitial impurities (Oxygen, Hydrogen, Nitrogen and Carbon) regardless of the localized alloy chemistry. Holding diffusivity and temperature as constant, the net one-dimensional flow of atoms from a sufficiently large source as to not deplete the end point allows for the application of Fick's 2nd Law, shown as a second-order partial differential in Equation A-2, solved for a diffusion couple of Alloy A and B in Equation A-3, where Alloy A acts as the source of a given element 'N_A' that is diffusing into alloy B.

$$\frac{\partial N_A}{\partial t} = \frac{\partial}{\partial x}\widetilde{D}\frac{\partial N_A}{\partial x} = \widetilde{D}\frac{\partial^2 N_A}{\partial x^2} \qquad \textbf{Equation A-2} \text{ [Abbaschian, 1991]}$$

$$N_A(x,t) = N_{A_A} + \frac{(N_{A_B} - N_{A_A})}{2}\left[1 + erf\,\frac{x}{2\sqrt{\widetilde{D}t}}\right] \qquad \textbf{Equation A-3} \text{ [Abbaschian, 1991]}$$

Where:

$\widetilde{D}$ = Diffusivity

x = Distance from initial interface

t = Time

N_A = Atomic percent of element 'A'

N_{A_A} = Bulk atomic percent of element ' A' in Alloy A

N_{A_B} = Bulk atomic percent of element 'A' in Alloy B

To generate inputs for Equation A.3, diffusivity data from Elliot is tabulated in Table A-1, while typical compositions are used for Ti-6242 and Ti54M and shown in both weight and atomic percent in Table A-2. Time and temperature are selected arbitrarily; however, thermal profiles of a Ti-6Al-4V to Ti-6Al-4V butt weld generated experimentally by Edwards, shown in Figure A-1, are used as a guide.

Table A-1: Diffusivity data for selected elements in beta titanium.

Temperature (C)	Diffusivity			
	Zr	Mo	V	O
900	6.66E-10	8.07E-11	2.60E-10	9.26E-10
1000	1.90E-09	**3.00E-10**	9.67E-10	1.98E-08
1100	9.97E-09	7.47E-10	2.49E-09	2.16E-07
1200	1.60E-08	**1.38E-09**	7.64E-09	4.41E-07
1300	5.40E-08	4.00E-09	2.92E-08	1.57E-06
*Bolded values are interpolated from a linear fit				

Table A-2: Nominal composition of Ti-6242 and Ti54M [Boyer, 1994][Kosaka, 2003].

Ti54M		
Element	**Weight %**	**Atomic %**
Hydrogen	0.004	0.19
Carbon	0.00	0.00
Nitrogen	0.00	0.00
Oxygen	0.15	0.44
Aluminum	5.00	8.71
Silicon	0.00	0.00
Chlorine	0.00	0.00
Vanadium	4.00	3.69
Chromium	0.00	0.00
Manganese	0.00	0.00
Iron	0.40	0.34
Nickel	0.00	0.00
Zirconium	4.00	2.06
Niobium	0.00	0.00
Molybdenum	0.60	0.29
Tin	0.00	0.00
Titanium	85.85	84.28

Ti6242		
Element	**Weight %**	**Atomic %**
Hydrogen	0.004	0.19
Carbon	0.00	0.00
Nitrogen	0.00	0.00
Oxygen	0.18	0.53
Aluminum	6.00	10.53
Silicon	0.12	0.20
Chlorine	0.00	0.00
Vanadium	0.00	0.00
Chromium	0.00	0.00
Manganese	0.00	0.00
Iron	0.50	0.42
Nickel	0.00	0.00
Zirconium	4.00	2.08
Niobium	0.00	0.00
Molybdenum	2.00	0.99
Tin	2.00	0.80
Titanium	85.20	84.26

A sample calculation is presented in Equation A-4, showing the concentration of Zirconium 3 microns away from the initial interface of a diffusion couple compromised of Ti-6242 and Ti54M, at 1100°C for 5 seconds. Note that the coordinate system selected calculates a value 3 microns into Ti54M half of the diffusion couple:

$$(.3550) = (2.076) + \frac{((0)-(2.076))}{2}\left[1 + erf\frac{(0.0003)}{2\sqrt{(9.97E-09)(5)}}\right] \qquad \textbf{Equation A-4}$$

Continuing through a series of calculations that increment x by 0.5μ steps from -25μ to 25μ away from the initial interface at five different temperatures and plotting the results yields the composition profiles shown in Figure A-2, and can easily be replicated for any element having a known diffusivity at a given temperature.

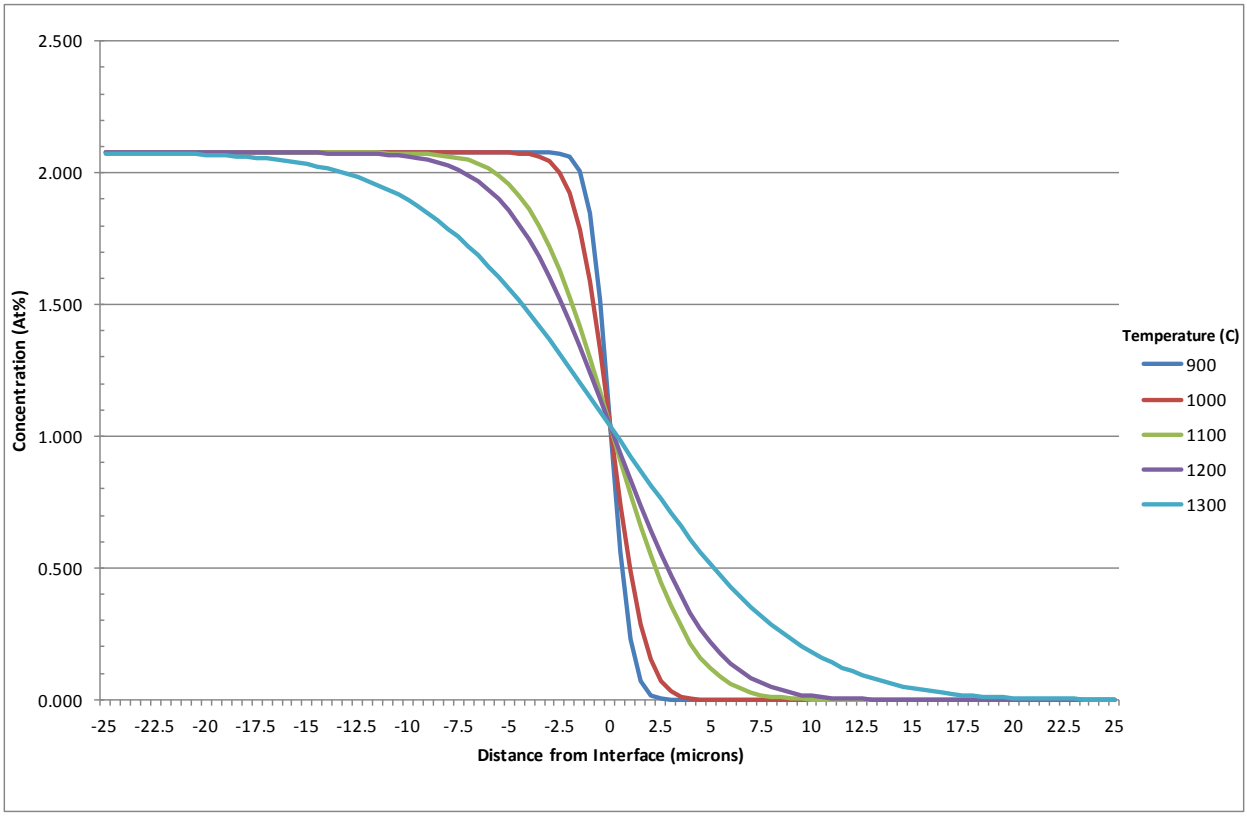

Figure A-2: Calculated concentration profile of Zirconium in a Ti-6242/Ti54M diffusion couple held at 1100°C for 5 seconds.

APPENDIX B: FRICTION STIR WELD MACHINE FORCES

An instrumented FSW machine was used to produce the nine welds between Ti-6Al-4V and β21S discussed in **Chapter 5**. Force data is collected by a single load cell in the X (pin travel) direction, a single load cell in the Y direction and by the average of three load cells in the Z (forge load) direction. Full force curves in these three directions (from machine start up to shut down) are provided, as well as a table summarizing average loads in the three directions for each weld condition during steady state welding. Load averages are calculated for 50% of the total weld seam length, starting 4mm away from the withdraw of the pin.

Table B-1: Average forces during steady state welding for nine Ti-6Al-4V/B21S friction stir welds.

Weld Identification Number	Advancing Side Alloy	Retreating Side Alloy	Stock Thickness (mm)	Weld Seam Length (mm)	Tool Rotation (RPM)	Travel Speed (mm/min)	X-Direction Load Average (N)	Y-Direction Load Average (N)	Z-Direction Load Average (N)
1	Ti-6Al-4V	β21S	4.5	274	600	75	-960	1413	15010
2	Ti-6Al-4V	β21S	4.5	274	400	125	2107	4783	25063
3	Ti-6Al-4V	β21S	4.5	274	225	100	7325	8481	69521
4	Ti-6Al-4V	β21S	4.5	268	275	100	5943	6961	53181
5	Ti-6Al-4V	β21S	4.5	272	275	125	4985	7065	62421
6	Ti-6Al-4V	β21S	4.5	276	275	150	4375	8152	63011
7	Ti-6Al-4V	β21S	4.5	274	325	125	5854	6547	49236
8	Ti-6Al-4V	β21S	4.5	177	150	150	9935	7166	95215
9	β21S	Ti-6Al-4V	4.5	274	275	275	2776	335	37405

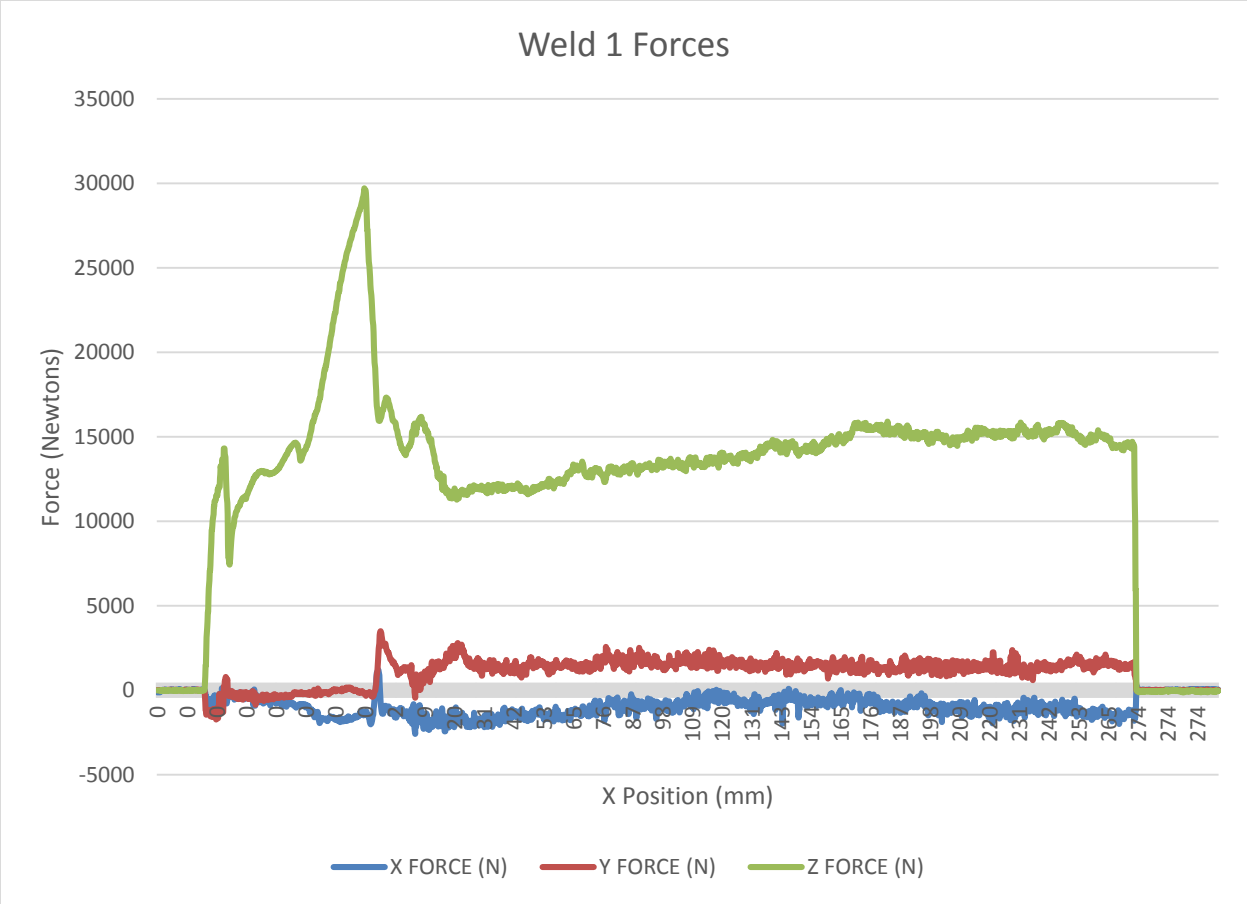

Figure B-1: X, Y and Z forces for Weld 1, Ti-6Al-4V (advancing side) to B21S, 600RPM spindle speed, 75mm/min travel speed.

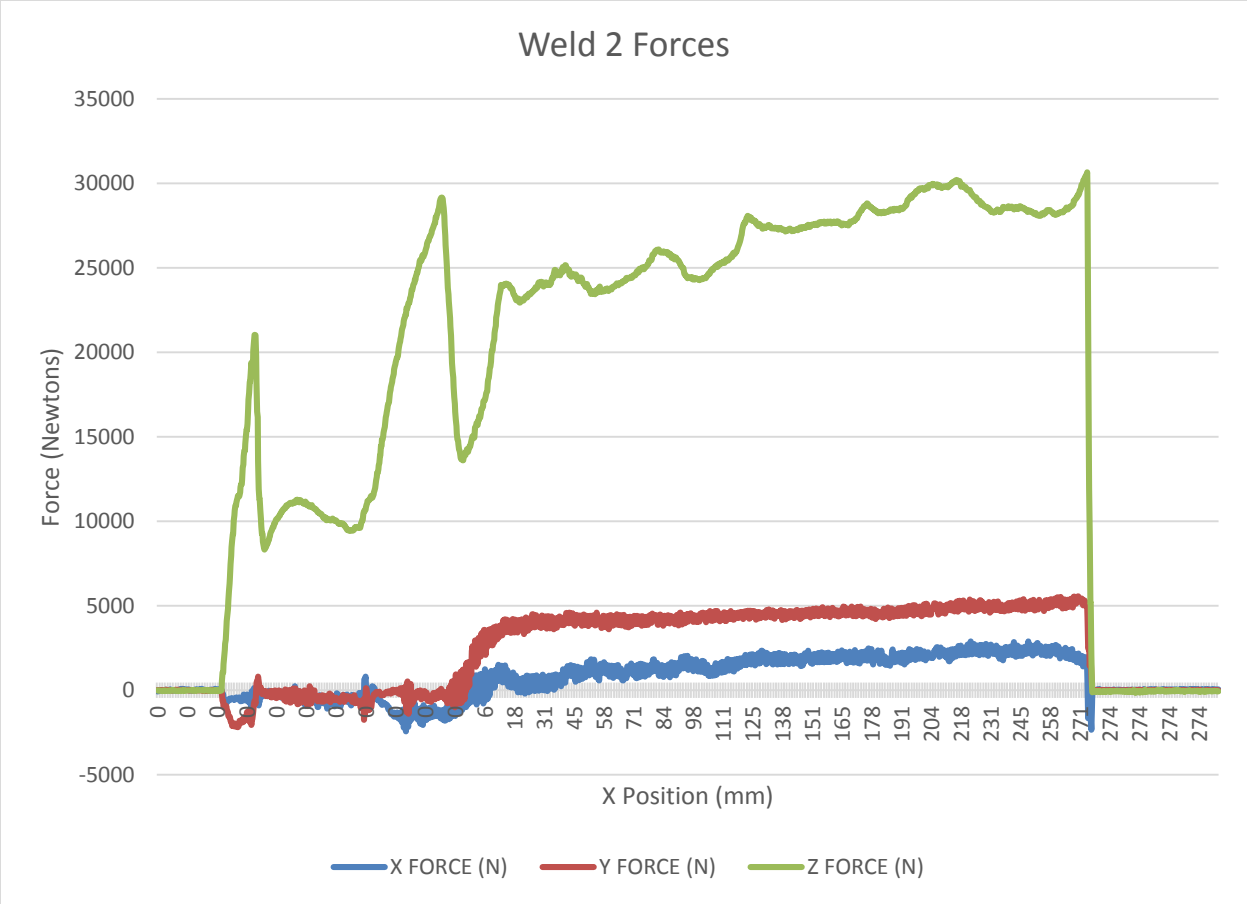

Figure B-2: X, Y and Z forces for Weld 2, Ti-6Al-4V (advancing side) to B21S, 400RPM spindle speed, 125mm/min travel speed.

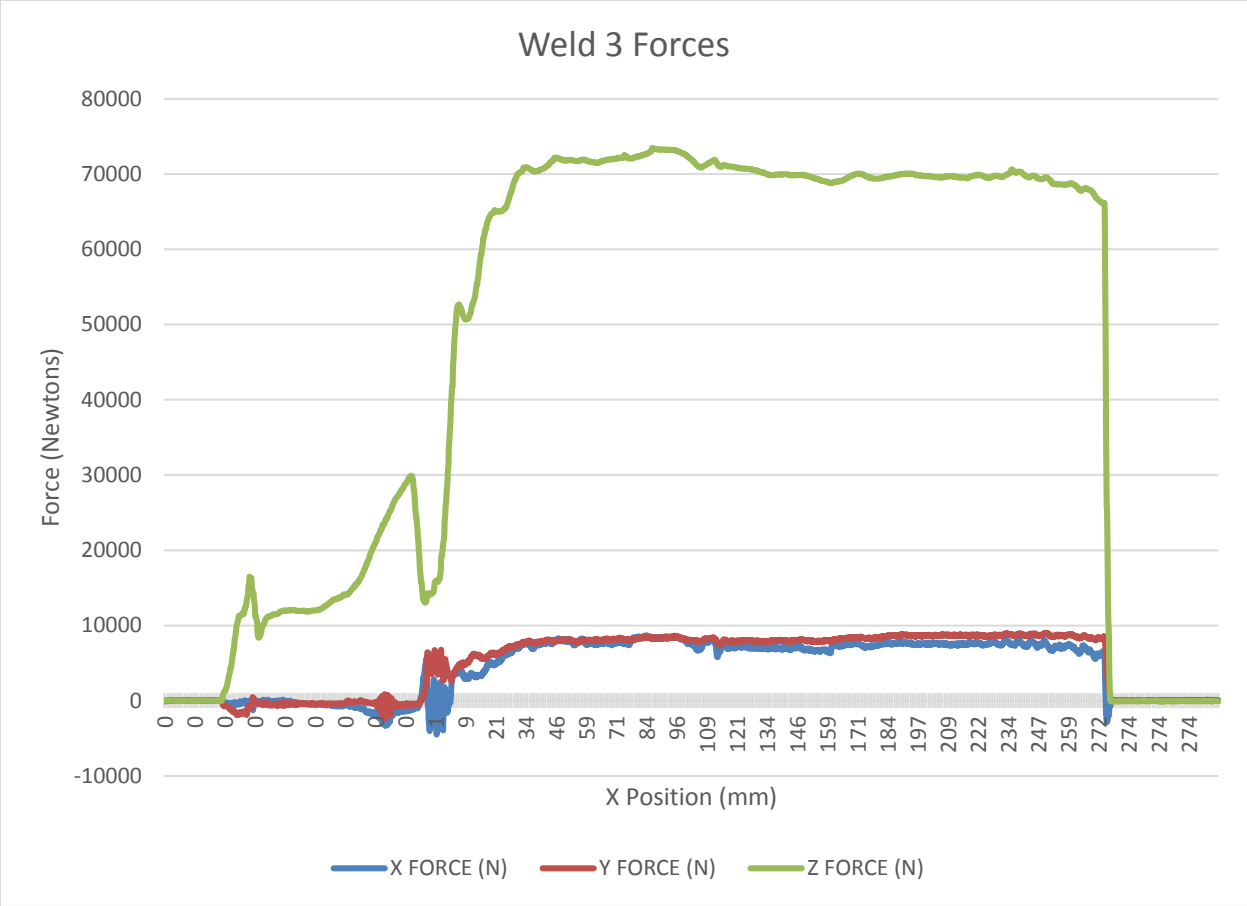

Figure B-3: X, Y and Z forces for Weld 3, Ti-6Al-4V (advancing side) to B21S, 225RPM spindle speed, 100mm/min travel speed.

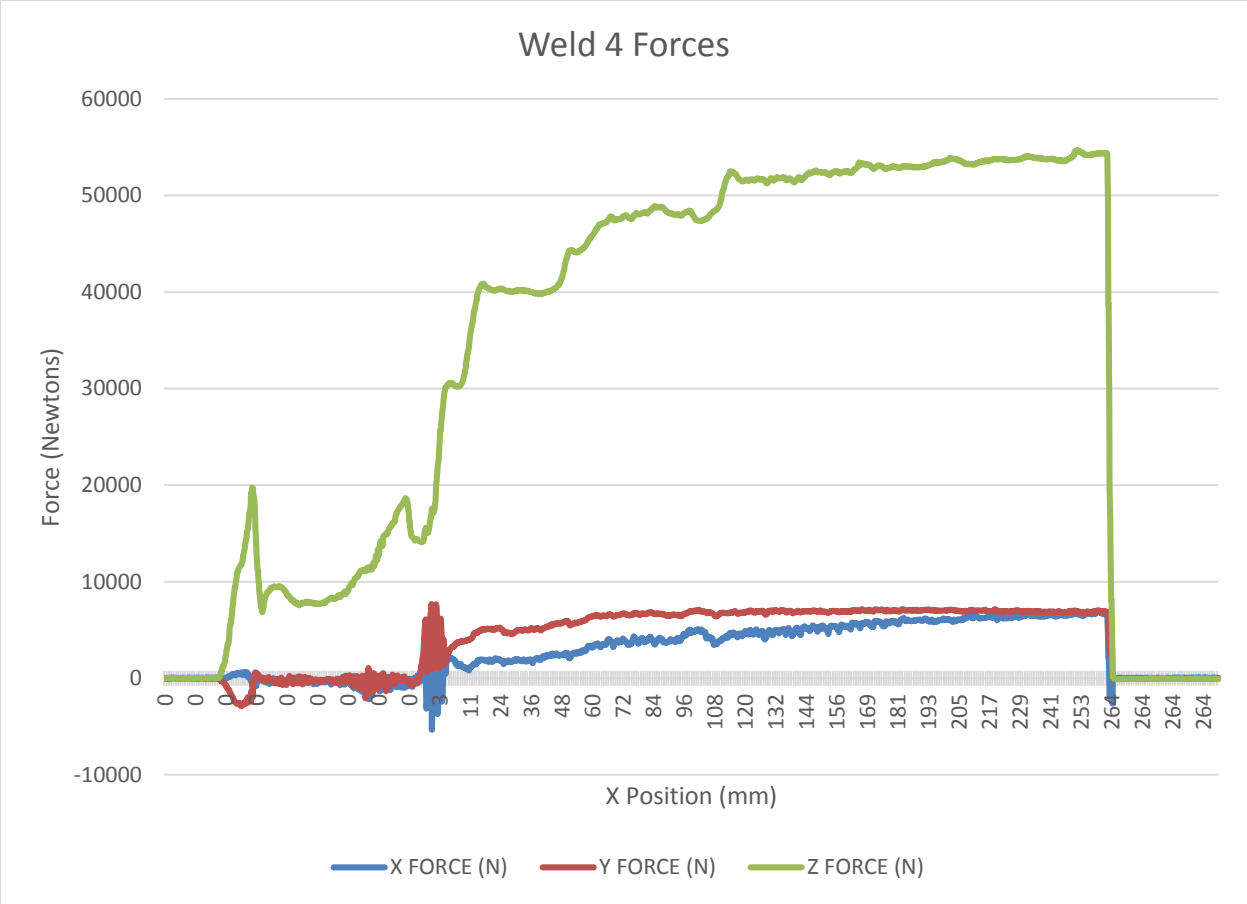

Figure B-4: X, Y and Z forces for Weld 4, Ti-6Al-4V (advancing side) to B21S, 275RPM spindle speed, 100mm/min travel speed.

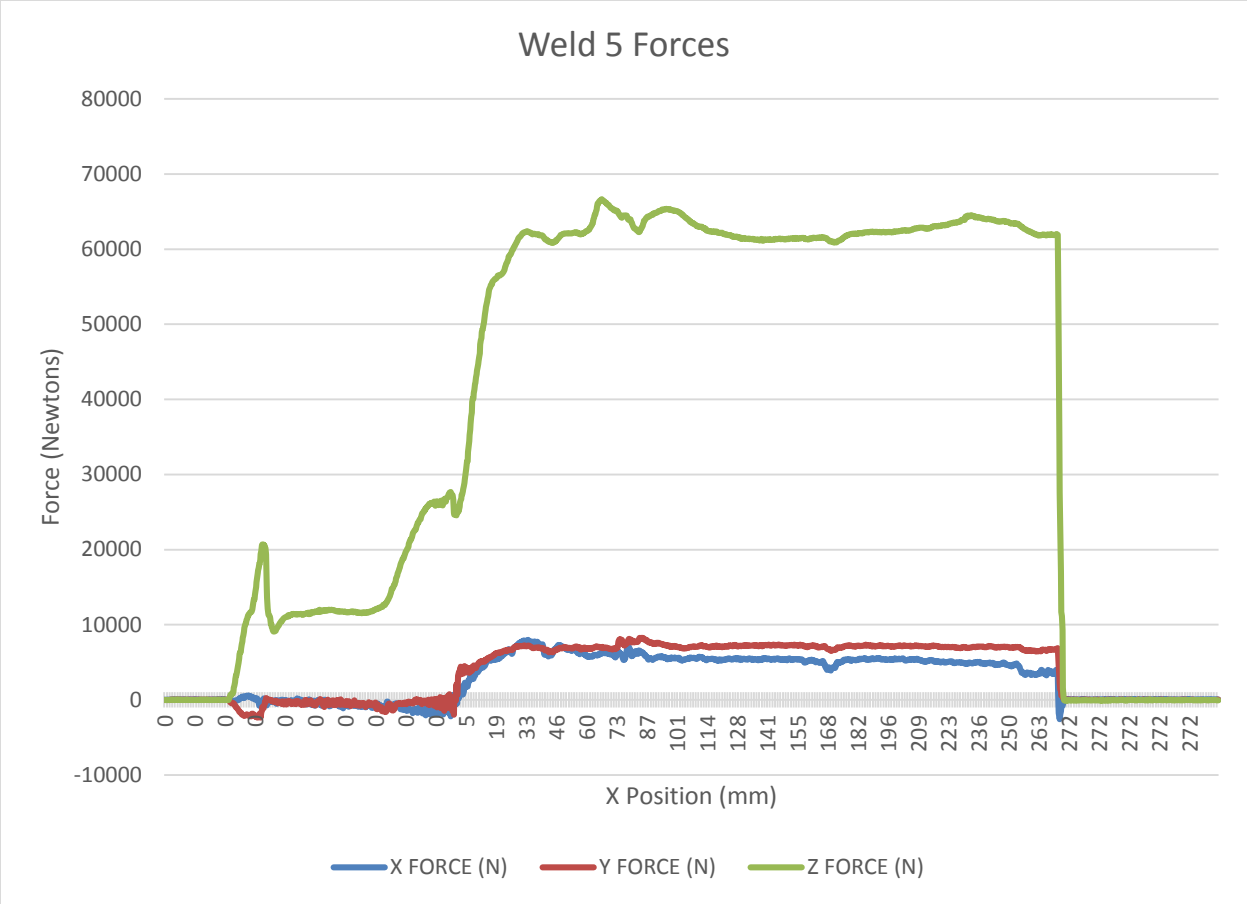

Figure B-5: X, Y and Z forces for Weld 5, Ti-6Al-4V (advancing side) to B21S, 275RPM spindle speed, 125mm/min travel speed.

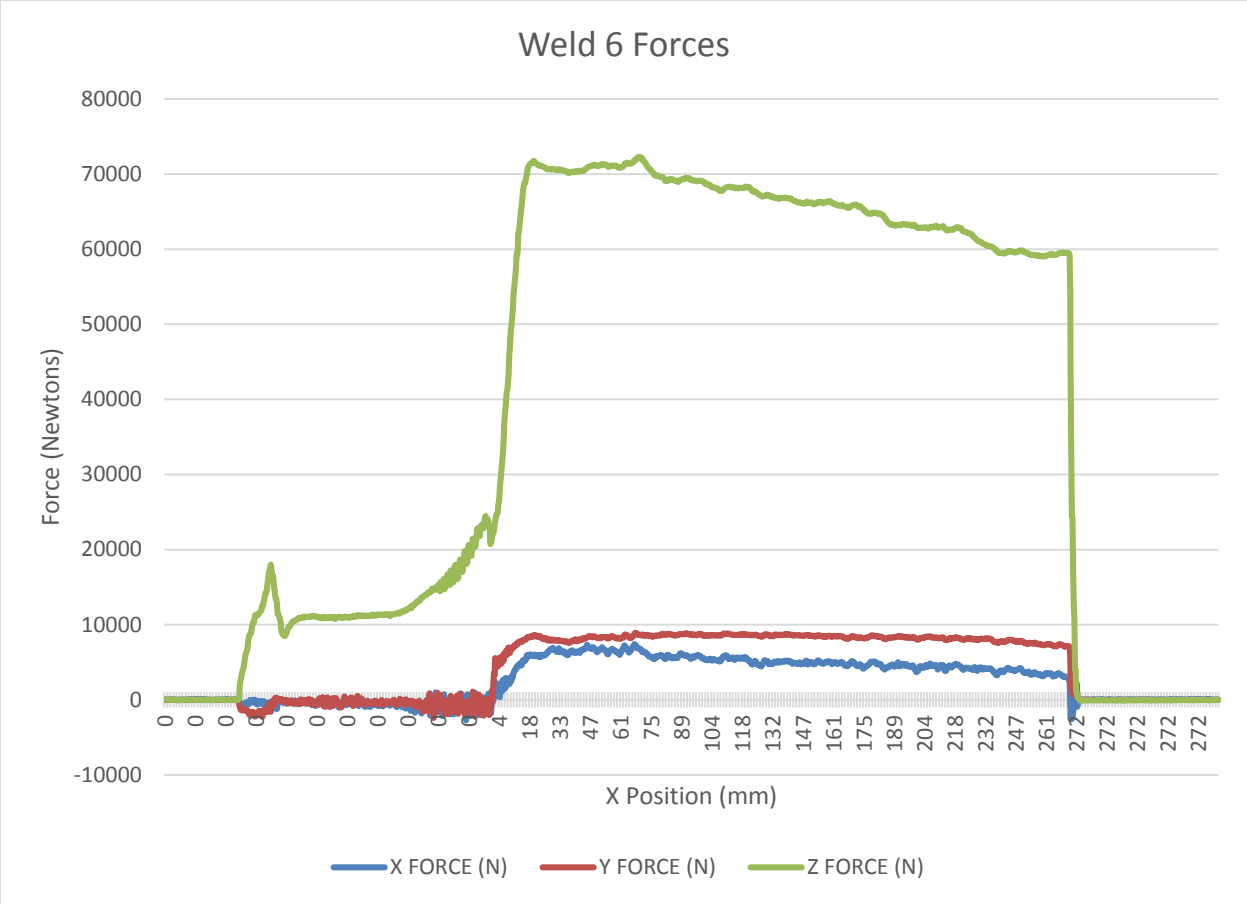

Figure B-6: X, Y and Z forces for Weld 6, Ti-6Al-4V (advancing side) to B21S, 275RPM spindle speed, 150mm/min travel speed.

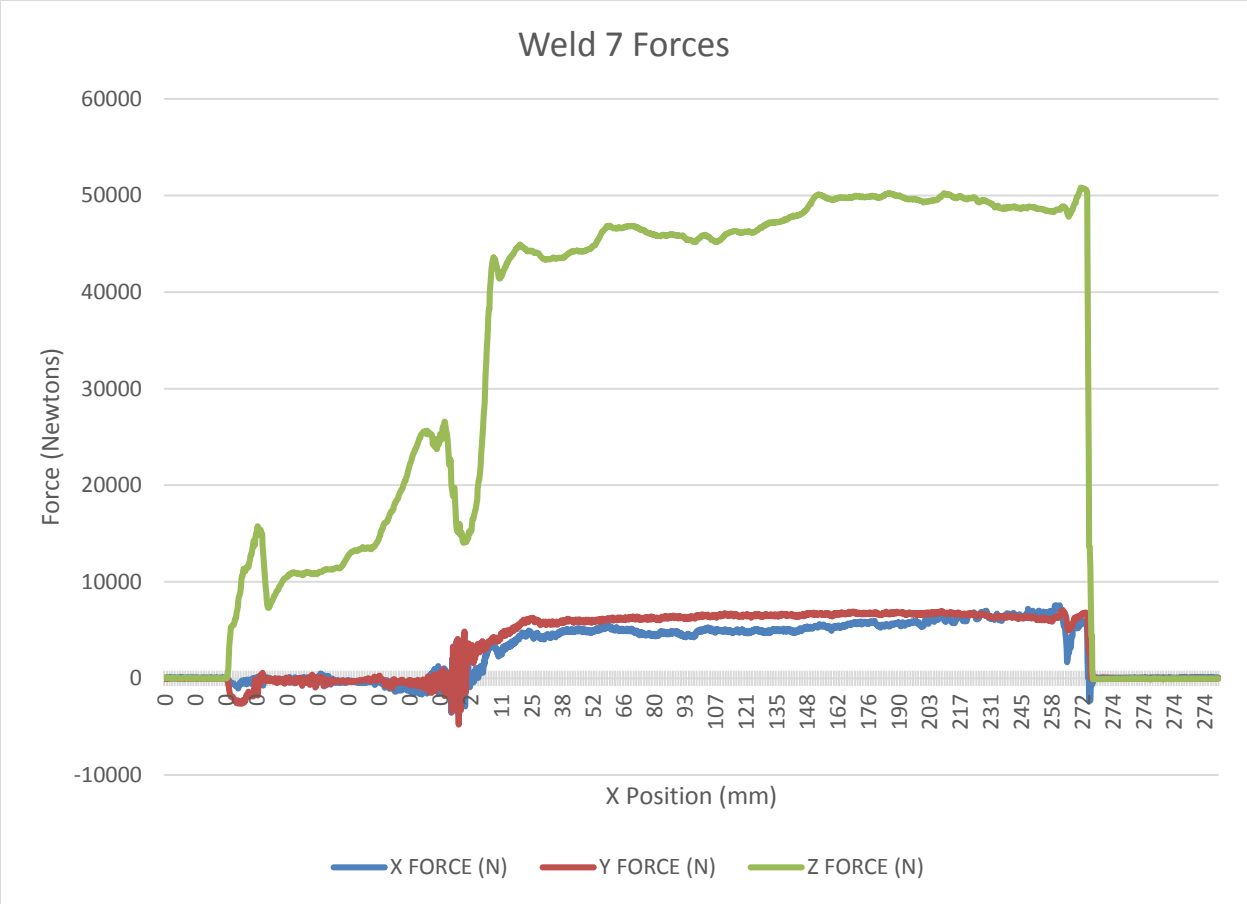

Figure B-7: X, Y and Z forces for Weld 7, Ti-6Al-4V (advancing side) to B21S, 325RPM spindle speed, 125mm/min travel speed.

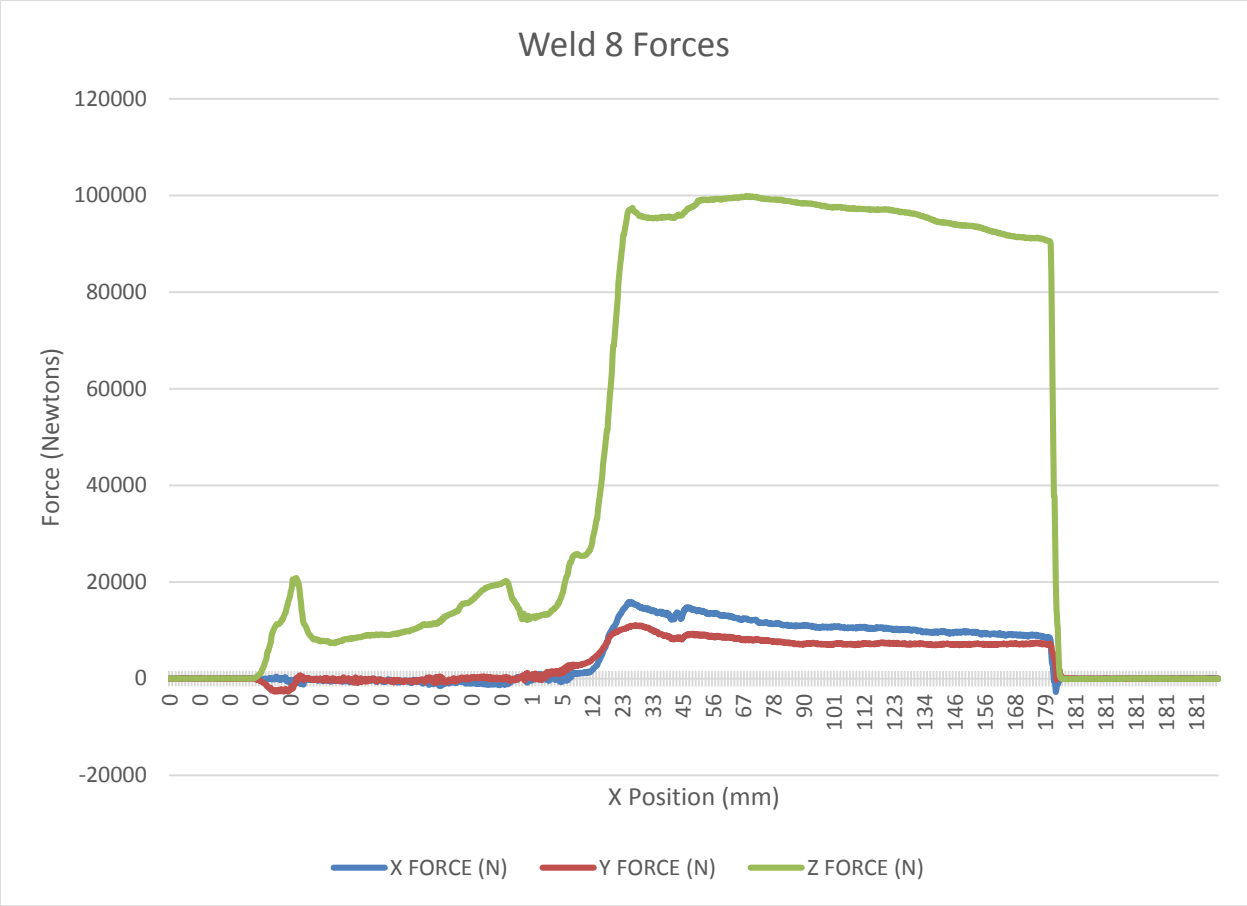

Figure B-8: X, Y and Z forces for Weld 8, Ti-6Al-4V (advancing side) to B21S, 150RPM spindle speed, 125mm/min travel speed.

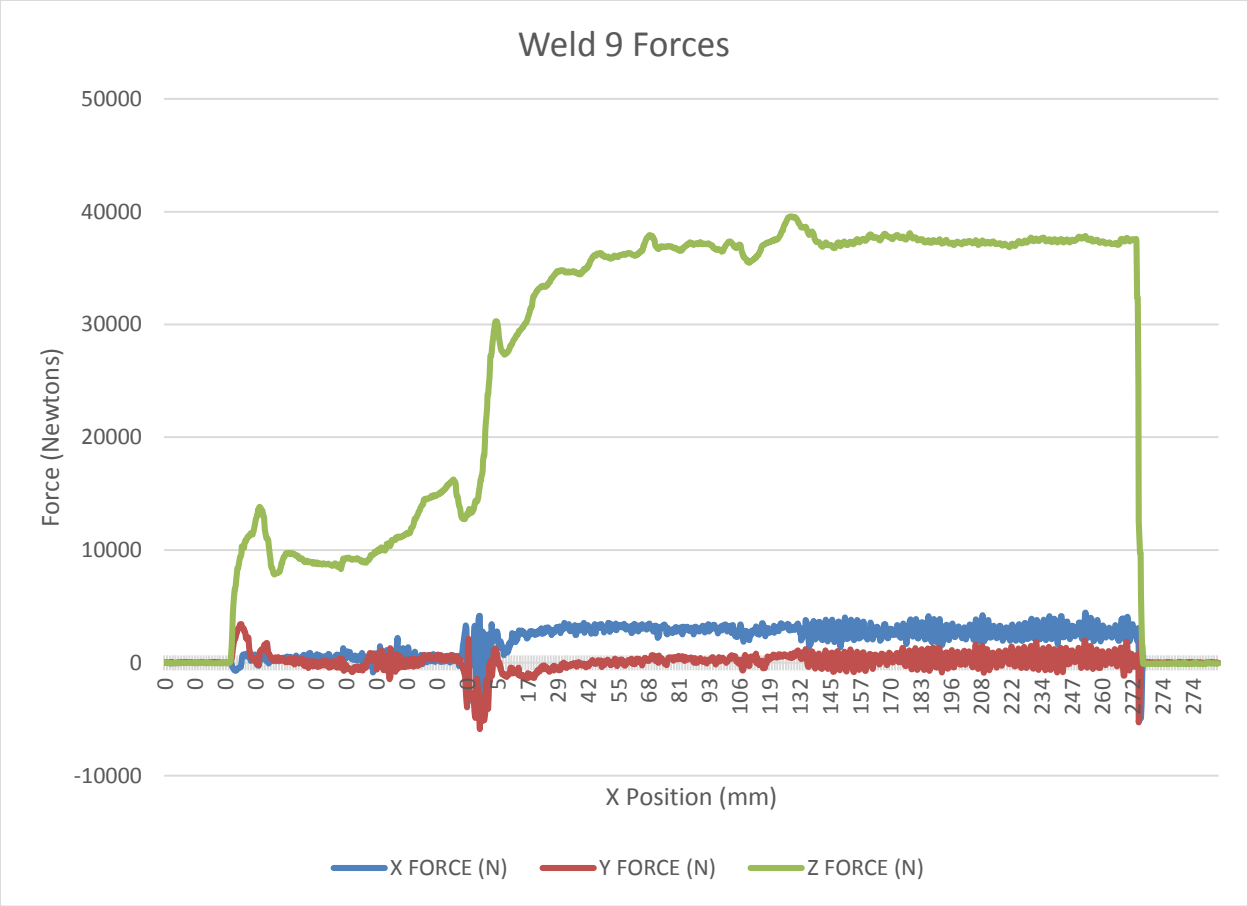

Figure B-9: X, Y and Z forces for Weld 9, Ti-6Al-4V (retreating side) to B21S, 275RPM spindle speed, 125mm/min travel speed.

APPENDIX C – ENERGY DISPERSIVE X-RAY SPECTROSCOPY LINE SCANS

Energy dispersive x-ray spectroscopy (EDS) line scans were gathered for the nine Ti-6Al-4V to B21S friction stir welds discussed in **Chapter 5**. Details for specimen preparation can be found in **Section 5.3** and **5.5**. Spectrum data for plotting is smoothed using a simple 5-point rolling average, with the elements Aluminum, Vanadium, Molybdenum and Chromium shown. A secondary electron image is provided at the same location, with the line path shown. Locations for data collection are denoted as Zone 1-4, representing characteristic locations in a FSW joint and are shown schematically in **Figure C-1**. Weld parameters are shown in **Table C-1**.

Table C-1: Weld parameters.

Weld Identification Number	Advancing Side Alloy	Retreating Side Alloy	Stock Thickness (mm)	Weld Seam Length (mm)	Tool Rotation (RPM)	Travel Speed (mm/min)
1	Ti-6Al-4V	β21S	4.5	274	600	75
2	Ti-6Al-4V	β21S	4.5	274	400	125
3	Ti-6Al-4V	β21S	4.5	274	225	100
4	Ti-6Al-4V	β21S	4.5	268	275	100
5	Ti-6Al-4V	β21S	4.5	272	275	125
6	Ti-6Al-4V	β21S	4.5	276	275	150
7	Ti-6Al-4V	β21S	4.5	274	325	125
8	Ti-6Al-4V	β21S	4.5	177	150	150
9	β21S	Ti-6Al-4V	4.5	274	275	275

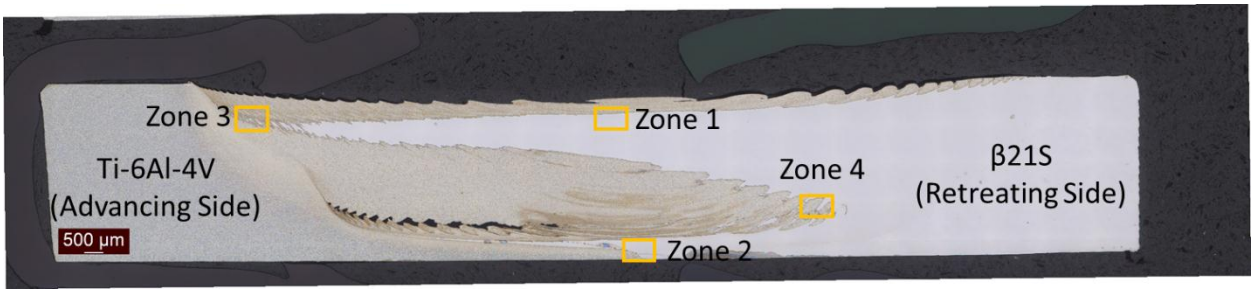

Figure C-1: EDS data collection sites; Weld 5 used as an example.

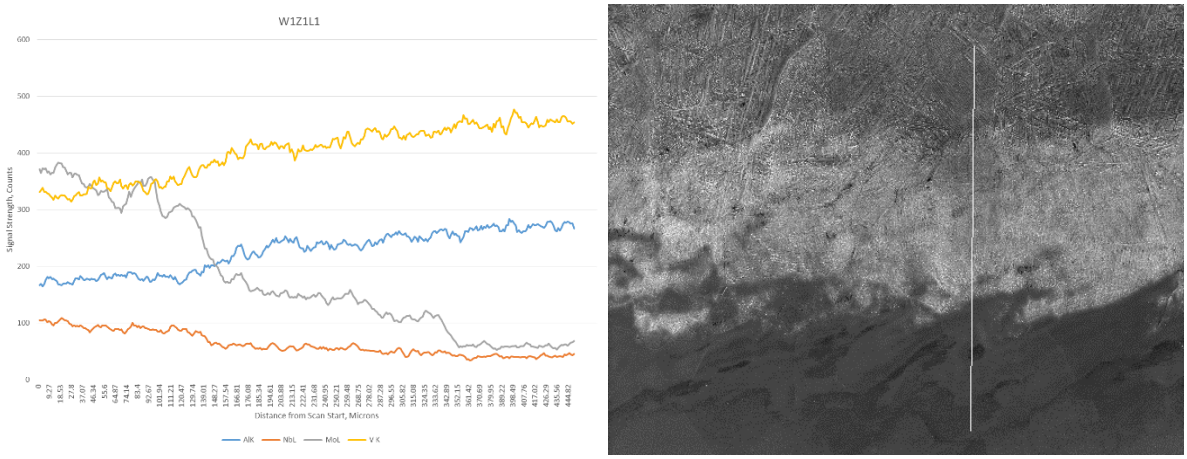

Figure C-2: Weld 1, Zone 1, Line 1.

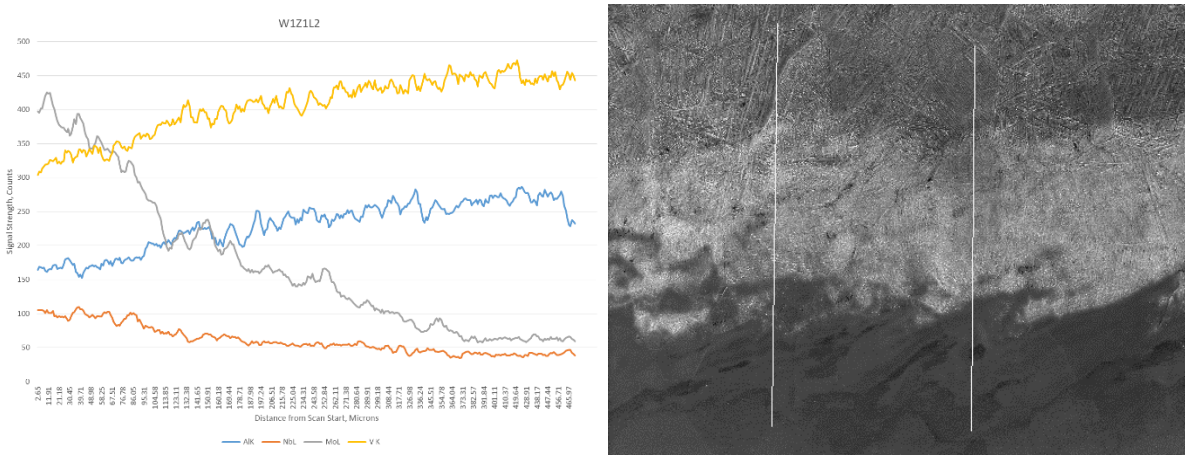

Figure C-3: Weld 1, Zone 1, Line 2 (left).

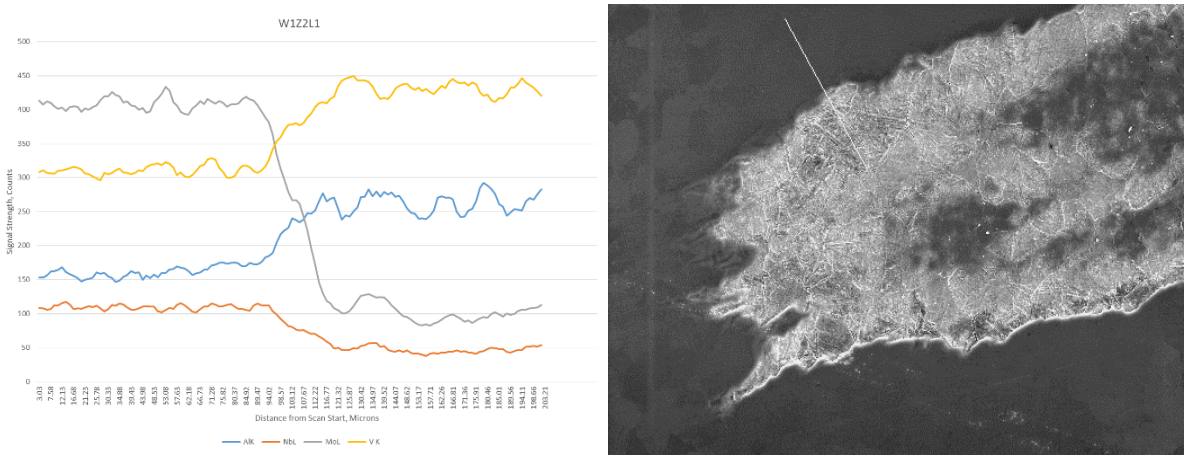

Figure C-4: Weld 1, Zone 2, Line 1.

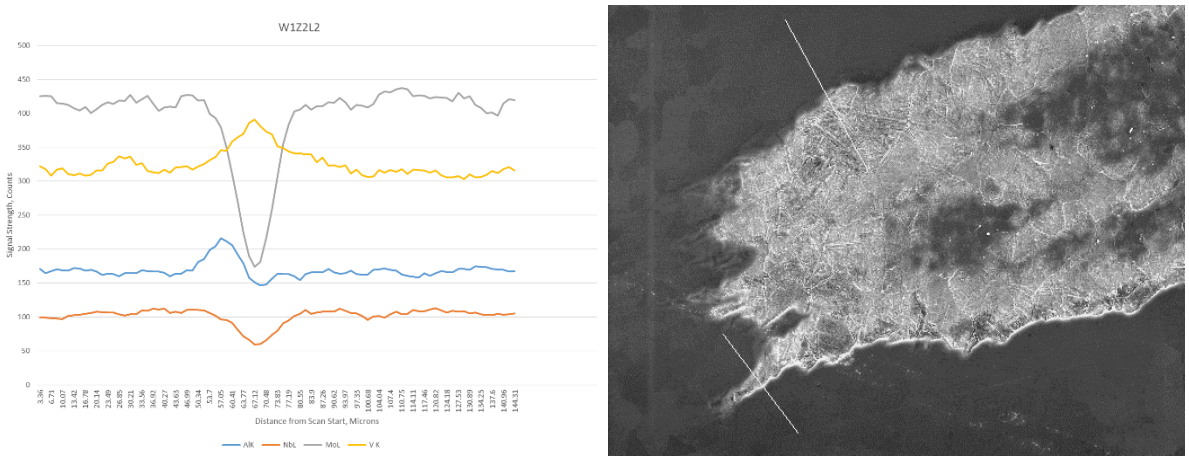

Figure C-5: Weld 1, Zone 2, Line 2 (left).

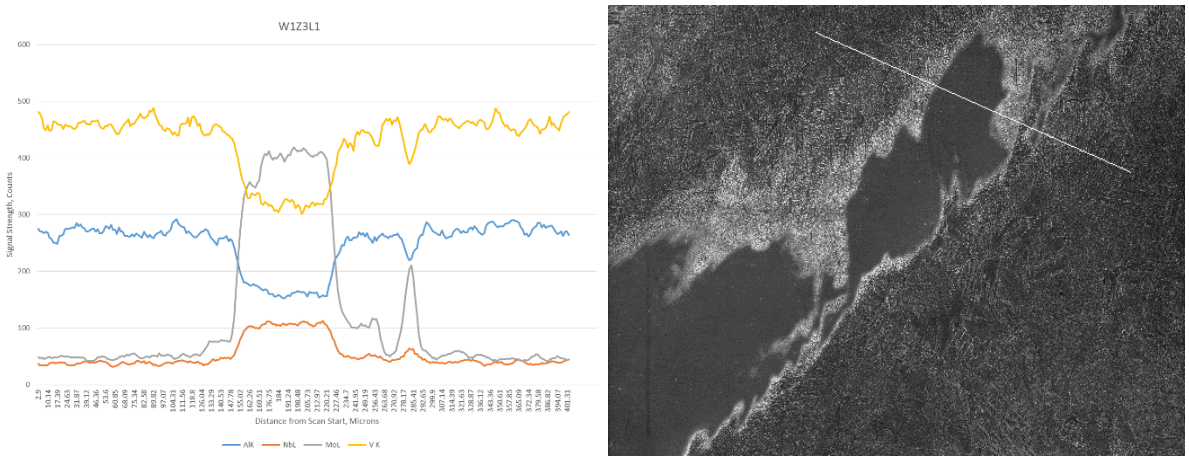

Figure C-6: Weld 1, Zone 3, Line 1.

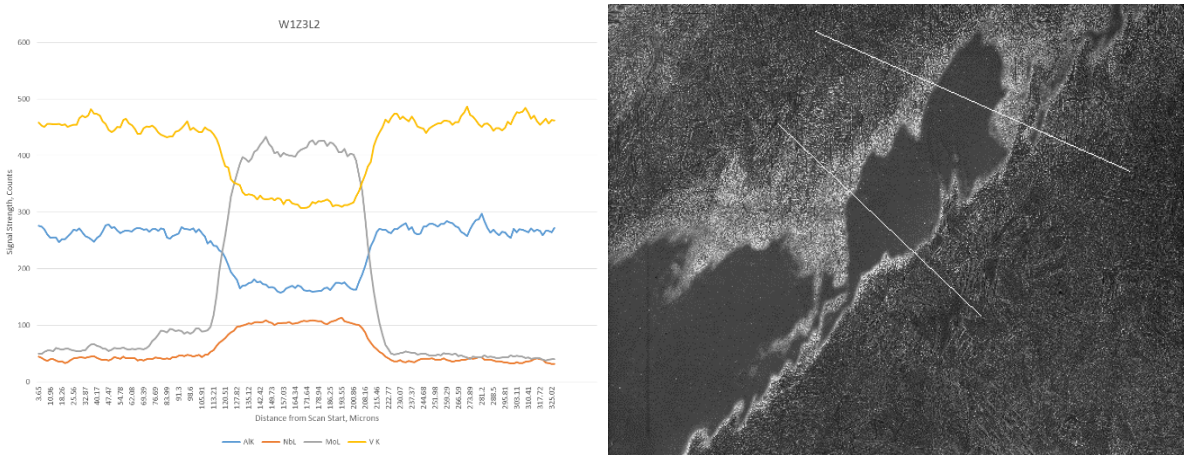

Figure C-7: Weld 1, Zone 3, Line 2 (bottom).

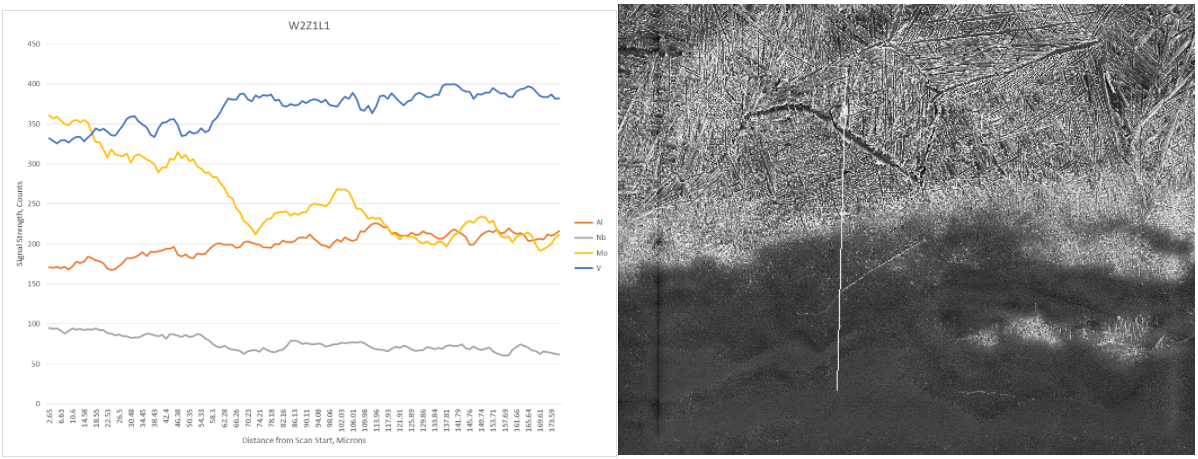

Figure C-8: Weld 2, Zone 1, Line 1.

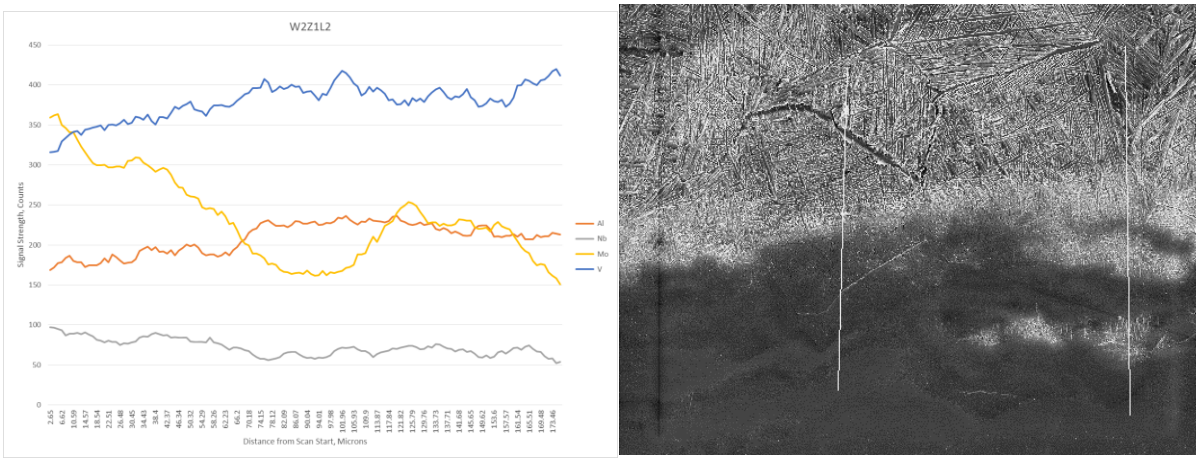

Figure C-9: Weld 2, Zone 1, Line 2 (right).

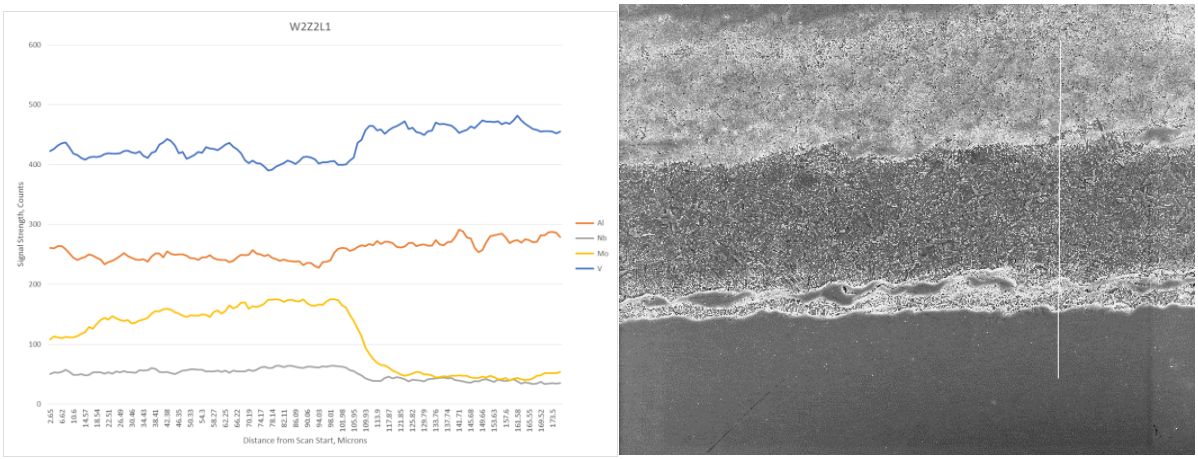

Figure C-10: Weld 2, Zone 2, Line 1.

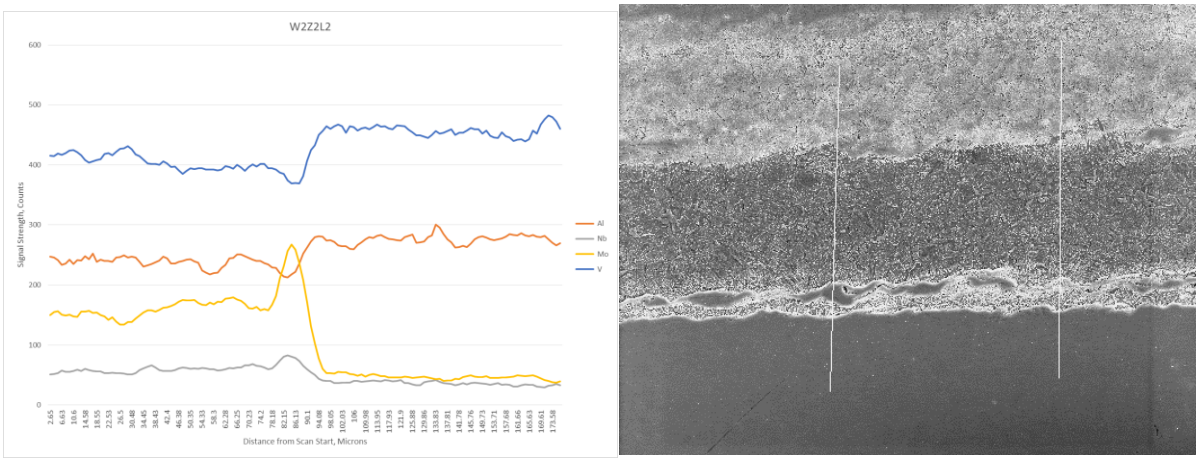

Figure C-11: Weld 2, Zone 2, Line 2 (right).

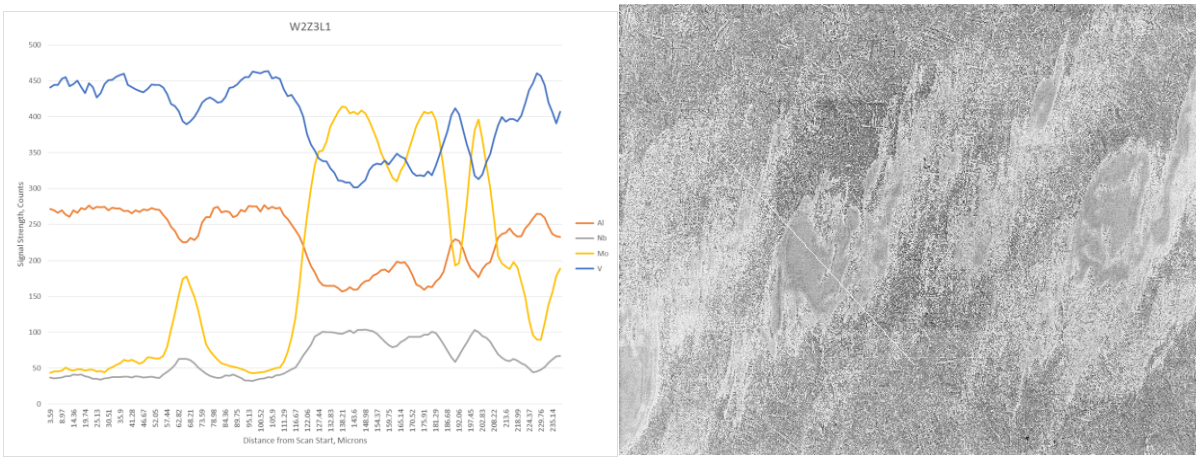

Figure C-12: Weld 2, Zone 3, Line 1.

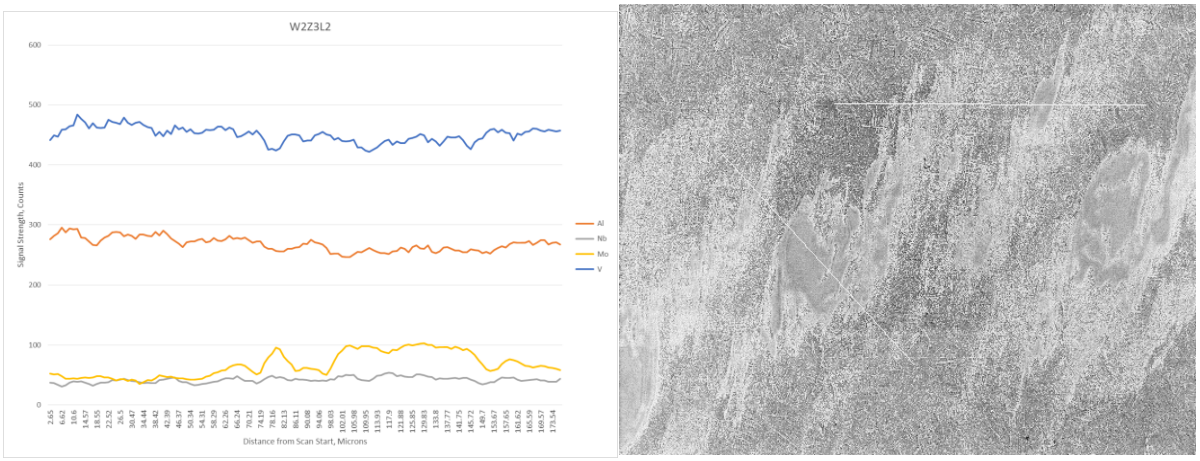

Figure C-13: Weld 2, Zone 3, Line 2 (top).

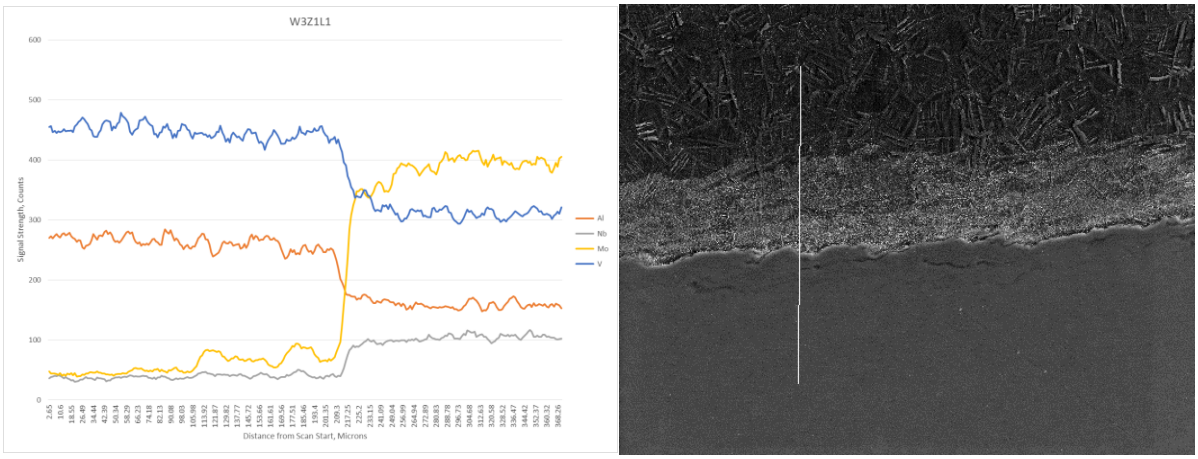

Figure C-14: Weld 3, Zone 1, Line 1.

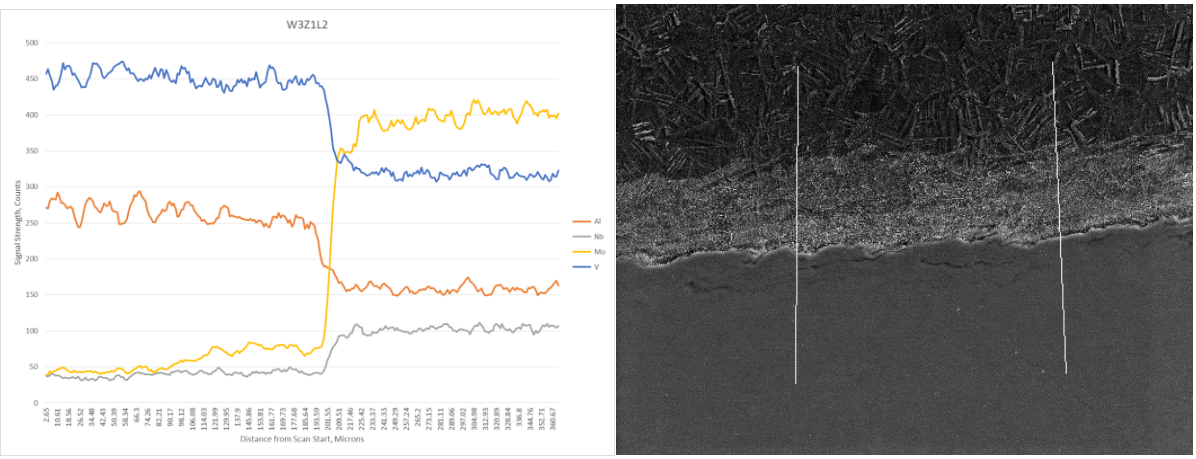

Figure C-15: Weld 3, Zone 1, Line 1 (right).

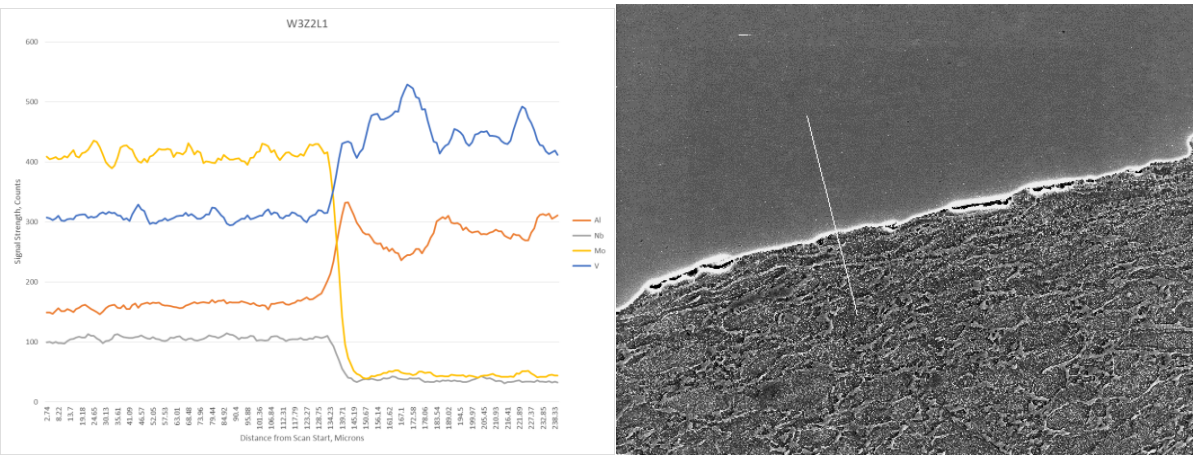

Figure C-16: Weld 3, Zone 2, Line 1.

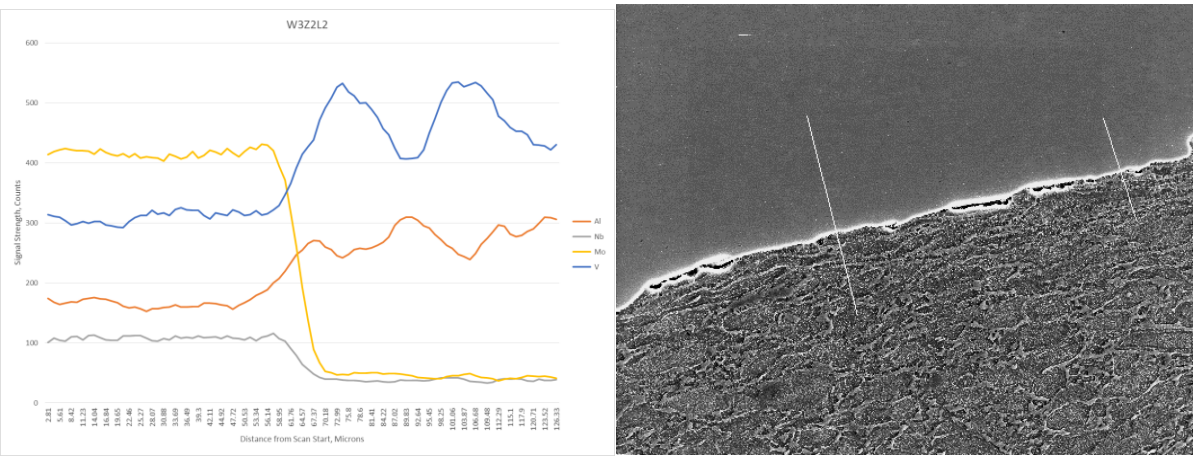

Figure C-17: Weld 3, Zone 2, Line 2 (right).

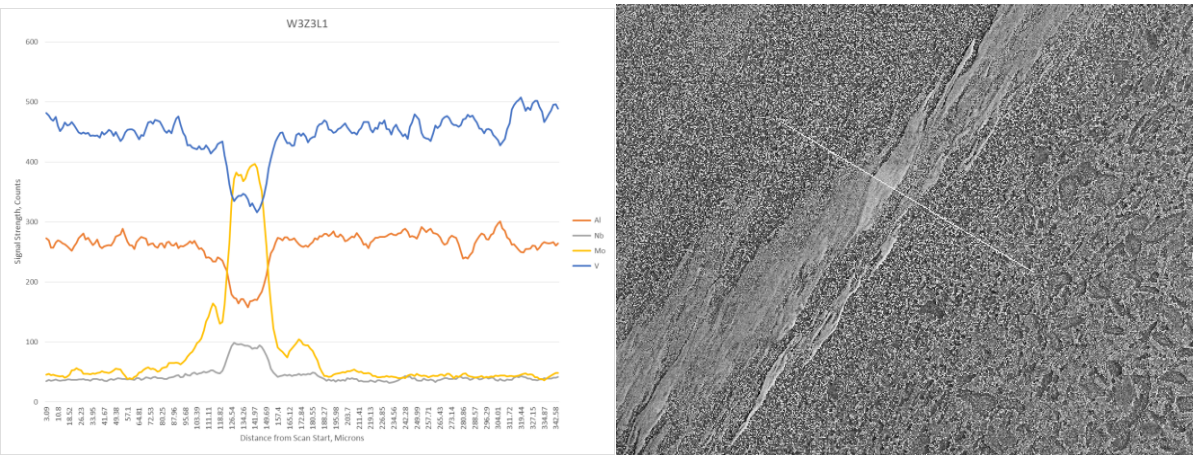

Figure C-18: Weld 3, Zone 3, Line 1.

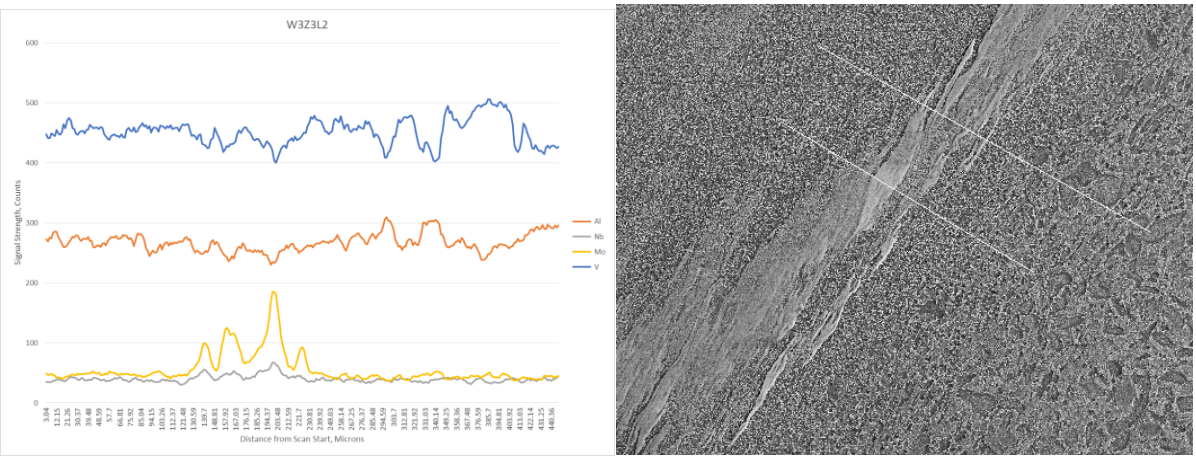

Figure C-19: Weld 3, Zone 3, Line 2 (top).

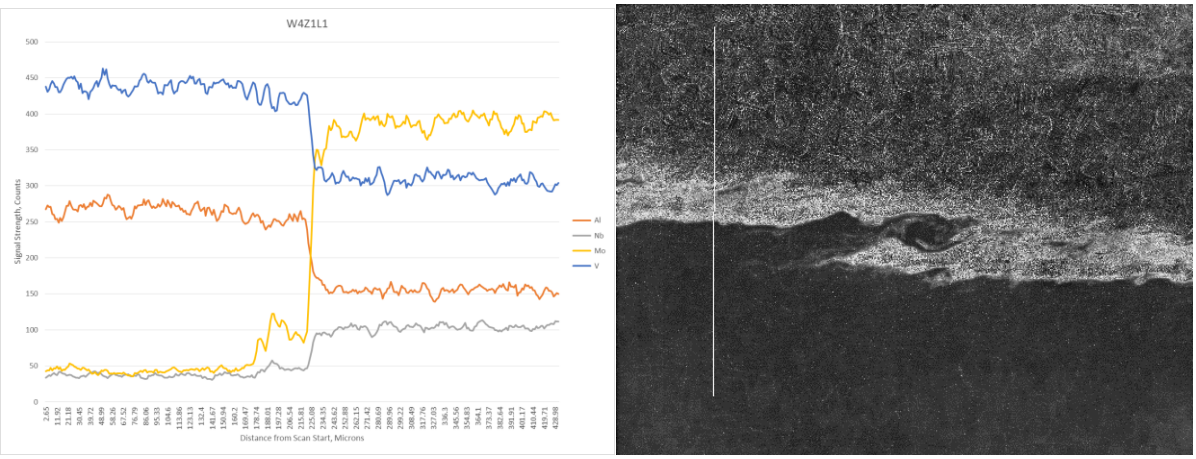

Figure C-20: Weld 4, Zone 1, Line 1.

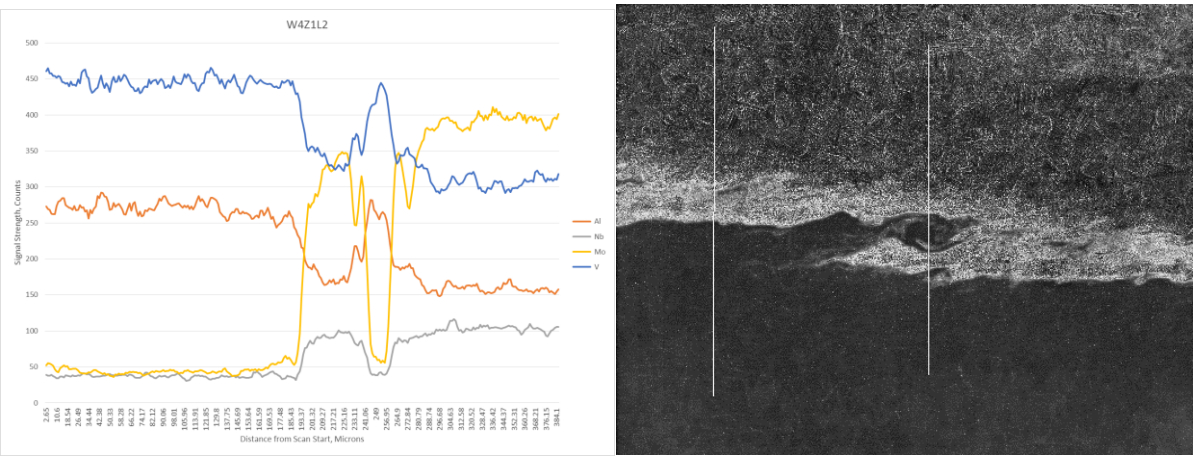

Figure C-21: Weld 4, Zone 1, Line 2 (right).

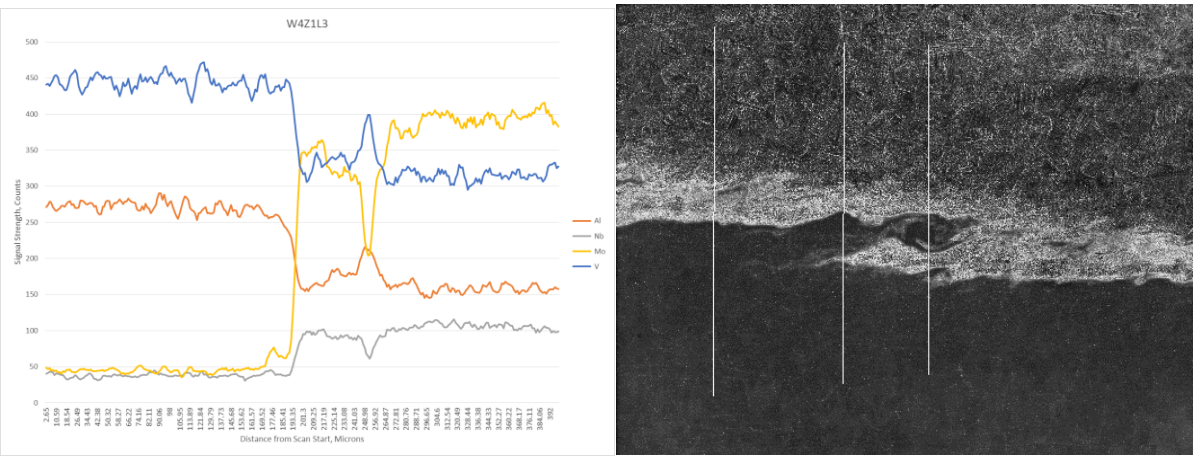

Figure C-22: Weld 4, Zone 1, Line 3 (middle).

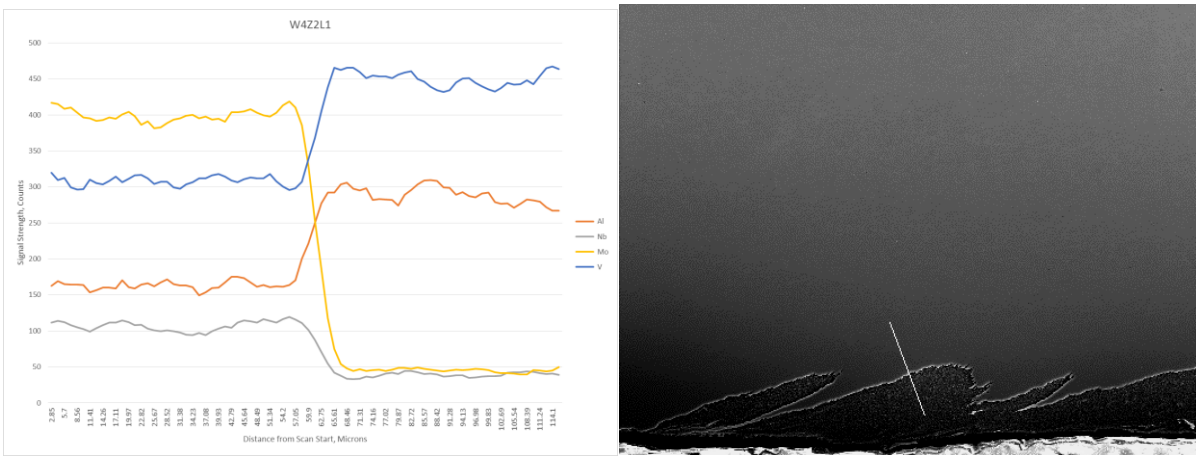

Figure C-23: Weld 4, Zone 2, Line 1.

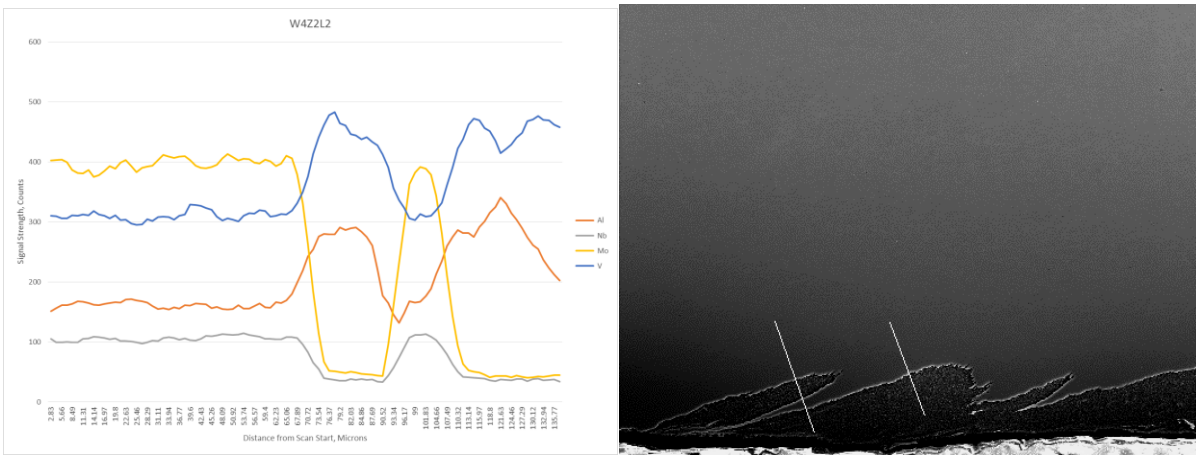

Figure C-24: Weld 4, Zone 2, Line 2 (left).

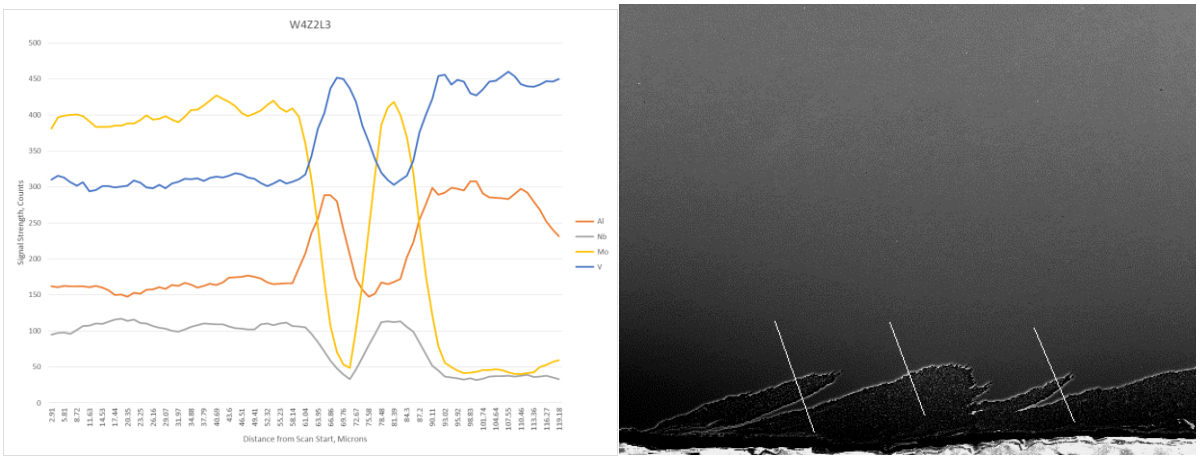

Figure C-25: Weld 4, Zone 2, Line 3 (right).

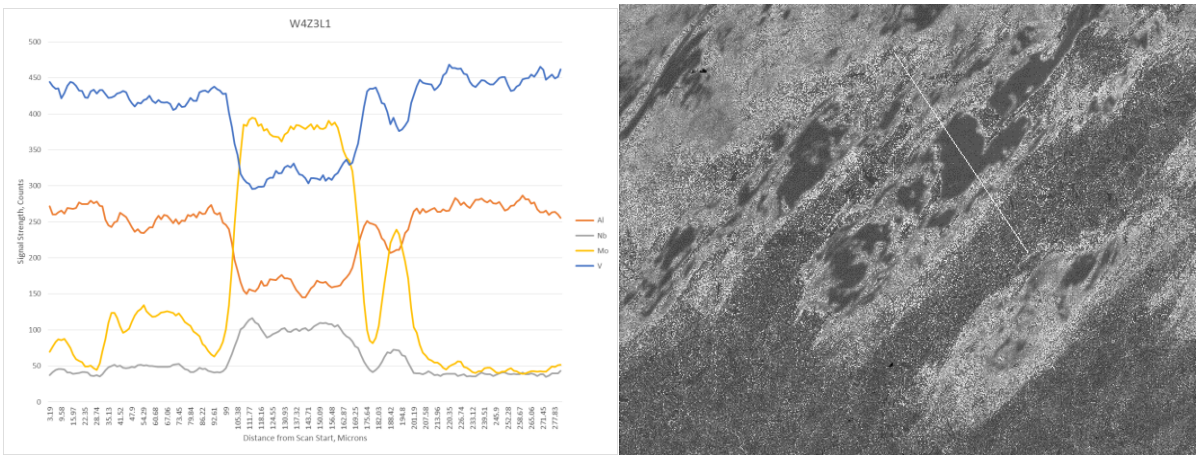

Figure C-26: Weld 4, Zone 3, Line 1.

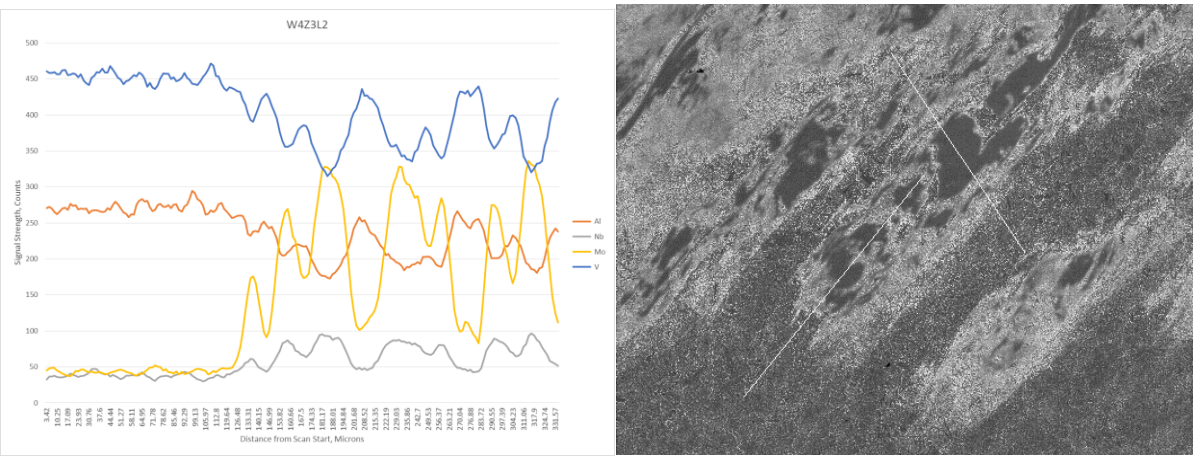

Figure C-27: Weld 4, Zone 3, Line 2 (bottom).

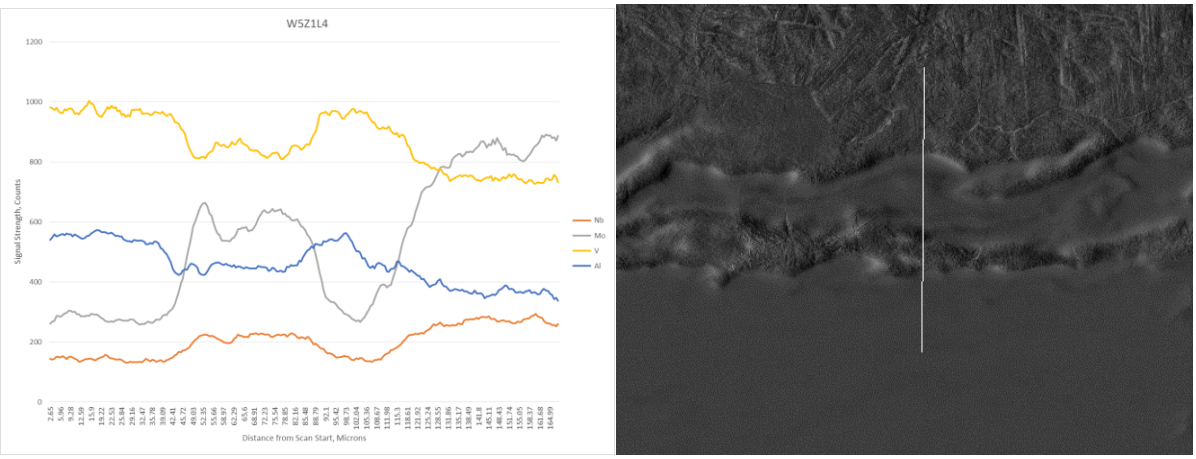

Figure C-28: Weld 5, Zone 1, Line 4.

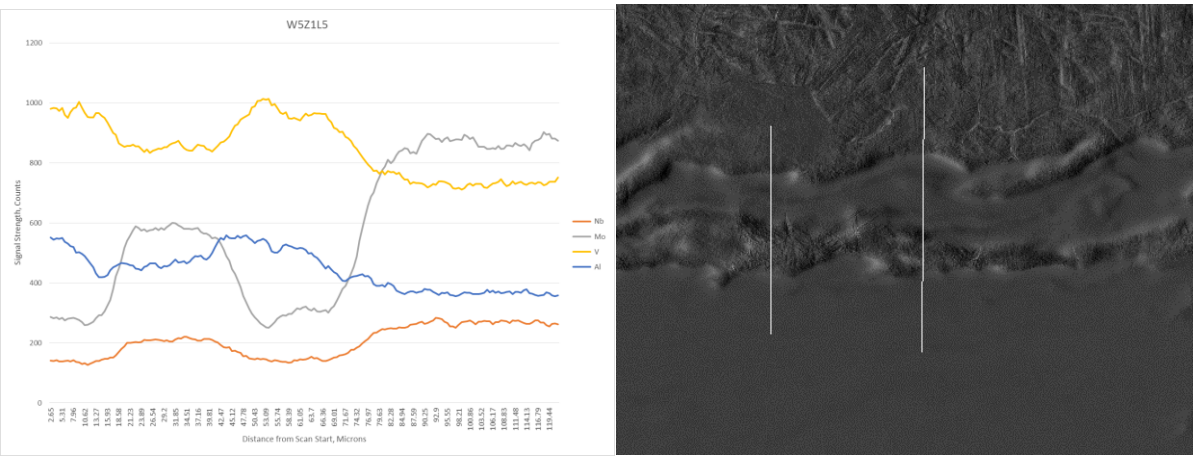

Figure C-29: Weld 5, Zone 1, Line 5 (left).

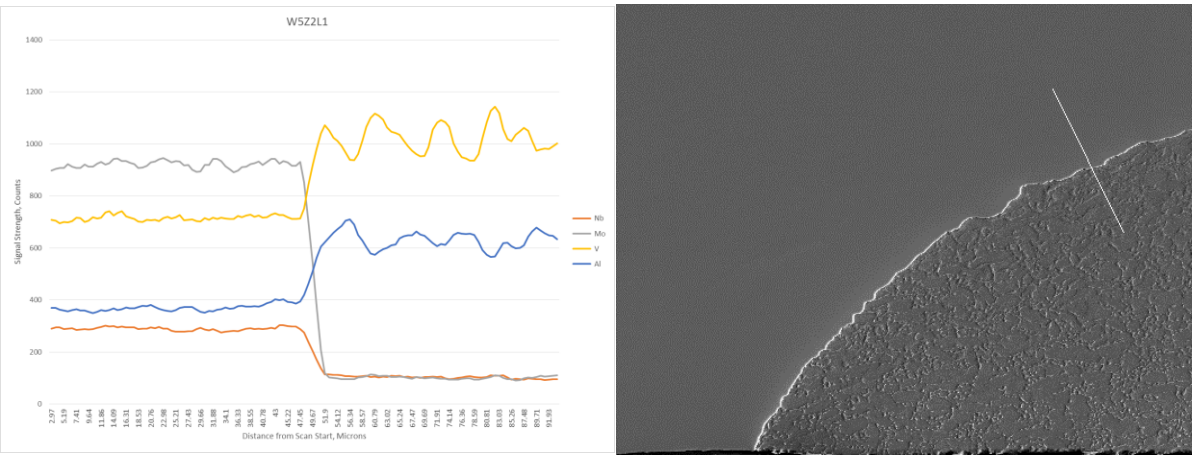

Figure C-30: Weld 5, Zone 2, Line 1.

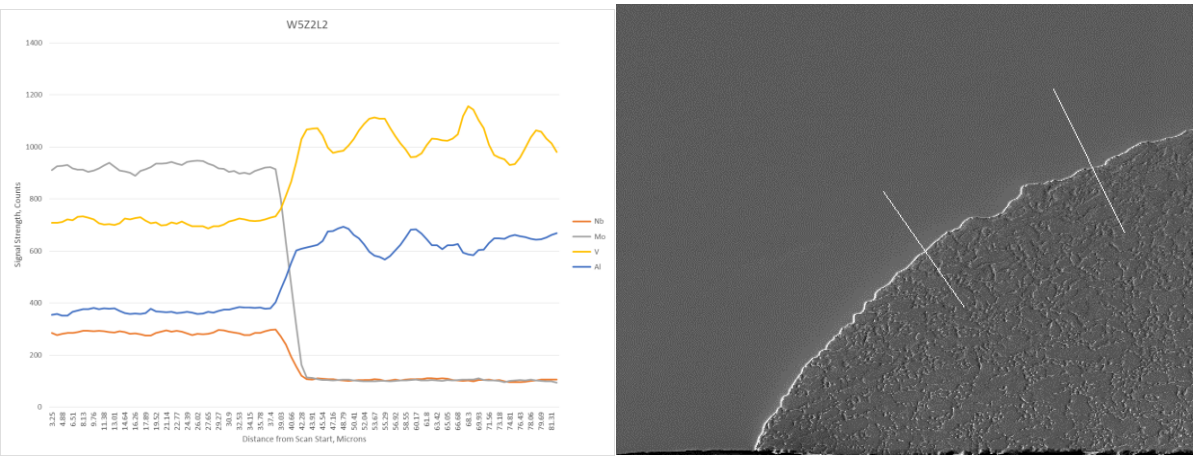

Figure C-31: Weld 5, Zone 2, Line 2 (left).

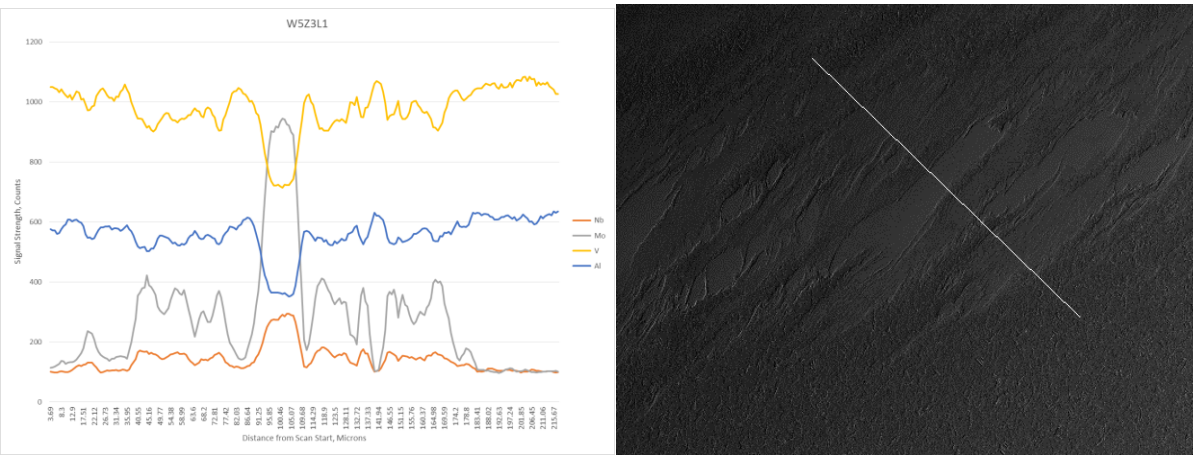

Figure C-32: Weld 5, Zone 3, Line 1.

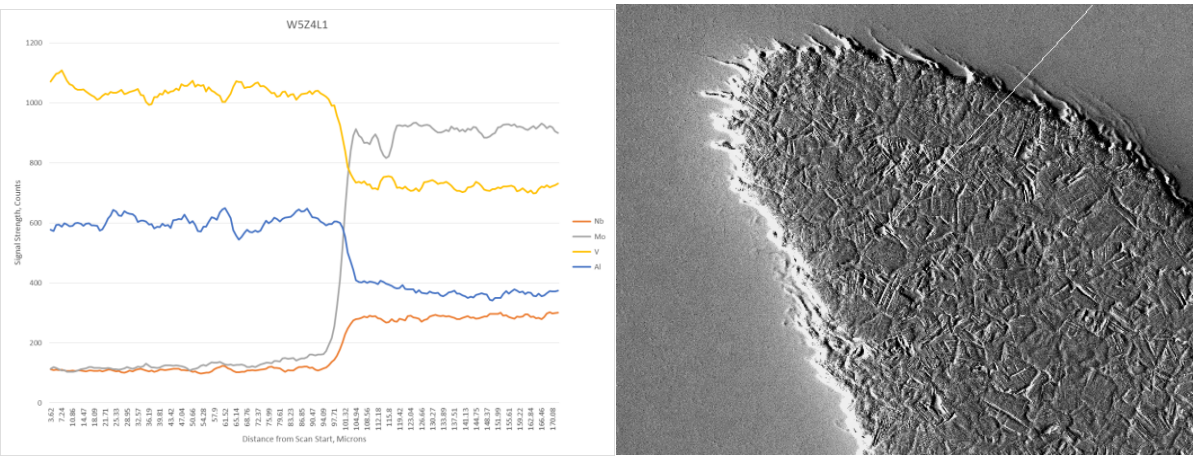

Figure C-33: Weld 5, Zone 4, Line 1.

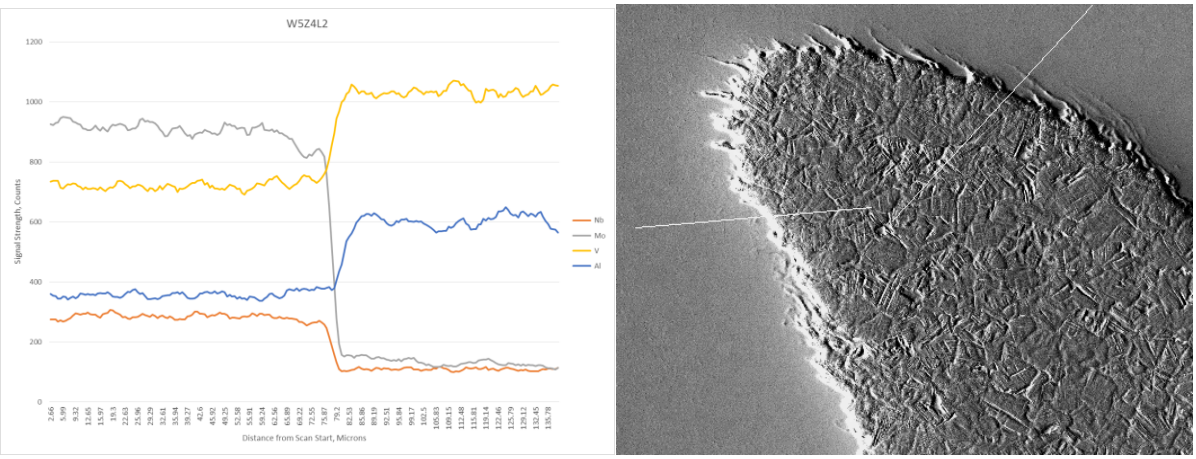

Figure C-34: Weld 5, Zone 4, Line 2 (left).

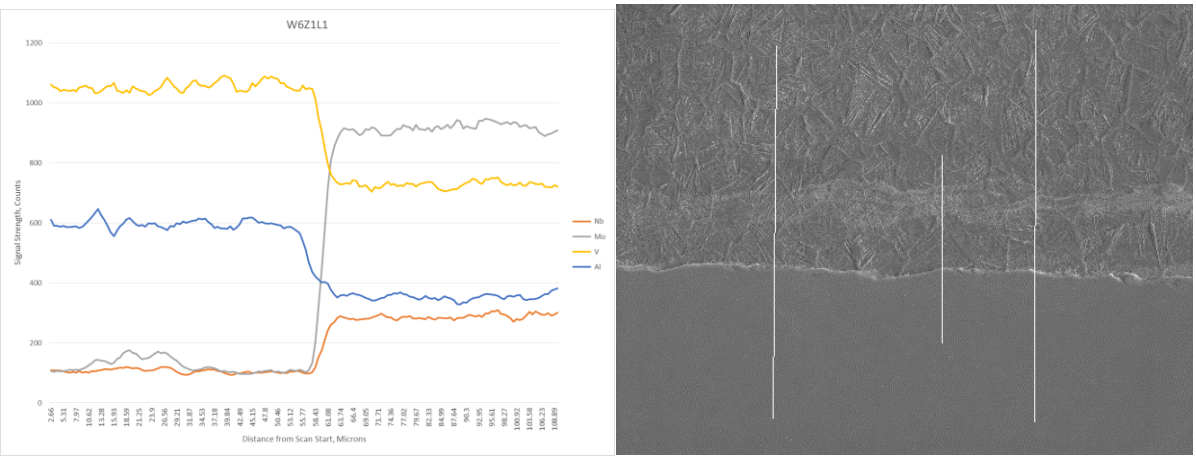

Figure C-35: Weld 6, Zone 1, Line 1 (left).

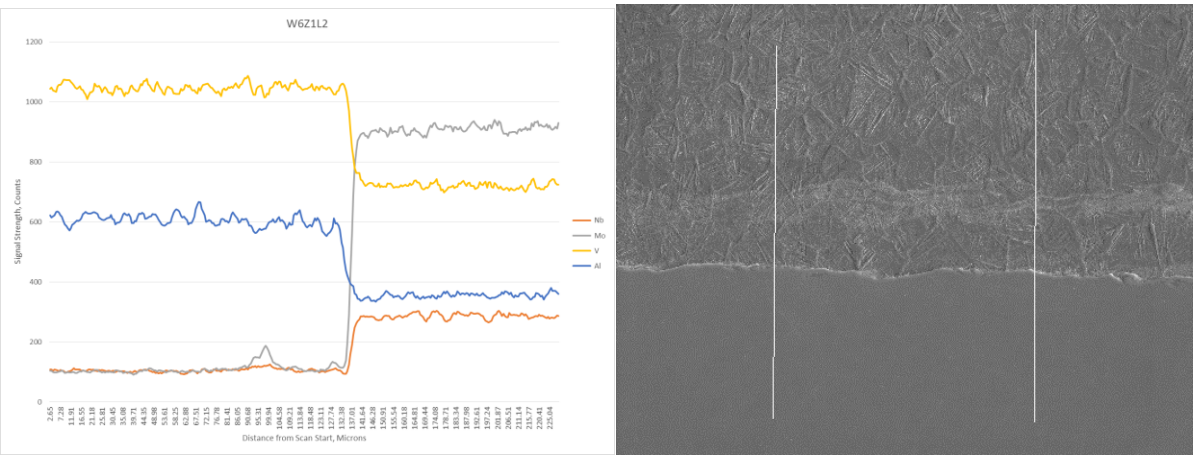

Figure C-36: Weld 6, Zone 1, Line 2 (right).

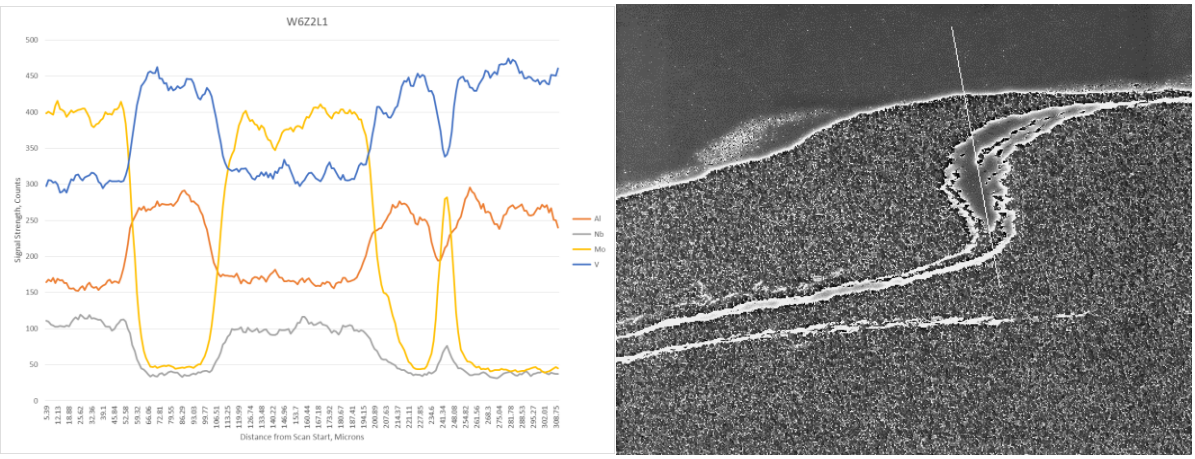

Figure C-37: Weld 6, Zone 2, Line 1.

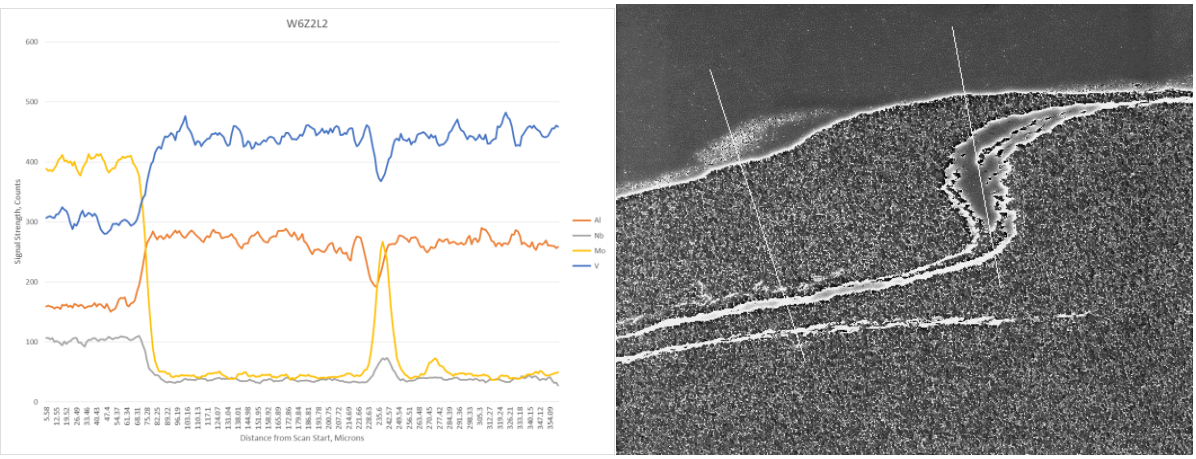

Figure C-38: Weld 6, Zone 2, Line 2 (left).

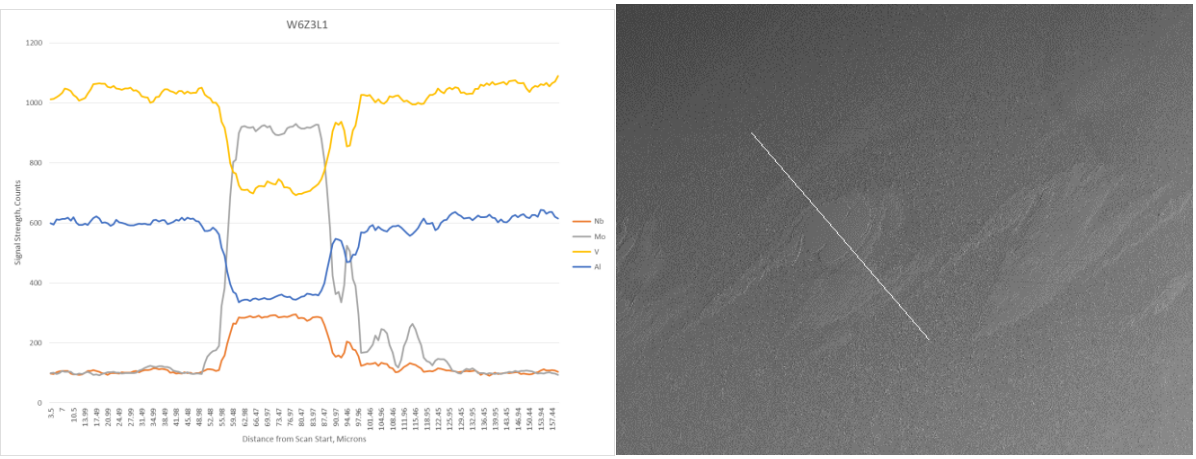

Figure C-39: Weld 6, Zone 3, Line 1.

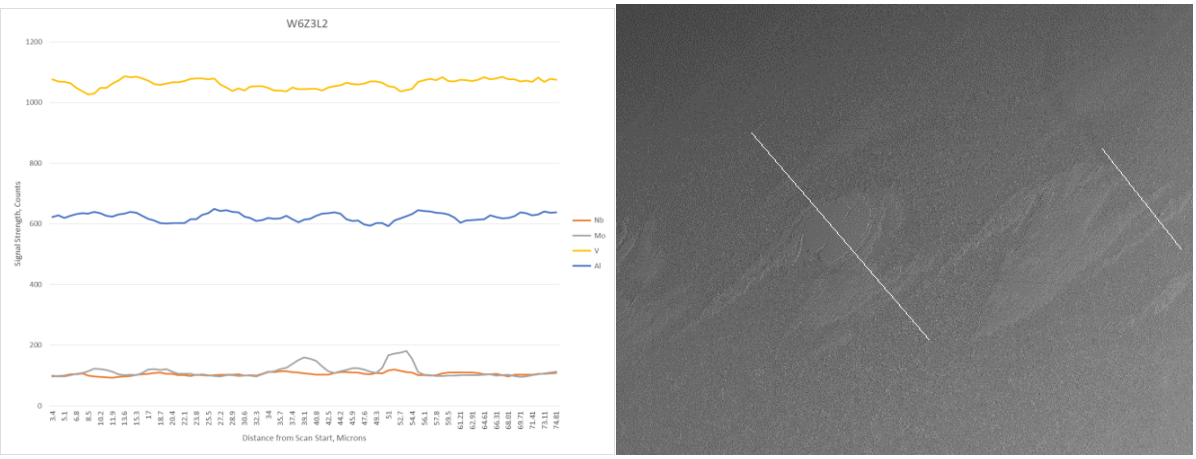

Figure C-40: Weld 6, Zone 3, Line 2 (right).

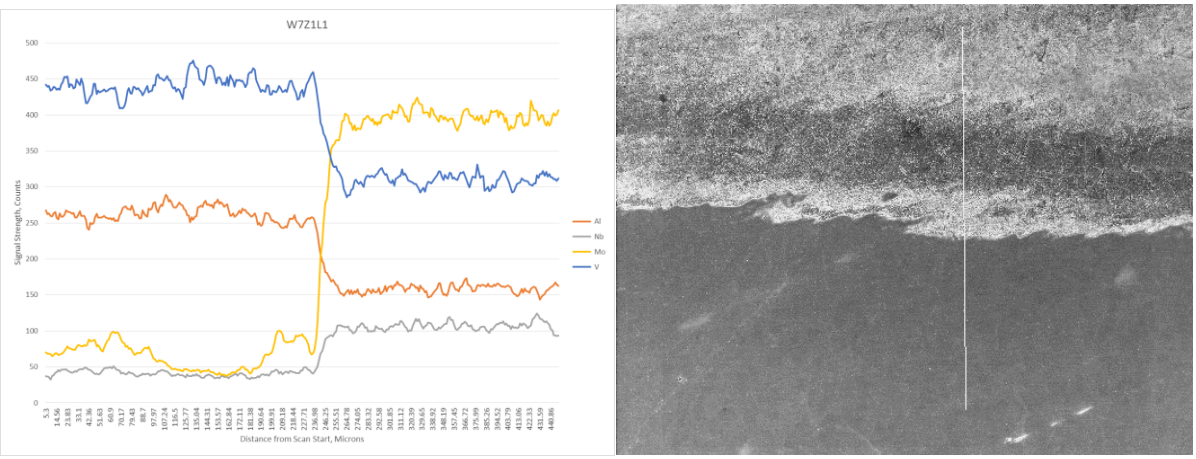

Figure C-41: Weld 7, Zone 1, Line 1.

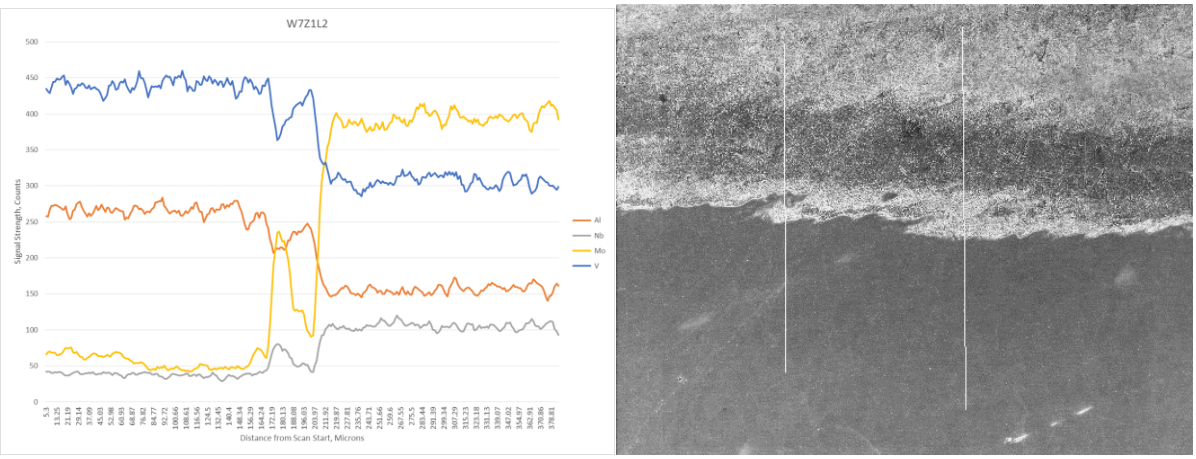

Figure C-42: Weld 7, Zone 1, Line 2 (right).

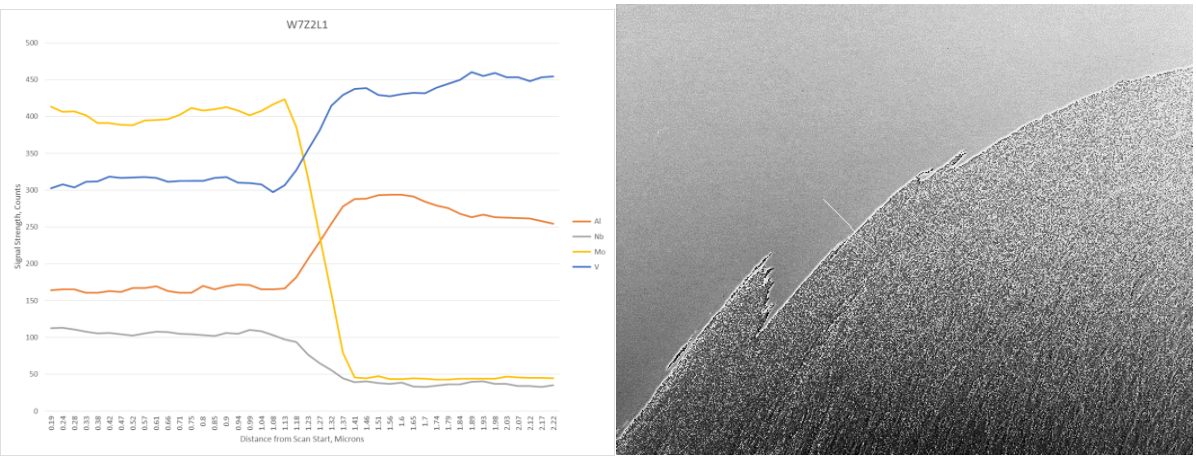

Figure C-43: Weld 7, Zone 2, Line 1.

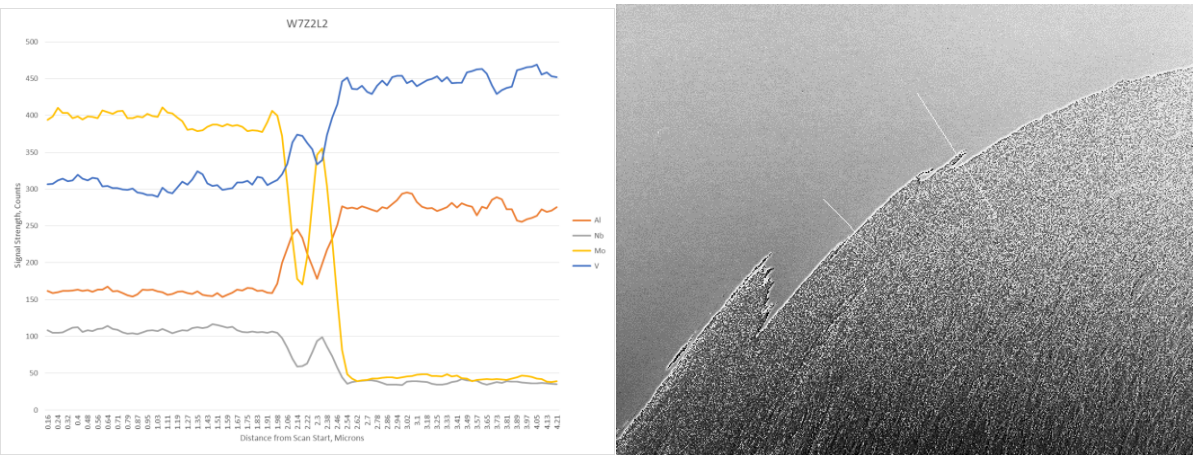

Figure C-44: Weld 7, Zone 2, Line 2 (top).

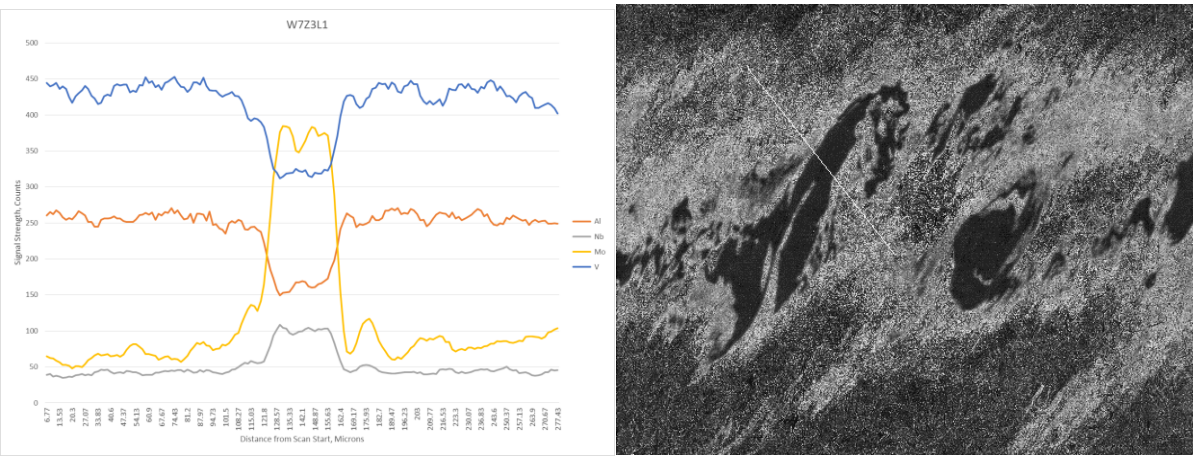

Figure C-45: Weld 7, Zone 3, Line 1.

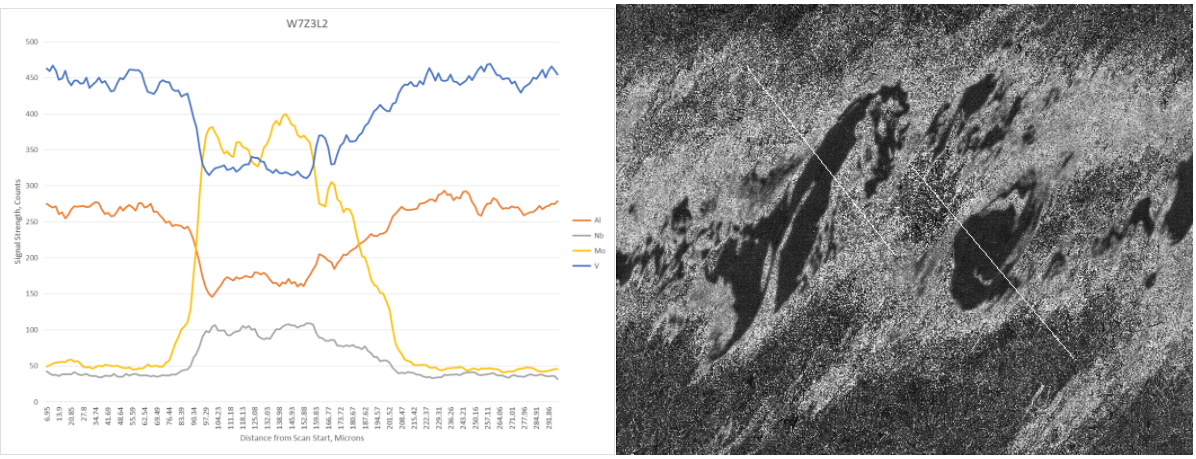

Figure C-46: Weld 7, Zone 3, Line 2 (right).

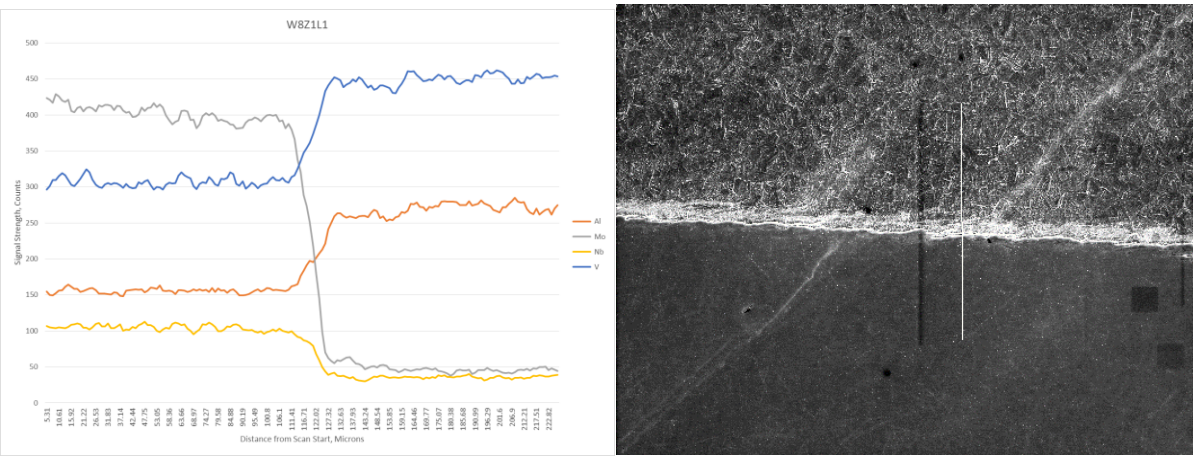

Figure C-47: Weld 8, Zone 1, Line 1.

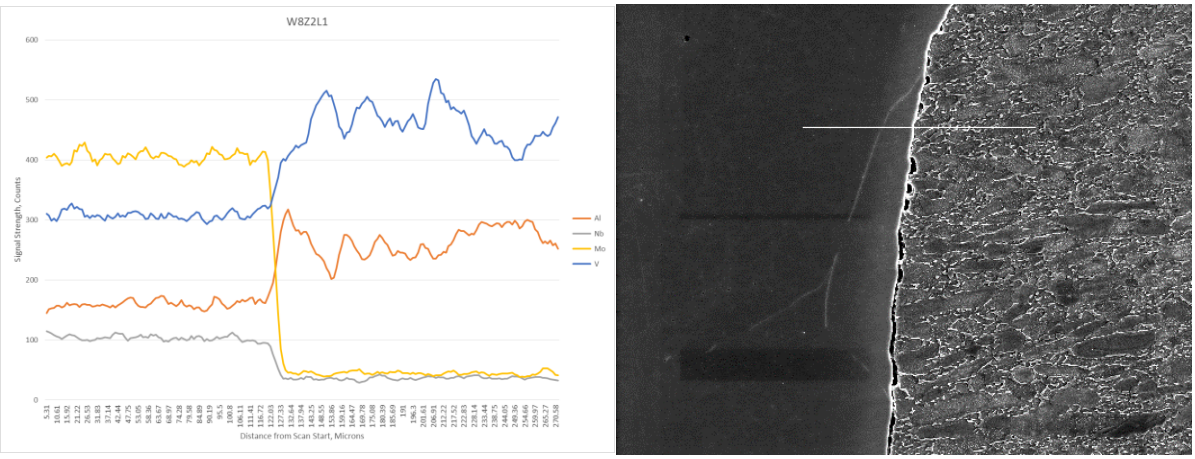

Figure C-48: Weld 8, Zone 2, Line 1.

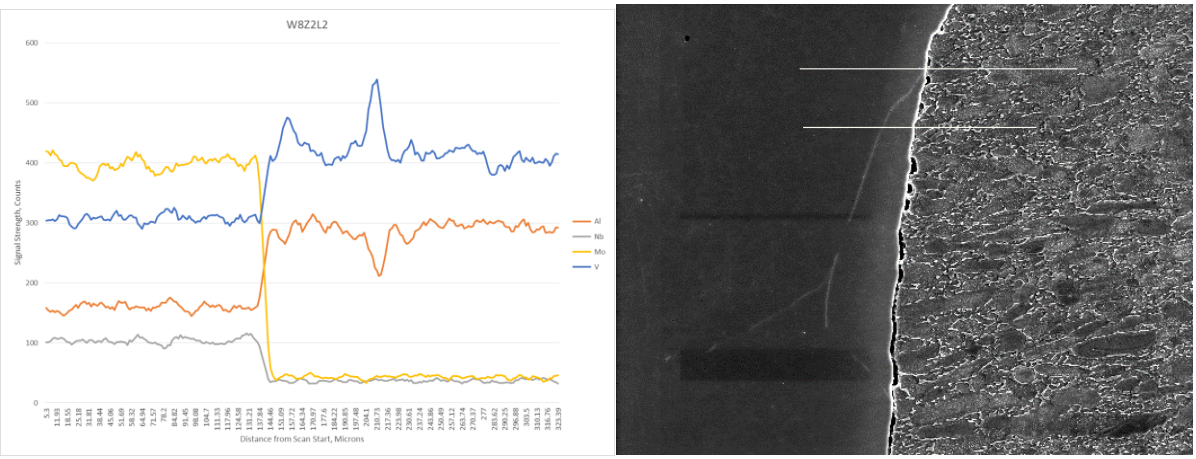

Figure C-49: Weld 8, Zone 2, Line 2 (top).

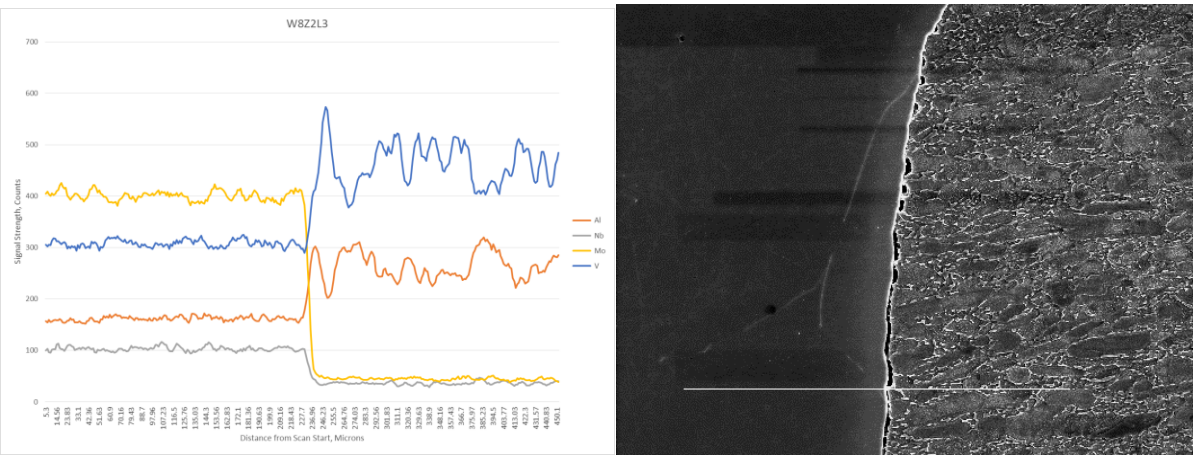

Figure C-50: Weld 8, Zone 2, Line 3.

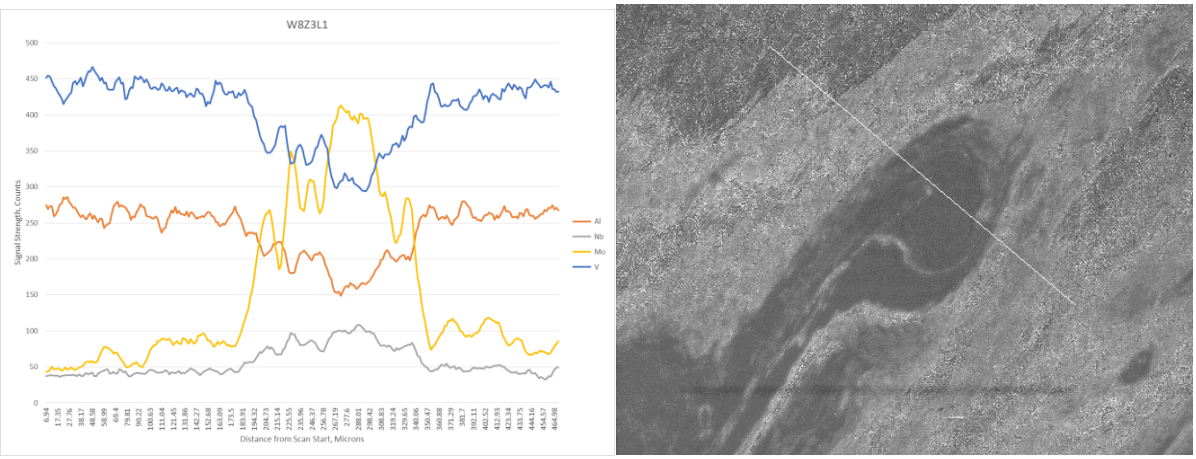

Figure C-51: Weld 8, Zone 3, Line 1.

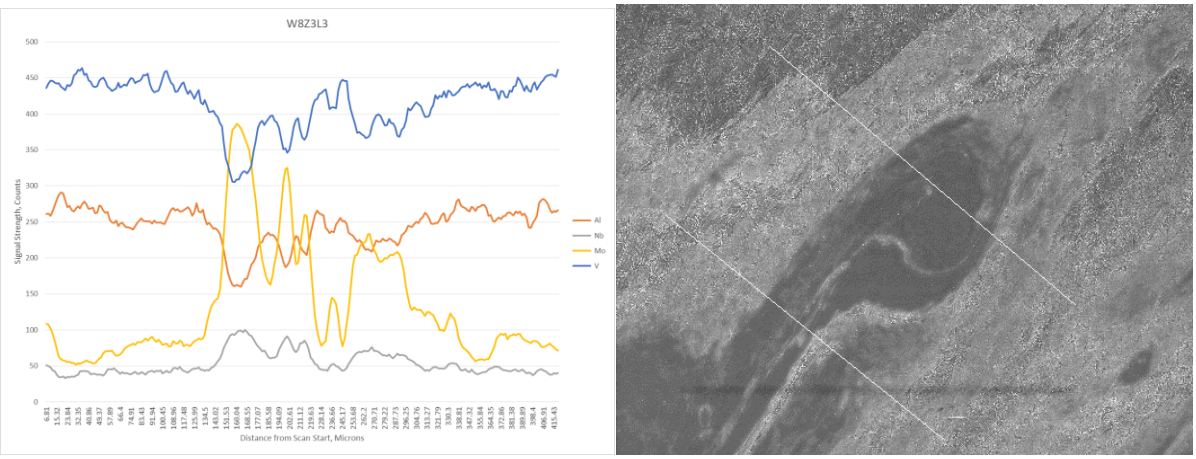

Figure C-52: Weld 8, Zone 3, Line 3 (bottom).

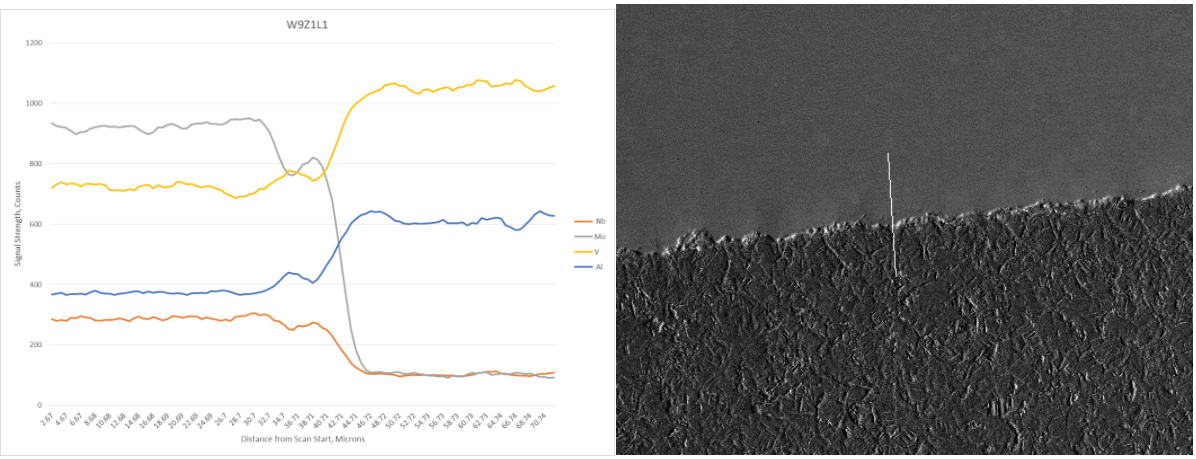

Figure C-53: Weld 9, Zone 1, Line 1.

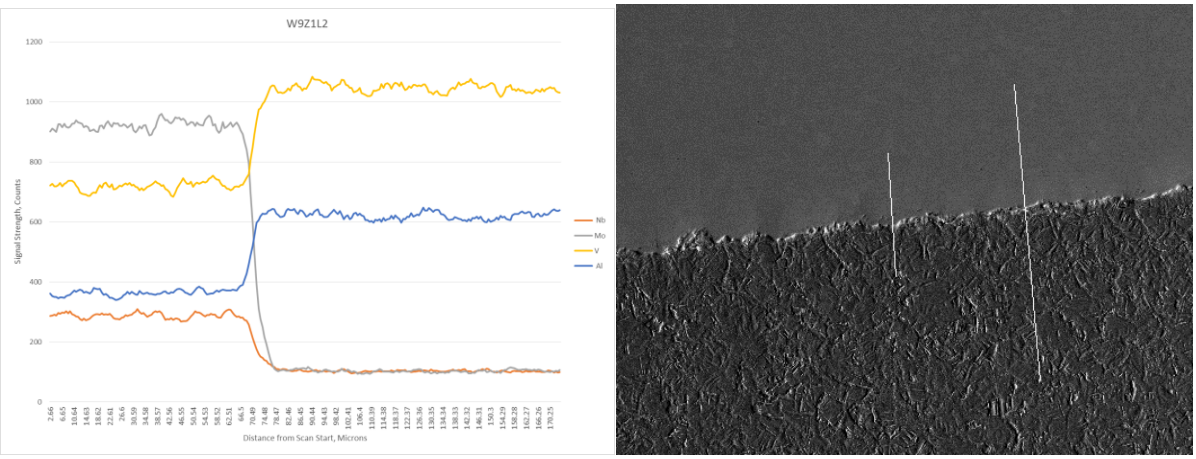

Figure C-54: Weld 9, Zone 1, Line 2 (right).

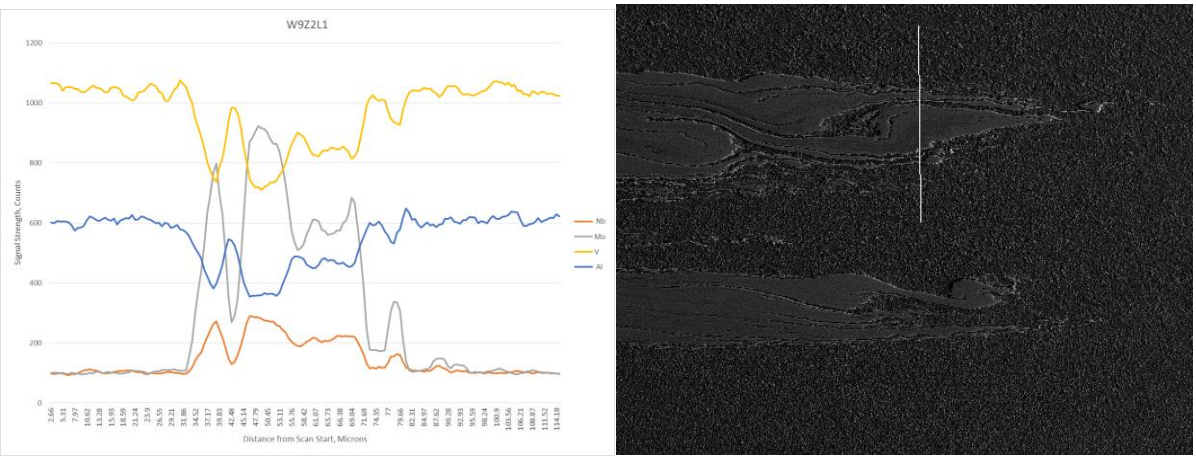

Figure C-55: Weld 9, Zone 2, Line 1.

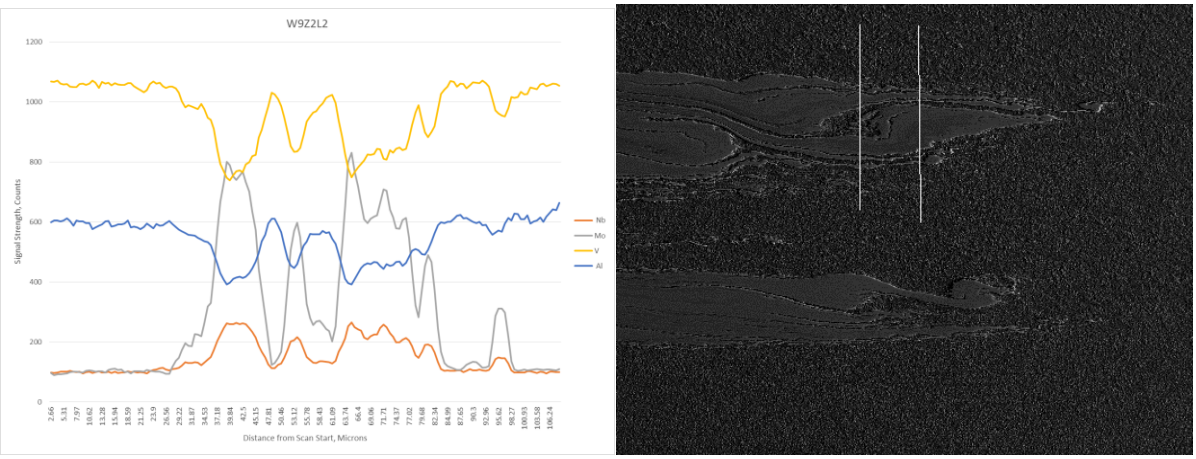

Figure C-56: Weld 9, Zone 2, Line 2 (left).

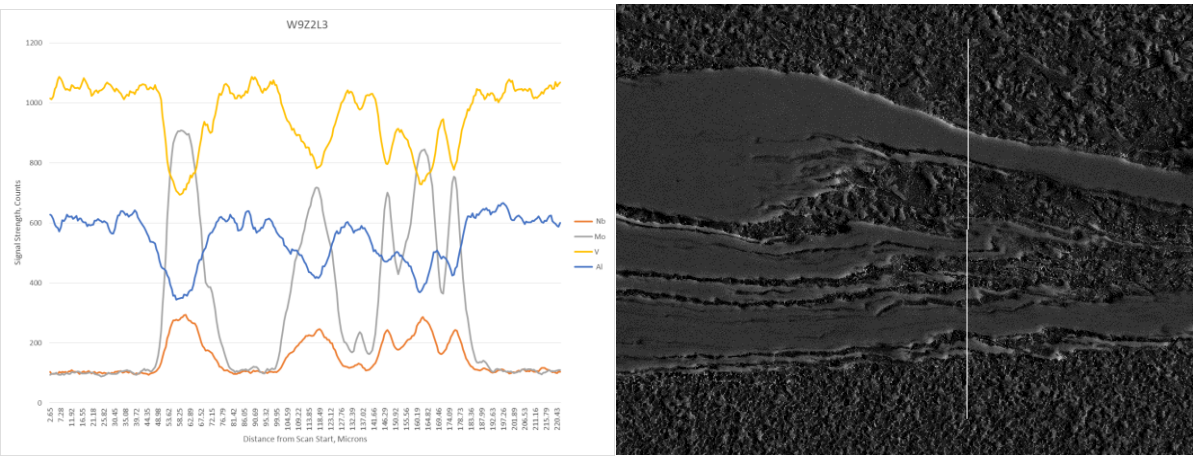

Figure C-57: Weld 9, Zone 2, Line 3.

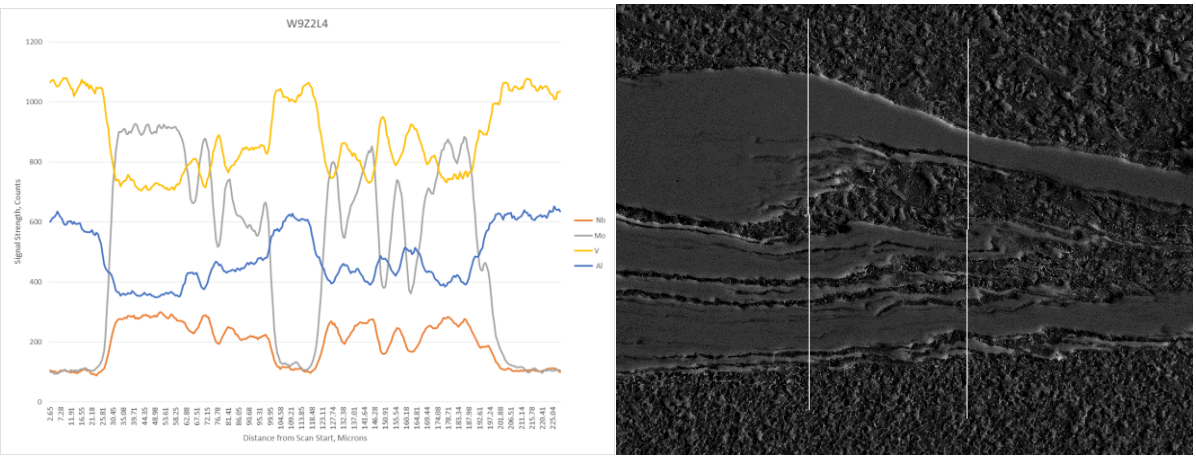

Figure C-58: Weld 9, Zone 2, Line 4 (left).

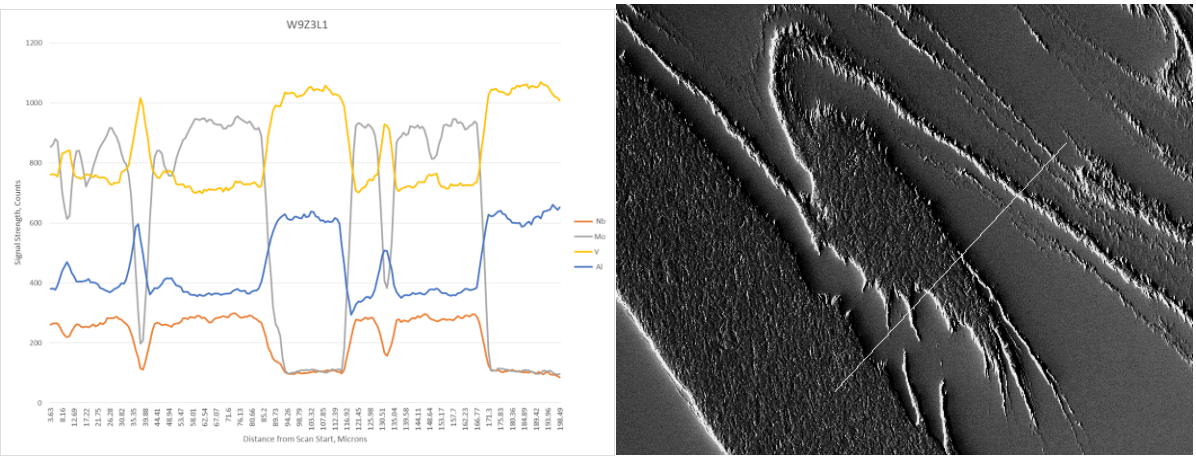

Figure C-59: Weld 9, Zone 3, Line 1.

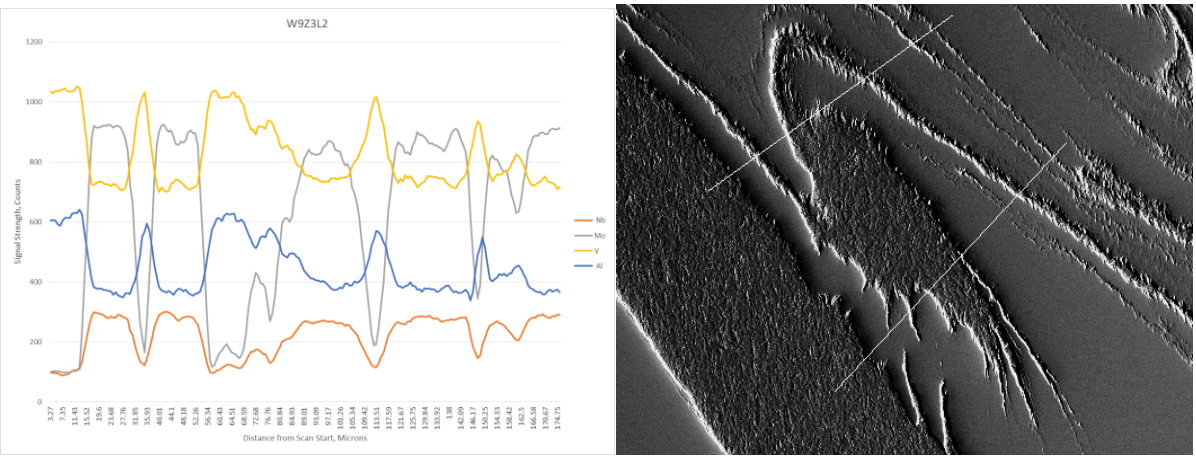

Figure C-60: Weld 9, Zone 3, Line 2 (top).

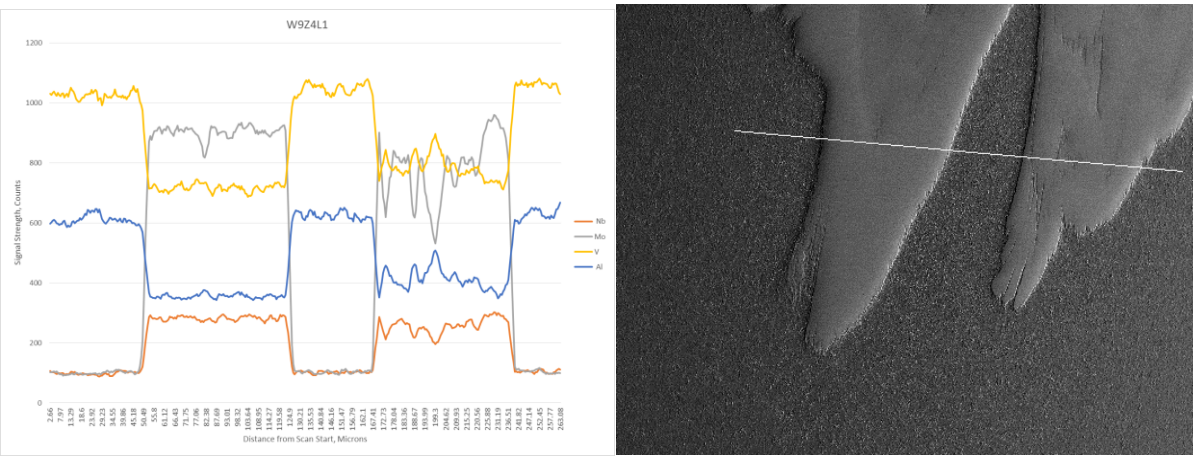

Figure C-61: Weld 9, Zone 4, Line 1.

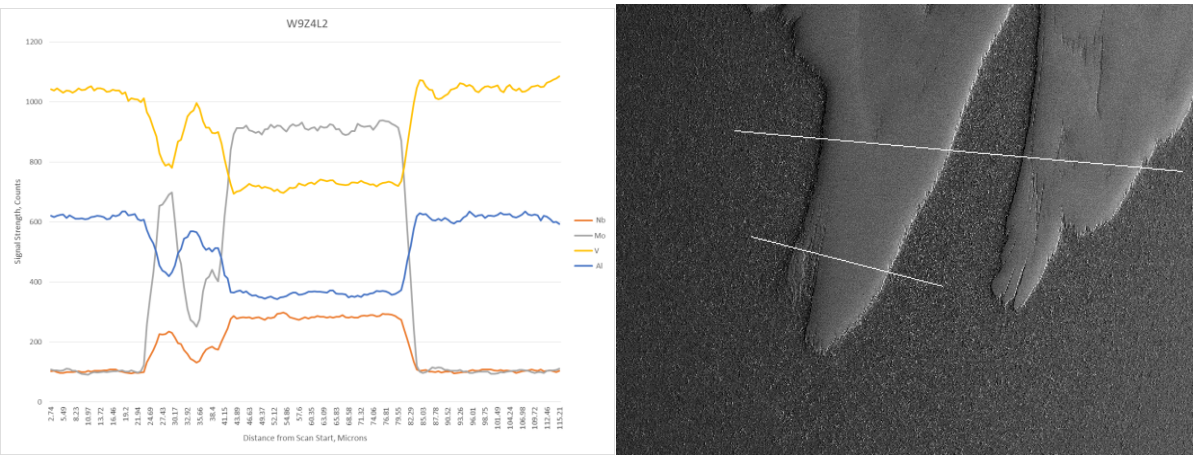

Figure C-62: Weld 9, Zone 4, Line 2 (bottom).

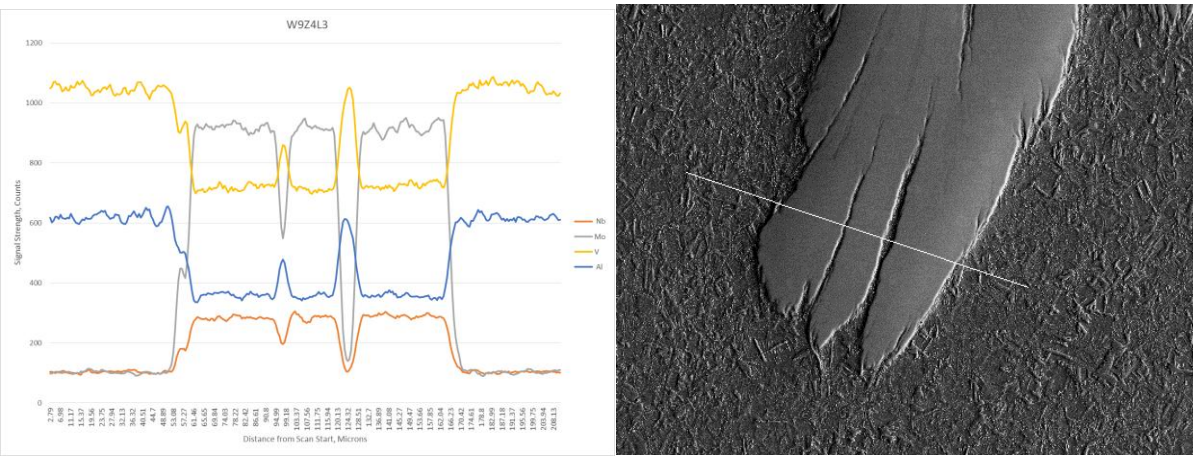

Figure C-63: Weld 9, Zone 4, Line 3.

VITA

Todd Wesley Morton

EDUCATION

Ph.D., August 2015

Materials Science and Engineering, University of Washington, Seattle, WA

Dissertation: Solid State Joining of Dissimilar Titanium Alloys

BSMSE, June 2007

Materials Science and Engineering, University of Washington, Seattle, WA

PROFESSIONAL EXPERIENCE

Materials, Process and Physics Engineer 2006-2015

Boeing Research and Technology, Seattle, WA

- Boeing Subject Matter Expert for titanium powder metallurgy; led development of technology, supply base, specifications and design allowables for low-cost powder metallurgy net and near-net shapes.
- Principle Investigator for multiple Metals Affordability Initiative consortium projects in the areas of titanium alloy development and computational modeling with budgets totaling over $2M.
- Technology Transfer Award for work on β21S plate in support of 737 MAX
- Led and executed research and development in the areas of titanium forging processing, hearth melting, microstructure characterization and modeling, alloy development and design value generation.

PUBLICATIONS AND PRESENTATIONS

P. Edwards, T. Morton, G. L. Ramsey, "Laser Welding ATI 425® Alloy", Key Engineering Materials, Vol. 436, pp. 205-211, May. 2010

Diffusion Bonding and Friction Stir Welding of Dissimilar Titanium Alloys, ICCES 2013, Bellevue, WA, 2013.

Powder Titanium: Near-Net Shapes and Beyond, Boeing Commercial Airplanes Technology Exchange, Everett, WA, 2013.

Titanium Materials & Development for Machining, Boeing Titanium Advanced Machining Group, Auburn, WA, 2014.

Boeing Research & Technology Titanium Alloy Development, Boeing Manufacturing & Fabrication Technology Review, Portland, OR, 2012.